

PROMETEUSZ KRYSPIN JASINSKI

ANALYSIS OF DIFFRACTIVE DISSOCIATION OF K^-
INTO $K^-\pi^+\pi^-$ ON A LIQUID HYDROGEN TARGET AT
THE COMPASS SPECTROMETER

ANALYSIS OF DIFFRACTIVE DISSOCIATION OF K^- INTO $K^-\pi^+\pi^-$
ON A LIQUID HYDROGEN TARGET AT THE COMPASS
SPECTROMETER

Dissertation
zu Erlangung des Grades
"Doktor der Naturwissenschaften"
am Fachbereich Physik der
Johannes Gutenberg-Universität in Mainz



JOHANNES GUTENBERG
UNIVERSITÄT MAINZ

PROMETEUSZ KRYSPIŃ JASINSKI
geb. in Duszniki Zdr. (Polen)
Mainz, den 02.01.2012

Prometeusz Kryspin Jasinski: *Analysis of diffractive dissociation of K^- into $K^- \pi^+ \pi^-$ on a liquid hydrogen target at the COMPASS Spectrometer,*
© 02.01.2012 Mainz D77

TAG DER MÜNDLICHEN PRÜFUNG: 22.12.2011

Dedicated to my beloved *Julia*
who made me the best gifts ever:
my lovely children,
Leonie & Paul.

ABSTRACT

The systematic exploration of excited meson and baryon states was the central topic of the COMmon Muon Proton Apparatus for Structure and Spectroscopy (COMPASS) physics program in the years 2008 and 2009 at the CERN facility. Particularly states non fitting a constituent quark model were searched for, identified by their exotic quantum numbers which are forbidden by a simple $q\bar{q}$ scheme. A high energetic hadron-beam on a fixed target yielded in resonances decaying into a large variety of final states. The diffractive and central production mechanisms allowed for a clean exclusive selection of channels such as $\pi^- p \rightarrow \pi^+ \pi^- \pi^+ p_{recoil}$, which then were analysed with a high precision and a huge number of events.

Apart from the main pion component in the negative hadron beam a small fraction of kaons of about 2.5% allowed the study of light strange resonances in the $K^- \pi^+ \pi^-$ decay channel. The best measurement in this channel was quoted to be so far the measurement of the WA03 experiment at CERN. The ACCMOR-collaboration has the data recorded and analysed with an experimental set-up very similar to the COMPASS-spectrometer [1]. COMPASS had therefore not only the ability to remeasure this channel with a significantly higher number of events and better precision to cross-check those over 30 years old results. Moreover, improved analysis methods together with new evidences from other experiments, are expected to enlighten our present picture of the hadron spectrum.

Chapter 1 introduces the concept of meson spectroscopy. The formation of bound quark anti-quark systems allows to interpret our measurements in terms of coupled quantum numbers, with properties as spin, charge conjugation and parity. Particularly kaonic isospin $I = \frac{1}{2}$ resonances are classified as proposed by group theory and differences to $I = 1$ and $I = 0$ states, formed mainly by u and d quarks and their anti-quarks, are pointed out.

That chapter introduces also the production mechanisms used to access those resonances and summarizes briefly the results obtained so far from previous experiments. Special emphasis is put on single diffraction of beam particles at high beam energies. Important observables as well as the main properties of the production mechanisms are defined, to understand how excited beam particles were identified in the COMPASS spectrometer.

Chapter 2 describes the most important parts of the COMPASS spectrometer as it was assembled in the years 2008 and 2009 under light meson spectroscopy considerations. The beam line and beam properties of the hadron beams are discussed since beam divergence was affecting the kaon identification in the initial state significantly. Detectors used to measure the large variety of processes are presented as well as information

about triggers, the [DAQ](#) and event reconstruction is given. As strategies had been developed for this analysis, to distinguish kaons from pions with the [CEDAR](#) detectors in the initial channel as well as with the [RICH](#) detector in the final states, those detectors are treated of in two separate chapters.

The [CEDAR](#) detector, designed to identify one kind of particles in the beam is described in chapter 3. The set-up, performance and measurement of it is discussed as well as stability issues of those detectors filled with pressurized helium are pointed out. The calculation of the separation-purity is described and alternative methods to analyse the signals of this detector are shown.

Chapter 4 deals with the final state [PID](#) at [COMPASS](#) with the help of the [RICH](#) detector. The [PID](#), based on individual likelihood cuts, is explained and a measurement of the performance of this detector for the data of the year 2008 is presented. This is particularly important as the resulting efficiency and purity distributions were used directly as an input to the [MC](#) acceptance simulations.

The strategy for the selection of diffractively produced $K^-\pi^+\pi^-$ events is shown in chapter 5. Apart from the detailed explanation of cuts applied to the data, quality studies showing the impact by initial state pions are presented. The model of a two-body decay of resonances into the final states is already motivated by observations of resonances in the invariant mass distributions of $K^-\pi^+$ and $\pi^+\pi^-$ track combinations as well as the corresponding Dalitz plots. About 270 000 events served finally as an input to [PWA](#).

As Partial Wave Analysis ([PWA](#)) needs further information on the available $K^-\pi^+\pi^-$ phase space and the spectrometer acceptance of it, a detailed [MC](#) simulation study was performed as depicted in chapter 6. There, the methods to simulate the signal response of several detectors are presented, used to process in total 44 million [MC](#) decays in the range of $0.8 \leq m(K^-\pi^+\pi^-) [\text{GeV}/c^2] < 3.0$.

Finally all information from event selection and [MC](#) studies was combined in the [PWA](#) to observe resonances, suspected to contribute to the invariant $K^-\pi^+\pi^-$ mass spectrum. The continuous momentum basis of final states was expanded in terms of discrete states with spin, parity and orbital angular momentum. A partial wave set was found with the help of mass independent fit algorithms, able to describe the observed $K^-\pi^+\pi^-$ spectrum and its dynamics in narrow bins of the invariant $K^-\pi^+\pi^-$ mass. Individual partial wave resonances are discussed and a proposal for a partial wave amplitude parametrization is made. The results of the mass independent analysis studies are the fundamental basis for a prospective mass dependent fit giving finally the information about poles, widths and coupling constants of contributing resonances.

ZUSAMMENFASSUNG

Das Hauptziel des COMmon Muon Proton Apparatus for Structure and Spectroscopy (COMPASS) Physikprogramms in den Jahren 2008 und 2009 am CERN Forschungszentrum war die systematische Erforschung angeregter Mesonen und Baryonen. Es wurden hauptsächlich Zustände gesucht, die nicht in ein Konstituentenquark-Modell passten, weil ihre exotischen Quantenzahlen im simplen $q\bar{q}$ -Schema verboten waren. Ein hochenergetischer Hadronstrahl auf einem festen Target erzeugte Resonanzen, die in eine große Vielfalt von Endzuständen zerfielen. Die diffraktiven und zentralen Produktionsmechanismen erlaubten eine saubere Auswahl von Kanälen wie $\pi^- p \rightarrow \pi^+ \pi^- \pi^+ p_{recoil}$, welche mit hoher Präzision und einer großen Anzahl von Ereignissen untersucht werden konnten.

Abgesehen von der pionischen Hauptkomponente des negativen Hadronstrahls erlaubte ein kleiner Anteil mit 2,5% an Kaonen das Studium leichter *seltsamer* Resonanzen im $K^- \pi^+ \pi^-$ Zerfallskanal. Die bis dato beste Messung in diesem Kanal kam vom WA03-Experiment am CERN. Die ACCMOR-Kollaboration hatte mit einem experimentellen Aufbau, sehr ähnlich dem des COMPASS-Spektrometers, die Daten aufgenommen und analysiert [1]. COMPASS hatte demnach nicht nur die Möglichkeit diesen Kanal mit einer deutlich höheren Anzahl von Ereignissen und besserer Präzision wieder zu untersuchen, um die über 30 Jahre alten Ergebnisse zu überprüfen. Vielmehr erwartete man, dass fortgeschrittene Analysemethoden zusammen mit den neuen Erkenntnissen anderer Experimente unser derzeitiges Bild des Hadronspektrums verbessern werden.

Kapitel 1 führt in das Konzept der Mesonenspektroskopie ein. Die Bildung von gebundenen Quark Anti-Quark Systemen erlaubt es, unsere Messungen mit Eigenschaften gekoppelter Quantenzahlen zu verstehen wie Spin, Ladungskojugation und Parität. Insbesondere werden kaonische Isospin $I = \frac{1}{2}$ Resonanzen klassifiziert, so wie es von der Gruppentheorie vorgeschlagen wird. Es werden die Unterschiede zu $I = 1$ und $I = 0$ Zuständen aufgezeigt, die hauptsächlich aus u- und d-Quarks sowie deren Anti-Quarks bestehen.

Das Kapitel führt auch in die Produktionsmechanismen ein, die verwendet wurde, um die Resonanzen zu erzeugen. Zudem werden die Ergebnisse vorangegangener Experimente kurz zusammengefasst. Dabei wird ein besonderer Schwerpunkt auf die einfache Diffraktion von Strahlteilchen bei hohen Strahlenergien gelegt. Die wichtigsten Observablen sowie die Haupteigenschaften der Produktionsprozesse werden erörtert, um die Identifikation angeregter Strahlteilchen im COMPASS Spektrometer zu verstehen.

Kapitel 2 beschreibt die wichtigsten Teile des COMPASS Spektrometers, wie es in den Jahren 2008 und 2009 aufgebaut wurde unter dem Aspekt der leichten Mesonenspektroskopie. Die Strahlführung und die

Strahleigenschaften der Hadronstrahlen werden diskutiert, da die Strahldivergenz die Kaonenidentifikation im Eingangszustand besonders beeinflusst hatte. Die Detektoren werden vorgestellt, die für die Messung der großen Anzahl von Prozessen benötigt werden. Zudem werden auch Informationen über die Trigger, die Datenaufnahme (DAQ) und Ereignisrekonstruktion vermittelt. Da im Rahmen dieser Analyse Strategien entwickelt wurden, um Kaonen von Pionen im Eingangskanal mit CEDAR Detektoren, als auch im Ausgangskanal mit dem RICH Detektor zu trennen, werden diese Detektoren in zwei gesonderten Kapiteln abgehandelt.

Der CEDAR Detektor, der entwickelt wurde um einen Typ von Teilchen im Strahl zu identifizieren, ist im Kapitel 3 beschrieben. Der Aufbau, die Leistung, deren Messung sowie Stabilitätsschwierigkeiten dieser Detektoren, die mit Helium unter hohem Druck gefüllt waren, werden behandelt. Die Berechnung der Separationsreinheit und alternative Methoden der Signalanalyse dieses Detektors werden gezeigt.

Kapitel 4 befasst sich mit der Endzustands-Teilchenidentifikation (PID) mit Hilfe des RICH Detektors. Die Teilchenidentifikation basierend auf individuellen Wahrscheinlichkeitsschnitten wird beschrieben und es wird eine Messung der Leistungsfähigkeit dieses Detektors für die Daten des Jahres 2008 vorgestellt. Dies ist besonders wichtig, da die resultierenden Effizienz- und Reinheitsverteilungen direkt als Eingangsgröße in den MC-Akzeptanzsimulationen verwendet wurden.

Die Strategie für die Auswahl diffraktiv erzeugter $K^-\pi^+\pi^-$ Ereignisse wird in Kapitel 5 gezeigt. Neben einer detaillierten Erklärung der Schnitte, die auf die Daten angewendet wurden, werden Qualitätsstudien vorgestellt, die den Einfluss von Pionen im Eingangszustand zeigen. Auf Grund der Beobachtungen von Resonanzen in den invarianten Masseverteilungen der $K^-\pi^+$ und $\pi^+\pi^-$ Teilchenspuren sowie in den dazugehörigen Dalitzplots wird bereits das Modell eines Zweikörperzerfalls der Resonanzen motiviert. Etwa 270 000 Ereignisse dienten letztendlich als Grundlage für eine Partialwellenanalyse (PWA).

Da die PWA weitere Informationen über den zur Verfügung stehenden Phasenraum und dessen Spektrometerakzeptanz benötigt, wurde eine detaillierte MC-Simulationsstudie durchgeführt, was in Kapitel 6 geschildert wird. Dort werden die Methoden zur Simulation der SSignalantwort verschiedener Detektoren vorgestellt. Dies wurde verwendet, um im Ganzen 44 Millionen MC Zerfälle im Bereich von $0.8 \leq m(K^-\pi^+\pi^-) [\text{GeV}/c^2] < 3.0$ zu simulieren.

Am Ende wurden alle Informationen der Ereignisauswahl und MC-Studien in der PWA zusammengeführt, um Resonanzen zu beobachten, von denen man vermutet, dass sie zum invarianten $K^-\pi^+\pi^-$ Massenspektrum beitragen. Die kontinuierliche Teilchenimpulsbasis der Endzustände wurde in Zustände mit Spin, Parität und Bahndrehimpuls entwickelt. Mit Hilfe von massenunabhängigen Fit-Algorithmen wurde ein Partialwellenset gefunden, welches das beobachtete $K^-\pi^+\pi^-$ Spektrum und dessen Dynamik in schmalen Abschnitten der invarianten $K^-\pi^+\pi^-$ Masse beschreiben konnte. Die individuellen Partialwellenresonanzen wer-

den diskutiert. Außerdem wird ein Vorschlag für eine Parametrisierung der Partialwellenamplituden gemacht. Die Ergebnisse der massenunabhängigen Analysestudien sind die grundlegende Basis für zukünftige massenabhängige Fits, die schlussendlich die Informationen über die Pole, Breiten und Kopplungskonstanten der beitragenden Resonanzen liefern.

CONTENTS

1	INTRODUCTION	1
1.1	Bound quark anti-quark systems	2
1.2	Strange Mesons	6
1.3	Diffractive hadron collisions at high energies	9
1.3.1	Observables	9
1.3.2	The reggeon picture	10
1.3.3	Production mechanisms at COMPASS	11
1.3.4	Competing experiments	13
2	THE COMPASS-EXPERIMENT	17
2.1	The COMPASS physics program	18
2.1.1	Physics with muon beams	18
2.1.2	Physics with hadron beams	19
2.2	Particle beams for COMPASS	22
2.3	The COMPASS spectrometer	29
2.3.1	Overview	29
2.3.2	The target region	29
2.3.3	Tracking	31
2.3.4	Calorimetry	34
2.3.5	Particle Identification	35
2.3.6	Further Detectors	36
2.3.7	Trigger	37
2.4	Summary	38
3	THE CEDAR DETECTOR	39
3.1	The functional principle	39
3.2	The mechanical design	42
3.3	Electronic processing	43
3.4	MC simulation	43
3.5	Comparison of online and offline pressure scans	48
3.6	Estimation of efficiency and purity	50
3.7	Performance for separation of kaons and pions	53
3.7.1	Dependence on beam divergence	53
3.7.2	Dependence on diaphragm opening	54
3.7.3	Dependence on beam intensity	54
3.7.4	Stability in the hadron runs 2008 and 2009	55
3.8	Performance for separation of protons and pions	58
3.9	PID with likelihood functions	59
3.10	Summary	61
4	THE RICH DETECTOR	63
4.1	Technical layout	63
4.2	PID with likelihood functions	64
4.3	Evaluation of the performance	66
4.4	Performance for different likelihood ratios	72
4.5	The simulation of the detector performance	75

4.6	Summary	76
5	EVENT SELECTION	79
5.1	Applied cuts	79
5.2	Invariant mass distributions of $K^-\pi^+\pi^-$ events	85
5.3	Armenteros diagrams of isobars	87
5.4	Selected Dalizplots	89
5.5	Background from pions in the beam	89
5.6	Summary	91
6	THE COMPASS MC SIMULATION	93
6.1	The Monte-Carlo simulation chain	93
6.2	Primary vertex properties	98
6.3	The CEDAR acceptance	100
6.4	The response of the RPD	100
6.5	The RICH performance	102
6.6	Simulation of $K^-\pi^+\pi^-$ flat phase space events	104
6.6.1	Spectrometer resolutions	104
6.6.2	Spectrometer acceptances	106
6.7	Summary	111
7	PARTIAL WAVE ANALYSIS	113
7.1	The parametrisation of the reaction process	113
7.2	The fit procedure	116
7.3	The PWA set	117
7.4	Mass independent fit results	119
7.4.1	The final partial wave set	120
7.4.2	The total intensity	121
7.4.3	$J^P = 1^+$ waves	122
7.4.4	$J^P = 2^-$ waves	126
7.4.5	$J^P = 0^-$ waves	129
7.4.6	$J^P = 2^+$ waves	131
7.4.7	$J^P = 1^-$ waves	133
7.4.8	Higher spins	134
7.4.9	The flat wave	134
7.5	Kinematic validation	137
7.6	Systematic influences	139
7.6.1	Central production	139
7.6.2	Background by pions in beam	140
7.6.3	Incoherent sources	141
7.7	Summary	142
	Conclusion	145
A	BEHIND THE CURTAINS	147
A.1	More details on partial wave analysis	147
A.1.1	The fully differential cross section of the diffractive process	147
A.1.2	Parametrizations of resonances	151
A.1.3	The reflectivity basis	154
A.1.4	The reference frames	154
A.2	Examples for a partial wave construction	156

A.3	Clebsch-Gordan coefficients and the isospin	159
B	PWA OF EVENTS WITH A RICH VETO	161
B.1	Event Selection	161
B.2	Spectrometer acceptances	162
B.3	Partial wave analysis	164
B.4	Summary	166
C	MORE DETAILS ON CEDARS	167
C.1	CEDAR photon propagation matrices	167
C.2	The Frontend-Electronics	168
D	SOFTWARE DOCUMENTATION	173
D.1	Basics for PHAST	173
D.2	The CEDAR Helper	174
D.3	The RPD Helper	174
D.4	CEDAR PID analysis	174
D.5	CEDAR offline pressure scan analysis	175
D.6	The CEDAR MC Simulation	176
D.7	Partial wave analysis packages at COMPASS	176
	BIBLIOGRAPHY	179

LIST OF FIGURES

Figure 1.1	A quark anti-quark pair in a potential	2
Figure 1.2	A schematic meson energy level diagram	4
Figure 1.3	The meson octet	8
Figure 1.4	Observables in diffractive processes	9
Figure 1.5	Diffractive dissociation and central production	12
Figure 1.6	Illustration of rapidity gaps	12
Figure 1.7	WA03: invariant $K^- \pi^+ \pi^-$ mass distribution	14
Figure 2.1	The COMPASS spectrometer 2008/2009	17
Figure 2.2	COMPASS physics program	18
Figure 2.3	CERN accelerator overview	22
Figure 2.4	The M2 beamline	23
Figure 2.5	The composition of the hadron beam	24
Figure 2.6	Extrapolated beam track distributions	26
Figure 2.7	A x-y beam track distribution at beam focus	27
Figure 2.8	Beam track divergence in the CEDAR region	27
Figure 2.9	The spectrometer 2008/2009 top and side view	28
Figure 2.10	A cut through the target region	30
Figure 2.11	Principle of Micromegas and GEMs	32
Figure 2.12	The layout of ECAL ₁ and ECAL ₂	34
Figure 2.13	Positions of trigger elements	37
Figure 3.1	A picture of a CEDAR detector	39
Figure 3.2	The principle of a CEDAR detector	40
Figure 3.3	A sliced CEDAR detector	44
Figure 3.4	Photon distributions at the diaphragm	46
Figure 3.5	A two dimensional photon distribution	47
Figure 3.6	The MC simulation compared to data from 1979	48
Figure 3.7	The MC simulation compared to data from 2008	49
Figure 3.8	A comparison of online and offline pressure scans	50
Figure 3.9	Mirroring of a pressure scan	52
Figure 3.10	The track angle acceptance	53
Figure 3.11	Pressure scans with different lid settings	55
Figure 3.12	Pressure scans with different beam intensities	56
Figure 3.13	CEDAR 2 pressure over time	56
Figure 3.14	CEDAR 2 temperature over time	57
Figure 3.15	Pressure over temperature in time	58
Figure 3.16	The purity over time	59
Figure 3.17	A pressure scan over protons and pions	59
Figure 3.18	Correlation of majority distributions	60
Figure 3.19	An invariant mass distribution of $\pi^- \pi^0$ tracks	60
Figure 4.1	An Illustration of the RICH detector	63
Figure 4.2	Reconstructed Cherenkov light angles	66
Figure 4.3	An Armenteros diagram of V_0 events	68

Figure 4.4	Invariant mass distributions of $\Lambda/\bar{\Lambda}$'s	68
Figure 4.5	An invariant mass distribution of K_s s	69
Figure 4.6	The invariant mass distribution for a $\phi(1020)$ hypothesis	70
Figure 4.7	Efficiency/purity matrices for π^- tracks	72
Figure 4.8	Efficiency/purity matrices for \bar{p} tracks	73
Figure 4.9	Efficiency/purity matrices for K^- tracks	74
Figure 4.10	Systematic impurity studies	77
Figure 4.11	Systematic efficiency studies	78
Figure 5.1	Primary vertex distributions	80
Figure 5.2	The co-planarity distribution	81
Figure 5.3	The energy distribution	82
Figure 5.4	The t' distribution	83
Figure 5.5	t' distribution over the invariant $K^-\pi^+\pi^-$ mass	83
Figure 5.6	t' slopes over the invariant $K^-\pi^+\pi^-$ mass	84
Figure 5.7	Reconstructed Cherenkov light angles after all cuts	84
Figure 5.8	Track properties at the RICH detector	85
Figure 5.9	RICH acceptance distributions	85
Figure 5.10	The invariant $K^-\pi^+\pi^-$ mass distribution	86
Figure 5.11	The invariant $K^-\pi^+$ mass distribution	86
Figure 5.12	The invariant $\pi^+\pi^-$ mass distribution	87
Figure 5.13	Armenteros plots for $K^-\pi^+$ track combinations	88
Figure 5.14	Armenteros plots for $\pi^+\pi^-$ track combinations	88
Figure 5.15	Selected Dalitz plots	89
Figure 5.16	The $K^-\pi^+\pi^-$ mass distribution for initial pions	90
Figure 5.17	the $K^-\pi^+$ mass distribution for pions in the beam	90
Figure 5.18	The $\pi^+\pi^-$ mass distribution for pions in the beam	91
Figure 6.1	Illustration of a COMPASS MC-chain	93
Figure 6.2	A dalitz plot of MC data	94
Figure 6.3	MC simulated t' distribution over invariant mass	95
Figure 6.4	The CORAL library	96
Figure 6.5	PHAST data processing scheme	97
Figure 6.6	beam track properties in MC data	98
Figure 6.7	primary vertex distribution in MC data	99
Figure 6.8	The energy distribution in MC data	100
Figure 6.9	CEDAR 2 MC accepted track angle distributions	101
Figure 6.10	The t' distribution in MC data	102
Figure 6.11	The coplanarity distribution in MC data	103
Figure 6.12	The RICH acceptance in MC data	103
Figure 6.13	The COMPASS energy resolution	104
Figure 6.14	The COMPASS invariant mass resolution	105
Figure 6.15	The COMPASS t' resolution	105
Figure 6.16	Invariant mass bin movement	106
Figure 6.17	Acceptance in the $K^-\pi^+\pi^-$ invariant mass	107
Figure 6.18	Acceptance in the $K^-\pi^+$ and $\pi^+\pi^-$ invariant mass	107
Figure 6.19	Acceptance over t' and the invariant $K^-\pi^+\pi^-$ mass	108
Figure 6.20	Acceptance over rapidities and the $K^-\pi^+\pi^-$ mass	109

Figure 6.21	Acceptance over $\cos \theta_{GJ}$ and the $K^-\pi^+\pi^-$ mass	110
Figure 6.22	Acceptance over ϕ_{TY} and the $K^-\pi^+\pi^-$ mass	110
Figure 7.1	Diffractive dissociation of kaons	114
Figure 7.2	Total intensity	121
Figure 7.3	Spin total of $J^P = 1^+$ waves	122
Figure 7.4	$J^P = 1^+$ $M = 0/1$ waves	124
Figure 7.5	$J^P = 1^+$ $M = 0$ D-waves	125
Figure 7.6	WA03: $J^P = 1^+$ $M = 0$ waves	125
Figure 7.7	Spin total of $J^P = 2^-$ waves	126
Figure 7.8	$J^P = 2^-$ waves	128
Figure 7.9	Spin total of $J^P = 0^-$ waves	129
Figure 7.10	$J^P = 0^-$ waves	130
Figure 7.11	Spin total of $J^P = 2^+$ waves	131
Figure 7.12	$J^P = 2^+$ $M = 1$ waves	132
Figure 7.13	Spin total by $J^P = 1^-$ waves	134
Figure 7.14	$J^P = 1^-$ $M = 1$ waves	135
Figure 7.15	Exemplary $J^P = 3^+$ waves	135
Figure 7.16	Impact of $J^P = 3^+$ on $J^P = 2^-$ waves	136
Figure 7.17	The flat wave	136
Figure 7.18	Kinematic validation for a low mass bin	137
Figure 7.19	Kinematic validation for a high mass bin	138
Figure 7.20	Rapidities over the invariant $K^-\pi^+\pi^-$ mass	139
Figure 7.21	Impact of $\pi^-\pi^+\pi^-$ background on $J^P = 2^-$ waves	141
Figure 7.22	The flat wave for different ranks	141
Figure 7.23	$J^P = 0^-$ waves for rank 1 and rank 2 fits	142
Figure A.1	Diffractive dissociation of kaons	148
Figure A.2	Argand diagram of the $(\pi^+\pi^-)$ -S wave	153
Figure A.3	Illustration of the production plane	155
Figure A.4	Illustration of the Gottfried-Jackson rest frame	156
Figure A.5	The isospin CG-coefficients	159
Figure B.1	$K^-\pi^+\pi^-$ invariant mass distribution	161
Figure B.2	Acceptance in the $K^-\pi^+\pi^-$ invariant mass	162
Figure B.3	Acceptance over $\cos \theta_{GJ}$ frame and $K^-\pi^+\pi^-$ mass	163
Figure B.4	Acceptance over ϕ_{TY} and $K^-\pi^+\pi^-$ mass	163
Figure B.5	$J^P = 1^+$ $M = 0$ waves	164
Figure B.6	kinematic validation for a low mass bin	165
Figure C.1	The CEDAR frontend electronics	170
Figure C.2	The frontend signal processing	171
Figure D.1	A screenshot of the pressure scan analysis gui	175

LIST OF TABLES

Table 1.1	Light quark properties	2
-----------	------------------------	---

Table 1.2	Strange mesons in the PDG review	7
Table 2.1	Summary of channels under investigation	21
Table 2.2	ECAL module properties	35
Table 3.1	CEDAR relevant beam properties in the H2 and M2 beam lines	47
Table 6.1	RPD key properties	101
Table 7.1	Initial partial wave isobars	118
Table 7.2	The final partial wave set	120
Table 7.3	$K_2^*(1430)$ fit parameter	133
Table 7.4	Summary of observed resonances	143
Table A.1	Isobars in an example	157
Table C.1	CEDAR dimensions	168

ACRONYMS

ACCMOR	Aamsterdam-CERN-Cracow-Munique-Oxford-Rutherford laboratory
ADC	Analog to Digital Converter
BC	Beam Counter
BMS	Beam Momentum Station
CEDAR	ChErencov Differential counter with Achromatic Ring focus
CERN	European Organization for Nuclear Research
CF	Constant Fraction
CHEOPS	CHarm Experiment with Omni-Purpose Setup
cms	center of mass system
COMGEANT	COMPASS GEANT
COMPASS	COMmon Muon Proton Apparatus for Structure and Spectroscopy
CORAL	COMPASS Reconstruction Library
CPU	Central Processor Unit
DAQ	Data Acquisition
DC	Drift Chamber
DCS	Detector Slow control
ECAL ₁	first electromagnetic calorimeter

ECAL₂ second electromagnetic calorimeter
ECAL Electromagnetic CALorimeter
ECL emitter coupled logic
EMC European Muon Collaboration
fwhm full width at half mean
GEM Gas Electron Multiplier
GJ Gottfried-Jackson
GPU Graphics Processor Unit
GUI Graphical User Interface
HCAL₁ first hadronic calorimeter
HCAL Hadronic CALorimeter
HMC Hadron Muon Collaboration
HV High Voltage
LAS Large Angle Spectrometer
LASS Large Angle Superconducting Solenoid
LAT Large Area Trackers
LBL Lawrence Berkeley National Laboratory
LE Leading Edge
lg length
LVDS Low-Voltage Differential Signaling
MC Monte Carlo
mDST mini Data Storage Tape
Micromega Micromesh Gaseous Structure
MW₁ first muon wall
MW Muon Wall
MWPC MultiWire Proportional Chamber
NIM Nuclear Instrumentation Module
NMC New Muon Collaboration
PC Personal Computer
PDG Particle Data Group

PHAST	PHysics Analysis Software Tools
PID	Particle Identification
PM	Photo Multiplier
PWA	Partial Wave Analysis
QCD	Quantum Chromo Dynamics
RICH	Ring Imaging CHerencov
rms	root mean square
RPD	Recoil Proton Detector
SADC	Sampling Analog to Digital Converter
SAS	Small Angle Spectrometer
SAT	Small Area Trackers
SciFi	Scintillating Fibre
Silicon	Silicon microstrip
SLAC	Stanford Linear Accelerator Center
SM ₁	first Spectrometer Magnet
SM ₂	second Spectrometer Magnet
SMC	Spin Muon Collaboration
SPS	Super Proton Synchrotron
Straw	Straw tube drift chamber
TDC	Time to Digital Converter
TY	Treiman-Yang
VME	VERSAModule Eurocard bus
VSAT	Very Small Area Trackers
W ₄₅	large area drift chambers
WLS	optically active WaveLength Shifting

INTRODUCTION

Our present understanding of matter and the forces inside is based on the *standard model*, describing an interplay of elementary particles in the framework of field theory [2]. Three generations of spin 1/2 matter-particles, *fermions*, are known. Each generation consists of two leptons and two quarks as well as their anti-particles. The interaction between those is mediated via *bosons*, spin-one particles. While electroweak forces are coupling to all fermions, only quarks are bound by strong forces to hadrons. Strong, as no matter how much energy is applied, no free quarks were observed so far. This experimental finding is also known as the *confinement*.

The interaction of quarks and gluons is the topic of Quantum Chromodynamics (QCD) [3, 4], a field theory describing the structure and dynamics of hadrons. At large energies (small scales) where coupling of gluons and quarks is small, perturbative techniques can be applied to solve those complex equations. On that basis the structure of nucleons can be understood as a pool of *asymptotically free* particles, called *partons* [5].

At low energies (large scales) classic perturbative techniques fail as coupling must be taken into account. Mainly two approaches were developed to calculate strong forces and the dynamics of light bound systems:

Chiral perturbation theory is motivated by the a left-right symmetry of the QCD Lagrangian in the limit of mass-less quarks. An effective field is constructed, consisting of the lightest pseudo-scalar mesons instead of quarks and gluons. It allows to calculate light meson interactions and decays, but is affected by the broken symmetry due to the non vanishing mass of the quarks [4].

Direct calculations based on the original QCD Lagrangian are possible by quantisation of the space-time dimensions. Calculations on the *lattice* became popular in the past years, as increasing computing power allowed for the precise determination of both, static and dynamic properties of bound quark systems [6] starting from the first QCD principles.

Despite the very promising developments of physics theories in the past years, the large number of experimentally observed states is to this day not fully understood. This is why new particle states are presented in the framework of a *constituent quark model*. It turned out to be very successful to describe the observed particles as bound quark anti-(quark) systems in the case of mesons or three-quark systems for baryons [7, 8] as it is discussed in the following. Particularly the status of strange light meson spectroscopy is summarized, giving also an introduction to the production mechanisms of resonances.

property/flavour	d	u	s	\bar{d}	\bar{u}	\bar{s}
Q electric charge	$-\frac{1}{3}$	$+\frac{2}{3}$	$-\frac{1}{3}$	$+\frac{1}{3}$	$-\frac{2}{3}$	$+\frac{1}{3}$
$ \vec{I} $ isospin	$\frac{1}{2}$	$\frac{1}{2}$	0	$\frac{1}{2}$	$\frac{1}{2}$	0
\vec{I}_z z-component	$-\frac{1}{2}$	$+\frac{1}{2}$	0	$+\frac{1}{2}$	$-\frac{1}{2}$	0
\mathcal{S} strangeness	0	0	-1	0	0	+1

Table 1.1: The quantum numbers of light quarks as summarized in the PDG review [11].

1.1 BOUND QUARK ANTI-QUARK SYSTEMS

The combination of a quark with an anti-quark creates a state belonging to the class of mesons, particles with integral spin. In order to classify and group those states further, some results as derived by group theory [9] [10] are recalled:

The three lightest quarks (u, d, s) and their anti-quarks (\bar{u} , \bar{d} , \bar{s}) with their basic quantum numbers as given in table 1.1. For further classification a quark wave function is considered as

$$\chi \equiv |L, I_z\rangle \otimes |s, s_z\rangle \otimes |\vec{r}\rangle \otimes |Q\rangle \otimes |\mathcal{S}\rangle \quad (1.1)$$

containing in addition to the quantum states like isospin \vec{I} , spin \vec{s} , the charge Q and the strangeness \mathcal{S} also the spatial information \vec{r} . The anti-quark function is denoted to be orthogonal to the quark function with χ^* and explicit representations are discussed in the following. Notice that the quark mass is here neglected.

A meson is represented by a superposition of coupled $q\bar{q}$ states in a Hilbert-space.

$$M = \sum_{i=u,d,s} \sum_{j=\bar{u},\bar{d},\bar{s}} C_i^j (\chi^i \otimes \chi_j^*) \quad (1.2)$$

C_i^j is a normalization factor.

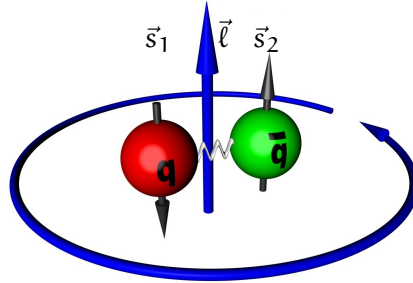


Figure 1.1: Illustration of a quark anti-quark pair in a potential. The two spins \vec{s}_1 and \vec{s}_2 of the quarks couple together with the angular orbital momentum \vec{l} between them to a total spin \vec{j} .

The corresponding picture 1.1 describes not only the simple coupling of quark spins but also a possible angular momentum between those two quarks in a central potential.

One can draw now conclusions on meson properties based on the available coupled quantum numbers.

TOTAL SPIN The spin state is specified by the magnitude of the spin $|\vec{s}| = s = \frac{1}{2}$ and it's spin projection $s_z = -\frac{1}{2}, \frac{1}{2}$. Obviously only two combinations are possible. One where the spins are anti-parallel and one where the spins couple to zero.

$$\vec{S} = \vec{s}_1 + \vec{s}_2 \rightarrow S = 0, 1 \quad (1.3)$$

In addition orbital angular momentum between those quarks couples with the spin to the total spin \vec{J} .

$$\vec{J} = \vec{S} + \vec{\ell} \quad (1.4)$$

Following the familiar spin coupling rules one obtains the possible magnitudes of the total spin.

$$|\ell - S| \leq J \leq |\ell + S| \quad (1.5)$$

The magnitude J is one of the quantum numbers used for classifications of mesonic states.

SPATIAL FUNCTION AND PARITY According to the picture of a $q\bar{q}$ system in a central potential one usually uses the orbital representation for the spatial function state

$$|\vec{r}\rangle \mapsto |r\theta\phi\rangle = R_\ell(r)Y_{\ell J_z}(\theta, \phi) \quad (1.6)$$

where the radial component is separated from the orbital component represented by spherical functions. One can show that the application of the reflection operator \tilde{P} to the meson function

$$\tilde{P}\chi(\vec{r}, \dots) = \chi(-\vec{r}, \dots) \quad (1.7)$$

to the eigenvalues P, also called parity, leads since spherical functions eigenstates of the reflection operator are. The eigenvalues are given by

$$P = (-1)^{(\ell+1)} \quad (1.8)$$

taking the intrinsic parity of $q\bar{q}$ pairs into account. The parity P is used for the classification of mesons.

CHARGE AND C-PARITY Charge, a scalar, couples in a trivial way to integer values.

$$Q_\Sigma = -1, 0, 1 \quad (1.9)$$

The charge conjugation operator \tilde{C} exchanges the quarks by their anti-quarks.

$$\tilde{C}\chi = \chi^* \quad (1.10)$$

Wave functions of neutral particles $Q = 0$ containing a quark and the corresponding anti-quark are eigenstates of the charge conjugation with the eigenvalues called C-parity C . It can be shown that C-parity depends only on the coupled spin S and angular momentum ℓ .

$$C = (-1)^{(\ell+S)} \quad (1.11)$$

C-parity is also used to classify mesonic states. For charged states the C-parity of the corresponding neutral state is used and is therefore not a strictly separating quantum number as it will be shown for the case of mesons with strangeness.

	S=0					S=1				
$\ell=$	0	1	2	3	4	0	1	2	3	4
J=	0	1	2	3	4	1	0,1,2	1,2,3	2,3,4	4,5,6
P=	-	+	-	+	-	-	+	-	+	-
C=	+	-	+	-	+	-	+	-	+	-
Mass [GeV/c ²]										
0.5										

Figure 1.2: Schematic meson level diagram as it is the topic of meson spectroscopy. The energy of the $q\bar{q}$ in a central potential corresponds to the mass of the meson. The ground state would be a kaon for isospin $I = 1/2$ mesons. The remaining excited states are drawn with arbitrary masses. For a detailed discussion of the measured level schemes is found for example in [12].

MESON LEVEL SCHEME The figure 1.2 shows a schematic meson level scheme as it is the topic of meson spectroscopy since the idea of bound $q\bar{q}$ systems. The energy level depends on the spin and orbital angular momentum and corresponds to the mass of the meson. The evaluation of the potential is one of the fields of research that need input from experiments providing masses and widths of the states [13]. In order to distinguish states with the same total spins J one has also to take the parity P and charge conjugation C into account.

MESON MULTIPLETS, NATURALITY It is common to sort mesons according to their total spin, parity and C-parity. A $q\bar{q}$ state can only couple (compare scheme 1.2) to

$$J^{PC} = 0^{-+}, 1^{--}, 1^{+-}, 0^{++}, 1^{++}, \text{etc.} \quad (1.12)$$

while

$$J^{PC} = 0^{+-}, 1^{-+}, 2^{+-}, 3^{-+}, \text{etc.} \quad (1.13)$$

are states that cannot be described in a simple $q\bar{q}$ model. These exotic quantum numbers are of prime interest for COMPASS. QCD models [11] predict so called glue balls, states consisting of only excited self coupling gluons g , or hybrids, $q\bar{q}g$ states that can have these forbidden quantum numbers. Those states are not the topic of this thesis but are touched in chapter 2 as they are an important topic of the COMPASS hadron program.

It was mentioned that C-parity is only defined for neutral states. It will be shown that it is possible to generalize C-parity in order to separate also charged states.

ISOSPIN AND STRANGENESS The introduction of isospin \vec{I} to quarks was mainly motivated by the similar properties of neutrons and protons when neglecting proton charge. Werner Heisenberg introduced a symmetry between these particles in order to treat them as one and the same particle with different states. The term of isospin was then mapped in a later stage on quantum numbers of the quarks forming the baryons. Heavier quarks as the s quark have an isospin of $|\vec{I}| = 0$. In order to separate the s quark wave function from other quarks, strangeness S is introduced.

Group theory teaches us that the coupling of the triplet flavours with the anti-triplets gives nine different combinations of $q\bar{q}$ pairs where three of them are superpositions of wave functions with isospin $I_3 = 0$.

A possible representation was introduced with so called Gell-Mann-matrices [14] and is summarized in the familiar picture 1.3 developed also by Nishijima [15]. Drawing the possible $q\bar{q}$ states in a plane spanned by strangeness ¹ and the isospin projection I_3 . The lower figures show the physical $\ell = 0$ and (anti-)parallel spin states assigned to the $q\bar{q}$ states of the *meson nonet*.

G-PARITY Charged states consisting of u and d quarks and their corresponding anti-quarks can be separated in case of same J^P by a new operator \tilde{G} performing a rotation in the isospin space in addition to the quark anti-quark transition of the \tilde{C} operator 1.10.

$$\tilde{G} = \tilde{C} \exp(i\pi I_2) \quad (1.14)$$

Now it is possible to separate also charged mesons by classifying them by their isospin and G-parity eigenvalues I^G . This separation is an extension of the J^{PC} classification in the $SU(2)$ subgroup formed by the u d states.

¹ Correctly speaking hypercharge $\mathcal{Y} = \mathcal{B} + S$ was introduced where also the baryon quantum number \mathcal{B} is used to separate baryon wave functions from meson wave functions.

U-SPIN V-SPIN T-SPIN Similar operations can be found in the Gell-Mann-matrix representation for the $SU(3)$ (u,d,s) group. A \tilde{T} operator performs then the rotation in the isospin space without changing the strangeness while \tilde{U} and \tilde{V} operators would rotate the isospin space and in addition the strangeness ².

This is not discussed here in detail as a physical complication is found: The mass of the strange quark is much larger than that of the u and d quarks. This causes a spontaneous breaking of the so far developed $SU(3)$ symmetry. It is thus not possible to find an operator corresponding to \tilde{G} or \tilde{C} for eigenstates of $q\bar{q}$ pairs with masses in the isospin $I_3 = \frac{1}{2}$ sector.

The wave function of the $q\bar{q}$ system is therefore experimentally not uniquely distinguishable. Regarding figure 1.2 again, showing the possible meson masses in a level diagram, one will notice that total spins $J^P = 1^+$ or $J^P = 2^-$ are found as a singlet state with the spin $S = 0$ as well as a triplet state $S = 1$. Wave functions formed by u, \bar{u}, d, \bar{d} , are further categorized by their C-parity or G-parity. Strange mesons with same J^P will mix.

1.2 STRANGE MESONS

Table 1.2 gives an overview of light strange mesons as listed in the PDG's review [11]. Those are grouped to same total spins and parities. Immediately one notices the large number of entries quoted to need further confirmation as there exists no sufficient evidence for those resonances. In addition the observed mass in a charged 3-particle decay is given when observed in this particular channel. Observations by different experiments in different channels were grouped by the PDG even when masses differed significantly. This is for example the case for the $K_1(1650)$ that was observed at $1.8 \text{ GeV}/c^2$ in the charged 3-particle decay.

The access to the strange meson spectroscopy is often granted by initial strangeness in a beam. At lower energies, so called formation experiments analysing processes as $K^-p \rightarrow K^-\pi^+n$ [16] provided first high precision measurements of resonances decaying into $K\pi$ channels. Three particle decays on the other hand are mostly the result of so called diffractive scattering on a nucleus. In the following the production of strange resonances decaying into charged $K\pi\pi$ channels is considered. Other channels are reviewed in [17].

² The U-parity would connect mirrored particles lying on the equi-charge line in figure 1.3 while T-parity expresses the symmetry on the isospin line.

J^P	name	mass	width	seen in $K^\pm\pi^\mp\pi^\pm$	note
0^-	K	0.494	—	—	
0^-	K(1460)	1.460	0.260	$1.460 \Gamma 0.260$	needs confirmation
0^-	K(1830)	1.830	0.250	—	needs confirmation
0^+	$K_0^*(1430)$	1.425	0.270	—	
0^+	$K_0^*(1950)$	1.945	0.201	—	needs confirmation
1^-	$K^*(892)$	0.892	0.051	—	
1^-	$K^*(1410)$	1.414	0.232	—	
1^-	$K^*(1680)$	1.717	0.322	—	
1^+	$K_1(1270)$	1.272	0.090	$1.270 \Gamma 0.090$	
1^+	$K_1(1400)$	1.403	0.090	$1.410 \Gamma 0.195$	
1^+	$K_1(1650)$	1.650	0.150	$1.800 \Gamma 0.250$	needs confirmation
2^-	$K_2(1580)$	1.580	0.110	$1.580 \Gamma 0.110$	needs confirmation
2^-	$K_2(1770)$	1.773	0.186	$1.780 \Gamma 0.210$	
2^-	$K_2(1820)$	1.816	0.276	$1.840 \Gamma 0.230$	
2^-	$K_2(2250)$	2.247	0.180	—	needs confirmation
2^+	$K_2^*(1430)$	1.426	0.099	$1.421 \Gamma 0.100$	
2^+	$K_2^*(1980)$	1.973	0.373	—	needs confirmation
3^-	$K_3(1780)$	1.776	0.159	—	
3^+	$K_3(2320)$	2.324	0.180	—	needs confirmation
4^-	$K_4^*(2500)$	2.490	0.250	—	needs confirmation
4^+	$K_4^*(2045)$	2.045	0.198	—	
5^-	$K_5^*(2380)$	2.382	0.178	—	needs confirmation

Table 1.2: List of strange mesons as summarized in the PDG review [11]. Masses and widths are given in $[\text{GeV}/c^2]$. If a decay into $K^-\pi^+\pi^-$ or the charged conjugated channel was observed this mass and width are given in addition.

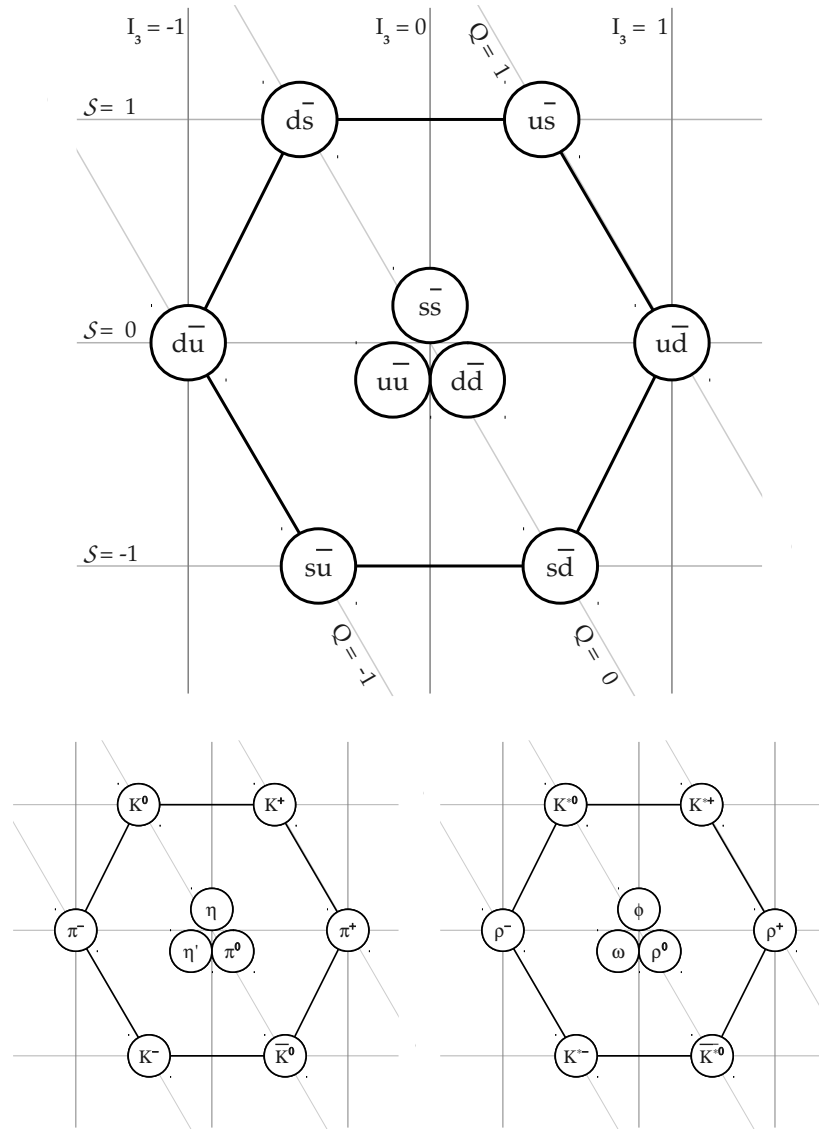


Figure 1.3: Top: Meson nonet as it is representing quark anti-quark eigenstate wave functions [11]. Particles assigned to those wave functions are shown for $l = 0$ $S = 0$ lower left and $S = 1$ lower right. π^0 corresponds to an isospin $I_3 = 1$ wave function. η and η' are a mixture of the symmetric and anti-symmetric $I_3 = 0$ wave functions. For a parallel quark anti-quark spin the $\phi(1020)$ is understood to be a nearly pure $s\bar{s}$ state.

1.3 DIFFRACTIVE HADRON COLLISIONS AT HIGH ENERGIES

The description of a particle by a wave function leads to two different classes in high energetic hadron-hadron collisions. One, the elastic scattering, can be described mostly based on methods derived from the classical analogous, to the diffraction of light on a black disc. The differential cross section falls rapidly as a function of the momentum transfer \sqrt{t} between scattered hadrons and is therefore a mechanism of minor importance at higher t compared to the second, the diffractive mechanism [18].

The data analysed in this thesis contains only events of high t . The reason is described in section 2.3.7 and is the acceptance of the trigger set-up in the years 2008 and 2009. For a deeper discussion of elastic processes the reader is referred to [19].

So the dominant process here is diffraction of either one hadron or even both hadrons. In order to measure those processes, observables in a collision will be recalled for a diffractive process before introducing finally the picture of a reggeon and it's subgroup, the pomeron.

1.3.1 Observables

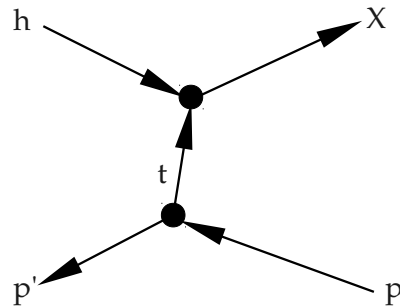


Figure 1.4: Illustration of kinematic variables in a diffractive two-body reaction in the *cms*. A hadron h scatters off a proton p . Four-momentum (see text for the meaning of t) is transferred to the hadron that might be excited to a particle X higher in mass with a scattered proton p' in the final state. Here t has apart from the large transversal component a small longitudinal as $m_X > m_h$.

Consider a hadron h recoiling on a proton p as illustrated in figure 1.4 in it's *cms*. In that case momentum \sqrt{t} is transferred from the proton to the hadron. The first mandelstam [20] variable specifying this process is then defined by

$$t = (X - h)^2 = (p' - p)^2 \quad (1.15)$$

where X , h , p' and p four-vectors of the respective particles of the same name are. The kinematic limit for a scattering angle of $\theta = 0$ is given by

$$t_{\min} = \left[\frac{m_h^2 - m_X^2 - m_p^2 + m_{p'}^2}{2\sqrt{s}} \right]^2 - (h - p_X)^2 \quad (1.16)$$

where the second mandelstam variable is already included in the total center of mass energy \sqrt{s} .

$$s = (h + p)^2 = (X + p')^2 . \quad (1.17)$$

Moreover $|t_{\min}|$ simplifies for a high energetic hadron beam on a proton target that stays intact ($m_p = m_{p'}$) to

$$|t_{\min}| \approx \frac{(m_X^2 - m_h^2)^2}{4 |\vec{h}_{lab}^2|} \quad (1.18)$$

with the beam momentum \vec{h}_{lab} as given in the laboratory frame [21]. In other words is t_{\min} the longitudinal component of the exchanged four-momentum transfer in the [cms](#).

For elastic scattering it follows

$$m_h = m_X \Rightarrow t_{\min} = 0 \quad (1.19)$$

meaning that t is purely transversal. Since an excited state X is larger in mass than h , $t \mapsto t(m_X)$ depends on the mass of the resonance. To eliminate this mass dependence of the production process one introduces a new variable

$$t' = |t| - |t_{\min}| . \quad (1.20)$$

Ideally, t' would be separated from the produced resonance X and one is able to analyse the production amplitudes in bins of t' independent of m_X . In reality it will be shown in [chapter 5](#) that those quantities still depend on each other as the exchanged reggeon (see next section) is still sensitive to the internal structure of X .

Finally it is obvious that an excited state X decays emitting particles. The available phase space τ for the decay particles and a fixed beam energy is then fully determined by 5 variables. The most evident variables here are the four-vector of the resonance X and the reduced momentum transfer t' .

1.3.2 The reggeon picture

Diffraction as described by M. L. Good and W. D. Walker 1960 [22] was able to predict important properties of processes that are observed at high energy hadron collisions. The connection to a polarized light wave passing a disc with different refractive indices for the two polarization vectors leads to the conclusion that the intrinsic quantum numbers of

the beam particle h as electric charge, isospin and $C(G)$ -parity have to be conserved by the resonance X while the target proton has to stay intact. The second is pointed out to be not strictly conserved as G -parity is not an eigenstate of the baryonic wave functions and protons might be excited to N^* resonances, too.

The diffractive picture gained predictive power by the introduction of a reggeon as the exchanged particle [23]. It was well known how to expand a scattering amplitude in terms of Legendre-Polynomials P_ℓ where ℓ is the orbital angular momentum between the two scattered particles. T. Regge extended this theory by introduction of a complex orbital angular momentum showing the universality of this expansion in the complex s - t -plane also for resonant processes. The application of this theory to diffraction of pions on nucleons [24] 1963 helped to understand the process as a multi particle exchange in the t -channel. The exchanged particles do not carry any charge nor color.

The most important extension of this theory was the introduction of the so called pomeron by Vladimir Gribov. A pomeron is a reggeon with the quantum numbers of the vacuum $J^{PC} = 0^{++}$ and was predicted to become the dominant exchange particle at high energies. That way the problem was solved where regge theory alone could not explain the slowly raising cross section of hadron-hadron collisions at very high energies [18].

Although this theory is mostly motivated and tuned by experimental observations it is still a popular terminology in high energy collisions. QCD, developed about 10 years later, is surely a more fundamental basis to describe the particle exchange in strong processes. Nevertheless predictive power in kinematic descriptions is still low. Up to today some efforts are spent to connect the regge-theory with non perturbative QCD. Reggeon exchange is understood as quark anti-quark gluon structures bound to objects and exchanged between the interaction vertices. The most famous expression is the BKFL-pomeron named after the authors of the original paper [25]. For an overview the reader might also consider [26].

As the production mechanism itself is not the topic of this thesis, only experimental facts with the defined terminology are summarized.

1.3.3 Production mechanisms at COMPASS

In section 1.3.1 the diffractive process for a hadron beam on a proton target was already introduced in quite some detail. The most important experimental facts needed for further analysis are summarized and completed by the picture of a reggeon exchange. In addition the central production is introduced as a special diffractive process where both interaction particles stay intact.

Figure 1.5 shows the two processes recorded by the COMPASS set-up in the years 2008 and 2009. While diffractive dissociation involves one exchanged reggeon exciting the beam hadron to a resonance X , central production is believed to be the fusion of two gluons to a resonance X .

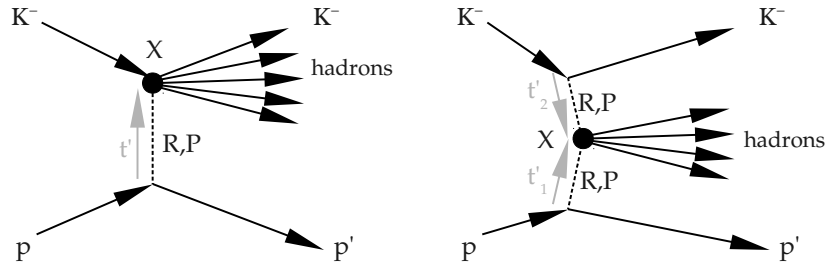


Figure 1.5: Feynmanlike graph for single diffractive dissociation of kaons (left) and central production (right) on a nuclear target. The two processes can be distinguished by rapidity gaps between the fastest particle and the remaining hadrons.

RAPIDITY GAPS The classification of diffractive mechanisms is done for high energy collision experiments in the laboratory frame. The *rapidity* y of the particles [11] is defined by

$$y = \frac{1}{2} \ln \left(\frac{E/c + p_z}{E/c - p_z} \right) = \tanh^{-1} \left(\frac{p_z}{E/c} \right) \quad (1.21)$$

with the z -axis along the beam direction. The rapidity is a quantity expressing the speed of movement parallel to the beam axis. The difference in rapidities between two particles is invariant under Lorentz-transformations. The maximum rapidity a beam kaon with a momentum of 190 GeV/c can have is $y \approx 6.65$, a pion would achieve already $y \approx 7.91$ and a proton only $y \approx 5.96$ for very small scattering angles.

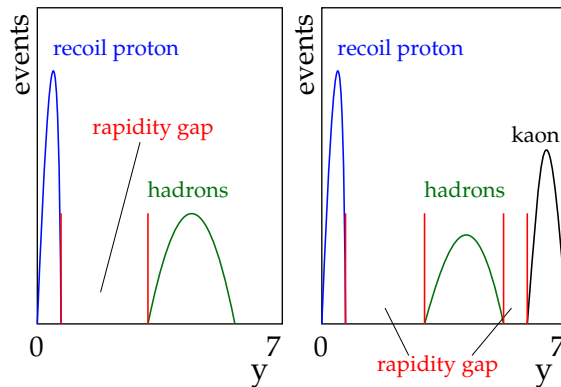


Figure 1.6: Illustration of rapidity gaps in single diffractive (left) and central (right) production mechanisms. Diffractive processes contain no rapidity gap between final state particles of the diffraction vertex. Centrally produced hadrons are slower than the fastest kaon as the kaon exchanged only a small momentum fraction by a reggeon.

The previously mentioned processes are then defined by one or more *rapidity-gaps*. Figure 1.6 illustrates experimentally found rapidity gaps in diffractive and central production mechanisms for a high energetic hadron beam on a fixed target. The diffractive process as well as the

central process show a large difference between the rapidity of the recoil proton and the rest of the final state particles. This leads to the assumption that *the upper production vertex factorizes off the lower interaction vertex*. Then one finds at very high [cms](#) energies two further classes of processes. For one class rapidities between the final state hadrons show no significant differences. Those events are believed to be of pure single diffractive nature. The other case is a rapidity gap that is found between one fast scattered beam particle and the system formed by the rest of the final state hadrons. Those events are called centrally produced. Naturally no resonant structure between the fast beam particle and the resonance X is expected then [19].

SUMMARY OF PROPERTIES The main properties of the diffractive processes needed for a distinct measurement are characterized by:

- Momentum is transferred between the target particle and the beam particle.
- The beam particle is excited and decays into several final state hadrons.
- Charge, energy, parity, C(G)-parity and flavour of the beam particle is conserved.
- The resonance X the beam particle h and the recoil proton lie in a production plane.
- The proton can be excited to an N* resonance.
- The deflection angle and thus t is small and follows an exponential form.

These properties motivated the experimental set-up for a measurement of diffractively produced resonances, not only at the [COMPASS](#) spectrometer.

1.3.4 Competing experiments

One of the first conclusive measurements of strange mesons decaying into three charged final states was performed at the Stanford Linear Accelerator Center ([SLAC](#)) with a 13 GeV/c kaon beam on a liquid hydrogen target. A dipole magnet followed by 9 planes of wire spark chambers measured momenta of the final particle in the diffractive reaction $K^\pm + p \rightarrow K^\pm + \pi^+ + \pi^- + p_{\text{recoil}}$. A pressurized multi-cell Cherenkov counter performed the final state Particle Identification ([PID](#)) of kaon and pion tracks. In total 72 000 events were recorded in the $K^+ + \pi^+ + \pi^-$ final state and 56 000 in the charge conjugated case. First evidence for two resonances in the $J^P = 1^+$ wave and a $J^P = 0^-$ resonance was found by a [PWA](#) in the range of 1.0 – 1.6 GeV/c² [27] published 1976.

Previous experiments as the one performed at the Serpukhov Proton Accelerator [28] suffered not only from a low number of events but also

from systematic uncertainties. The Serpukhov experiment for example analysed around 10 000 events from 5 periods of data taking with different incident beam energies where final state PID could not be performed due to technical difficulties.

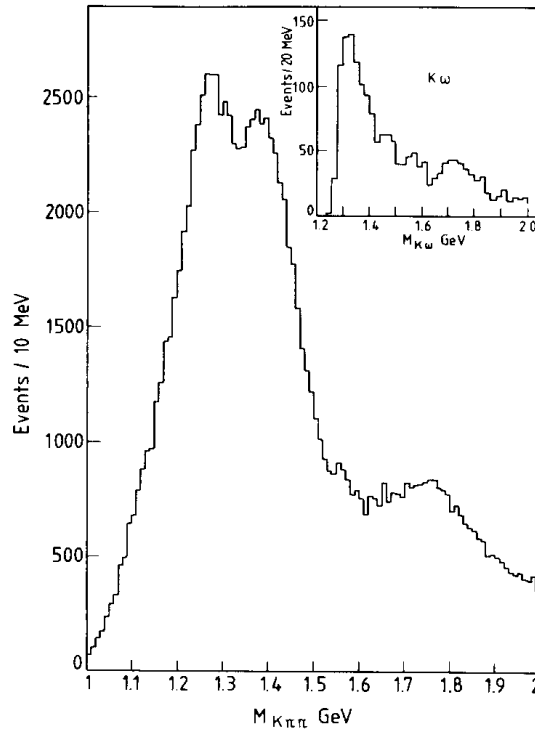


Figure 1.7: The $K^- \pi^+ \pi^-$ mass spectrum as published by the ACCMOR collaboration [1] in 1981. About 200 000 events were recorded in the momentum transfer region of $0 \leq t' \leq 0.7 \text{ GeV}^2/c^2$.

In 1980 the ACCMOR-collaboration published the analysis of diffractive production of strange mesons with a 63 GeV/c hadron beam on a 50 cm liquid hydrogen target. The particles were detected by a two stage spectrometer [29]. Kaons in the hadron beam were separated by two ChErenkov Differential counter with Achromatic Ring focus (CEDAR) detectors in front of the target. Final state PID detectors were two multi-cell Cherenkov counters in the second stage of the spectrometer. 200 000 events of the reaction $K^- + p \rightarrow K^- + \pi^+ + \pi^- + p_{\text{recoil}}$ were collected and dedicated to PWA giving the most evident results of resonances decaying in the $K^- \pi^+ \pi^-$ final state so far. The invariant $K^- \pi^+ \pi^-$ mass distribution is shown in figure 1.7 and shows the typical double structure around $1.3 \text{ GeV}/c^2$. A PWA in the invariant mass region up to $2.2 \text{ GeV}/c^2$ supplied a large number of resonances in the $J^P = 0^-, 1^+, 2^+$ and 2^- sector. Some of them are meanwhile well established and were seen also in other reactions, other still need confirmation. This measurement was always the benchmark for the analysis presented in this thesis. Not only the reaction was the same but also many similarities between the WA03 spectrometer and the NA58 set-up of COMPASS exist.

Most recent results in the $K^+\pi^+\pi^-$ final state channel were published in the year 2010 by the BELLE Collaboration. Up to now analyses of formation processes and diffractive production were dominating the results in the strange light meson regime. The BELLE Collaboration performed an analysis of $B^+ \rightarrow J/\psi K^+\pi^+\pi^-$ and $B^+ \rightarrow \psi' K^+\pi^+\pi^-$ decays at the KEK-facility demonstrating the possibility of strange meson spectroscopy in e^+e^- collision experiments. The $B^+ \rightarrow J/\psi K^+\pi^+\pi^-$ decay analysis led to 10 594 events used for PWA [30]. The relatively small number of events may not be competitive but the method shows the potential for exploration of strange resonances even above $4 \text{ GeV}/c^2$.

THE COMPASS-EXPERIMENT

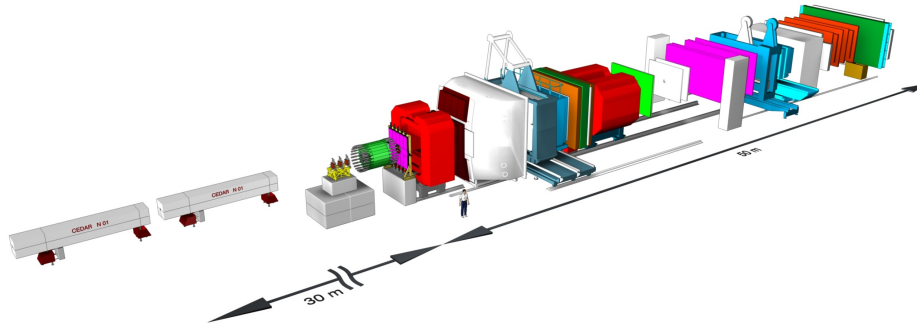


Figure 2.1: Illustration of the two stage COMPASS spectrometer as it was assembled in the years 2008 and 2009. For a detailed description see figure 2.9.

The COmmon Muon Proton Apparatus for Structure and Spectroscopy (COMPASS) collaboration is a community of more than 250 physicists from 11 countries all over the world. The roots of this group lie back in 1996 where two collaborations were merged to run one multi purpose spectrometer [31]. Both collaborations proposed two independent physics programs to be realized in the north area of the Super Proton Synchrotron (SPS) at European Organization for Nuclear Research (CERN).

The Hadron Muon Collaboration (HMC) collaboration, proposed originally 1995 a precise measurement of the polarisation of gluons [32] in nucleons. The strong interest to probe the spin structure of nucleons arose from results obtained first by the European Muon Collaboration (EMC) collaboration. It could be shown that the contribution by quarks to the total spin of a nucleon is rather small as obtained from a measurement of the spin dependant structure function $g_1(x)$ of a proton and a neutron [33]. Those results were even more confirmed by succeeding experiments run by the New Muon Collaboration (NMC) and Spin Muon Collaboration (SMC) [34]. Improved analysis and measurement methods could determine the quark contribution more precisely but the fraction of the nucleon spin remained small leading to the so called *spin crisis*. The polarization of the *glue-sea* was expected to be one more source contributing to the total spin of a nucleon. To measure this contribution it was necessary to refurbish the 20 years old SMC spectrometer.

In the same year the CHarm Experiment with Omni-Purpose Setup (CHEOPS) collaboration was formed [35]. Members of this collaboration were coming from the WA102 collaboration with the emphasis on the search of non $q\bar{q}$ states centrally produced by a high energy proton beam on a proton target, the WA89 collaboration searching for new charmed resonances in baryons and the Crystal Barrel experiment at

CERN investigating in searches of light glue balls and hybrid mesons in neutral decay channels. The main interest of the CHEOPS collaboration was a precise measurement of various hadron spectra.

As both collaborations proposed measurements with a spectrometer in the SPS north area, was it reasonable to form one collaboration to run the NA58 experiment placed downstream the M2 beam line (see sec. 2.2). The beam line was capable to provide longitudinally polarized muons as well as hadrons with high beam momenta so that the diverse physical measurements of both collaborations found one common set-up: The COMPASS spectrometer.

2.1 THE COMPASS PHYSICS PROGRAM

The main topics in the COMPASS physics program are sketched in fig. 2.2. The large variety of scientific fields can roughly be divided into two parts differing in the initial beam at the target.

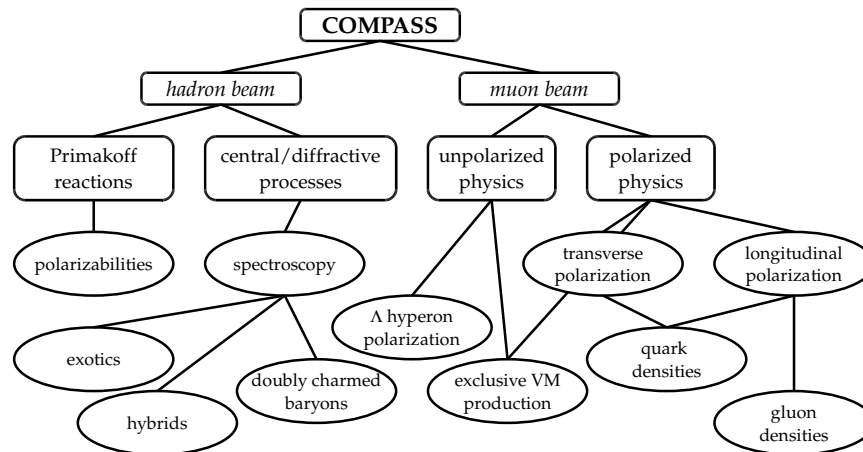


Figure 2.2: Overview of the COMPASS physics program (based on [36]).

2.1.1 Physics with muon beams

As already depicted, the muon program was dedicated mainly to solve the spin puzzle of a nucleon. It is believed in a simple parton model that the spin of a nucleon is composed by the spin of the quarks $\Delta\Sigma$ the spin of the glue-sea ΔG as well as the orbital momentum contributions by quarks and gluons. The contribution to the total spin by quarks was determined with high precision to be in the order of 20% to 35% [37] and the focus moved to the gluons. To access the information about the glue part of the nucleus, measurements with longitudinally polarized muons on polarized targets were performed. The deep inelastic scattering process was analysed semi-inclusively for open charm processes [38] and high transverse momentum hadron pairs [39], giving evidence for a

negligible gluon spin contribution. Moreover, results from previous experiments measuring the helicity distributions Δq were confirmed [40]. In addition a transversely polarized target was used to analyse the transverse spin distributions $\Delta_T q$ for protons and neutrons [41]. The latter parton distribution function was then proposed to be measured in the future also in a pion beam on a polarized proton target. A lepton anti-lepton pair in the Dell-Yann process would be sensitive to this quantity [42], too.

As exclusive vector meson production, the search for double spin asymmetries is denoted. The $\rho(770)$ was searched for in $\mu + N \rightarrow \mu' + N' + \rho$ production mechanisms where finally results compatible with zero were obtained [43]. The process $\mu + N \rightarrow \mu' + N' + \omega\pi^0$ was a channel where a radial excitation of the ρ^0 was reported previously. The $J^P = 1^-$ signal was successfully decomposed from a competing b -resonance decay in the same channel [44].

Another topic was the measurement of the longitudinal spin transfer to $\Lambda\bar{\Lambda}$ hyperons [45]. The polarization of Λ s was found to be compatible with zero while the $\bar{\Lambda}$ polarization was increasing as a function of x_F . Based on a parton model those results will be used to access the strange anti-quark distributions in the nucleon.

The largest fraction of the muon program of COMPASS was already finalized when the hadron program started in the years 2008 and 2009 after a small test run in 2004.

2.1.2 Physics with hadron beams

The hadron program can be subdivided into two physics processes, namely Primakoff reactions and diffractive/central processes. Primakoff reactions are used as a probe for the polarizability of pions. A pion scatters off a heavy nucleus by virtual γ exchange where the γ becomes real and is measured in the final state with the pion. The comparison between the angular distributions of a point like muon and the hadron angular distributions helps to understand systematic influences of the spectrometer [46]. Despite several experiments in the past measuring the polarizability, no final conclusion could be drawn so far as results are not in agreement. A further high precision measurement with the COMPASS spectrometer, as proposed for the year 2012, is necessary to clarify this strongly disputed property of a pion. Moreover a first measurement of the polarizability of kaons might be achieved as those are contained in the hadron beam, too.

Diffractive/central processes had to be measured separately in order to accumulate enough events for a later meson and baryon spectroscopy analysis. Primakoff reactions are happening with mostly small momentum transfers between the target and the beam particle. The diffractive processes can be separated due to signature of a recoiling proton emitting the target at high momentum transfers. So it was required in the trigger in contrast to a pure calorimetry decision of the Primakoff reaction. The

spectroscopy of hadrons, excited to resonances on a target, was therefore the main topic of the hadron runs 2008 and 2009. A huge number of final states was under investigation while writing this thesis and the work was by far not finalized.

Protons in the hadron beam for example were used to analyse baryon resonances in diffractive channels such as $p + p \rightarrow p^* + \pi^+ p' \rightarrow p + \pi^- + \pi^+ + p'$ [47]. The diffractive production of such resonances is an alternative way to access information about baryonic states mostly granted by γ production so far. The same initial state could in addition be used for the analysis of centrally produced events such as $p + p \rightarrow p + 4\pi + p'$. The search for the corresponding process with pions in the beam was also under investigation [48]. Several resonances decaying into this final state were not clearly specified by previous measurements.

Excited pions were measured in even more final states. The biggest number of events was found in the the $\pi^+ \pi^- \pi^+$ final state. Those events were observed at the COMPASS experiment already in the test run 2004 with a clear signature of a spin exotic state $J^{PC} = 1^{-+}$ [49]. The number of events obtained in the hadron runs 2008 and 2009 was 100 times larger, reducing statistic uncertainties to a minimum. In addition to the charged final state, the $\pi^- \pi^0 \pi^0$ channel was also analysed for a direct comparison of both channels [50]. As no dramatic differences could be observed it was concluded that systematic uncertainties, originating from the spectrometer set-up, were under control. It is expected to pin finally down the existence of the $J^{PC} = 1^{-+}$ spin exotic state with no room for misinterpretation.

The same resonance production mechanisms applied also to kaons in the hadron beam. The analysis of kaon resonances in the $K^- \pi^+ \pi^-$ final state was the topic of this thesis. This final state was the first and yet the only analysis of isospin $I = \frac{1}{2}$ states available from the hadron data.

The high charged track acceptance of the spectrometer allowed to expand the multiplicity of the final states even up to charged 5 pions. Already the data set of 2004 contained enough events for deeper studies [51]. It is remarkable that the mostly structureless invariant mass spectrum observed there could still be decomposed in resonances of different spin parity combinations giving a consistent picture of the processes. This was only possible with the development and application of a genetic algorithm searching for fitting partial wave sets. It is planned to generalize and apply this methods to all final states measured at COMPASS. The advantage of this method is that it is giving control over systematic uncertainties arising from the various and sometimes ambiguous solutions to describe one and the same angular distributions in the final states.

For a complete overview for all the channels under investigation at COMPASS the interested reader is referred to [52] where overview table 2.1 was extruded from.

beam particle	target	final state
π^-	$1\text{H}_2, \text{Ni, Pb}$	$\pi^- \pi^+ \pi^-$
π^-	$1\text{H}_2, \text{Ni, Pb}$	$\pi^- \pi^+ \pi^- \pi^+ \pi^-$
π^-	1H_2	$\pi^- \pi^0 \pi^0$
π^-	1H_2	$\pi^- \pi^0$
π^-	1H_2	$\pi^- \eta$
π^-	1H_2	$\pi^- \pi^- \pi^0 \pi^+$
π^-	1H_2	$\pi^- \eta \eta$
π^-	1H_2	$\pi^- \pi^+ \pi^- \eta$
π^-	1H_2	$\pi^- \pi^- \pi^0 \pi^0 \pi^+$
π^-	1H_2	$\pi^- \text{K}\bar{\text{K}}$
π^-	1H_2	$\pi^- (\pi \text{K}\bar{\text{K}})^0$
K^-	1H_2	$\text{K}^- \pi^+ \pi^-$
p	1H_2	$\text{p} \pi^- \pi^+$
p	1H_2	$\text{p} \text{K}\bar{\text{K}}$
p	1H_2	$\text{p} \pi^- \pi^+ \pi^- \pi^+$
p	1H_2	$\text{p} \eta \eta$

Table 2.1: Summary of channels from diffractive and central production under investigation at COMPASS [52]. Apart from several proceedings about ongoing analyses, no results from data of the years 2008 and 2009 were published so far.

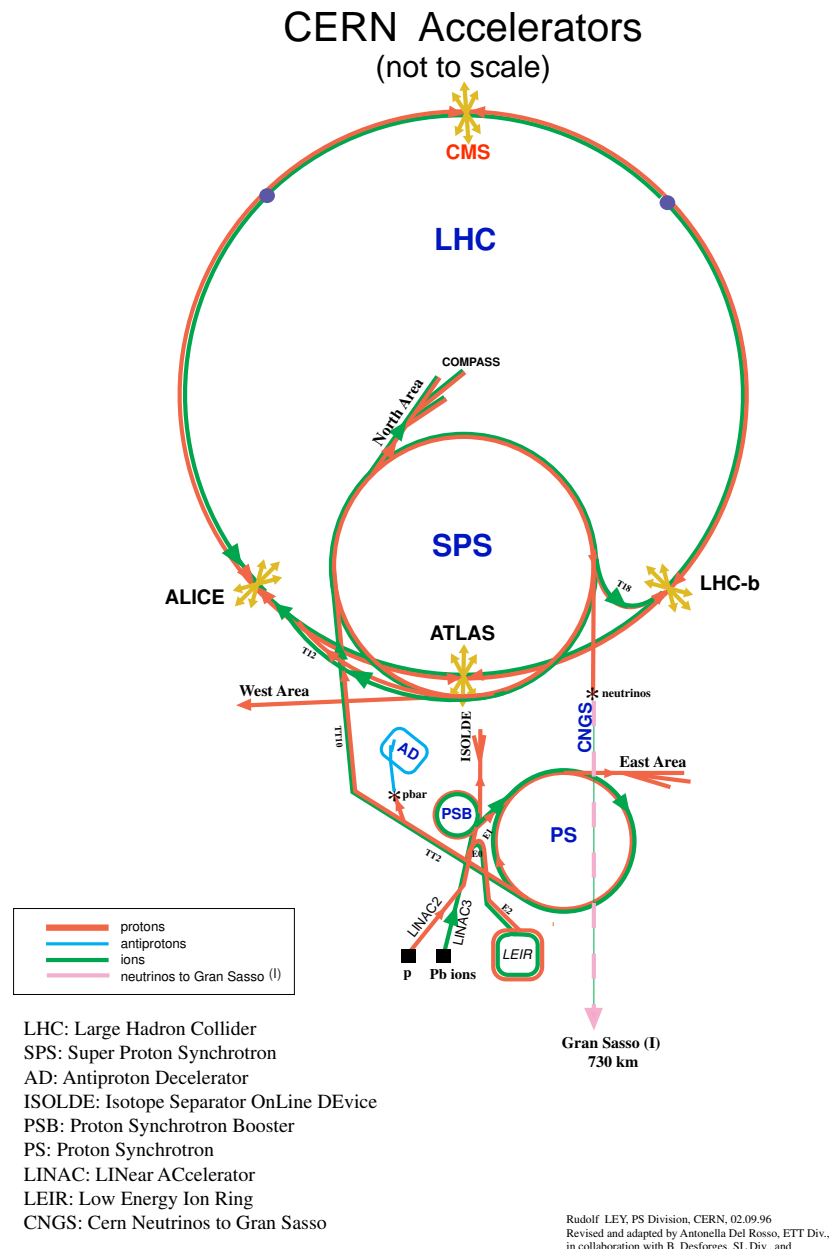


Figure 2.3: Overview of the CERN accelerator facility [53]. The COMPASS spectrometer is located at the north area of the SPS.

2.2 PARTICLE BEAMS FOR COMPASS

The European Organization for Nuclear Research (CERN) accelerator facility (fig. 2.3) features several experimental areas with various beam compositions and properties. The COMPASS experiment is placed in the North area of the Super Proton Synchrotron (SPS). Protons were accelerated to momenta of up to 450 GeV/c before extraction. The extracted

beam was distributed among several beryllium targets feeding diverse beam lines with secondary beams.

The **COMPASS** experiment is set up at the end of the M2 beam line, featuring a long decay tunnel to provide longitudinally polarized muons from pion decays. Before leaving the decay tunnel muons passed a beryllium filter in order to remove remaining hadrons in the beam. Without this filter hadrons were transported to the **COMPASS** target. Those particles were separated by their momenta by a combination of dipole magnets.

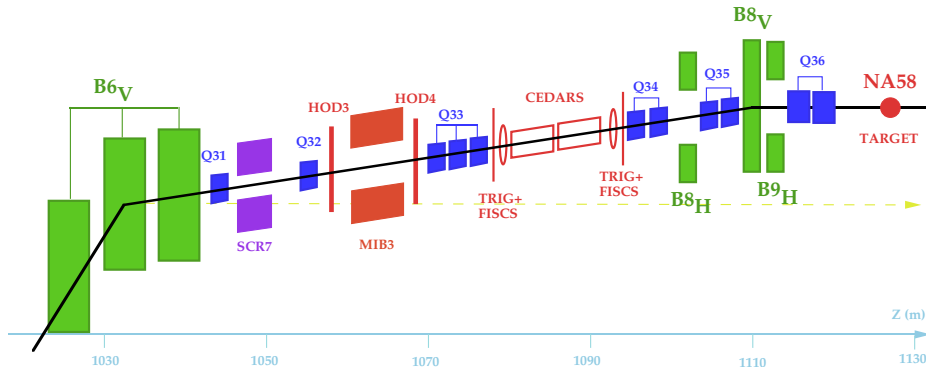


Figure 2.4: Side view of the M2 beam line set-up [54]. Only the last 100 m upstream of the **COMPASS** target are shown. Dipole magnets are displayed in green, quadrupole magnets in blue. For details see text.

Figure 2.4 shows a schematic view of the last 100 m of the 1.13 km long beam line. Apart from several beam steering and monitoring devices two **CEDAR** detectors are sketched for beam particle identification in hadron beams. The quadrupole magnets upstream and downstream the **CEDAR** detectors allowed for defocusing and focusing the beam in order to have a very parallel beam at the **CEDAR** region, and to focus the beam spot at the **COMPASS** target. The parallelism of the beam was crucial for an efficient operation of the **CEDAR** detectors as it will be discussed in chapter 3.

THE BEAM COMPOSITION The beam consisted mainly of charged pions kaons and (anti)protons when running in hadron mode. Both, positive or negative charges could be selected. The choice of the charge had direct impact on the beam composition and depend also on the selected beam momentum. This is illustrated in figure 2.5 where the fraction of particles for negative and positive beams is drawn over the beam momentum.

In the positive hadron beam, protons were dominant with a large contributions of pions. While protons dominated as they were originating mostly from the primary beam, anti-protons required a production process and were thus a minor component in the negatively charged hadron beam. There mostly pions were found. In both cases kaons were just a small component of several percent.

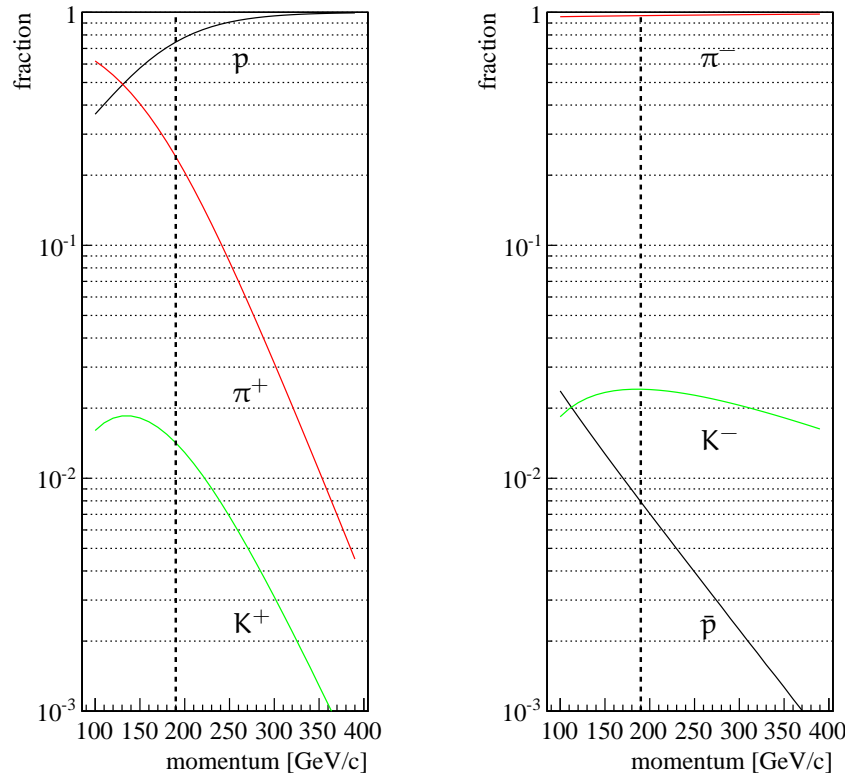


Figure 2.5: The calculated hadron beam composition 1100 m downstream of the primary T6 target. Left: Positive beam charge. Right: Negative beam charge. The contribution by electrons and muons was not taken into account. The composition behind the T6 target was known from previous measurements [55]. The values were calculated for a primary proton beam momentum of 400 GeV/c taking the lifetime of the secondary particles into account [11]. The COMPASS beam momentum of 190 GeV/c in the years 2008/2009 is indicated by a dashed line.

The beam momentum of hadron beams in test run in the year 2004 and the full runs in the years 2008 and 2009 was set to 191 GeV/c. The choice of the beam momentum was motivated in the negative charge case by the largest fraction of kaons in beam. For a positive hadron beam one needed only to swap the current signs of the magnets along the beam line. The particle composition was calculated to be

particle	π^+	K^+	p	π^-	K^-	\bar{p}
fraction at 0 m	0.255	0.029	0.715	0.947	0.046	0.007
fraction at 1100 m	0.240	0.014	0.746	0.968	0.024	0.008

In the following beam properties are given for a beam line set-up called M2A.009 for negative hadron beams. This set-up was applied most of the beam time 2008 and 2009. A few runs with improved beam track divergence were taken in the year 2009 but were not used for physics analysis. The beam momentum distribution was heavily distorted. It was

decided to continue measurements from 2008 with the same set-up in order to keep systematic influences under control.

THE BEAM PROPERTIES AT COMPASS Beam properties as track distributions and track angles at the COMPASS experiment were measured in front of the target by a silicon station (see fig. 2.9). Those detectors allowed a precise measurement and extrapolation of incoming particle tracks (see section 2.3.3 for details).

The beam profile had a diameter of less than 1.5 cm at the target region, fitting exactly the target face dimensions. The focal point was set to be 30 m downstream of the target¹ with a diameter of less than 1 cm. The beam spot and beam direction is visualized in figure 2.6 by extrapolating measured beam tracks along the COMPASS spectrometer. In the vertical plane a slight twist to the ground was observed. The dipole field of the COMPASS spectrometer was not taken into account here what results in straight beam tracks in the horizontal plane. The track distribution 2.7 shows the corresponding beam profile 30 m downstream of the target and is a direct measure for the beam divergence 30 m upstream of the target as discussed in the next paragraph.

To complete the beam properties the measured beam particle energy from chapter 5 is anticipated here. It was reconstructed with the COMPASS spectrometer for exclusive $K^-\pi^+\pi^-$ final states (see figure 5.3) to a mean value of

$$P_{\text{mean}} = (191.29 \pm 0.04) \text{ GeV}/c \quad (2.1)$$

with a width of

$$P_{\sigma} = (1.79 \pm 0.03) \text{ GeV}/c . \quad (2.2)$$

THE BEAM PROPERTIES AT THE CEDARS To calculate the beam properties at the CEDAR region 30 m upstream the target, a particle transportation matrix based on known magnet field intensities was used [56]. This transportation matrix correlates beam track properties at the focal point 30 m downstream of the target with those at the CEDAR region. The relations are

$$\begin{aligned} x(z_1) &= x(z_0) \cdot 0.398 + \theta_{\text{horiz}}(z_0) \cdot 47.160 \frac{\text{mm}}{\text{mrad}} \\ y(z_1) &= y(z_0) \cdot 0.749 + \theta_{\text{vert}}(z_0) \cdot 73.374 \frac{\text{mm}}{\text{mrad}} \\ x(z_2) &= x(z_0) \cdot 0.670 + \theta_{\text{horiz}}(z_0) \cdot 47.160 \frac{\text{mm}}{\text{mrad}} \\ y(z_2) &= y(z_0) \cdot 0.924 + \theta_{\text{vert}}(z_0) \cdot 73.374 \frac{\text{mm}}{\text{mrad}} \\ \theta_{\text{horiz}}(z_1..z_2) &= x(z_2) - x(z_1)/(z_1 - z_2) \\ \theta_{\text{vert}}(z_1..z_2) &= y(z_2) - y(z_1)/(z_1 - z_2) \end{aligned} \quad (2.3)$$

¹ A limited beam hole size in Hadronic CALorimeter (HCAL)₂ required a precise passage of this area to reduce pile up signals in the calorimeter blocks around this hole

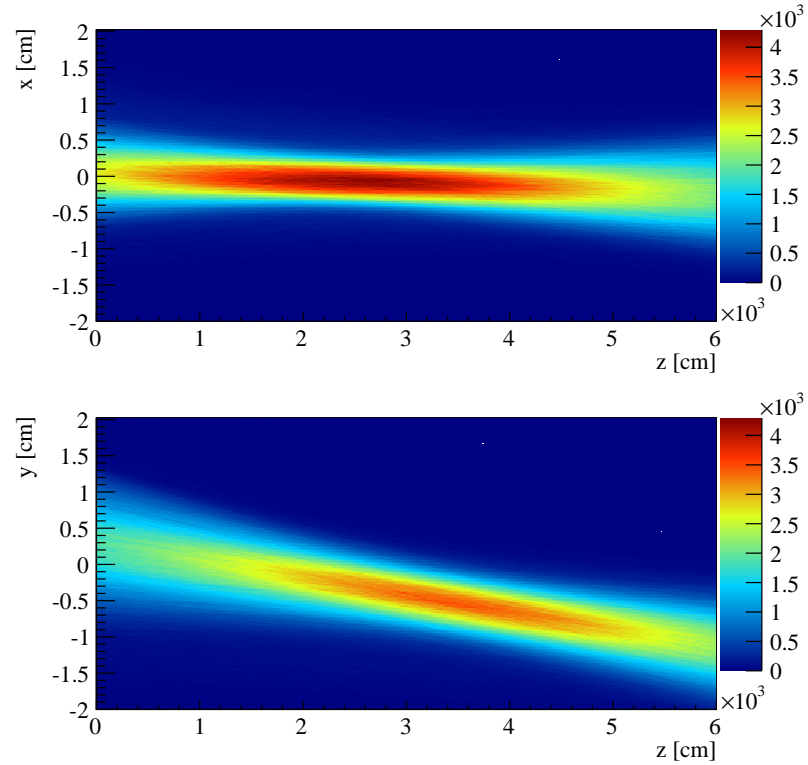


Figure 2.6: Extrapolated beam tracks along the COMPASS spectrometer as measured in the run 2008. Top: Beam tracks in the horizontal plane. Bottom: Beam tracks in the vertical plane. The intention to focus the beam at 30 m behind the target is clearly visible although some displacement was observed in both planes.

with

$$z_0 = 0 \text{ m}; z_2 = 69.396 \text{ m}; z_1 = 82.230 \text{ m}. \quad (2.4)$$

The z_0 position is 30 m downstream of the target in the COMPASS reference system. The propagation is reverse in time and thus oppositely signed in z . z_2 is downstream CEDAR 2, z_1 upstream CEDAR 1. The beam track divergence in the horizontal plane $\theta_{\text{horiz}}(z)$ and vertical plane $\theta_{\text{vert}}(z)$ at COMPASS translates to a track displacement $x(z)$ and $y(z)$ at the CEDARs and vice versa. Or in other words: The wider the beam spot was, the larger was the beam divergence at the CEDAR region.

Of course is the transportation matrix only valid for ideal dipole and quadrupole magnet fields. Uncertainties arising from imprecise magnet currents or fringe fields were assumed to be negligible.

The resulting angular track distributions in the horizontal and vertical plane are shown in figure 2.8. The width in the horizontal plane was about $200 \mu\text{rad}$ (full width at half mean (*fw*hm)) and $110 \mu\text{rad}$ (*fw*hm) in the vertical plane. The beam divergence was the main contribution to the inefficiency of the CEDAR detectors as the track angle acceptance was limited. Details are discussed in chapter 3.

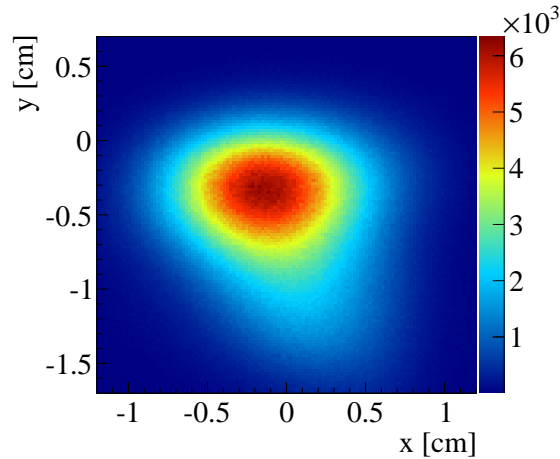


Figure 2.7: The x-y distribution of beam tracks extrapolated to the focal point at 30 m behind the target. The size of the beam spot, as measured in the run 2008, was directly correlated with the beam divergence at the CEDAR detector region.

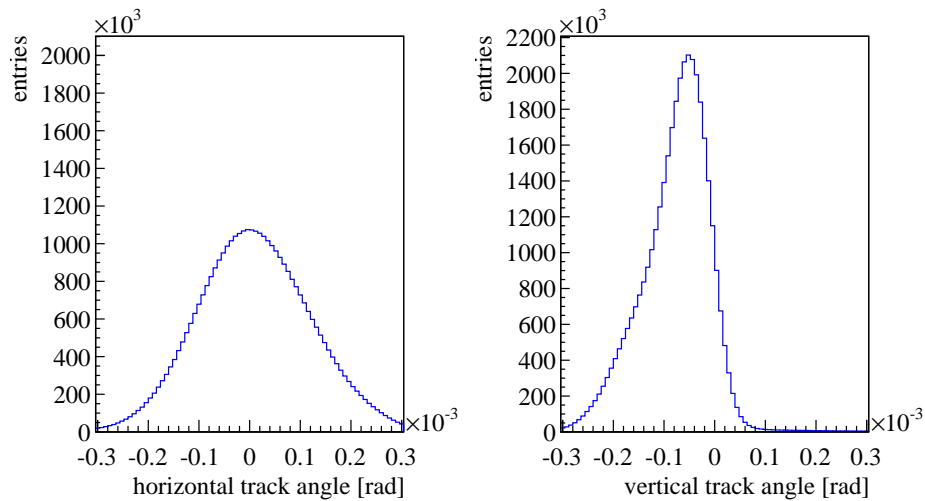


Figure 2.8: The beam track divergence distributions as deduced by particle track propagation through beam optics to the CEDAR region for the hadron run 2008. In the horizontal plane a width (left) $200 \mu\text{rad}$ (*fwhm*) was measured. The vertical plane was $110 \mu\text{rad}$ (*fwhm*) wide.

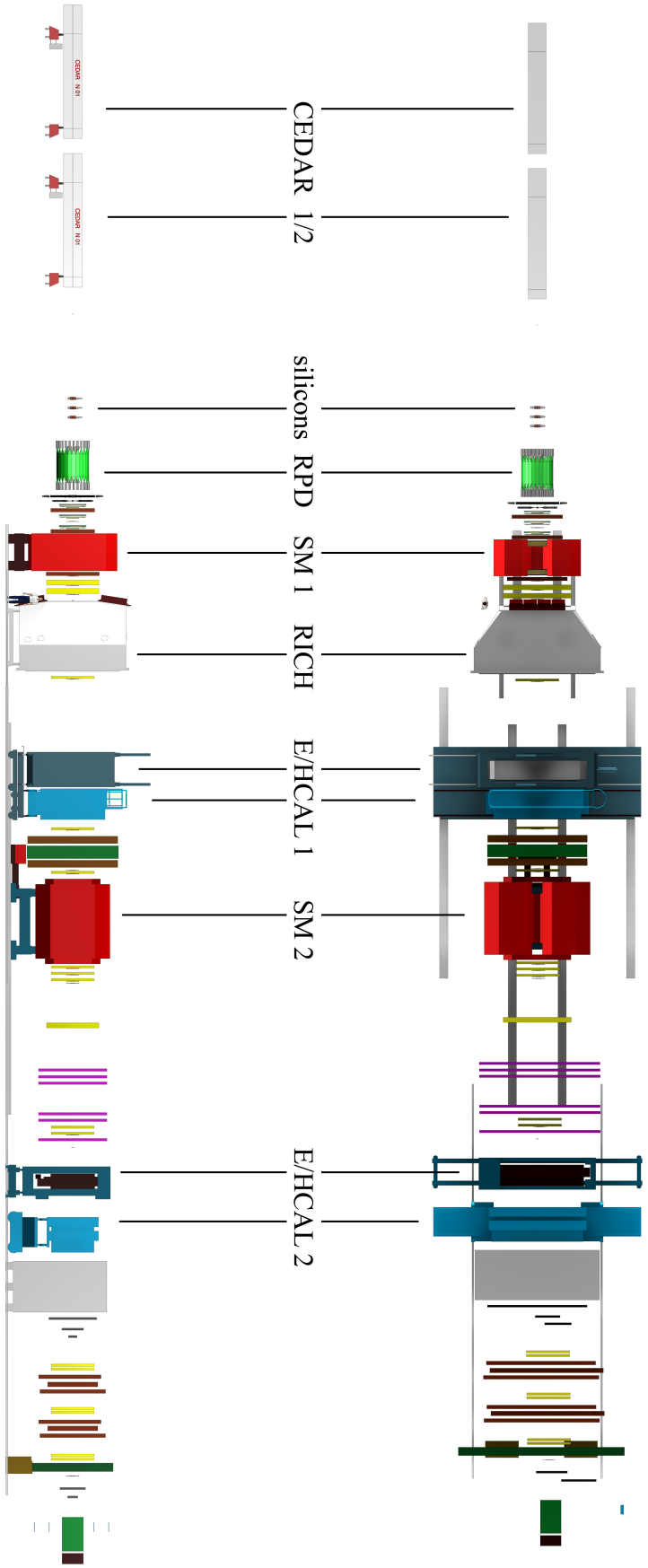


Figure 2.9: Top and side view of the COMPASS spectrometer as assembled in the years 2008/2009. The hadron beam is coming from the left impinging on a 40 cm long liquid hydrogen target. Each of the two CEDAR detectors 30 m upstream the target identified one kind of particles. Exclusive diffractive processes were identified by the recoil proton detector (RPD) around the target. The 50 m long two-stage spectrometer consisted of two dipole magnets, the corresponding track measurement detectors, electromagnetic and hadronic calorimetry as well as muon identification in each stage. In addition stage one featured charged final state particle identification by a ring imaging cherenkov (RICH) detector. See section 2.3 for a detailed description of the spectrometer.

2.3 THE COMPASS SPECTROMETER

This section can give only a short insight to the COMPASS spectrometer. A very detailed summary is given in [57] for a set-up of the years 2004 and 2006. The set-up of the years 2008 and 2009 was very similar. Important modifications will be pointed out here.

2.3.1 Overview

The drawing 2.9 provides an overview of the 2-stage COMPASS spectrometer indicating important parts of it. The target was surrounded by a Recoil Proton Detector (RPD) measuring the signature of diffractive processes, the recoil proton. The final states, neutral and charged, of decaying resonances excited in the target were identified and measured by the spectrometer behind the target. The principle of a spectrometer is bending of charged particle tracks by dipole magnets in order to measure their momentum with high accuracy and acceptance over a wide momentum range. To do so the spectrometer was built up in two stages.

The first Spectrometer Magnet (SM₁) was a 110 cm long dipole and it was located about 4 m downstream the target. The field integral was about 1 Tm and the angular acceptance of ± 180 mrad defined the required detector acceptance in the first stage of about ± 250 mrad in the horizontal plane. The first stage, which is also called Large Angle Spectrometer (LAS), featured besides various tracking detectors also a charged final state PID with the Ring Imaging CHerenkov (RICH) detector, the first electromagnetic calorimeter (ECAL₁) for neutral state identification, the first hadronic calorimeter (HCAL₁) and the first muon wall (MW₁) for muon identification. A momentum range starting from below 1 GeV/c up to about 60 GeV/c was covered by this stage.

Particles higher in momenta than 60 GeV/c were passing the second Spectrometer Magnet (SM₂). It's field integral of 4.4 Tm deflected charged particles up to ± 30 mrad and was therefore defining the required acceptance of the Small Angle Spectrometer (SAS). It was featuring a similar set-up as found in the LAS apart from a RICH. It was originally foreseen to place also one RICH in the second stage but has not been realized yet mostly due to financial reasons.

2.3.2 The target region

The target was in the year 2008 and partially in 2009 a 40 cm long liquid hydrogen cell operating at very low temperatures of around 14 Kelvin. The sketch 2.10 illustrates the near target region. The target cell was placed in a conical cryostat cooling not only the cell itself but also the Silicon microstrip (Silicon) detectors located downstream of the target and described in section 2.3.3.

The RPD consisted of two rings of scintillating slabs. The inner ring was formed by 12 elements while the outer ring consisted of 24 elements

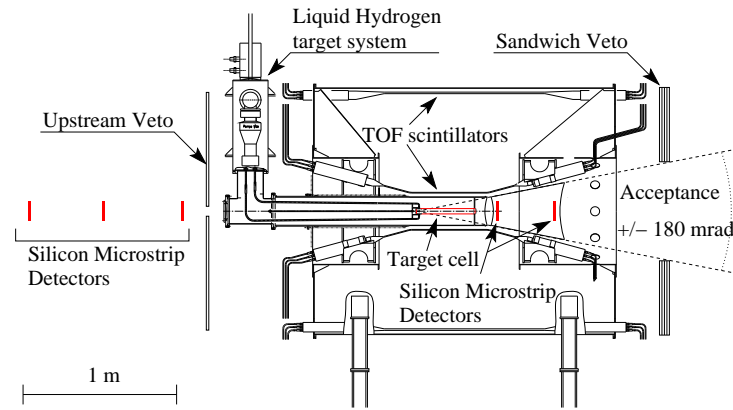


Figure 2.10: Cut through the RPD as a part of the target region [58]. A 40 cm long target cell was hold by a conical cryostat including two silicon microstrip detectors just behind the target operating at about 14 Kelvin. The track measurement upstream the target was done by three further silicon detectors. The recoil proton kicked out of the target was identified by the time of flight through two barrels of 12 and 24 scintillating slabs around the target. In addition a measurement of the energy loss in the scintillating slabs was performed. Halo from beam was rejected by an upstream veto while a sandwich veto downstream the target was matching the acceptance of the cryostat.

rotated by $\frac{24}{360} \cdot \frac{1}{2} = 7.5$ degree in respect to the inner ring. The theoretical azimuthal resolution is then

- 7.5 degree for even outer slabs and
- 15 degree for odd outer slabs

which is further reduced by effects like multiple scattering.

The inner slabs consisted of BC404 5 mm thick organic scintillator constructed at Mainz University [58]. As a proton had to traverse both rings to get identified with time-of-flight methods, very slow protons from a momentum transfer of below $t = 0.06 \text{ GeV}^2/c^2$ were not seen. They got stuck in the inner ring losing the complete kinetic energy there. A positively identified recoil proton was used for trigger purposes with a timing resolution of better than 350 ps (root mean square (rms)).

Furthermore the sketch 2.10 is showing two veto devices. The upstream veto detector was used as a trigger anti-coincidence for beam halo particles. The second one just behind the target was newly constructed to reduce non exclusive background reactions not matching the spectrometer acceptance [59]. The simulated efficiency of 98% was achieved by 12 $80 \times 40 \text{ cm}^2$ large sandwich type organic scintillator plates with cut-outs in the central acceptance region. The scintillator plates were bond to arrays and read out by optically active WaveLength Shifting (WLS) fibres. The overall surface covered $2 \times 2 \text{ m}^2$, enriching the recorded number of exclusive events by a factor of 3.5.

The target region in front of the **SM₁** contained in addition to the **Silicons** an array of two Scintillating Fibre (**SciFi**) stations, two Drift Chamber (**DC**)s detectors and three Micromesh Gaseous Structure (**Micromega**) detectors for a precise track measurement of charged tracks entering the **LAS**. Those detectors are discussed in the following section as an important part of the charged track's momentum measurement at **COMPASS**.

2.3.3 Tracking

When talking about a tracking detector one means in most of the cases detector stations including several detector planes. A measurement of a track passage in a plane needs at least two coordinates (**XY**). Two further coordinates of a reference system rotated by 45 degree in the (**XY**)-plane span a new reference system (**UV**) reducing the number of ambiguous solutions significantly.

The **COMPASS** spectrometer featured a large variety of tracking detectors consisting of more than 200 planes. The detector types applied to the **COMPASS** spectrometer can be roughly divided into three subgroups:

VERY SMALL AREA TRACKERS Very Small Area Trackers (**VSAT**) were built to be placed in the beam region. Obviously this requires high rate capability and very good spacial and time resolution.

SciFi stations consisted of several planes of scintillating fibres. They stand a hit rate of up to $3 \cdot 10^6 \text{ s}^{-1}$ per fibre. Due to the very good time resolution of 350 – 450 ps combined with a large efficiency of 96% - 99% those were used apart from tracking also partially as beam counters in the trigger set-up. In total 8 stations along the spectrometer were placed. The active area was increasing with the distance to the target starting from $3.9 \times 3.9 \text{ cm}^2$ up to $12.3 \times 12.3 \text{ cm}^2$. The corresponding number of channels varied between 192 and 462 per detector plane.

Silicons were designed for the near target region. A set of semiconductor plates covered an active area of $5 \times 7 \text{ cm}^2$ and were structured into 1024×1280 strips per surface of a plate. As one plane was rotated by 90 degree an enormous spacial resolution of up to $8 \mu\text{m}$ (**rms**) was achieved. The disadvantage was a lessened time resolution of about 2.5 ns (**rms**). In addition semiconductors are known to suffer from radiation damage. To confine the loss of doping all **Silicon** stations were cooled below temperatures of 200 kelvin in 2009 with liquid nitrogen. Three detector stations of that kind were used upstream the target measuring the incoming beam properties. Eight planes assembled to two stations were placed inside the conical cryostat just behind the target.

SMALL AREA TRACKERS The intermediate region around the beam (2.5 – 40 cm) was covered by Small Area Trackers (**SAT**). Still a good spacial resolution was required combined with quite large active surfaces. Two competing detector layouts turned out to fit the demands. Both

based on the principle of detection with ionized gas as sketched in figure 2.11.

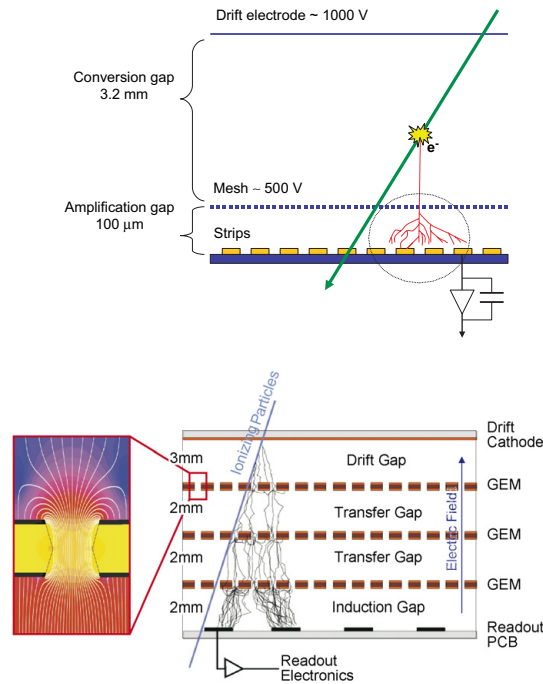


Figure 2.11: The functional principle of [Micromegas](#) (top) and [GEMs](#) (bottom) at [COMPASS](#) [57]. Both detectors identified ionized particles in a gas mixture. [Micromegas](#) had a large drift space separated from the avalanche region by a micro mesh. The signal was readout by strips. Every dimension in a plane needed a separate detector plane. [GEMs](#) contained perforated polyimide foils with copper cladding on both sides. Moreover both dimensions of a plane were read out simultaneously as readout strips were forming a grid.

In front of [SM1](#) three sets of [Micromegas](#) detector stations were placed measuring 4 orientations (XYUV) each. Electrons from ionized particles in those detectors were drifting to a metallic micro mesh. This mesh separated the drift area from an amplification gap where electrons are accelerated finally producing an avalanche of electron/ion pairs. Those signals were read out by strips with a pitch of 360 – 420 μm. The active area of 40 × 40 cm² contained a small dead zone of 5 cm in diameter for the nominal beam region. In total 1024 channels per detector resulted in a spacial resolution of 90 μm (rms). The time resolution of 9 ns (rms) was very good compared to other gaseous tracking devices.

Compared to [Micromegas](#) detectors, [GEM](#) detectors had a slightly worse time resolution of 12 ns but a better spacial resolution of 70 μm. The active area of 31 × 31 cm² was readout by 1536 crossed strips with a pitch of 400 μm providing a simultaneous measurement of two orientations per active volume. The ionized gas was sectionated by three layers of 50 μm thick polyamide foils with copper cladding on both sides. It was perforated by chemical etching with micro-holes where electrons were

separated from the ions reducing the conversion time significantly. 11 GEM stations were placed along the COMPASS spectrometer measuring the (XYUV) components. A small inner region was not powered at standard beam intensities as strip occupancy would be too high.

To attack the problem of a too high occupancy near the beam a modified version of the GEMs was developed for the hadron runs 2008 and 2009. The inner region was divided into 32×32 pixels with a pitch of 1 mm replacing the strips there. The rest of the $10 \times 10 \text{ cm}^2$ active area was covered with conventional strips. The detector performances were the same with the difference that the inner region was not dead anymore. Five pixel GEM detectors were distributed in three stations along the spectrometer, one in front of SM₁ and two in front of and behind of SM₂. The latter two stations measured in addition to (XY) components also (UV) components of the plane. Those GEMs were replacing 5 SciFi stations to reduce the material budget in the spectrometer. Therefore the pixel area should be counted as an VSAT component.

LARGE AREA TRACKERS The outer region around the beam was covered by Large Area Trackers (LAT). The orders of magnitudes lower beam flux allowed for the use of conventional drift chambers. Three different type of those were installed at COMPASS.

Next to SM₁ were three DCs mounted, two upstream SM₁ and one just behind. The active area of $180 \times 127 \text{ cm}^2$ was a bit larger than the acceptance of the spectrometer magnet itself. The gas volume was wired with 176 pairs of filaments per detector plane. As the pairs were opposite in charge an electric drift field was generated. In combination with the drift time a spacial resolution of $190 \mu\text{m}$ was obtained.

The Straw tube drift chamber (Straw)s were spanning even larger areas covering large scattering angles of $15 - 200 \text{ mrad}$. In contrast to other drift chambers at COMPASS the drift field was created by a potential difference between a wire and a surrounding tube. Two tube diameters were used. The smaller with 6.14 mm for the inner region the larger with 9.65 mm for the outer region. 12440 tubes were assembled to 15 planes with an active area of $323 \times 280 \text{ cm}^2$. Two sets of planes were placed upstream the RICH detector and another array just in between SM₂ and second electromagnetic calorimeter (ECAL₂). The resolution of $190 \mu\text{m}$ for the tubes with the smaller diameter was the same as for DCs.

The largest number of LAT detectors were MultiWire Proportional Chamber (MWPC)s. Several layers of wires were stretched in an active volume of $178 \times 120 \text{ cm}^2$ ². A charged particle passing this volume generated multiple hits at several wires. The application of a clustering algorithm resulted in a special resolution of 1.6 mm (rms) for a wire pitch of 2 mm. MWPCs were placed all over the spectrometer often combined with GEMs just fitting the central dead zone.

² Actually there were three subgroups of this detector where one type spanned only $178 \times 80 \text{ cm}^2$.

The largest active area was provided by large area drift chambers (W_{45}). 500 channels per detector plane were covering $500 \times 250 \text{ cm}^2$. Those were placed in front of $ECAL_2$ even exceeding the required spectrometer acceptance with a good spacial resolution of 0.5 mm (rms) for an anode wire pitch of 4 cm. The drawback for this performance was a large dead time forcing a central dead region of 50 – 100 cm in diameter.

All in all an enormous number of detector planes was providing a nearly 100% spacial acceptance of charged tracks that was completed by calorimetry for neutral (and charged) tracks.

2.3.4 Calorimetry

The electromagnetic calorimeters at COMPASS were upgraded in major parts for the runs in 2008 and 2009 [60]. Five different types of modules were stacked to Electromagnetic CALorimeter (ECAL)s in each stage of the spectrometer. The composition is shown in figure 2.12.

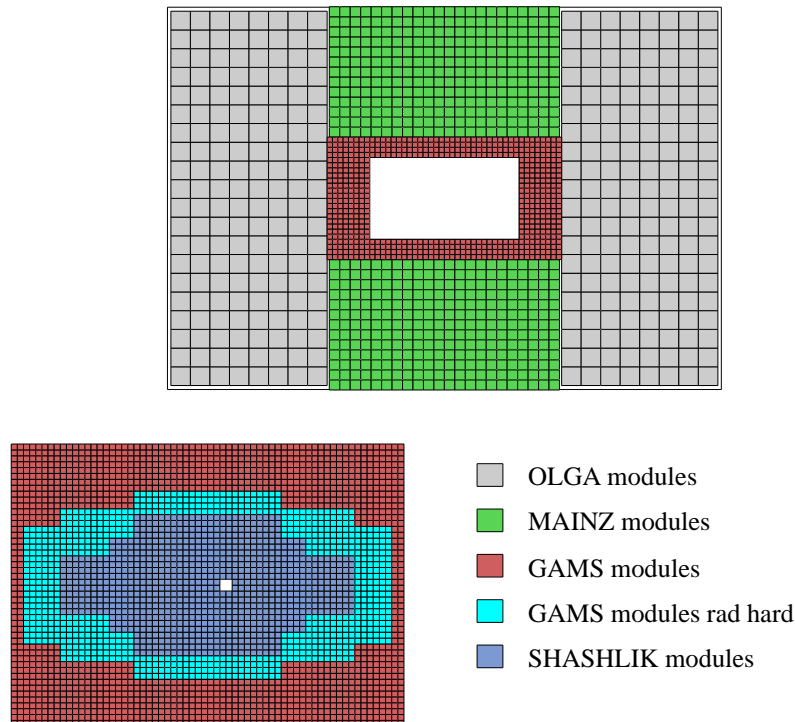


Figure 2.12: Module layout of $ECAL_1$ (top) and $ECAL_2$ (bottom) looking upstream. Properties of modules are listed in table 2.2. $ECAL_1$ featured an active area of $3.97 \times 2.86 \text{ m}^2$ with a central hole of $1.07 \times 0.61 \text{ m}^2$. It was constructed of three diverse types of lead glass modules originating from different successor experiments. In total 1500 channels were read out. $ECAL_2$ consisted of 2168 GAMS modules partially radiation hard and 900 SHASHLIK modules spanning an area of $2.43 \times 1.82 \text{ m}^2$. The beam hole of $8 \times 8 \text{ cm}^2$ was not centred as the non interacting beam was deflected by the spectrometer magnets.

PROPERTY	GAMS	OLGA	MAINZ	SHASHLIK
face [cm ²]	3.82 × 3.82	14 × 14	7.5 × 7.5	3.82 × 3.82
length [cm]	45	47	36	40
X ₀ [cm]	2.74	2.54	1.55	17.5
rel. E res. ($\frac{\sigma_E}{E}$)	$\frac{0.07}{\sqrt{E}} \oplus 0.01$	$\frac{0.056}{\sqrt{E}} \oplus 0.01$	$\frac{0.061}{\sqrt{E}} \oplus 0.04$	$\frac{0.066}{\sqrt{E}} \oplus 0.01$

Table 2.2: Key properties of COMPASS ECAL modules. The energy resolution was energy dependent and was determined in a high energetic electron beam [60].

ECAL₁ consisted of 1500 lead glass modules. The outer parts were large OLGA modules and smaller MAINZ modules. The inner part contained GAMS modules to provide the best spacial resolution at small angles next to the beam. ECAL₁ was placed about 11 m behind the target. With an active area of $3.97 \times 2.86 \text{ m}^2$ an angle of up to 8 degree was covered then. In the previous set-up each module had a light emitting diode placed in front of the lead glass for monitoring purposes. The LED monitoring system was replaced in 2008 by a optical fibre system distributing uniformly the light of one laser source. A temperature and time stable light source was important to record a reference signal for stability studies. Many time dependencies as radiation damage and Photo Multiplier (PM) instabilities could be corrected that way in an offline analysis.

ECAL₂ was placed 33 m behind the target. The surface of $2.43 \times 1.82 \text{ m}^2$ accepted angles smaller than 2 degrees. The central part was upgraded with a new type of SHASHLIK modules. Those modules consisted of an array of altering lead and scintillator plates. Those scintillating plates were nerved with WLS fibres leading the light to PMs at the back. The dimensions matched those of GAMS modules but SHASHLIK modules had a better linearity at high particle rates as well as a better energy resolution. The intermediate part was built up with radiation hard GAMS modules the outer part with GAMS modules of the simple type. All in all 2168 channels were read out by Sampling Analog to Digital Converter (SADC)s replacing the older fast integrating Analog to Digital Converter (ADC)s. As the complete signal form was recorded overlapping signals from pileup events could be identified and rejected.

Each ECAL was followed by a HCAL. Those detectors played a minor role in the measurements with hadron beams. In muon beams those were used to trigger on inelastic muon scattering events as well as to measure the energy of hadrons from the target.

2.3.5 Particle Identification

PID plays a key role in COMPASS data analysis. On the one hand hadron beams had to be tagged by the incoming particle type. On the other hand

beam particles after interaction produced long living final states that had to be distinguished by their masses.

Charged tracks at high energies have the advantage to emit Cherenkov light cones in transparent media. The correct choice of the refractive index of the medium allows for separation of those light cones in a certain momentum range. Focusing the light into a focal plane creates light rings that can be detected. This simple principle was adapted to both kind of detectors at COMPASS. Beam PID done by so called CEDAR detectors is discussed in detail in chapter 3. Two detectors of this type were placed 30 m upstream the target in the beam line. The final state particle identification was performed by the RICH detector in the first spectrometer stage. It's application and performance is discussed in chapter 4.

2.3.6 Further Detectors

Some detectors in the COMPASS spectrometer played a minor role during the hadron run. The HCALS for example were already noted. The interested reader is once again referred to the complete description [57]. Nevertheless for the sake of completeness detectors more important in the muon runs are touched here.

MUON WALLS Two Muon Wall (MW)s were used quite obviously for muon track identification in both stages of the spectrometer. Two drift chamber detector stations per MW were separated by 60 cm thick iron. Only muons were able to pass this massive volume giving hits in front and behind the absorber. A tracking efficiency of higher than 80% was reached which is remarkable for minimum ionizing particles in gas.

VETO PLANES Apart from the presented VETO planes around the target many more planes were placed around the spectrometer. Muon beams produced a beam halo orders of magnitudes higher than hadron beams combined with a less focused beam spot. Unwanted events missing the target were excluded from data recording.

HODOSCOPES Large detector walls consisting of scintillating slabs were mounted mostly in the second spectrometer stage. Those detectors were not used for tracking but were a part of the muon trigger system. A coincidence matrix between several planes was able to decide on a fast basis if a muon track was pointing to the target region or not. In combination with the VETO planes only physically relevant muon tracks were filtered which was of great importance for low interacting muon beams and inclusive measurements.

BEAM MOMENTUM STATION Speaking of inclusive events in muon beams one needed to measure the beam energy. The Beam Momentum Station (BMS) determined the track displacement in the dipole bending

region of the M2 beam line. The information of the track distance to the nominal beam axis given by the dipole currents provided the nominal momentum to each recorded muon beam track. It would be a nice feature to know the momentum also for hadrons. Unfortunately the material budget of the **BMS** planes was by far too large for hadron beams, which are very sensitive to multiple scattering and energy loss. For a well defined hadron beam the **BMS** was therefore removed. The exclusivity of an event could only be reconstructed then by the measurement of all final states. Semi-inclusive reactions cannot be reconstructed from hadron data of the years 2008 and 2009.

2.3.7 Trigger

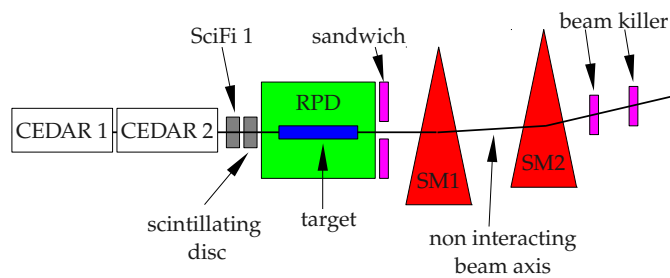


Figure 2.13: Schematic top view showing important trigger elements in the **COMPASS** spectrometer. The beam is entering the hall from the left. The two **CEDAR** detectors were set most of the beam time for kaon identification. The beam particles were triggered by two planes of the first **SciFi** station and in addition by a scintillating disc. A recoil proton from single diffractive scattering in the target was identified by the **RPD**. The sandwich veto was rejecting non exclusive events outside the spectrometer acceptance. A non interacting beam particle would be deflected along the nominal beam axis hitting further scintillator discs referred as the beam killer.

A set of triggers was set up for the hadron runs in the years 2008 and 2009 focused mostly on the diffractive dissociation and central production of resonances. Main components of the trigger system are sketched in figure 2.13. Those were

- **RPD** identifying a recoil proton kicked out of the target
- **SciFi** planes in the first detector station for a beam particle detection
- A Beam Counter (**BC**) consisting of a scintillating disc with a diameter of 32 mm and a thickness of 3 mm
- **VETOs** including a *beam killer* consisting of two scintillating discs placed in nominal axis of the non interacting beam downstream the target.
- **CEDARs** for a positive beam kaon identification with majorities greater than 6 (see also chapter 3)

- random noise source.

The most important trigger was the so called DT0 trigger:

$$DT0 = BT \wedge RPD \wedge \overline{VETO} \quad (2.5)$$

All events with interacting particles of diffractive signature were recorded. For a typical beam trigger intensity of $1.8 \cdot 10^8$ events per spill about 0.6% events were found to have diffractive signature. Those events contribute mainly to the recorded data.

Furthermore about 30% of all recorded events were triggered by the kaon trigger (KT):

$$KT = BT \wedge CEDAR1 \wedge CEDAR2 \wedge \overline{VETO} \quad (2.6)$$

This trigger was enabled for negative hadron beams as the CEDAR detectors were set for positive kaon identification. In positive hadron beams the trigger was disabled as CEDARs were set for pion and proton identification, the main component of the hadron beam.

For detector studies it is recommended to use minimum biased triggers. A small part of the data was recorded for events with randomly generated triggers as well as for beam triggers only. Random triggers allow the analysis of detector efficiencies as no reconstruction mechanism is biasing measured detector times and hits. It is clear that a large fraction of those events contained no relevant data. The beam trigger on the other hand was not affected by any physical threshold, cross sections nor production mechanisms. This trigger was mostly used to study the CEDAR efficiencies in COMPASS data (see chapter 3).

2.4 SUMMARY

The CERN facility provided a very flexible beam line allowing to switch between muon beams and hadron beams on a short timescale. This was the main reason to merge two collaborations with basically different physical aims into one strong community with a very broad field of interest.

The COMPASS spectrometer matched all criteria for this versatile physics program on a fixed target. Naturally still many modifications had to be adapted to change from a muon set-up to a hadron set-up. Major improvements in calorimetry and tracking were made. In addition the target region was completely rebuilt. Apart from those changes, the spectrometer set-up was mostly the same as for muon runs before 2008, featuring a large acceptance for charged and neutral tracks. Merely the acceptance of final state PID, designed for inclusive reactions with large multiplicities, is shown in chapter 4 to be critical in the hadron program.

THE CEDAR DETECTOR



Figure 3.1: Picture of [CEDAR](#) detector in the M2 beam line overlaid by an illustrated cut through the detector. The high pressure vessel containing helium was covered by an insulation box to shield the vessel against thermal and physical influences.

Two Cherenkov Differential counter with Achromatic Ring focus ([CEDAR](#))-N detectors were placed about 30 m upstream of the [COMPASS](#) target in the beam line (see figure 2.4). Those detectors were built in the late 70s and provided since today a tool to the physicists for beam particle identification at high beam energies. Only basic knowledge about those detectors, important for the comprehension of performances, is committed here. A very detailed description of this detector can be found in [61, 62].

3.1 THE FUNCTIONAL PRINCIPLE

The sketch 3.2 depicts the principle of particle separation in hadron beams of fixed particle momenta. Charged particles traversing a transparent medium faster than the speed of light in this matter emit Cherenkov light. Having same momentum but different masses the angles of the light cones differ. Already a simple concave mirror at the very end of the

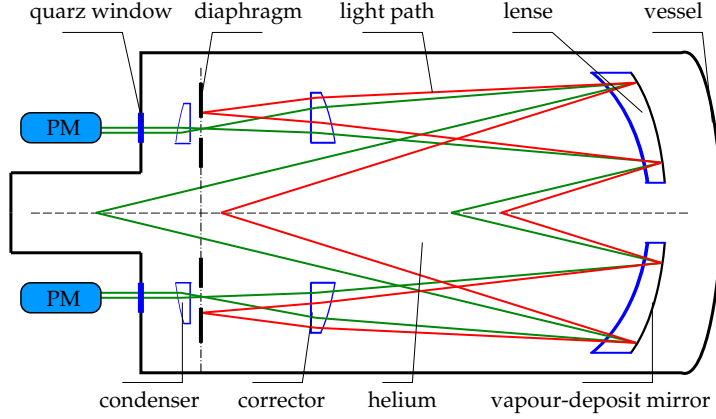


Figure 3.2: The principle of CEDAR detectors. Beam particles as kaons (green) and lighter pions (red) are passing the radiator volume from left to the right. Assuming to have the momentum but different masses those particles differ in their velocity. The Cherenkov photons, emitted in the pressurized helium gas, are focused to two rings. A diaphragm in the focal plane separates wanted from unwanted photons before detecting those by 8 PMs arranged perpendicularly. The sketch is a distorted view of a 6 m long vessel.

radiator would concentrate the cones into light rings in the focal plane. However, this is only true for one wavelength. The Cherenkov angle

$$\cos(\theta(\lambda)) = \frac{1}{n(\lambda)\beta} \quad (3.1)$$

depends not only on the relative velocity β of this particle and the refractive index n . The refractive index varies also as a function of the emitted wavelength λ under the assumption that density of the matter is constant. The range of the emitted wavelengths spans the whole optical transparency and the number of photons N_{ph} over the wavelength follows the well known

$$\frac{dN_{ph}}{d\lambda} = 2\pi\alpha L \frac{\sin^2(\theta)}{\lambda^2} \quad (3.2)$$

dependence [63]. L is the length of the radiator and α the Fine-structure constant. Obviously dispersion makes the application of a simple mirror difficult as the beam spot would be widened and necessitates therefore the use of an achromatic system. A fixed combination of two lenses with a vapour deposit mirror was optimized for the highest beam momenta reducing the beam spot in the focal plane from 2 mm without correction down to 0.02 mm at 190 GeV/c.

This was necessary as the difference between the two light rings of a kaon and a pion

$$\Delta R = f \cdot \Delta\theta \approx \frac{f (m_K^2 - m_\pi^2)c^2}{\theta 2p^2} \quad (3.3)$$

was only 0.4 mm¹. It would be possible to separate kaons from pions by a diaphragm with an lid opening as narrow as the light ring wide is. But the light ring was broadened by some more effects forcing one to open the lid to minimum 0.5 mm.

MULTIPLE SCATTERING Particles passing the medium undergo the effect of multiple scattering.

$$\Delta R_{m.s.} = f \frac{15}{\beta p} \sqrt{\frac{LP}{3X_0}} \quad (3.4)$$

In addition to the focal length f and the momentum p , the pressure P of the gas radiator and its radiation length X_0 are needed to calculate a ring width of about 0.01 mm. Thanks to the choice of helium as a radiation gas was it possible to reduce this effect to a negligible value, even with the usual high pressure setting of above 10 bar.

TEMPERATURE GRADIENTS A temperature gradient ΔT along the radiator had an influence on the detector resolution. As pressure in a closed small gas vessel is the most constant value along the volume, temperature differences are compensated by the gas density. The gas density itself is directly related with the refractive index n . Emission Cherenkov angles hence vary along the volume. This effect can be estimated with

$$\Delta R_T = \frac{1}{2\sqrt{3}} \frac{(1-n)}{n} \frac{f}{\tan \theta} \frac{\Delta T}{T} \quad (3.5)$$

It is important to keep the temperature uniformity better than $\Delta T = 0.1$ Kelvin for a stable operation at high beam momenta.

BEAM DIVERGENCE The sketch 3.2 is valid for particles passing parallel to the principal axis. In reality beam divergence was mostly the source of non parallel beam tracks. A tilted track displaced the light ring in the focal plane by

$$\Delta R_{div} = f \cdot \Delta \theta_{div} \quad (3.6)$$

A tilt of only 100 μ rad results in a displacement of 0.388 mm. This is almost the difference of the radii of kaon and pion light rings at 190 GeV/c beam momentum.

However, after separation photons were identified with 8 PM tubes arranged in a circle outside the helium volume. To match the active surface for each PM a condenser lens was applied behind the diaphragm. Light rings were mostly identified by a coincidence between the PMs. A typical majority restriction was minimum 6 of 8 PMs giving the best performance for pion and kaon separation. This will be shown later in this chapter.

¹ This was calculated for a focal length of 3.88 m and an Cherenkov angle of 25.76 mrad at 580 nm.

One important point about operating this detector at different beam momenta was not touched so far: The fixed aperture of the diaphragm required the Cherenkov photons of wanted particles to be emitted with an angle of 25.76 mrad at 580 nm wavelength. The light optics were fixed. The only free parameter in formula 3.1 remains the refractive index. It was controlled by the pressure in the vessel. For a correct setting on a wanted particle a so called *pressure scan* was performed before. Starting at high pressures angles of particles were large and out of the lid acceptance. The stepwise reduction of the pressure made the light rings pass the lid giving signals at the PMs. A typical pressure scan from 1979 in a parallel shorter beam line is demonstrated by the graph 3.6 [62]. Clearly visible are signals from pions and kaons giving the correct setting at the peak positions. Typical pressure settings were beyond 10 bar. Pressure scans were the most important tool to analyse performances of CEDAR detectors and are treated throughout this chapter.

3.2 THE MECHANICAL DESIGN

Technical details are made visible in the cut 3.3 through the detector. Some facts are particularly informative:

Actually there were two types of CEDAR detectors available. The presented CEDAR-N detector was filled with helium separating kaons from pions up to 300 GeV/c. The lowest momentum measurable was about 60 GeV/c for protons. As the west area at the CERN facility was fed with beams of lower momenta CEDAR-W detectors were designed to match those criteria. The main difference was the nitrogen radiator gas with modified light optics. The identification range started at 12 GeV/c for protons but ended at 150 GeV/c for pions. Too low for an application at the M2 beam line in the North Area.

The optical tower with a length of 4.5 m had a thermal expansion of 0.05 mm/Kelvin and was holding the diaphragm and the two lenses with central cut outs for the beam as well as the Cherenkov light cone. One lens had a vapour deposit mirror surface on the back with a reflectivity better than 80%. The lenses made from Suprasil focused the light rings on the focal plane where the diaphragm was placed. The lid could be adjusted from 0 mm to 20 mm with an accuracy of 0.01 mm.

The lower momentum cut was simply due to the pressure restrictions of the steel vessel. The vessel wall thickness was 24 mm and it could handle pressures up to 15 bar. For a temperature uniformity along the vessel aluminium and copper shells were clamped to the vessel. In addition to improved temperature conductivity a 10 cm thick PU-foam was forming a thermal shield around the vessel. Three platinum wire thermometers were screwed into the vessel flanges for monitoring purposes. One was placed at the nose the second at the beginning and the last at the end of the vessel. All heat sources, particularly the passive bases, were placed outside the heat shielding.

Eight quartz windows with a thickness of 4 mm were separating the highly pressurized gas volume from the PMs. Those windows held a UV cutoff filter each where the purpose of a better resolution was confirmed by own simulation studies presented later in this chapter.

The whole detector was 6.2 m long and had a mass of 2.4 tons. It was held by motorized platforms allowing to adjust the detector along the nominal beam axis. The accuracy of the motorized stand was 0.01 mm resulting in an angular resolution of 2.3 μ rad.

The pressure was measured with a transducer that is an oscillating cylinder in a temperature stabilized small volume. The frequency was proportional to the pressure and was calibrated with the help of refractometers. As this procedure was done only once for commissioning a systematic offset of the measured pressure value was observed after years without recalibration.

3.3 ELECTRONIC PROCESSING

The CEDAR detectors were maintained mostly by CERN staff. Not only the gas supply but also signal processing was under the control of those employees. But the original idea to provide only majority output to physics triggers at the experiments was not sufficient for the COMPASS physics program. To have some control over the individual channels, active splitters just behind the PM output were installed. In this way an independent Data Acquisition (DAQ) chain was set up recording hits of each individual PM. This explains some differences between online and offline detector feedback later in this chapter. A detailed description of the readout chain is given in appendix C.2. Speaking of *online* values, direct feedback from M2 beam line electronics is meant. *Offline* means the analysis of recorded COMPASS data.

3.4 MC SIMULATION

The work with this detector started with a diploma thesis [64] in the year 2006. At this time there was no experience running those detectors in a stable way at COMPASS. But to get a feeling about the detector behaviour before running those in reality a simple Monte Carlo (MC) simulation based on distribution functions was developed showing already qualitatively some basic features. In order to quantify various effects, the simulation was completely rewritten based on photon propagation matrices.

PHOTON PROPAGATION APPROACH Cherenkov photon propagations were calculated by optic matrix operations with the paraxial approach[65]. For each refraction and reflection surface one matrix was written down. The matrices (see appendix C.1) propagate the properties of the photon from the emission point to the diaphragm plane. The properties are represented by the distance to the optical line Y and the angle Θ to it.

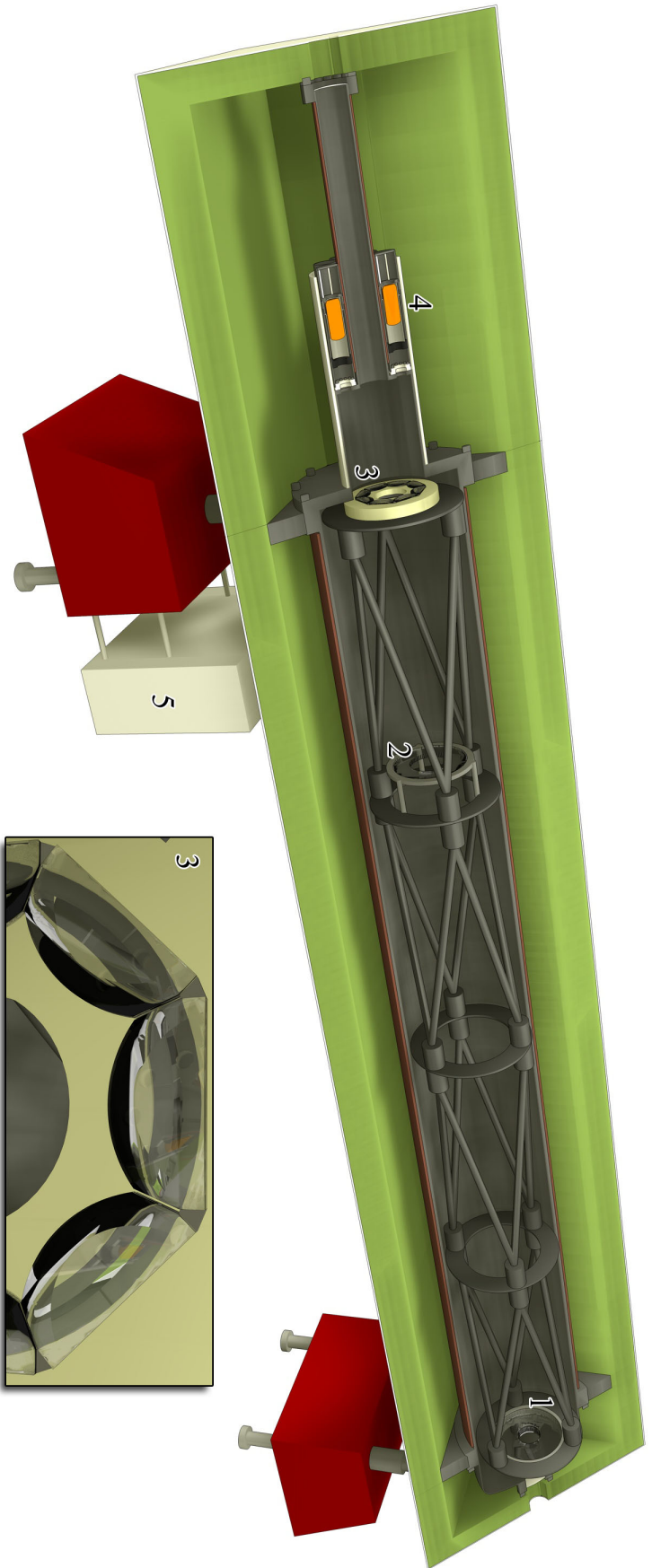


Figure 3.3: Illustrated cut through a 6 m long CEDAR detector. The particle beam was entering the pressurized helium tank from left and emitting Cherenkov photons during the passage of the radiator. The light cone was reflected by a mirror vapour-deposit onto the back of a concave lens (1) that acted together with a convex lens (2) as an achromat. A diaphragm (3) was placed in the focal plane of the optical tower and separated the Cherenkov light rings for the wanted particle mass. Behind the diaphragm's slid eight lenses were mounted condensing the passed photons on the photo cathode of eight PMs (4) arranged in a circle. The vessel volume was separated from the PMs by quartz windows where also UV-light filters were applied. Passive voltage dividers (5) were placed outside a 10 cm thick PU-foam isolation. Copper filaments along the steel body ensured together with the isolation a uniform temperature gradient along the vessel. A motorized support allowed to align the whole detector in the beam line.

SIMULATION STEPS Only pions and kaons were considered in the simulation. The number of simulated pions equalled the number of simulated kaons until results of both particle types were combined. There the correct ratio between pions and kaons was taken into account as calculated in section 2.2.

The overall number of emitted photons is given by equation 3.2 and can be expressed as

$$N_{\text{ph}} = \frac{\pi}{\alpha} \cdot \sin^2(\theta(\lambda_0)) \cdot L \cdot (\lambda_{\text{min}}^{-1} - \lambda_{\text{max}}^{-1}) \quad (3.7)$$

where wavelength and thus photon emission angle were taken as constant, matching the aperture acceptance. At the beginning of one particle event all photons were propagated uniformly along the particle track. The track path itself was tilted according to a Gaussian shaped track divergence distribution. In addition each photon emission point was smeared due to multiple scattering effects in the gas. The probability for a wavelength was following the $1/\lambda^2$ dependence [63]. The Cherenkov photon angle was given then by the momentum of the particle and its wavelength. The momentum spread of the beam track (see sec. 2.2) was taken into account as well as the beam track divergence. Only photons within the sensitive range of the PMs were simulated [66]:

$$[\lambda_{\text{min}}, \lambda_{\text{max}}] = [190 \text{ nm}, 600 \text{ nm}] \quad (3.8)$$

The propagation matrix \hat{M} depends on the temperature and the pressure of the helium gas as well as the wavelength of the Cherenkov photons. Temperature and pressure were assumed to be uniform and constant for a group of simulated particles. In principle one should calculate for each wavelength a propagation matrix. In order to reduce time consuming matrix calculations for each photon, the sensitive range of PM photo cathodes was divided into steps of 1 nm. For each step one mean matrix was calculated taking the temperature in the detector into account.

Finally the quantum efficiency curve of the PMs was parametrized as a function of the wave length [61]. The propagated photon, reflected by the mirror and passing the diaphragm was then identified with the probability given by this curve. In addition an overall efficiency of the electronics was multiplied as a constant term with this quantum efficiency in order to simulate effects not taken into account separately as thresholds, resolutions and smearing.

RESULTING PHOTON DISTRIBUTIONS To illustrate various influences on photon distributions at the diaphragm, 100 000 particles were simulated with beam properties as measured in the years 2008 (see sec. 2.2).

Figure 3.4 shows the radial photon impact distributions on the diaphragm for all Cherenkov photons. A slit of the diaphragm separating wanted photons (black) by kaons from unwanted photons (gray) by pions

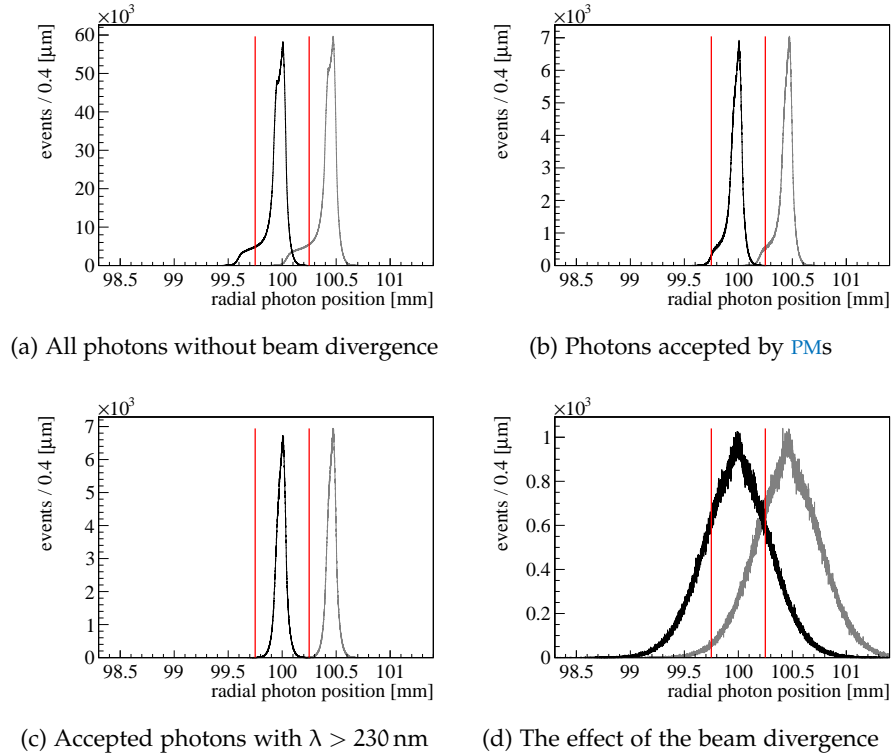


Figure 3.4: Cherenkov photon distributions on the diaphragm originating from kaons (black) and same number of pions (gray). The influence of various variables is demonstrated as they were noted in the year 2008. The diaphragm's slit is indicated with red lines. See text for a discussion.

of 0.5 mm is indicated with red lines. It should be kept in mind that mainly pions contributed to the beam composition. Therefore the gray distributions have to be imagined scaled by many orders.

Simulating a fully parallel beam led to the photon distributions 3.4a. The difference between the radius of kaon and pion light rings is less than 500 μm . The width of the light ring is about 150 μm (*fwhm*) and around 500 μm at the wider base. The width of the ring is reduced taking the quantum efficiency of the PMs into account but still separation quality is not optimal (fig. 3.4b). The wide base is mostly due to photons with a very short wave length. Simulating an additional cutoff of wavelengths below 230 nm the distribution becomes narrower (fig. 3.4c). This cut off in the wave length was indeed realized by applying filters to the quartz windows which are separating the pressurized vessel and the PMs [62].

Nevertheless the most dramatic influence on the light ring width was due to the beam divergence. Particles crossing the radiator not parallel to the optical axis produced a displacement of the light ring. The one dimensional photon distributions 3.4d became very broad. The pion ring seems to overlap too much for a clean separation. But still it is possible to distinguish between pions and kaons: When looking on the two dimensional photon distribution 3.5 on the diaphragm where all

divergent tracks were tilted into one plane one notices regions along the ϕ angle where good separation is possible. Of course other regions will suffer from the wider light rings.

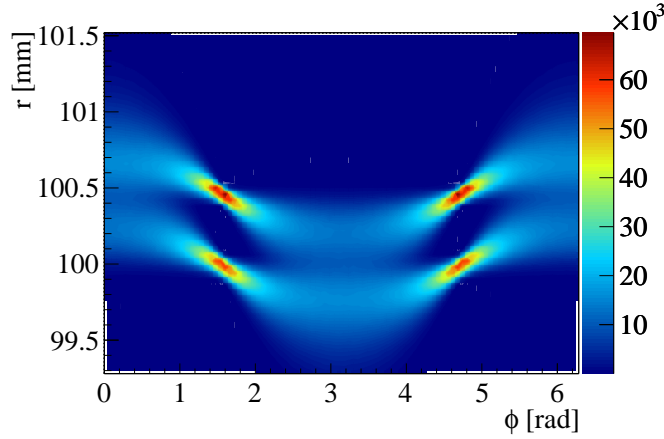


Figure 3.5: Simulated two dimensional distribution of photons on the diaphragm with a beam divergence as found for the years 2008 and 2009. The divergence was generated in one plane for illustration. Regions exist where the separation along ϕ still is possible whereas other regions have strongly mixing photons originating from pions and kaons.

COMPARISON OF SIMULATION AND DATA To tune MC variables and to test the quality of this simulation, a published pressure scan [62] with carefully optimized settings was used to compare to. The key values for that pressure scan performed in a different beam line are listed in table 3.1 in direct comparison to typical values in the M2 beam line for the COMPASS spectrometer in the year 2008. A remarkably good

value	H2(1979)	M2(2008)
dist. prim. target	470 m	1050 m
beam momentum	200 GeV/c	191 GeV/c
particles per spill	$1.9 \cdot 10^5$	$2.1 \cdot 10^6$
$\Delta\theta_{\text{horiz}}(\text{fwhm})$	50 μrad	210 μrad
$\Delta\theta_{\text{vert}}(\text{fwhm})$	100 μrad	110 μrad
diaphragm opening	0.405 mm	0.490 mm

Table 3.1: Beam properties as measured 1979 in the H2 beam line [62] and 2008 in the M2 beam line during a CEDAR pressure scan.

agreement was found when setting the CEDAR efficiency to 80% (see figure 3.6). However, runs in the years 2008 and 2009 provided at the end real pressure scans taken in the M2 beam line to test the predictions of the simulation. A comparison of the MC simulation with a pressure scan of 2008 showed that the simulation failed to describe the pressure

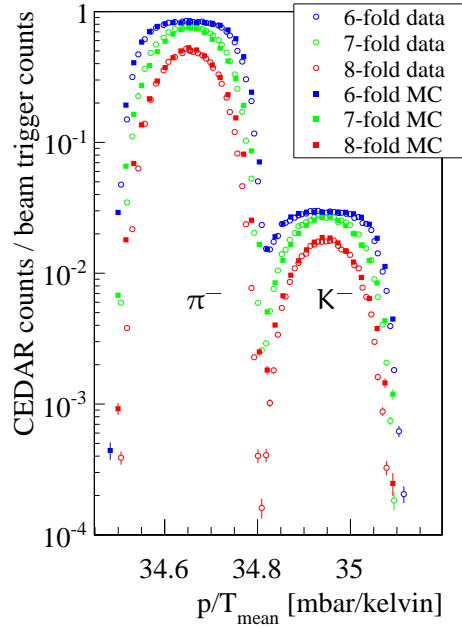


Figure 3.6: A CEDAR pressure scan in a MC simulation (open markers) in comparison to data recorded with a CEDAR in the H2 beam line (filled markers) in 1979 [62]. The simulation was able to reproduce the real shape.

scan quantitatively in the region between pion and kaon setting (see figure 3.7).

The efficiency of the simulation had to be reduced artificially in order to follow the real curve although PMs and electronics were proven to be efficient. This is not surprising as other effects occurring in the real data as pileup, not optimal alignment and non uniform temperature along the vessel were not taken into account in the simulation. The effects of those additional influences will be discussed in later sections when inspecting real pressure scans measured under different circumstances. The simulation was not improved as no more benefits were expected from it.

3.5 COMPARISON OF ONLINE AND OFFLINE PRESSURE SCANS

Before inspecting online pressure scans from 30 upstream of the COMPASS target, it had to be confirmed that efficiencies and purities deduced there were also found at the target region. This was not clear as measured online multiplicities of CEDARs may have completely different characteristics than offline values. The beam trigger for online pressure scans was placed next to the CEDARs whereas beam triggers for COMPASS DAQ were placed next to the target. Not only did beam optics differ but also many other sources of uncertainties like dead times were found. To confirm results taken online, recorded COMPASS data was combined with Detector Slow

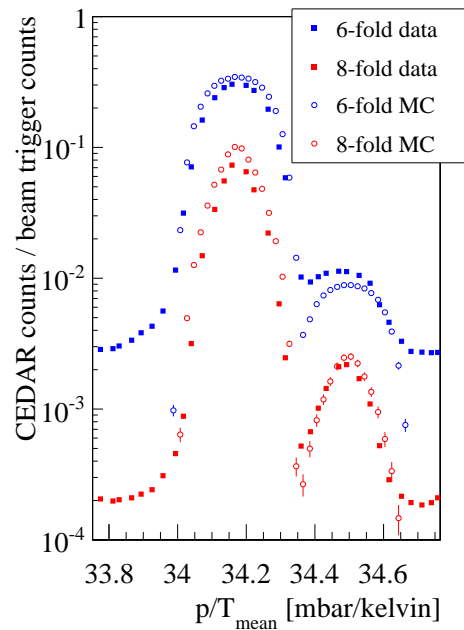


Figure 3.7: A CEDAR pressure scan in a MC simulation (open markers) in comparison to data recorded with a CEDAR in the M2 beam line (filled markers) in 2008. Only poor agreement was found in the region between kaon and pion separation. The overall simulated efficiency had to be reduced artificially to describe the shape at least qualitatively.

control (DCS) values containing pressures and temperatures as measured at the CEDARs.

Those offline pressure scans were not recorded for every pressure scan. One pressure scan took about one hour. But the DAQ mandatory for this analysis had to be shared among other detector groups. Nevertheless some dedicated runs were taken to perform those cross-checks. One result is presented in the pressure scans in figure 3.8. The number of beam trigger events in the offline data was much lower than in online results as the trigger was pre-scaled. This explains large statistical uncertainties compared to online pressure scans. In addition each spill is shown in the offline data whereas online pressure scan software accumulates data only every 2 to 3 spills to wait for a stabilized pressure after a pressure step. This synchronization could not be done automatically for offline pressure scans. Also one may recognize that background for 6-fold events was systematically significantly lower in offline data. This can be explained by beam halo particles at the CEDAR region producing additional counts by PMs not recorded by the M2 beam triggers. Offline data was triggered by the COMPASS trigger and took thus only particles in the main beam spot into account. Particles outside this beam spot were rejected by the VETO detectors. Online pressure scans on the other hand, counted self triggered on the majorities and used the beam trigger only for normalization.

Another difference was found in the efficiency for CEDAR 2. The number of recorded events was lower than the number seen by the M2 electronics.

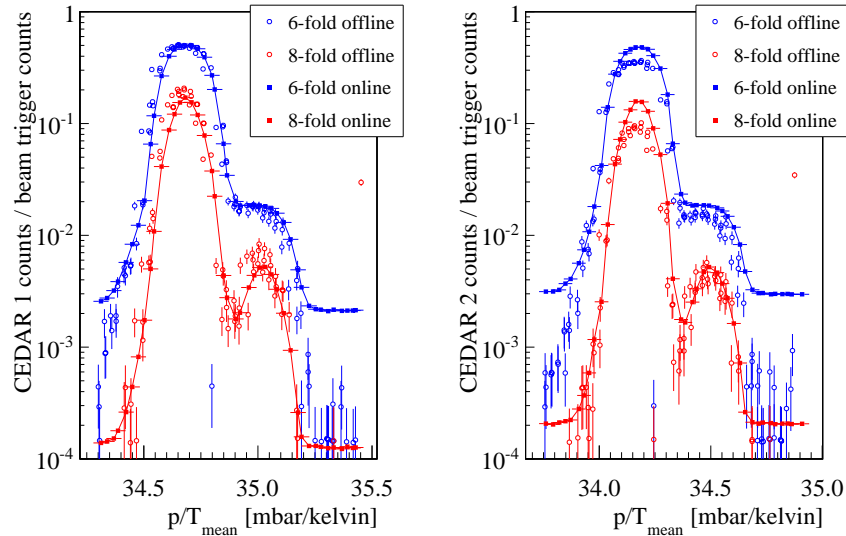


Figure 3.8: Comparison of offline majorities recorded with the [COMPASS](#) beam trigger and the corresponding online pressure scan with [CEDAR 1](#) (left) and [CEDAR 2](#) (right). The background from halo particles in the online pressure scans is not visible in offline data. The separation between pions and kaons is comparable. The efficiency for pions is reduced in [CEDAR 2](#).

[CEDAR 2](#) showed a problem with reflected signals extending the dead time at the leading edge discriminators.

Apart from these minor differences a very good agreement was found in the shape of the pressure scans online and offline. Therefore it was deduced that it is sufficient to only analyse online pressure scans that were not interfering with the [COMPASS](#) experiment.

3.6 ESTIMATION OF EFFICIENCY AND PURITY

The efficiency and purity of [CEDAR](#) detectors in hadron beams was estimated by inspection of pressure scans. A direct measurement of those properties was not possible due to the special set-up of the [COMPASS](#) spectrometer for diffractive physics. This was mainly due to the trigger settings that were requiring a measured recoil proton in most of the cases. No diffractive nor centrally produced resonances had a clear signature allowing for distinction between kaon or pion induced events. And just a few events were recorded unbiased, too few to investigate in systematic studies for example on the free kaon decay into three charged pions.

To estimate the performance of kaon pion separation it was needed to unfold the overlapping region between the kaon and pion peak (see figure 3.9a). This was done by mirroring the non overlapping opposite shoulders at the peaks, assuming a symmetric structure for one kind of particles. The resulting unfolded signals (figure 3.9b) were added as the sum of both signals had to follow the curve of the pressure scan (figure 3.9c).

The difference between the real pressure scan and the sum of both evaluated unfolded signals was used to estimate the systematic uncertainty for the signals. The overall normalized count rate C_+ was the sum of the pion C_π and kaon C_K count rates determined by mirroring.

$$C_K + C_\pi = C_+ \quad (3.9)$$

Two assumptions were made. One that the difference ΔC_+ between the sum of both signals to the real curve C_r was the sum of two errors on the individual count rates

$$|\Delta C_+| = |C_+ - C_r| = |\Delta C_K| + |\Delta C_\pi| \quad (3.10)$$

and another that the relative errors contributed by the same amount

$$\frac{|\Delta C_\pi|}{C_\pi} = \frac{|\Delta C_K|}{C_K}. \quad (3.11)$$

This led to the systematic uncertainties of the determined count rates

$$\Rightarrow |\Delta C_K| = \frac{|C_+ - C_r|}{C_\pi/C_K + 1} \quad (3.12)$$

$$\Rightarrow |\Delta C_\pi| = \frac{|C_+ - C_r|}{C_K/C_\pi + 1} \quad (3.13)$$

while background C_B was already contained in both count rates and assumed to be a constant noise term. As background was the lowest count rate in a pressure scan taken. It was either the for very low or very high pressure setting used.

The purity p_K over the p/T value of the CEDAR could easily be calculated based on the unfolded signals and the background to be

$$p_K = \frac{C_K - C_B}{C_K - C_B + C_\pi - C_B + C_B} = \frac{1}{1 + C_\pi/(C_K - C_B)} \quad (3.14)$$

taking the background as an impurity into account. Statistical uncertainty could be easily neglected due to the large number of events while systematic errors were propagated to

$$\Delta p_K^{sys} = \left(1 + \frac{C_\pi}{C_K - C_B}\right)^{-1} \sqrt{\left[\frac{C_\pi \Delta C_K}{(C_K - C_B)^2}\right]^2 + \left[\frac{\Delta C_\pi}{(C_K - C_B)}\right]^2} \quad (3.15)$$

neglecting the correlation between both errors.

The efficiency η_K was estimated by a rescaling of the kaon count rate according to the fraction in the beam.

$$\eta = (C_K - C_B)/2.4\% \quad (3.16)$$

Of course it was studied to describe the signal shape with an analytic function like for example a double Gaussian distribution for each particle type or even more complex functions. But all functions failed to describe the count rates at low efficiencies which is essential for unfolding the region between the kaon and pion setting.

Mirroring was therefore the only proper method, able to describe two folded signals from kaons and pions with background into account. Only the contribution from muons was not treated correctly, but was assumed to be of a second order effect.

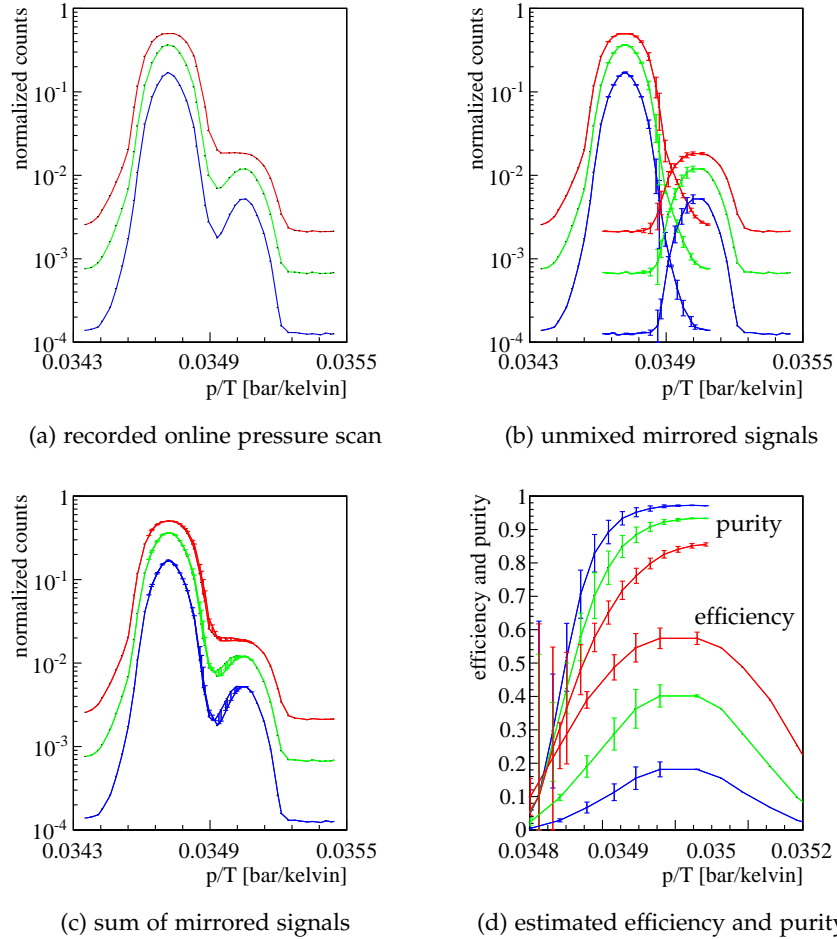


Figure 3.9: CEDAR pressure scan analysed by mirroring opposite shoulders at the peaks for 6 (red), 7 (green) and 8 (blue) fold events. Upper left: An online pressure scan as an input for analysis. Upper right: The pion shoulder left of the peak mirrored to the right and the right shoulder of the kaon peak mirrored to the left. The systematic uncertainty is already estimated based on the difference of the sum of both signals to the original pressure scan (lower left). The purity is as expected the highest for 8-fold events whereas 6-fold events show the highest efficiency (lower right).

3.7 PERFORMANCE FOR SEPARATION OF KAONS AND PIONS

3.7.1 Dependence on beam divergence

The offset of a light ring at the focal plane is given by the track angle times the focal length. Relatively small track angles of several microns result in large offsets that could not easily be compensated by opening the diaphragm. A compensation led to a loss of purity as demonstrated in section 3.7.2. Therefore tracks with large angles were detected with a lowered efficiency.

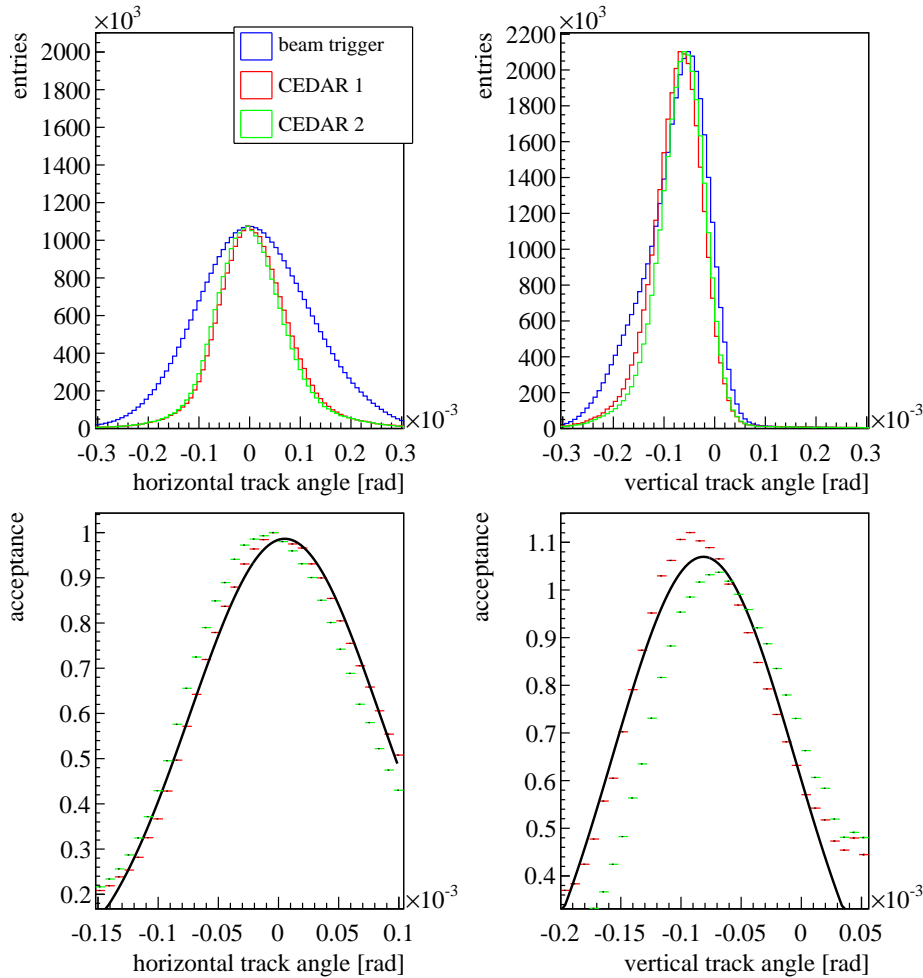


Figure 3.10: CEDAR accepted track distributions over the track angle in the horizontal and vertical plane. Top: Distributions for all events and CEDAR 1/2 accepted beam tracks. CEDAR accepted events were normalized to the bin entry with the highest number of entries. Bottom: Upper distributions normalized to all track distributions. A simple Gaussian fit for CEDAR 1 accepted events is drawn as a line (see text for details).

This effect is clearly observable in figure 3.10. The track angle for each beam track was measured at the COMPASS target region and propagated back to the CEDAR region as described in section 2.2. The comparison of

the track distributions of all tracks with those tagged by a 6-fold event in the CEDARs shows a significant loss of tracks with large angles. In order to estimate the acceptance effects, tagged track distributions were scaled to the same height independently in both planes. This was done as properties in both planes were uncorrelated and full acceptance for parallel tracks could be assumed. The ratio between both distributions was the angular track acceptance for the CEDAR detectors.

A fit of a simple Gaussian distribution to the acceptance plots gives the acceptance of the detector in terms of standard deviations. The obtained values are

- $(6.246 \pm 0.003) \cdot 10^{-5}$ rad for CEDAR 1
- $(6.696 \pm 0.004) \cdot 10^{-5}$ rad for CEDAR 2

with an overall offset of

- $(-1.770 \pm 0.003) \cdot 10^{-5}$ rad for CEDAR 1
- $(-6.600 \pm 0.003) \cdot 10^{-5}$ rad for CEDAR 2

for an analysis of partial 2008 data. The overall offset originates in wrong magnet currents used to calculate the track propagation matrices as discussed in section 2.2. Two dipole magnets between the CEDAR detectors and the COMPASS target were tuned after those calculations but this has not been taken into account afterwards. This finding had no effect on the further analysis as all calculations were based on those matrices.

3.7.2 *Dependence on diaphragm opening*

The possibility to increase the acceptance of the CEDARs by opening the diaphragm's lid was tested. Three consecutive pressure scans were performed in order to compare those under controlled conditions. Figure 3.11 shows the results for 6-fold and 8-fold events for CEDAR 2 and makes clear that opening the diaphragm had a dramatic effect on the separation quality. The effect of beam divergence lowering the efficiency could be easily compensated, but to operate the CEDARs with a purity of at least 80%, the lid had to be closed down to 0.5 mm leaving an overall efficiency of 30% for pions.

3.7.3 *Dependence on beam intensity*

An additional effect, not mentioned in literature yet, was observed when comparing online pressure scans at different beam intensities. Figure 3.12 is a comparison of three pressure scans with different beam intensities. It is evident that separation between pions and kaons was lowered at higher beam intensities. This effect can be explained by divergent pileup events from pions. In case ring size does not match the lid acceptance of either type of particle a shifted partially accepted ring might be completed by another incomplete one.

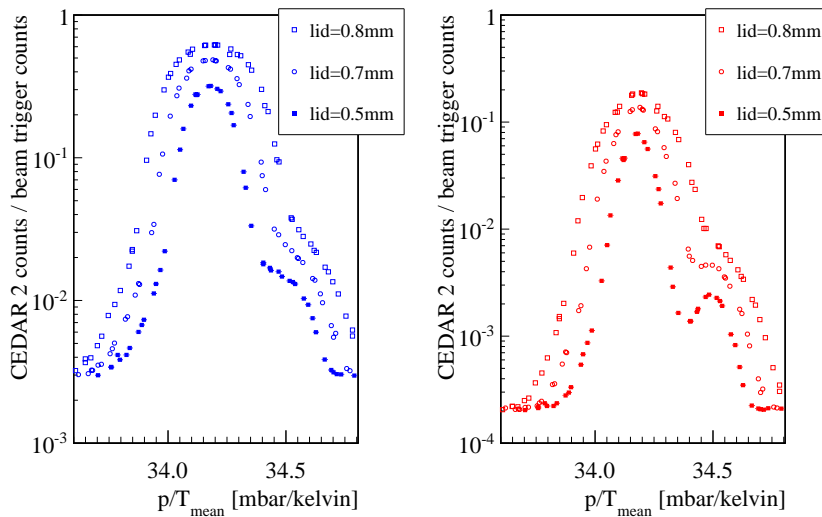


Figure 3.11: A comparison of consecutive pressure scans with 3 different lid settings at high beam intensities of $1.9 \cdot 10^7$ particles/spill. Left: pressure scans for 6-fold events. Right: pressure scans for 8-fold events. It was not possible to open the lid more than 0.5 mm without losing too much separation quality at 6-fold events.

3.7.4 Stability in the hadron runs 2008 and 2009

The refractive index, important for a correct setting of the Cherenkov angle of the wanted particles, depends on many variables and the most important ones as temperature and pressure are discussed here. Ideally having found the correct pressure for a given temperature by performing a pressure scan one can close up the CEDAR knowing the refractive index to be mostly independent from outside influences. Helium is unfortunately a very volatile gas, specially with 10 bar pressure. The observables are hence discussed over time in the following to give an impression of the stability of this detector in the years 2008 and 2009.

PRESSURE Even the massive construction of the pressure vessel was not able to keep helium in a closed volume. Gas connectors and optical windows were sources of leakages, small compared to the enclosed volume, large in terms of p/T differences between pion and kaon settings.

Figure 3.13 illustrates the loss in pressure over one day in CEDAR 2. This day a loss of 27.4 mbar was observed but this value depended strongly on the temperature in the detector.

TEMPERATURE The COMPASS experimental hall was exposed to large day night as well as seasonal temperature fluctuations. Even the thick isolating cover around the CEDAR was not able to keep those fluctuations away from the vessel as visible in figure 3.14. Only the temperature uniformity along the vessel could be kept somehow stable for CEDAR 2. CEDAR 1 was placed directly at the exit of the beam tunnel (see picture 3.1). The magnets in the beam tunnel heated up the air in there significantly.

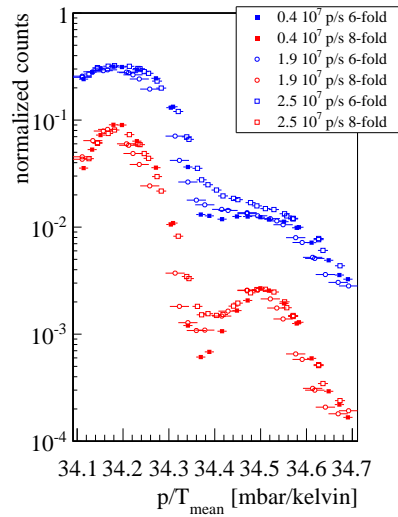


Figure 3.12: A direct comparison of 3 pressure scans at beam intensities starting from $0.4 \cdot 10^7$ particles/spill up to $2.5 \cdot 10^7$ particles/spill. The separation quality is significantly lost for 6-fold events at high beam energies. Pileup events from divergent pion tracks can artificially increase the efficiency for kaon identification.

The difference between the temperature in the tunnel and the hall induced a huge temperature divergence of up to 1 degree along CEDAR 1 clearly visible during cold days at the end of the run 2008. This temperature non uniformity is taken as a systematic uncertainty in the p/T values in pressure scans into account.

PRESSURE OVER TEMPERATURE AND THE PURITY Combining the information on the temperature in the CEDAR vessel with the pressure, the corresponding mean pressure over temperature graph is obtained and drawn as a black curve in figure 3.15 for the run 2008. This value was kept as stable as possible in the years 2008 and 2009 for specific CEDAR settings. The very large values at the end of the run 2008 correspond to a

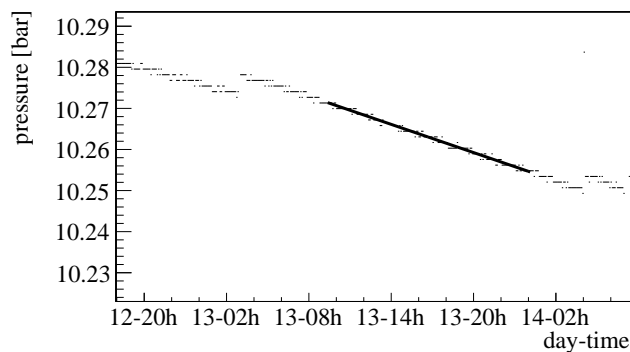


Figure 3.13: Recorded pressure of CEDAR 2 the 13th of September 2008. A constant decrease of in total 27.4 mbar helium pressure per day was observed in between CEDAR gas refills.

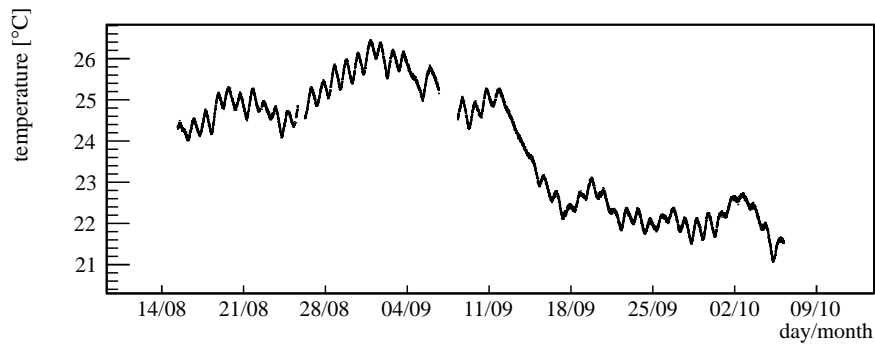


Figure 3.14: Recorded vessel temperature of CEDAR 2 in 2008. Small oscillations due to day night temperature fluctuations in the hall are visible as well as large seasonal temperature variations.

setting for proton identification discussed later in this chapter. The red graphs correspond to the minimum and maximum value obtained by the lowest and highest temperature measured along the vessel and were found to be much larger for CEDAR 1 at cold days than for CEDAR 2 due to the large temperature divergence along the vessel.

The purity as retrieved from mirroring reference pressure scans (see figure 3.9d for an example) was combined with the information on the pressure over temperature in the vessel to produce a database for the analysis. This database was optimized at several points. Purity at a specific time point in the data base was set to *zero* when

1. the p/T value was exceeding the range of calculated values in the reference pressure scan.
2. the systematic uncertainty in the reference pressure scan was greater than 10%.
3. the analysed reference pressure scan was made with a temperature deviating by more than 2 degree.
4. the measured diaphragm lid opening was a different one than those during the reference pressure scan.

In addition values were removed differing by less than 1% in respect to the previous in the data base. This increased the speed and decreased the allocated memory size significantly as p/T values were originally recorded nearly on a minute by minute basis.

A small time window of this optimized purity database for 6, 7 and 8-fold events is shown in figure 3.16. With this information the user is able to ask for a purity and the corresponding systematic uncertainty for each CEDAR and each event in his analysis without deeper knowledge about the behaviour this specific detector.

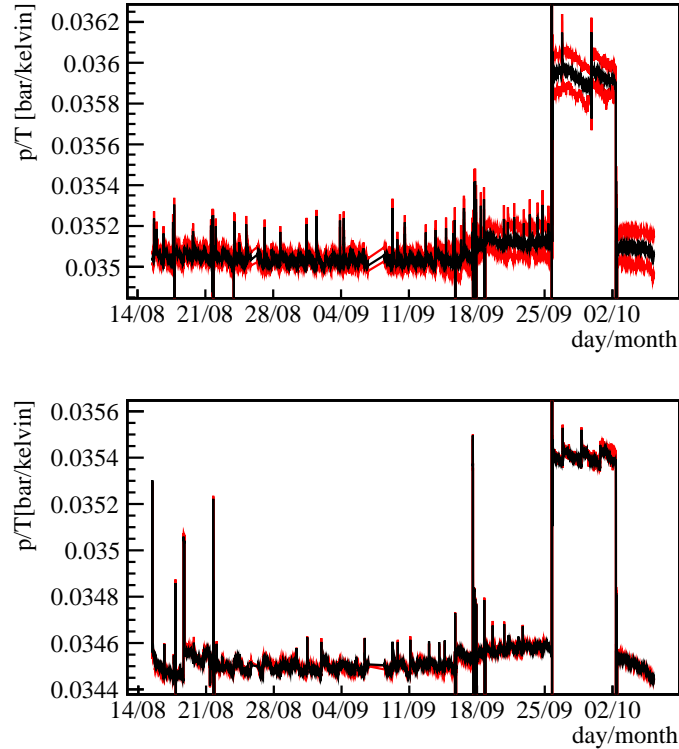


Figure 3.15: Pressure over temperature in dependence of the time in the hadron run 2008. The black curve corresponds to the mean pressure over temperature in the vessel. The red curves are the minimum and the maximum value. CEDAR 1 (upper plot) was affected by a much larger temperature divergence along the vessel at cold days. This was mostly the case at the end of the run.

3.8 PERFORMANCE FOR SEPARATION OF PROTONS AND PIONS

One week in the year 2008 and a partial run in 2009 was dedicated to the analysis of centrally produced events and baryon spectroscopy in protons beams. The charge of the beam was set to positive in order to have protons as a main component in the beam (see section 2.2). As protons have a much larger mass than pions and kaons, the separation between those was far easier than the separation between pions and kaons.

The diaphragm was opened to 1.2 mm compensating any acceptance effect by beam divergence. The resulting pressure scan is shown in figure 3.17. Here one can see the main advantage of recording each PM channel separately. While M2-beamline electronics allowed only majorities larger than 6 of 8 PMs, COMPASS offline analysis was not limited by this issue. A reduced efficiency due to dead times of the electronics could be compensated by requiring 4 or more of 8 PMs or more for analysis. The separation between protons and the lighter particles was still excellent with an efficiency better than 90%.

To illustrate the quality of the separation the majority distribution of CEDAR 2 versus CEDAR 1 is drawn in figure 3.18 for the run number

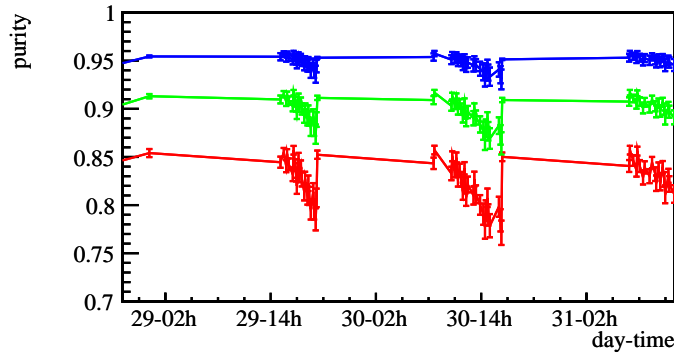


Figure 3.16: Typical values of the optimized purity data base in a small time range. The purity for 6-fold events is shown in red, 7-fold in green and 8-fold events in blue.

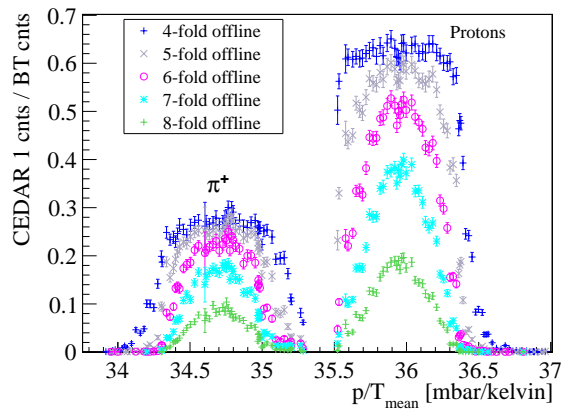


Figure 3.17: An Offline CEDAR 1 pressure scan for separation of pions/kaons from protons with a diaphragm lid opening of 1.2 mm. The efficiency was larger than 90% for offline 4-fold events.

77922. CEDAR 2 was set for pions while CEDAR 1 for proton identification. Even in a logarithmic scale nearly no correlation between both CEDARs is visible. A clean separation of pions and kaons from protons is proved.

3.9 PID WITH LIKELIHOOD FUNCTIONS

At a very late stage of this thesis Jan Friedrich developed an efficient way of CEDAR signal treatment in some late runs of the year 2009 dedicated to measurements with Primakoff signature [67]. The trigger was set up to identify events with a very low scattering angle and at least one photon in the negative hadron beam. A large number of free kaon decays into $\pi^- \pi^0 \rightarrow \pi^- \gamma \gamma$ were recorded together with Primakoff events. The invariant mass spectrum of those events, see figure 3.19, contains also the signal of a ρ decay induced by pions in the beam. Therefore a clean kaon signature as well as pion signature in the initial channel was given. It allowed for calculation of likelihood functions based on the information of the track angle and the corresponding PM response of kaons and pions.

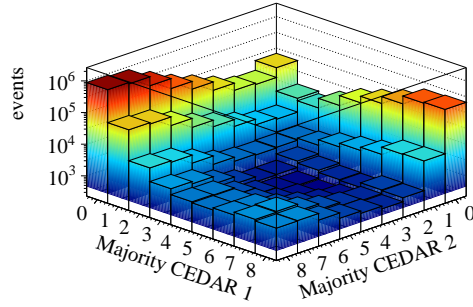


Figure 3.18: CEDAR majority distributions for CEDAR 1 identifying protons and CEDAR 2 pions/kaons. Very little correlation between the two was found which demonstrates a very clean separation.

An efficiency of more than 80% for both CEDARs together was achieved with a high purity similar to the one of 6-fold events.

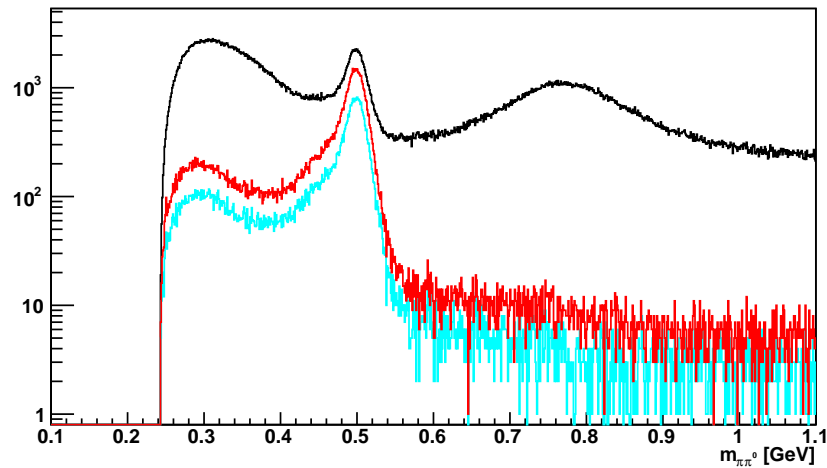


Figure 3.19: The invariant mass distribution of $\pi^- \pi^0$ tracks in three Primakoff test runs in the year 2009 [67]. The black curve shows all events containing the reconstructed invariant mass of the free kaon decay in the target as well as the strong $\rho(770)$ resonance from pion induced processes. Applying a cut on 6-fold events in the CEDARs resulted in the blue distribution separating clearly the free kaon decay. The efficiency with same purity was more than doubled when applying a likelihood cut as developed by Jan Friedrich.

This method could not be studied more deeply for the diffractive analysis presented here as basic problems need to be solved first: Clean kaon and pion initial state identification by the final state signature is mandatory to calculate the likelihood functions. Unfortunately, the trigger set-up for diffractive physics was not recording large numbers of events of the free kaon decay. Moreover, methods as the likelihood analysis depend strongly on the p/T setting of the CEDARs which was not stable as demonstrated in the previous sections. The possibility to

apply those methods anyhow to hadron data in the years 2008 and 2009 was the topic of separate studies under investigation.

3.10 SUMMARY

Stability and efficiency of the CEDAR detectors in the hadron runs were the main issues when separating kaons from pions. As beam divergence was shown to be large, the slit in the diaphragm had to be opened as far as possible, resulting in overlapping signals of kaons and pions in the pressure scans. Still a relatively small efficiency of about 30% was measured for 6 or more hits in 8 PMs per CEDAR detector.

A method was derived to estimate the purity out of a pressure scan in order to determine the correct pressure setting. As pressure was lost over time it was needed to reset the pressure over temperature value constantly. Constant monitoring of this value helped to stay in the required range and a stable operation was ensured for the years 2008 and 2009.

Based on the knowledge of the track divergence of each particle passing the CEDAR detectors, a new likelihood method was derived by Jan Friedrich for the Primakov run in 2009, replacing the simple majority cuts of PM signals. This method led to an efficiency of about 80% but was not applied to the run in the year 2008 as correctly determined likelihood functions for this data were not available at the time the present analysis was performed. In the future, it is expected to increase the number of recorded kaons in the beam by at least a factor of two with a similar purity compared to the presented majority selection.

THE RICH DETECTOR

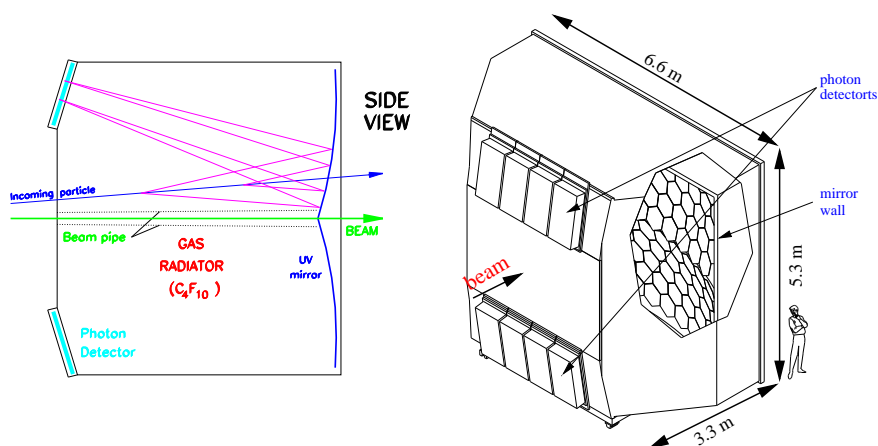


Figure 4.1: Illustration of the COMPASS RICH detector[68]. Left: Cut through the detector. Particles in the RICH volume emitted Cherenkov light cones that were focused by a mirror wall on pixelized photon detector planes. Non interacting beam particles or particles with only a small deflection angle passed the beam pipe. Those particles were not identified. Right: Perspective view of that detector to illustrate the dimensions.

Since a spectrometer measures only momenta of charged particle tracks one has to assume the invariant masses of those particles in order to obtain the full four-vectors. This leads in many analyses to ambiguous solutions that have to be clarified using detectors for final state Particle Identification (PID). COMPASS designed for this purpose the Ring Imaging Cherenkov (RICH) detector that was placed in the first stage of the spectrometer. A similar detector was planned for the second stage as well but never realized mostly due to financial reasons.

This chapter contains a brief description of that detector. The particle identification itself was not straight forward. The formalism was using likelihood methods and is discussed in section 4.2. As the performance of the detector depended on the applied likelihood cuts, a measurement of it is presented in section 4.3 giving a tool to tune cuts and to reuse the measured purities and efficiencies in further MC studies.

4.1 TECHNICAL LAYOUT

The technical layout is discussed in [57] and is shortly reviewed here. Figure 4.1 illustrates the construction of the RICH detector at COMPASS. Charged particles emitted Cherenkov light in a gas radiator filled with C_4F_{10} . The density is relatively large compared to other gases at ambi-

ent pressures which results in a refractive index of about 1.0015. The corresponding particle thresholds are discussed in section 4.3. Despite the large density of the gas, transparency is still very good even for wavelengths down to 160 nm.

To collect Cherenkov photons, polygonal mirrors were assembled to two spherical mirror walls with a total area larger than 21 m². The radius of curvature of 660 cm reflected and focused the emitted Cherenkov photons to light rings on the photon detectors located outside of the spectrometer track acceptance. Before 2006, photons were recorded by large MWPCs behind CsI photo-cathodes only. A major upgrade was then performed by replacement of parts in the central photon detection by multi-anode PMS, coupled to fused silica lens telescopes. In addition the readout was upgraded to faster F1-chip based Time to Digital Converter (TDC) cards allowing for rates of up to 100 kHz per each individual channel [69].

It is pointed out that particles with very small angles and thus next to the nominal beam axis, hit or even entered the RICH-pipe (see figure 4.1). That steel pipe purposely separated non-interacting beam particles with a very high flux from the radiating volume in order to reduce the occupancy of the photon detectors. It is clear that this additional material budget affected physical channels with low particle emission angles like exclusive neutral final states decaying into photons.

4.2 PID WITH LIKELIHOOD FUNCTIONS

The RICH PID was not based on a simple determination of track Cherenkov angles. Since only a few photons were detected, wanted photons had to be distinguished from background as noise and pileup as well as from photons belonging to neighbouring tracks. Instead of searching and fitting light rings, likelihoods for those rings were calculated based on all detected photons, a mass assumption and the expected Cherenkov angle from the measured particle track. This is described in detail in the notes [70] [71] and is reviewed shortly here.

The reconstructed photon distributions by light rings from charged particles can be described as a Gaussian distribution $G(\theta_{rec,k}^{photon}, \phi_{rec,k}^{photon})$ in the $(\theta^{photon}, \phi^{photon})$ polar angle plane for a fixed ϕ^{photon} angle. The index k stands for the type of the final state particle with the corresponding invariant mass. Considered particles were pions, kaons, protons, electrons and muons. The standard deviation of the Gaussian distribution is given by $\sigma_{rec,k}^{photon}$.

As a starting point, background was assumed to be flat in $B(\theta_{rec,k}^{photon}) \propto \theta^{photon}$ and was describing random sources as detector noise. For the non-flat background description of photons coming from other particles, that background function was modified based on data.

For each particle passing the RICH the corresponding momentum was reconstructed by the spectrometer. The Cherenkov photon emission angle Θ^{mass} was known for each mass assumption since the refractive

index of the gas was calculated. That angle was then compared to each reconstructed angle θ^{photon} between the track and a detected photon leading to a probability density

$$L_N = \prod_{k=1}^N [(1 - \epsilon)G(\theta_{\text{rec},k}^{\text{photon}}, \phi_{\text{rec},k}^{\text{photon}}) + \epsilon B(\theta_{\text{rec},k}^{\text{photon}})] \quad (4.1)$$

where the explicit functions are given by

$$G(\theta_{\text{rec},k}^{\text{photon}}, \phi_{\text{rec},k}^{\text{photon}}) = \frac{1}{\sigma_{\text{rec},k}^{\text{photon}} \sqrt{2\pi}} \exp\left(-\frac{1}{2} \frac{(\theta_{\text{rec},k}^{\text{photon}} - \Theta_{\text{mass}})^2}{(\sigma_{\text{rec},k}^{\text{photon}})^2}\right) \frac{\theta_{\text{rec},k}^{\text{photon}}}{\Theta_{\text{mass}}} \quad (4.2)$$

and

$$B(\theta_{\text{rec},k}^{\text{photon}}) = \frac{2}{(\Theta_M)^2} \theta_{\text{rec},k}^{\text{photon}}. \quad (4.3)$$

The fraction of background is ϵ . The functions were normalized to unity where $B(\theta_{\text{rec},k}^{\text{photon}})$ was bound by the maximum Cherenkov photon opening angle Θ_M calculated from the spacial acceptance of the detector.

Finally, the likelihood distribution was normalized to the total number of photons N of the specific particle:

$$L = \sqrt[N]{L_N} \quad (4.4)$$

That way one retrieved a set of likelihoods ($L(M_K)$, $L(M_\pi)$, $L(M_p)$, ...) for each mass hypothesis of a pion, kaon, proton, muon, electron and the background and for each measured track. A simple PID would be based on the largest likelihood among all mass assumptions. Expressed in terms of likelihood ratios would be the algorithm for a positive PID:

```
set particle =
  (no, background, electron, muon, pion, kaon, proton);
particle pid = no ;
float likelihood_ratio = 1.0 ;
particle k, k';
MAX_L(electron ... proton, k);
MAX_L(background ... proton, k' != k);
if (L(k)/L(k') > likelihood_ratio) {
  pid = k;
}
```

The function `MAX_L(electron ... proton, k)` sets k to the particle with the greatest likelihood.

The expression `MAX_L(background ... proton, k' != k)` means that k' is set to the particle (including background) with the greatest likelihood among all likelihoods, skipping that of the particle k . A physical PID result is obtained when one likelihood ratio was greater than the applied likelihood ratio cut of 1. No PID would be returned when background is dominating.

Naturally highest [PID](#) efficiency is obtained with a that likelihood ratio cut. But for cases where likelihoods become very similar to each other, as it is the case at large track momenta where Cherenkov light ring radii do not differ much, purity is suffering. A likelihood ratio cut of greater than 1 would be recommended then. The quality studies of that likelihood ratio cut are the topic of the following sections.

4.3 EVALUATION OF THE PERFORMANCE

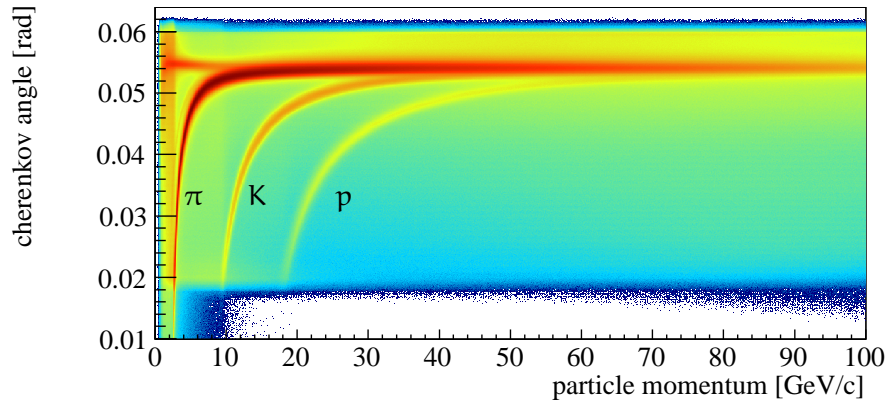


Figure 4.2: [RICH](#) reconstructed Cherenkov angles in the hadron beam 2008. Clear bands of pions, protons and kaons show up. A separation of kaons and pions becomes difficult for track momenta above 40 GeV/c. Protons can be distinguished from lighter particles up to 100 GeV/c.

It was possible to estimate the performance of the [RICH](#) detector already by viewing the reconstructed Cherenkov angles over the track momentum. Such a distribution for three charged track events is shown in figure 4.2 for data from the run 2008.

- The contribution of muons is visible but already negligible.
- Pions were identified above ~ 2 GeV/c.
- Kaons were identified above ~ 8 GeV/c and distinguished from pions up to ~ 50 GeV/c.
- Protons were identified above ~ 18 GeV/c and distinguished from pions and kaons up to ~ 100 GeV/c.
- Background and electrons should to be considered here in all cases specially for high momenta.

Cherenkov light thresholds were already calculated by the [RICH](#) group on a run-by-run basis as those were depending on the temperature and pressure inside the [RICH](#) detector volume. It was therefore taken in likelihood calculations into account.

The efficiency and purity of the [PID](#) based on [RICH](#) likelihood ratio cuts had to be quantified in order to measure the influence of the cuts on the

event selection. Thus rather clean sources of protons, kaons and pions were preferred to study those cuts. Easy and clean access to (anti-)protons and pions was given by analysis of $\Lambda \bar{\Lambda} K_s$, so called V_0 , decays. The first choice for a kaon source were $\phi(1020) \rightarrow K^+K^-$ decays due to the narrow width of that resonance.

The determination of the efficiency and purity of the RICH PID was already presented by Frederica Sozzi for 2006 muon beam data [72] and adapted successfully by Alexander Zvyagin for $D^* \rightarrow K\pi\pi$ analysis. But those methods had to be rewritten and retuned for 2008 hadron beam data. Specially the identification of $\phi(1020)$ decays needed a modification. In addition proton PID efficiency studies were added. All this is summarized in the following.

SELECTION OF V_0 DECAYS The concept of a forward spectrometer combined with the long lifetime of V_0 s allowed for separation of secondary vertices. Secondary vertices are reconstructed origins of tracks measured by the spectrometer with no associated incoming (charged) track. Those were selected in 2008 hadron data by the following cuts:

1. The vertex was a secondary vertex.
2. The vertex was located behind the target: $V_{0z} > -28$ cm.
3. The vertex was located in front of the first spectrometer magnet: $V_{0z} < 150$ cm.
4. The number of outgoing tracks was two.
5. Tracks had opposite charge.
6. The closest distance of a reconstructed V_0 track and a primary vertex was less than 30 mm.
7. Outgoing tracks were not associated to that primary vertex.

Only tracks outside the target were considered in order to increase the track resolution. Adding the restriction that the reconstructed neutral particle must point to a primary vertex allowed a clean separation from gamma conversion pairs ($\gamma \rightarrow e^+e^-$).

To demonstrate the high purity of this event selection the corresponding Armenteros plot is shown figure 4.3. Armenteros(-Podolanski) plots are traditionally used for direct identification of Λ , $\bar{\Lambda}$ and K_s^0 in secondary vertices in forward spectrometers. To obtain those plots the transverse momentum \vec{p}_T was determined in respect to the reconstructed V_0 direction over the longitudinal momentum \vec{p}_L asymmetry of both decay particles. Due to the large forward boost in the laboratory system the information of the mass of the decay particles is negligible and therefore only measured three-momenta were needed [73].

The resulting figure 4.3 shows clear bands of V_0 decays. Only very little contamination from e^+e^- pairs at low \vec{p}_T was found.

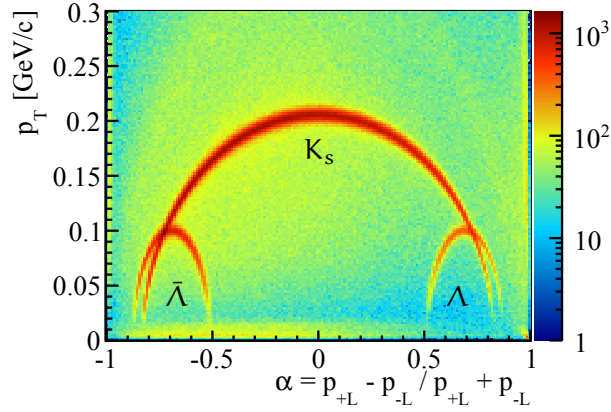


Figure 4.3: Armenteros diagram of V_0 events in 2008 data after cuts. Only a negligible contamination by e^+e^- pairs at low p_T is visible.

SELECTION OF Λ S AND $\bar{\Lambda}$ S To select Λ and $\bar{\Lambda}$ decays ambiguous solutions were removed that could have also been K_s s. In detail removed an anti-cut on the invariant mass of a K_s within $20 \text{ MeV}/c^2$ (compare also figure 4.5) events where the Armenteros ellipsis bands overlapped (figure 4.3). Finally cuts on the reconstructed invariant masses of Λ and $\bar{\Lambda}$ s (see figure 4.4) were chosen as narrow as the contribution by the background was kept below 3%. The background was determined by a fit of a double Gaussian with a linear background. The integral of the background over the signal was studied for different widths around the peak and fulfilled a below 3% criterion with:

- $1.11314 < m_\Lambda [\text{GeV}/c^2] < 1.11866$ what corresponded to $1.2 \times \text{fwhm}$ of the signal leaving 1.6% of background.
- $1.11475 < m_{\bar{\Lambda}} [\text{GeV}/c^2] < 1.11705$ what corresponded to $0.5 \times \text{fwhm}$ of the signal leaving 3% of background.

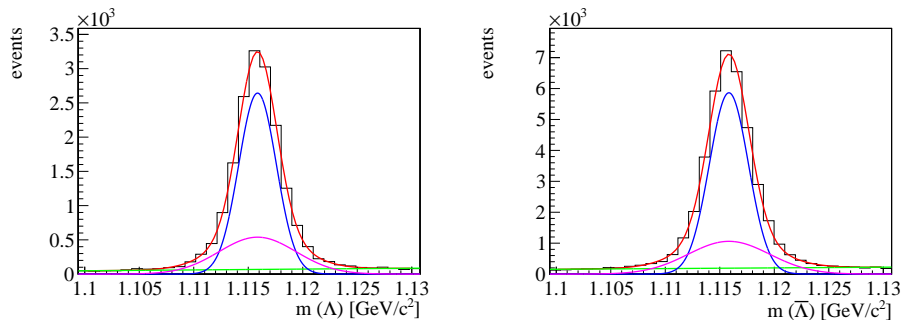


Figure 4.4: Reconstructed invariant mass distributions of a proton pion mass assumption after all cuts. The signal of Λ (left) and $\bar{\Lambda}$ (right) decays is already very clean. A fit (red) of two Gaussians (blue/purple) with a linear background (green) was performed to estimate the background contribution (see text for details).

SELECTION OF K_s DECAYS The width of the anti-cut on the invariant mass of reconstructed Λ and $\bar{\Lambda}s$ was set to $7 \text{ MeV}/c^2$ (compare also figure 4.4). The final cut on the reconstructed invariant masses of K_s s was (compare figure 4.5):

- $0.4850 < m_{K_s} [\text{GeV}/c^2] < 0.5106$ what corresponded to $2 \times \text{fwhm}$ of the signal leaving 1.6% of background.

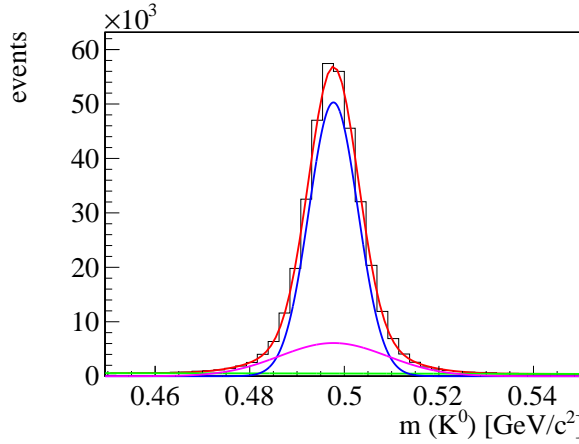


Figure 4.5: Invariant mass distribution of a K_s hypothesis after all cuts. A fit (red) of a double Gaussian (purple/blue) with a linear background (green) is shown. Background is barely significant.

SELECTION OF $\phi(1020)$ DECAYS The selection of $\phi(1020)$ decays into K^+K^- pairs needed modifications in large parts compared to previous analyses with a muon beam. The incident beam particle momentum was not measured in the hadron beam and thus no inclusive identification was possible.

The first one who presented an estimation for the **RICH** performance for kaons in 2008 hadron data was Matthias Schott. He demonstrated the enrichment of $\phi(1020) \rightarrow K^+K^-$ decays by the identification of one kaon [74]. The **PID** behaviour of the other particle was studied then. This principle method was applied and is discussed here. Following strategy was developed to filter a first set of $\phi(1020)$ decays:

1. Search for all primary vertices in the target region.
2. Search all opposite charge tracks in primary vertices.
3. Cut on minimum one positively identified kaon track¹.
4. Cut on the $\phi(1020)$ mass: $1.00 < m(K^+K^-) [\text{GeV}/c^2] < 1.05$.

The resulting K^+K^- invariant mass spectrum from a $\phi(1020)$ search is shown in the distribution 4.6 demonstrating already a fit over all events.

¹ Tracks with the largest likelihood for kaons among all likelihoods were searched what corresponds to a likelihood ratio of $\text{Like}(K)/\text{Like}(\text{not } K) > 1$

A Breit-Wigner shape with a polynomial background of second order was assumed to determine the number of $\phi(1020)$ events on top of the large combinatorial background. That number was essential for further analysis steps.

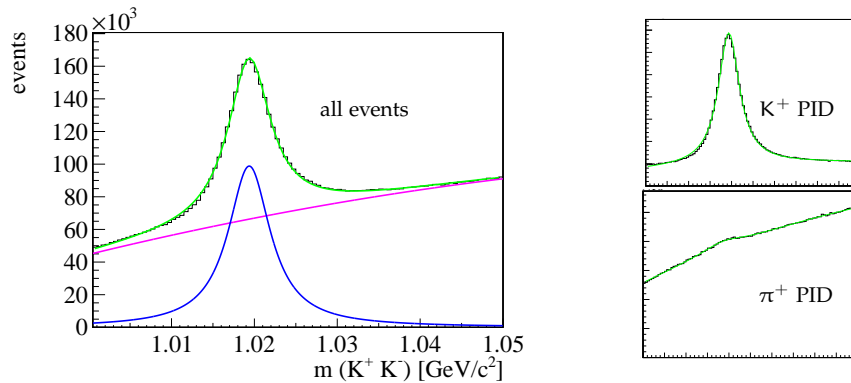


Figure 4.6: The invariant mass distribution for a $\phi(1020)$ hypothesis after all cuts. Left: No further cuts and all events. A Breit-Wigner curve (blue) with a polynomial background (purple) was fit to the data (green). Right: A RICH PID was applied to the positive track. Tracks with a K^+ PID had significantly reduced combinatorial background whereas tracks with a π^+ PID contained nearly no $\phi(1020)$ signal anymore.

EVALUATION OF PURITY/EFFICIENCY MATRICES Recall the likelihood ratio algorithm in section 4.2: A particle passing the RICH volume has in principle seven different PID possibilities. It can be identified as an electron, muon, pion, kaon or proton. In case the number of identified Cherenkov photons is low it may produce a signal comparable with background noise. And if the required likelihood ratio is greater than 1 it will also possibly give no PID decision. All probabilities must sum up to unity.

Furthermore depend those probabilities on the particle type, its charge, the track momentum and the track angle in the RICH volume in respect to the non deflected beam axis. The track angle is a one-dimensional representation of the spacial acceptance of the RICH detector. It was divided into two uncorrelated classes by the track's charge to study left-right asymmetries of the detector. The Cherenkov light emission angles are a function of the track momentum and the particle mass.

The probabilities were mapped to two dimensional histograms with the track momentum and the track angle at the axes giving in total seven probability distributions for each particle type and charge. In chapter 5 it is depicted that contribution by muons and electrons could be neglected in exclusive events of hadron data 2008/2009. Those particle types have been excluded from the studies below, reducing the total number of probability histograms.

The evaluation of the purity and efficiency histograms for (anti)protons and pions from V_0 decays was straightforward: The track PID, momentum

and angle were known as no background could be assumed. Applying the likelihood cuts resulted in a [RICH](#) evaluated [PID](#). The histogram corresponding to this determined [PID](#) was then filled with that event. Those tables were generated for $p\bar{p}$ and $\pi^+\pi^-$ tracks as demonstrated for π^- tracks in figure 4.7 and for \bar{p} in figure 4.8. The symmetric assembly of the [RICH](#) led to very similar tables for the corresponding charged conjugated particles and is hence not shown here.

Having a look for example into the tables 4.7 for π^- tracks (details on the performance are discussed in section 4.4) one can see on the upper left histogram the overall track distribution that was used for normalization of the remaining histograms. The upper right histogram represents the number of π^- tracks that were identified as pions normalized to all events or in other words the efficiency of the applied [RICH](#) likelihood cuts. The middle left histogram is then the probability for π^- tracks to be identified as K^- and the lower left is the corresponding impurity for the \bar{p} [PID](#). Inefficiencies of the likelihood analysis are drawn to the lower left histogram. The sum over all probabilities is visible in the lower right histogram. Only a few side bins are below unity as probability bins with a too large statistical uncertainty of greater than 30% were removed from the analysis.

To retrieve those histograms for kaons from $\phi(1020)$ decays, one further step was inserted since pure kaon tracks were not available. Starting with the tracks from the rough $\phi(1020)$ selection (see paragraph 4.3) the likelihood cuts on those tracks were applied. Thus both tracks per one event were tagged by a [RICH](#) [PID](#). The exact number of events was diluted by a huge, non constant background. Instead of counting those events the invariant mass of the $\phi(1020)$ decays was filtered into histograms, one for each bin in the efficiency/purity matrices. Afterwards the individual distributions were fitted with a Breit-Wigner signal over a polynomial background of second order as demonstrated by the exemplary distributions 4.6. That way the number of $\phi(1020)$ events for each bin in the tables was separated from background.

Of course this method led to large errors in the final results as visible in the tables 4.9 for K^- tracks. The binning was already chosen to be very coarse. Bin ranges were set, based on the one hand on the number of available events which are displayed in the upper left histogram. On the other hand physical motivations played a role like the Cherenkov light thresholds in the [RICH](#) detector.

It was not possible to determine a precise number of events for all bins in the matrices 4.9. For example, the signal for the misidentification as pions became very small for some bins and resulted in empty bins. The signal simply vanished and only the background distribution remained. Even for a determined number of events the error on this value was often large. It led to inconsistencies in the sum of probabilities as shown in the lower right plot. No bin had exactly the probability of 1. Even bins exceeding unity were observed and had to be treated separately in a later response simulation by the [RICH](#) detector (see section 4.5).

4.4 PERFORMANCE FOR DIFFERENT LIKELIHOOD RATIOS

LIKELIHOOD RATIO > 1 Figures 4.7, 4.8 and 4.9 show the resulting identification probabilities for π^- , \bar{p} and K^- tracks. The greatest likelihood for a π^- , \bar{p} or K^- hypothesis was searched for.

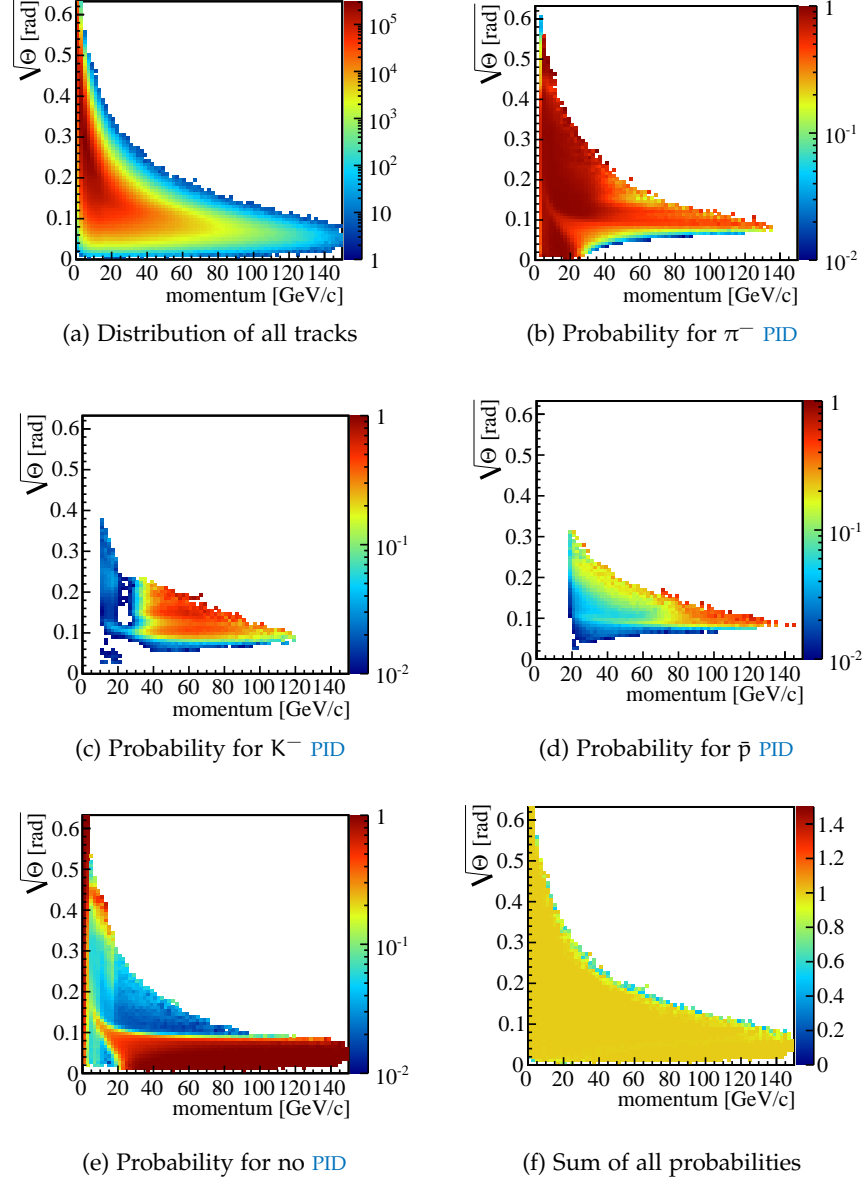


Figure 4.7: RICH efficiency/purity distributions for π^- tracks. See text for details.

Pions were identified with a high efficiency starting from the Cherenkov threshold up to momenta below 40 GeV/c then the efficiency decreased rapidly (fig. 4.7b). An inefficiency for low angles was observed. This can be explained by particles entering the RICH beam pipe. Below 35 GeV/c less than 10% of pion tracks were identified as kaons (fig. 4.7c). Above separation became difficult where the misidentification probability reached

more than 60% for large track angles. The probability to misidentify tracks as anti-protons stayed mostly below 20%(fig. 4.7d).

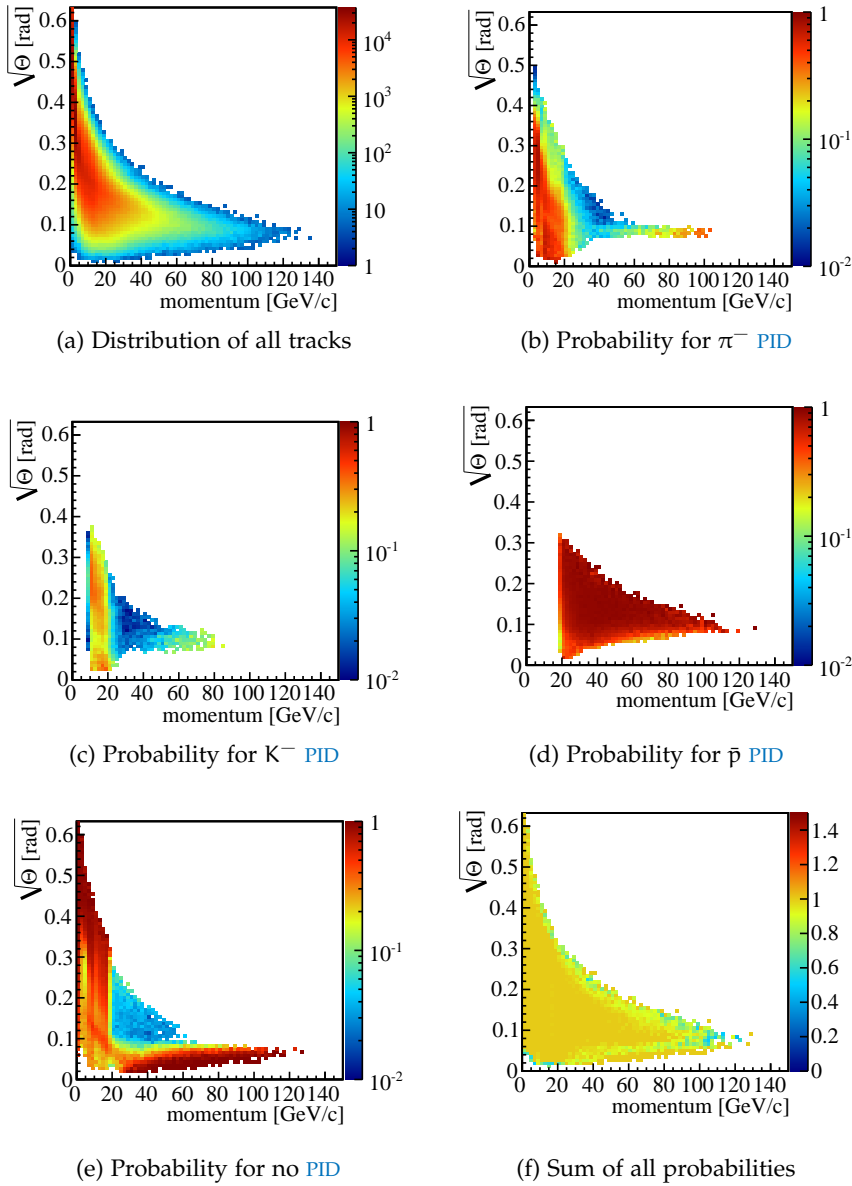


Figure 4.8: RICH efficiency/purity distributions for \bar{p} tracks. See text for a discussion.

Anti-protons were identified with a high efficiency starting from the Cherenkov emission threshold (figure 4.8d). An inefficiency for low angles was also observed here. The misinterpretation probability as kaons and pions was very low in the Cherenkov region but became large below the proton Cherenkov threshold of around 20 GeV/c. Specially the probability to identify pions, see figure 4.8b, became very high there. It is suspected that pileup events were the origin of miss-interpreted photons. Further tuning of the background distribution function would be needed in order to describe those photons coming from lighter particles correctly.

Since protons did not play a significant role in the analysis of $K^- \pi^+ \pi^-$ final states (see chapter 5) this effect was neglected.

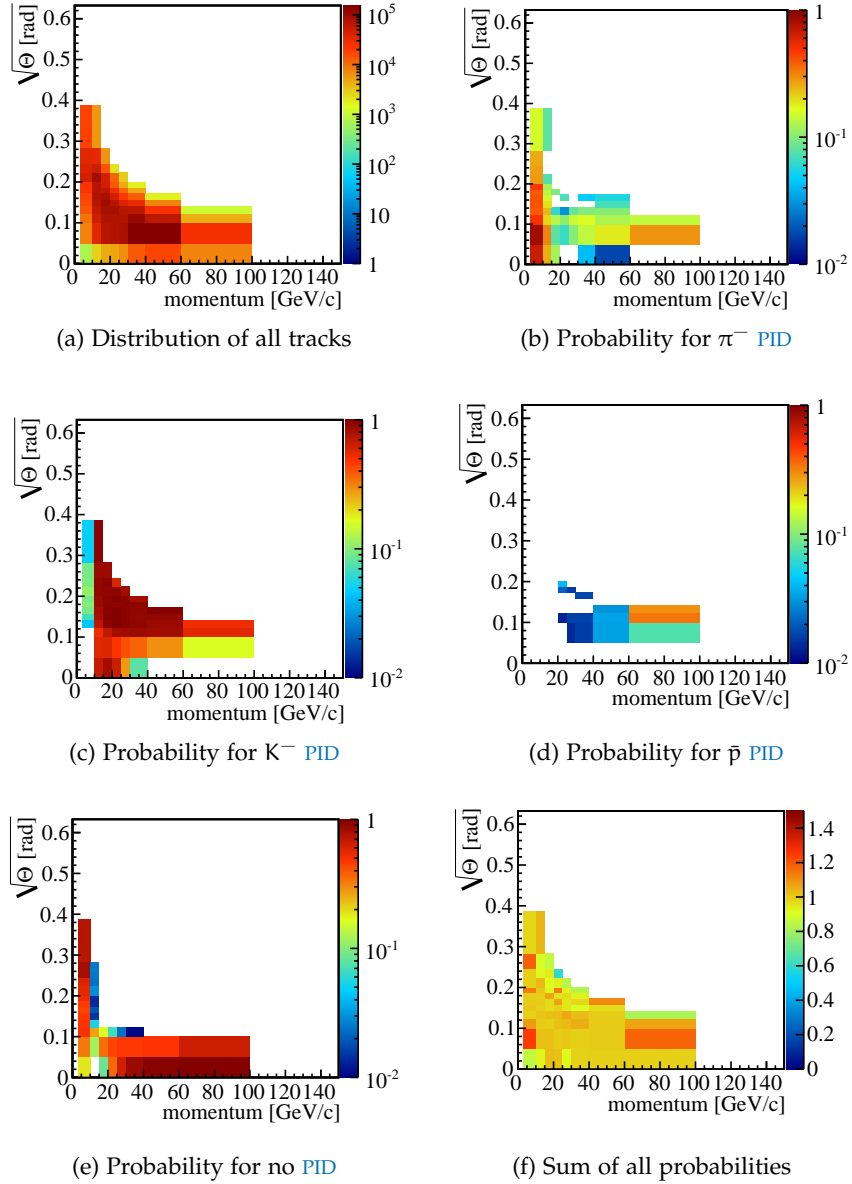


Figure 4.9: RICH efficiency/purity distributions for K^- tracks. For a discussion see the text.

Kaon PID probabilities were determined with large errors and a lower number of events. Thus a smaller range with lower precision than in proton and pion studies was covered (see figure 4.9a). The probability to identify kaons positively was determined the best (figure 4.9c). This could be expected since the $\phi(1020)$ signal to fit is the strongest in this case. All other cases led to very small signals that made it very difficult to determine the correct number of events. This explains many empty entries. Those entries had to be removed from the tables in order to preserve some quality.

The identification of tracks by the greatest likelihood was used as a starting point to check the highest possible efficiency. It gave thus the highest possible reduction of combinatorial background when using `PID` as a veto only but had at the same time the lowest purity. To increase the purity higher likelihood ratio cuts were studied.

TUNING OF LIKELIHOOD RATIOS In the following analysis only separation between kaons and pions was considered. Figure 4.10 and figure 4.11 show the impact of different likelihood ratio cuts that were applied on the kaon, pion and the background hypothesis. Figure 4.10 demonstrates the miss-identification probability dependence on ratios starting from 1.00 up to 1.25. As expected, purity was gained when increasing the ratio cut. Pions were less often misidentified as kaons. At the same time efficiency was dropping. Figure 4.11 shows the most dramatic effect at large momenta and angles. Finally good separation of pions and kaons was found with a likelihood ratio cut of 1.1 with the knowledge that track angles are mostly small for high track momenta. Particularly this is true for analyses of exclusive processes with low track multiplicities like the $K^-\pi^+\pi^-$ final state it was (compare figure 5.8). Details on the performance of an event selection with the `RICH` detector are discussed in chapter 5.

4.5 THE SIMULATION OF THE DETECTOR PERFORMANCE

`RICH` purity/efficiency matrices were used not only for a feedback to chosen cuts in data selection. The precise measurement of `RICH` identification probabilities gave moreover the possibility to simulate the `RICH` response in acceptance studies.

A `MC` simulation containing charged tracks from pions, kaons or even protons is anticipated here. For pions, `RICH` matrices as presented in figure 4.7 were used. Protons needed matrices as shown in figure 4.8 and kaons were connected with the distributions in figure 4.9.

The `RICH PID` probabilities were well defined for proton and pion tracks. The track angles and momenta were known from `MC` track properties. The bins corresponding to that track properties were collected in all distributions of the known particle type. In the case where pions were separated from kaons only, 3 probabilities were collected:

- $\rho(\pi \rightarrow \pi)$ the probability that a pion was identified as a pion
- $\rho(\pi \rightarrow K)$ the kaon misidentification probability
- $\rho(\pi \rightarrow \text{no PID})$ the inefficiency.

All three sum up in the ideal case to unity:

$$\rho(\pi \rightarrow \pi) + \rho(\pi \rightarrow K) + \rho(\pi \rightarrow \text{no PID}) \stackrel{!}{=} 1 \quad (4.5)$$

A random number between $[0, 1]$ was generated where the range was divided into 3 parts, weighted by the 3 given probabilities. This gave the

simulated detector [PID](#) response and took the efficiency as well as the purity into account.

The probabilities for kaon tracks were not well determined as already discussed in previous sections. The overall probabilities did not necessarily sum up to unity. One had to consider a re-weighting of the random number range. This was done for the case where the probabilities exceeded 1. Every probability was scaled then by the inverse total probability.

$$\rho(K \rightarrow \pi) + \rho(K \rightarrow K) + \rho(K \rightarrow \text{no PID}) = \rho_{\text{tot}} \quad (4.6)$$

$$\rho(X \rightarrow Y) \mapsto \frac{\rho(X \rightarrow Y)}{\rho_{\text{tot}}} \quad (4.7)$$

For a total probability smaller than 1 it was assumed to have missing entries and no rescaling was performed.

The application of those methods in [MC](#) simulations and its results is discussed in chapter 6.

4.6 SUMMARY

The [RICH PID](#) efficiency and purity was determined for different likelihood ratio cuts, showing the possibility to distinguish kaons from pions for track momenta up to 50 GeV/c. The corresponding efficiency and purity histograms for pions and protons were created based on V_0 decays as the identity of the decay tracks was unambiguously known. Very detailed performance distributions were obtained as practically no background was observed in V_0 decays.

The determination of kaon purity and efficiency matrices on the other hand encountered difficulties as no clean source for $\phi(1020)$ decays was accessible. The kaon track [PID](#) probability distributions had a significantly worse quality. Anyhow the principle how to use those matrices in [MC](#) simulations was shown and implemented.

For a high quality [PID](#) a likelihood cut of 1.1 is recommended. The efficiency was dropping for tracks greater than 40 GeV/c in momentum but high purity was preserved. It can be expected that exclusive diffractive or central processes with low hadron multiplicities are affected by large acceptance effects when requiring positive track identification of one or more tracks. This clear issue of the [COMPASS](#) set-up is revealed in the following chapters to be present in the $K^- \pi^+ \pi^-$ final state analysis.

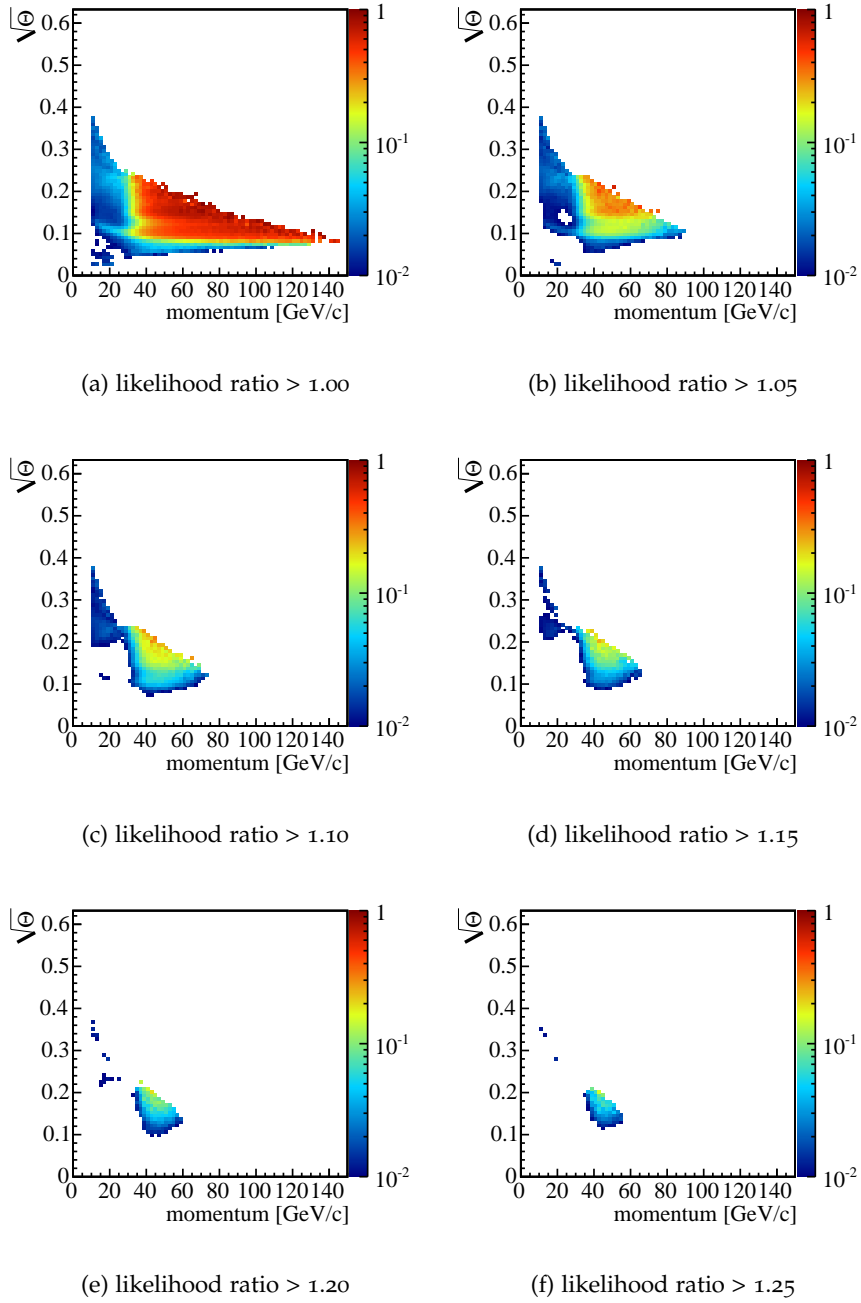


Figure 4.10: RICH purity distributions for the probability of a π^- to be identified as a K^- and various likelihood ratio cuts.

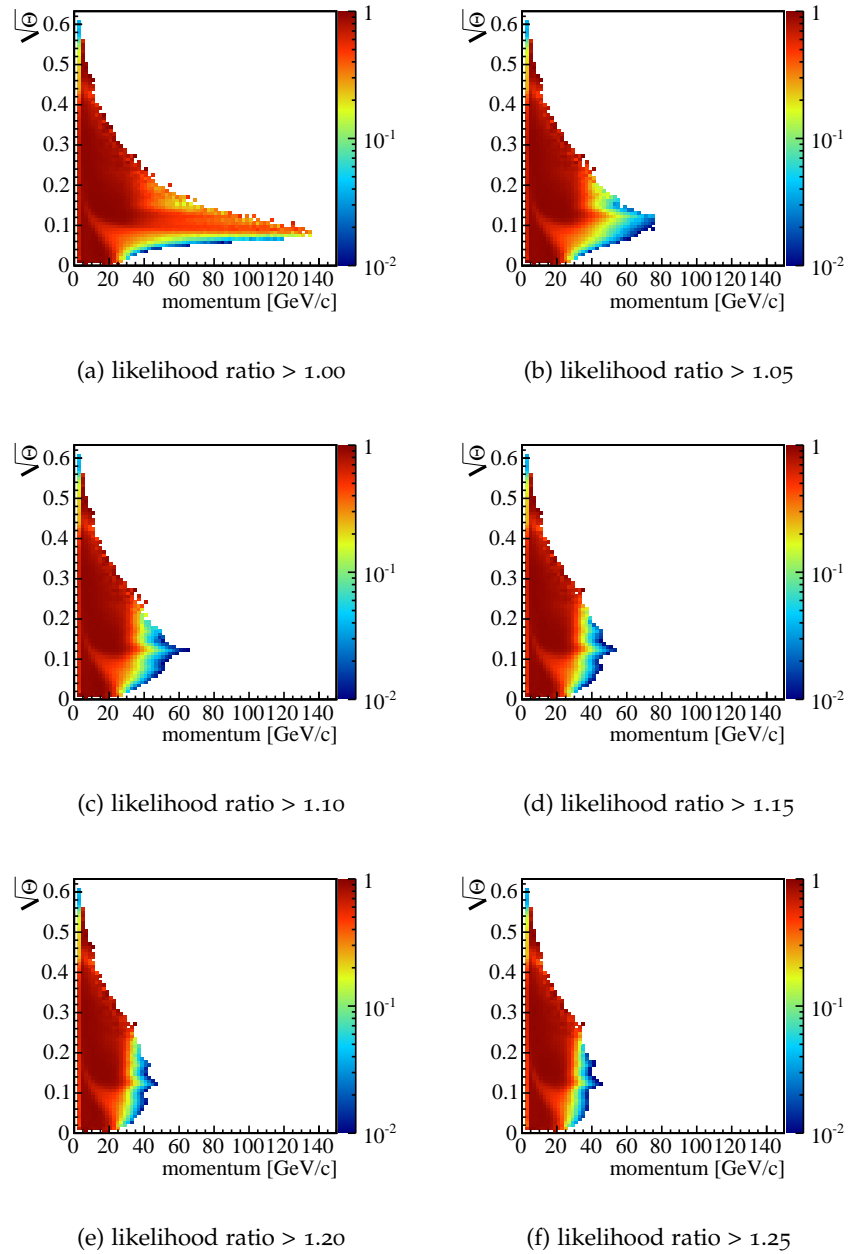


Figure 4.11: RICH efficiency distributions for the probability of a π^- to be identified as a π^- and various likelihood ratio cuts.

EVENT SELECTION

The selection of diffractively dissociated $K^-\pi^+\pi^-$ events in the initial kaon channel had many similarities to the leading final $\pi^-\pi^+\pi^-$ state in the initial pion channel. Nevertheless the cuts had to be chosen with greater care. On the one hand one had to clean this process as much as possible from leading processes in the pion beam on the other hand one had to preserve the small number of events compared to processes in the initial pion channel. In addition a choice of the correct K^- and π^- mass assumption for the two negatively charged tracks had to be made based on [RICH PID](#).

The final set of cuts presented in section 5.1 is the result of many iterations of data analysis. The quality and systematic studies of individual cuts are demonstrated in specific paragraphs, before showing the resulting invariant mass distributions in section 5.2. As background studies for pion induced events were necessary the event selection and resulting spectra are discussed as well.

5.1 APPLIED CUTS

Cuts applied to data recorded in the year 2008 are enumerated here. Some cuts will be discussed separately in the following.

1. The probability to have an incoming kaon was greater than 70% at least in one [CEDAR](#).
2. The primary vertex was located inside of the cylindrical hydrogen target: $R[\text{cm}] < 1.5$ and $-65 < z[\text{cm}] < -30$.
3. The number of forward outgoing charged tracks was exactly 3.
4. The combination of masses and charges fitted to the sample¹.
5. The recoil proton p_{recoil} and the reconstructed resonance spanned a production plane: $|\Delta\Phi - \pi|[\text{rad}] < 0.4$.
6. The four-momentum transferred to the recoil proton was restricted with $0.07 < t'[\text{GeV}^2/c^2] < 0.7$.
7. No veto was received by the [RICH](#) detector for a mass assumption that was applied.

¹ The developed code is feasible to search for any combination of wanted particles. In this case it means that outgoing 3 particles were searched where the $K^-\pi^+\pi^-$ masses can be applied. Thus one sample with $(-,+,+)$ charged tracks gives two possible combinations, namely (K^-, π^-, π^+) and (π^-, K^-, π^+)

8. At least one negatively charged track was identified as a kaon or a pion by the RICH detector.
9. The $p_{\text{recoil}}K^-\pi^-\pi^+$ system fulfilled the energy balance given by the incident beam particle: $185 < E [\text{GeV}] < 200$.

CEDAR CUT The separation of kaons and pions in the beam is discussed in chapter 3. Details to the performance are found in section 3.7. The estimated overall contribution by pions is 9.7% with a systematic uncertainty of 1.3%. It would be possible to apply an disjunction between CEDAR 1 and CEDAR 2 instead of the conjunction. This would increase the estimated purity to 94.4% leaving a contamination of 6.6% but this would also reduce the number of events by 25%.

TARGET CUT ON PRIMARY VERTEX POSITION As the reconstruction of charged tracks and vertices is done in advance by the COMPASS Reconstruction Library (CORAL) package [75] the search for fitting vertices is reduced to simple track multiplicity selections as well as the determination of the position as demonstrated in the corresponding distributions 5.1.

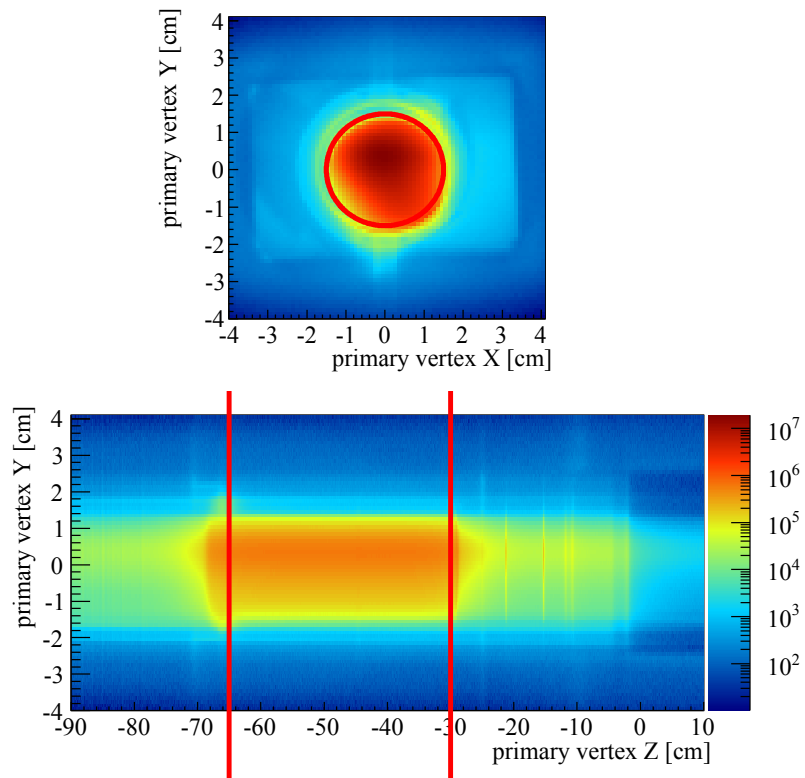


Figure 5.1: The primary vertex distribution in the x-y-plane (upper) and the vertical-plane (lower) for 3 outgoing charged tracks in the negative hadron beam. Clearly visible is the target cell as well as bounding materials together with tracking detectors. Target cuts are indicated as red lines specifying the region of liquid hydrogen.

The primary vertex distributions show several structures around the hydrogen target cell. Those were identified as the target support, cooling lines, entrance and exit windows as well as the two silicon tracking planes inside the conical cryostat (see section 2.3). The physically relevant region was restricted to be inside the volume where anyhow most of the three charged final states were found.

CUT ON THE PRODUCTION PLANE Simple kinematic rules require the resonance, decaying into 3 final state particles, to be in plane with the recoil proton, measured by the **RPD**, and the incoming beam particle. The production plane could be defined very precisely by the final state tracks and the incoming beam particle due to the very good spacial resolution of **COMPASS** tracking devices. The direction of the recoil proton was less precisely known. The azimuthal resolution of the **RPD** was dominated mostly by the granularity of the detector slabs (see section 2.3) and the multiple scattering along the proton's path. Distributions were observed like the one shown in figure 5.2. Having applied all cuts but the **RPD** cut itself a very clean signal was already retrieved to cut on. It came out that for charged final states energy balance and co-planarity cuts were strongly correlated.

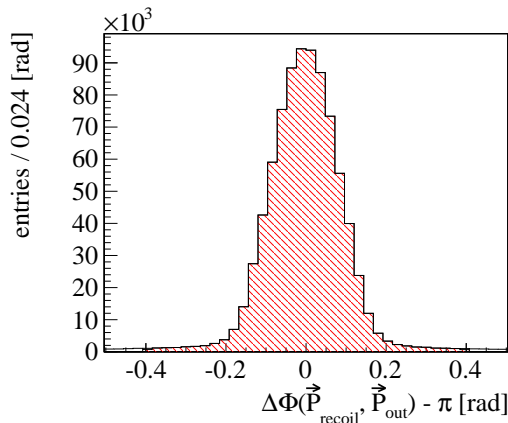


Figure 5.2: Relative difference of the reconstructed azimuthal angle of the outgoing $K^- \pi^+ \pi^-$ resonance to the azimuthal angle measured by the **RPD** after having applied all cuts but the co-planarity cut itself. The cut on the energy balance leaves a very clean sample with practically no background. Anyhow, only events were selected which were spanning a production plane. The range of the planarity cut is shaded in red.

ENERGY BALANCE The energy must be preserved. Since the energy of the incident particle was not measured a cut on the reconstructed energy of the outgoing resonance was applied. After all cuts but the energy cut itself the well defined Gaussian distribution 5.3 was retrieved. Due to the very small momentum transfer to the recoil proton the energy of the proton was neglected.

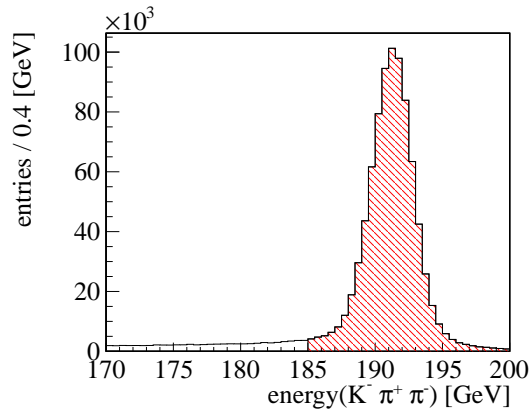


Figure 5.3: The reconstructed energy of the 3 outgoing charged tracks with applied $K^- \pi^+ \pi^-$ masses for a check of the energy balance. All cuts but the energy balance cut itself were applied. The range of the cut is shaded in red.

MOMENTUM TRANSFER CUT For a study of the t' dependence the **RICH** cut was only applied as a veto in order to overcome strong acceptance effects. Wrong combinations were tested in **MC** studies to give comparable results.

The t' distribution 5.4 shows a sharp cut off at low t' due to the acceptance of the **RPD** (see also section 2.3). Still events below $0.07 \text{ GeV}^2/c^2$ were observable. Those events were excluded from the selection since the origin was not studied yet. The upper cut on events above $0.7 \text{ GeV}^2/c^2$ was introduced to cut into the region dominated by single pomeron exchange, thus single diffractive scattering. For high t' values a second slope became visible which origin was believed to be found in central production, the fusion of two exchanged reggeons.

The t' distribution depended on the invariant $K^- \pi^+ \pi^-$ mass. This is demonstrated in figure 5.5. The t' distribution was normalized in every invariant mass bin independently to unity, in order to remove the resonant structure of the invariant mass itself. Low mass t' distributions had steeper slopes than the high mass t' distributions.

An exponential fit was performed in the region of the t' cut in order to determine the t' slope. The slopes are summarized in the graph 5.6. Low invariant masses were produced with mainly small momentum transfers. The slope variation seems to become constant for masses above $1.5 \text{ GeV}/c^2$. The distribution is in well agreement with observations in previous experiments analysing diffractive production of charged $K^- \pi^+ \pi^-$ states such as [1].

RICH PID Three charged tracks led to ambiguities since both possibilities to apply the masses of K^- and π^- to both negatively charged tracks contain obviously one wrong solution. To dismiss those wrong combinations a **PID** with the **RICH** was performed, not only to apply a veto on falsely assigned masses. One of both negatively charged tracks

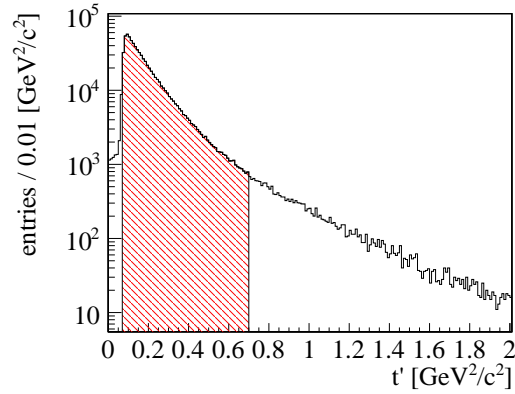


Figure 5.4: The reconstructed momentum transfer t' to the beam kaon distinguished from the angle between the incoming particle, the energy and angle of the outgoing particle system. The range of the cut is shaded in red indicating the region where RPD acceptance was well understood as well as single pomeron exchange was dominating. High t' regions show a second slope which origin is believed to be found in central production.

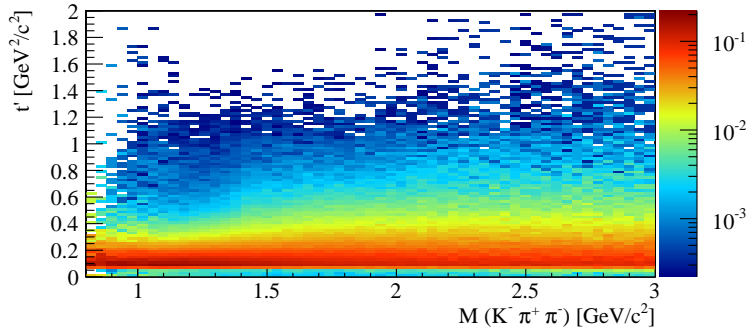


Figure 5.5: The reconstructed momentum transfer t' distributions in dependence of the invariant $K^-\pi^+\pi^-$ invariant mass. Low invariant masses were produced with a steeper slope.

had to be positively identified as a kaon or pion in order to know the correct assignment of masses. The PID efficiency decreased drastically for high track momenta. Therefore special attention to RICH likelihood cuts was drawn. The results of detailed performance studies are summarized in section 4.2.

It is illustrated in figure 5.7 that only kaon and pion separation had to be considered. All cuts for the $K^-\pi^+\pi^-$ selection were applied without the RICH cut itself. The histogram shows clear bands of pions and kaons. A contribution of protons was not visible and therefore not considered in the PID likelihood cuts.

Moreover, the track angle over momentum distributions 5.8 of the $K^-\pi^+\pi^-$ tracks were considered for a comparison with the probability distributions from chapter 4. Final state tracks from exclusive events had mostly high momenta at low angles. This was even more true for negatively charged tracks than for positively. A look into the RICH

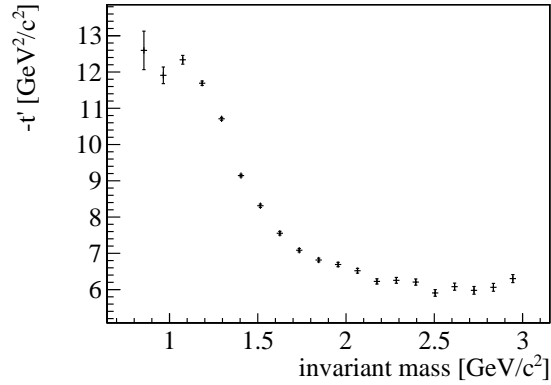


Figure 5.6: Fitted t' slopes over the invariant $K^-\pi^+\pi^-$ mass in the t' range of $0.07 \text{ GeV}^2/c^2 < t' < 0.7 \text{ GeV}^2/c^2$. This measured dependence is in agreement with previous observations in the $K^-\pi^+\pi^-$ final state channel and diffractive production mechanism [1].

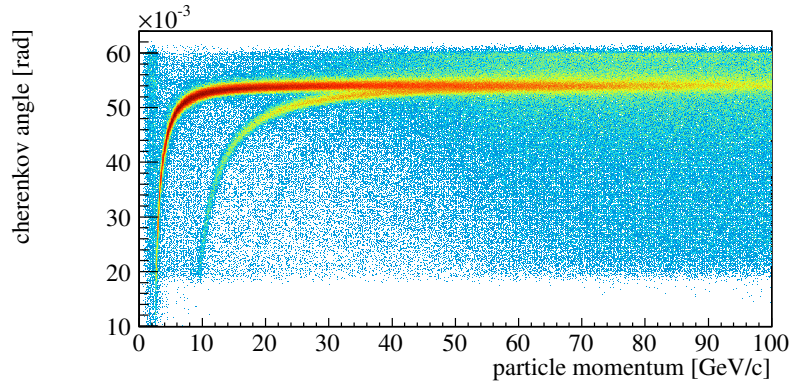


Figure 5.7: $K^-\pi^+\pi^-$ tracks after all cuts but the [RICH PID](#) cut itself. The reconstructed Cherenkov angles show clear bands originating from pions and kaons. In contrast to figure 4.2 protons are barely visible.

performance in dependence on the applied likelihood cut (see fig. 4.10 and fig. 4.11) led finally to the conclusion to have a good purity and still acceptable efficiency with a likelihood ratio cut of 1.1. But it is clear from those distributions that [RICH](#) momentum acceptance was mostly too small for efficient unambiguous event selection.

The application of the [RICH](#) cuts, on the one hand as a veto, on the other hand as a [PID](#) of at least one negative particle, led to the acceptance distributions 5.9. Those should be in the ideal case a sum over the products of the track distribution with the [RICH](#) purity/efficiency distributions when neglecting dynamics of the $K^-\pi^+\pi^-$ subsystems. As expected from [RICH](#) performance studies in chapter 4, [RICH](#) efficiency was dropping for track momenta above 40 GeV/c. Also the inefficient region in the [RICH](#) pipe became visible at small angles like it was previously observed in the [RICH](#) performance studies, too.

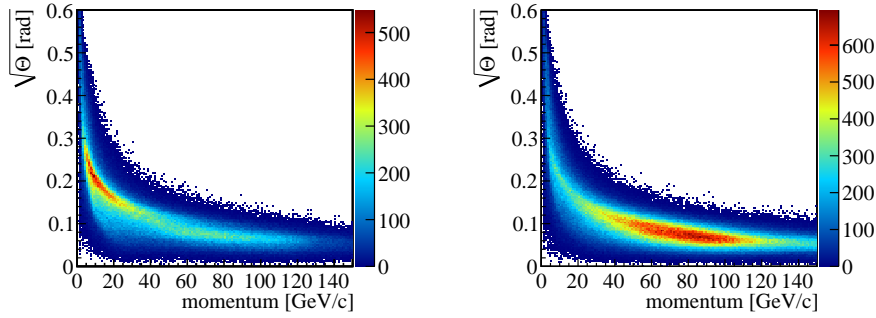


Figure 5.8: Positive (left) and negative (right) track properties in the $K^- \pi^+ \pi^-$ final state after all cuts without the **RICH** cut itself. Exclusive three particle events in a 190 GeV/c hadron beam are clustering in regions above the **RICH PID** momentum acceptance for pion and kaon identification.

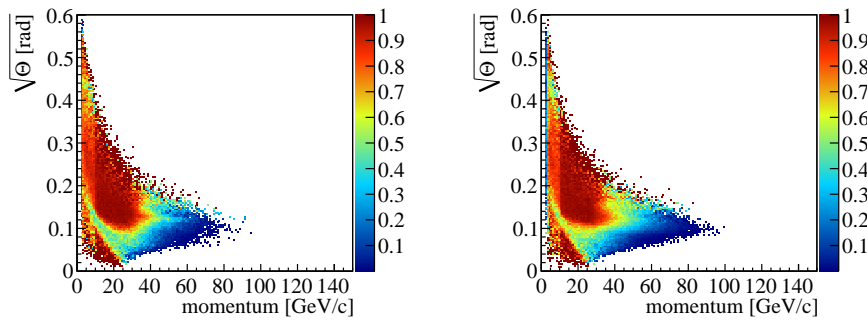


Figure 5.9: Positive (left) and negative (right) track identification probabilities in the $K^- \pi^+ \pi^-$ final state in dependence of the track momentum and azimuthal track angle. The efficiency dropped for track momenta above 40 GeV/c lowering the overall efficiency of the event selection significantly.

5.2 INVARIANT MASS DISTRIBUTIONS OF $K^- \pi^+ \pi^-$ EVENTS

The final event selection resulted in approximately 270 000 events. The invariant mass distribution of the $K^- \pi^+ \pi^-$ final state is shown in figure 5.10. The typical double peak structure of $K_1(1270)$ and $K_1(1400)$ as reported by previous experiments such as WA03 [1] is clearly visible. Also the $K_2(1770)$ can be seen by eye. It might appear that the high mass region is enhanced compared to the distribution 1.7 by WA03, but it is shown in section 6.6.2 that a worse **RICH** acceptance was dominating the low masses. A Partial Wave Analysis (**PWA**) clarified the composition of quantum numbers forming this spectrum and is the topic of chapter 7.

It was assumed that the resonances, resulting in $K^- \pi^+ \pi^-$ final states, decay in a chain via so-called isobars. The invariant masses of the subsystems formed by $K^- \pi^+$ tracks and $\pi^+ \pi^-$ tracks must show resonant structure in that case.

Figure 5.11 is the invariant mass distribution of the $K^- \pi^+$ branch. A clear signature of the $K^*(892)$ and the $K_{2/0}^*(1430)$ showed up. A contri-

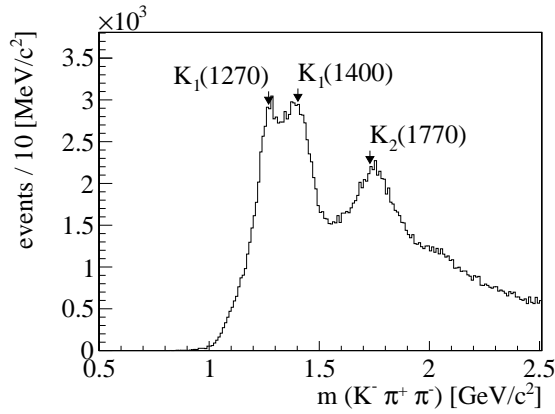


Figure 5.10: The invariant mass distribution of $K^- \pi^+ \pi^-$ tracks after all cuts. Established and visible resonances are indicated by labels and were also observed in WA03 (see figure 1.7). The distribution is bent mostly by the RICH acceptance as it is demonstrated in section 6.6.2.

bution of the $K^*(1680)$ and the $K_2^*(1780)$ was considered in PWA as well but was hardly seen by eye.

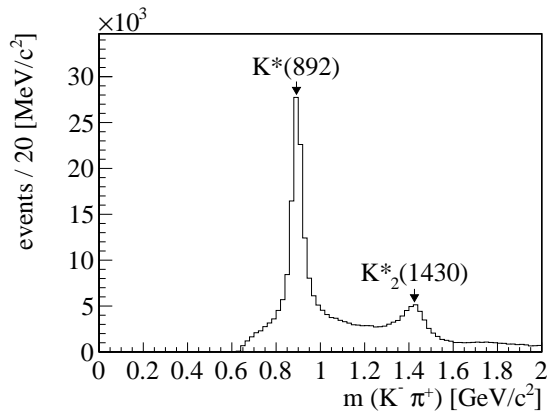


Figure 5.11: The invariant mass distribution of $K^- \pi^+$ tracks after all cuts. Apart from the dominating $K^*(892)$ resonance one observes also the $K_{2/0}^*(1430)$ resonance as indicated by labels. The distribution is not acceptance corrected and is distorted mostly by the RICH detector acceptance.

Figure 5.12 is the invariant mass distribution of the $\pi^+ \pi^-$ decay chain. Immediately the dominating $\rho(770)$ and $f_2(1270)$ can be identified. An $f_0(980)$ resonance over a broad $f_0(600)$ ² explains the small shoulder at $1 \text{ GeV}/c^2$. Also the $\rho_3(1690)$ was considered to contribute to the spectrum.

Still open questions were remaining when interpreting the invariant mass distributions of the isobars. It was observed that wrongly applied K^- and π^- mass assumptions are showing up as disturbed structures in the $\pi^+ \pi^-$ subsystems. Also it was recognized that the $\pi^+ \pi^-$ spectrum con-

² The $f_0(600)$ is better known as the σ

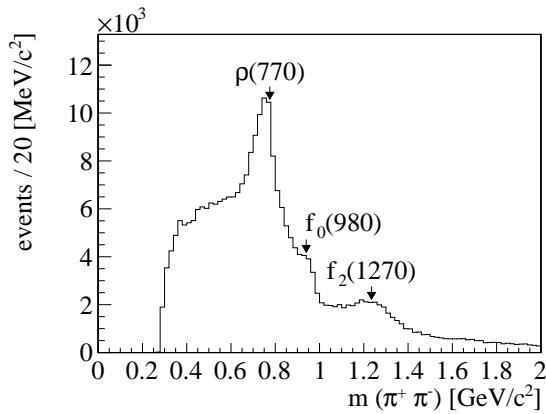


Figure 5.12: The invariant mass distribution of $\pi^+\pi^-$ after all cuts. Clearly visible are the $\rho(770)$ and $f_2(1270)$ resonances. The right hand shoulder is known to be the $f_0(980)$ contribution. The distribution is not acceptance corrected and is distorted mostly by the RICH detector acceptance.

tained an unexpected narrow peak at the threshold region. Those open questions coming from falsely applied mass assumptions are discussed in the following section where only measured momentum asymmetries were used for particle identification.

5.3 ARMENTEROS DIAGRAMS OF ISOBARS

Armenteros(-Podolanski) plots[73] are traditionally used for direct identification of Λ , $\bar{\Lambda}$ and K_s^0 in secondary vertices in forward spectrometers (compare fig. 4.3). Plotting the transverse momenta versus the asymmetries of longitudinal momenta of two tracks in the laboratory system one obtains ellipsis at regions of the resonances. Due to a large forward boost the information of the mass of the decay particles is negligible and therefore no particle identification is needed.

Figure 5.13 contains the Armenteros distributions for the $K^-\pi^+$ mass hypothesis and figure 5.13 those for the $\pi^+\pi^-$ mass hypothesis. In each case two representations of the same Armenteros distribution are shown. The left one is the pure distribution and right one is overlaid with ellipses from mean values of resonances. Apart from those resonances that were expected to be seen in the corresponding mass hypothesis, also two additional background ellipses are indicated in each track combination.

One would be visible when a false $K^-\pi^+\pi^-$ mass track hypothesis would have been applied to the tracks. In that case, a track combination determined to be a $\pi^+\pi^-$ one, would have been, in fact, a $K^-\pi^+$ one and vice versa. The background from a wrongly identified $K^-\pi^+$ subsystem is barely visible in the $\pi^+\pi^-$ Armenteros distributions in figure 5.14. A $K^*(892)$ resonance would give an antisymmetric ellipsis. The corresponding $\rho(770)$ resonance of a $\pi^+\pi^-$ track combination with applied $K^-\pi^+$ masses would give symmetric Armenteros ellipses in the distribu-

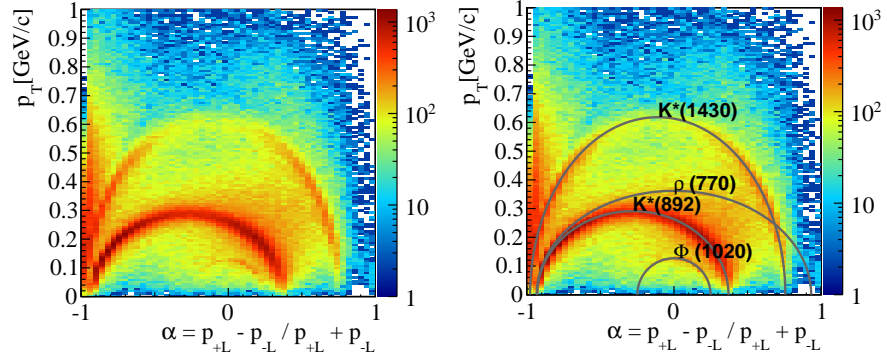


Figure 5.13: Armenteros distributions for $K^-\pi^+$ track combinations. Ellipses as calculated for the mean mass of the main resonances are indicated in the right plot. A narrow $\phi \mapsto K^+K^-$ resonance is visibly contained and is most probably originating from a falsely identified three kaon final state.

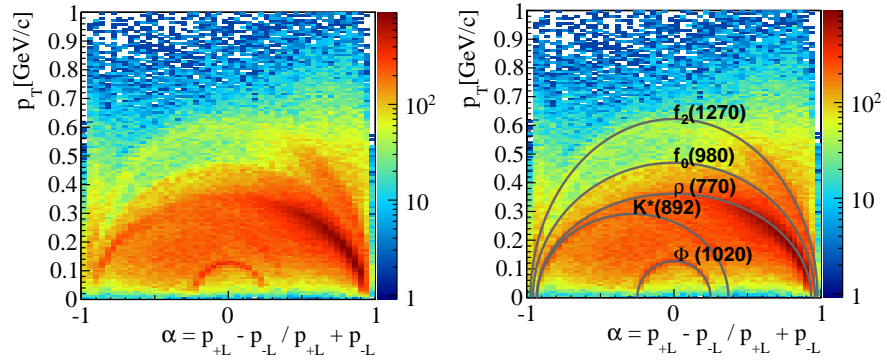


Figure 5.14: Armenteros distributions for $\pi^+\pi^-$ track combinations. Ellipses as calculated for the mean mass of the main resonances are indicated in the right plot. The narrow $\phi \mapsto K^+K^-$ band explains the small peak in figure 5.12 at the threshold region.

tions in figure 5.13. The absence of false $K^-\pi^+\pi^-$ track combinations demonstrates the high purity of the event sample selection with the **RICH PID** of at least one negative track.

Only an unwanted $\phi(1020)$ resonance can be directly identified in both subsystems. It is the case when both tracks were kaons and originated from other diffractive or central background processes. The $\phi(1020)$ resonance is the explanation for the small peak in the $\pi^+\pi^-$ invariant mass distribution 5.12. It is smeared out with a $K^-\pi^+$ track mass hypothesis and thus not visible in the distribution 5.11.

Moreover, a contribution of e^+e^- track pairs from γ -conversion can be neglected. Those pairs would lead to track pairs with very low transversal momenta without any resonant behaviour.

5.4 SELECTED DALIZPLOTS

The picture of a sequential decay via isobars is also nicely visible when plotting so-called Dalitz plots. The invariant mass squared of the $K^-\pi^+$ track combination is drawn over the $\pi^+\pi^-$ track combination for a small invariant $K^-\pi^+\pi^-$ mass range. Not only the resonant behaviour of the two-particle subsystems in three-particle decays is that way observed as bands in the Dalitz plots. Also the available phase space and therefore a visualization of the allowed mass region in the sub-systems is provided. The main contributing isobars can be directly observed and have to be considered in a later PWA.

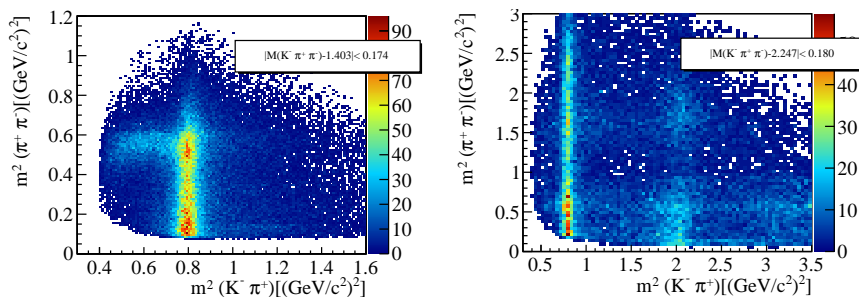


Figure 5.15: Dalitz plots for a cut in the invariant $K^-\pi^+\pi^-$ mass around $1.403 \text{ GeV}/c^2$ and $2.247 \text{ GeV}/c^2$ demonstrating the different available phase spaces for resonances in the low invariant mass region and the high invariant mass region. While particles with low invariant masses will decay presumably into $K^*(892)$ and $\rho(770)$ isobars, particles with higher masses could also decay into $K_{2/0}^*(1430)$ and $f_2(1270)$ isobars. The decays into these sub-resonances are clearly visible as bands in the available phase space.

Exemplary a cut to a lower mass region and a high mass region was chosen in the Dalitz plots of figure 5.15. Due to the small available phase space in the low mass region, a decay mainly into $K^*(892)$ and $\rho(770)$ sub-states was possible. In the higher mass region $f_2(1270)$ and $K_2^*(1430)$ sub-states were contained as well.

5.5 BACKGROUND FROM PIONS IN THE BEAM

In order to have an estimate for the behaviour of background pions in the beam, a full $K^-\pi^+\pi^-$ track selection was performed for a sub-sample of the 2008 pion data. It contained all cuts and assumptions unchanged apart from a CEDAR veto on the beam kaons. From pions in the beam diffractive $\pi^-\pi^+\pi^-$ events were expected to contribute the most to the invariant mass spectra.

The invariant mass distribution 5.16 shows a direct comparison between three particle events after cuts with positive beam kaon identification in red and a negative beam kaon identification in black. The spectra were scaled to contain the same number of weights. Visible is a distorted invariant mass spectrum of $\pi^-\pi^+\pi^-$ events where one negative pion

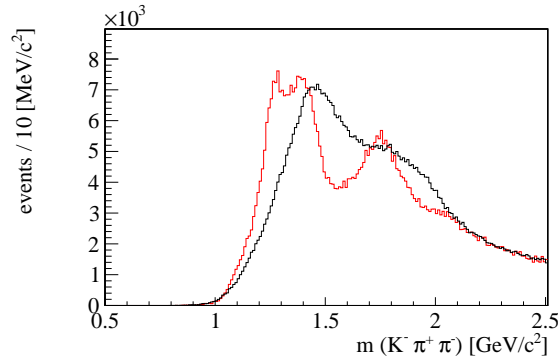


Figure 5.16: The invariant mass distribution of three tracks with an applied $K^- \pi^+ \pi^-$ hypothesis after all cuts. Black for pions in the beam and red for kaons in the beam. The red distribution was scaled to the same weights. Visible is the resonant structure of misinterpreted $\pi^- \pi^+ \pi^-$ events shifted to higher masses.

track was assigned with a kaon mass. This statement was checked by applying the correct $\pi^- \pi^+ \pi^-$ mass assumption on the event selection. The [RICH PID](#) acting as a veto with an additional identification of at least one negative track was not able to reject this background as individual track momenta were mostly too high for a positive particle identification. Other cuts as energy conservation or co-planarity did also not contribute significantly due to the low kinematic differences between a kaon and pion mass hypothesis on one negative track.

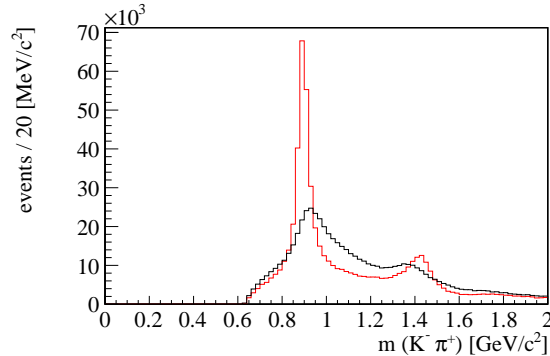


Figure 5.17: The invariant mass distribution of two tracks with the applied $K^- \pi^+$ hypothesis after all cuts. Black for pions in the beam and red for kaons in the beam. The red distribution was scaled to the same weights. Misinterpreted $\rho(770)$ and $f_2(1270)$ resonances appear as widened peaks. The contribution of combinatorial background in $K^- \pi^+ \pi^-$ events would have the same effect.

The sub spectrum [5.17](#) of the $K^- \pi^+$ hypothesis demonstrates nicely the impact of possible combinatorial background in $K^- \pi^+ \pi^-$ events as both tracks contained mostly two pions in the case of an anti-cut on the kaonic beam particles. This black distribution consists of widened resonances as the $\rho(770)$ and the $f_2(1270)$ giving an impression for the contribution of $\pi^+ \pi^-$ events with an $K^- \pi^+$ hypothesis.

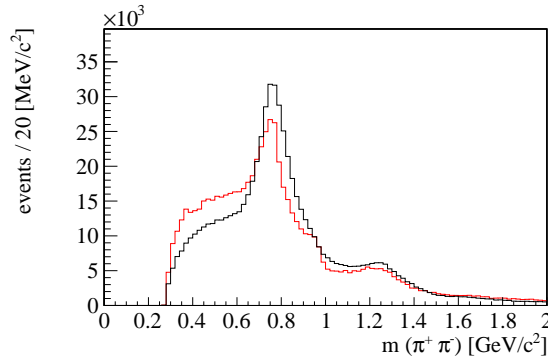


Figure 5.18: The invariant mass distribution of two tracks with an applied $\pi^+\pi^-$ hypothesis after all cuts. Black for pions in the beam and red for kaons in the beam. The red distribution was scaled to the same weights. The distribution for pions in the beam showed no $\phi(1020)$ resonance peak from misidentified K^+K^- tracks. For $\pi^-\pi^+\pi^-$ events both combinations of track mass assignments were correct in this branch.

The $\pi^+\pi^-$ invariant mass spectrum 5.18 on the other hand contains mostly correctly assigned masses. In the case of $\pi^-\pi^+\pi^-$ events even more than in the $K^-\pi^+\pi^-$ case. Three pion tracks will always provide a correct combination for a $\pi^+\pi^-$ mass assumption. One should notice in addition that a $\phi(1020)$ peak from falsely identified K^+K^- tracks did not appear in the $\pi^-\pi^+\pi^-$ case. The production of two kaons was mainly induced by kaons in the beam.

5.6 SUMMARY

A set of cuts was introduced to select a nearly clean sample of diffractively produced $K^-\pi^+\pi^-$ final states in the initial kaon beam. The most dramatic effects on the efficiency were known to come from CEDAR detectors suffering from the large beam divergence and the RICH detector when requiring at least one positive identification of a negative track in order to dismiss wrong track combinations for a track mass hypothesis.

Around 270 000 events were selected from all data of the run 2008, showing well known features of resonances decaying into the $K^-\pi^+\pi^-$ final state. Compared to previous measurements, particularly the 200 000 events analysed by the ACCMOR collaboration, no clear improvement might be expected. But looking into details the COMPASS data selection provided nearly twice as many events in the high mass region that is poorly determined by previous analyses. Moreover the selected t' region is tighter which is important in the later PWA analysis of production amplitudes as a function of the momentum transfer.

The resonant structure of $K^-\pi^+$ and $\pi^+\pi^-$ track combinations already motivated a sequential decay chain. The decay branches were shown to contain very little background by wrong mass combinations. Furthermore a set of events from an initial pion state was analysed showing mainly a

distorted $\pi^-\pi^+\pi^-$ spectrum for the assumption of $K^-\pi^+\pi^-$ final states. Those events were used for later studies of systematic influences in the [PWA](#) as the initial kaon beam sample was known to be diluted with a small fraction of pions.

All viewed variables showed distorted distributions where the origin was known to be the [RICH PID](#) cut with only a small efficient momentum range. It is therefore clear that further analysis must be regarded acceptance corrected based on [MC](#) simulations of the diffractive process.

THE COMPASS MC SIMULATION

For a partial wave analysis based on spin density determinations a good knowledge of the accepted phase space is required. Regions of lowered efficiencies in rest frames of the decaying particles might lead to distorted intensities in the partial waves. In the worst case resonances might appear or disappear.

This chapter describes technical details of acceptance studies based on the existing **COMPASS** software structure. The software had to be extended and modified in some parts in order to describe the **COMPASS** set-up in the years 2008 and 2009 properly. Finally 400 000 events were generated with a flat phase space in each of the of 110 invariant mass bins. The acceptance of the **COMPASS** spectrometer and it's simulated resolution was studied in several variables.

6.1 THE MONTE-CARLO SIMULATION CHAIN

Figure 6.1 shows a typical **COMPASS** Monte Carlo (MC) software chain as it was set up to simulate the acceptance of exclusive diffractive processes. Events, produced by an external generator, were propagated through the spectrometer by the **COMPASS** GEANT (**COMGEANT**) software [76]. The **COMPASS** Reconstruction Library (**CORAL**) [76] package was simulating most of the detector responses before writing those events to mini Data Storage Tape (**mDST**) container for final user event selection and analysis.

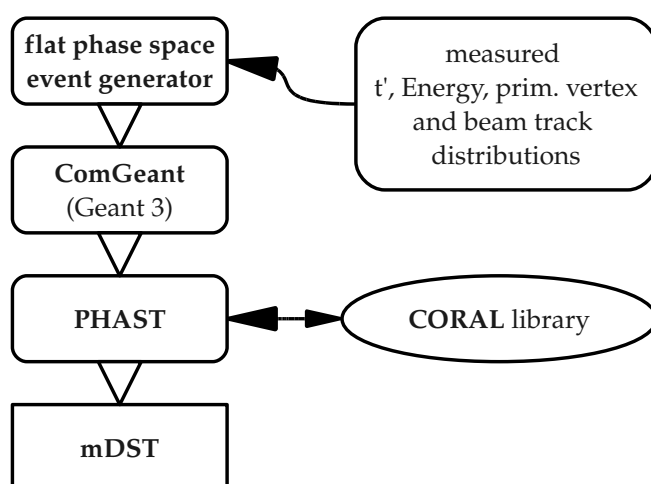


Figure 6.1: A MC chain illustrating the typical simulation flow for **COMPASS** analysis. Details are given in the text.

THE FLAT PHASE SPACE EVENT GENERATOR The $K^-\pi^+\pi^-$ final state as well as other diffractive processes were simulated by *genpw* that comes with the *rootpwa* software package (see chapter D for details to the software packages available to the COMPASS community). The decay of resonances in a given mass range was simulated to be flat in the invariant $K^-\pi^+\pi^-$ mass. No angular correlation between tracks was given which resulted in flatly distributed Dalitz plots as the plot 6.2 demonstrates for one invariant mass bin. The distribution is bound by the mass range where the $K_1(1270)$ resonance is expected. The generator is often referred to be *flat* in the available *phase space* what actually misleading as only the invariant $K^-\pi^+\pi^-$ mass distribution is uniformly distributed.

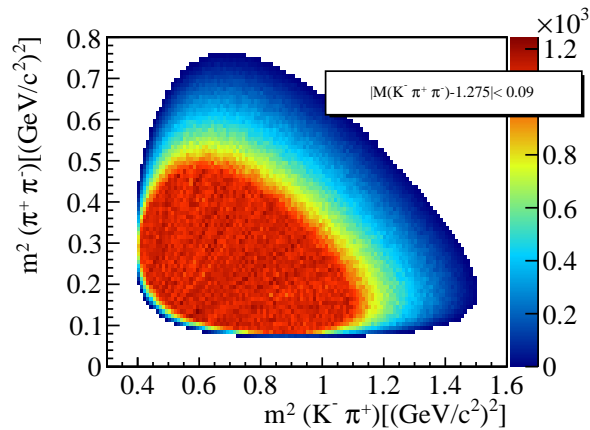


Figure 6.2: Example of a dalitz plot of MC generated $K^-\pi^+\pi^-$ final state events in the invariant mass range of the $K_1(1270)$ resonance. The events were uniformly distributed over the invariant $K^-\pi^+\pi^-$ mass and no correlation between final state tracks was applied.

The generator needed further input concerning the dynamics of single diffractive dissociation. Momentum of the beam particle was transferred to the target proton by reggeon exchange. The fraction of transferred momentum was given by the measured t' distribution 5.5 and the slopes 5.6 from an exponential fit. The dependence on the invariant mass of the produced resonance was taken into account as an linear interpolation between the fitted values.

The comparison of the real data t' distribution 5.5 to the MC distribution after event reconstruction is shown in figure 6.3. As only the low t' slope was fitted and used as an input to the generator, values in high t' regions differed the most. The relevant region covered by the t' cut showed a good agreement what is visible in the ratio of real data over MC data of mostly one. As the region of less agreement had a low number of events no further improvement was considered.

The properties of primary vertices as position, beam direction and beam momentum were taken from measured distributions. The method is described in detail in section 6.2.

As an output were four-vectors of all incoming and outgoing particles generated. Those events were already transformed to the laboratory

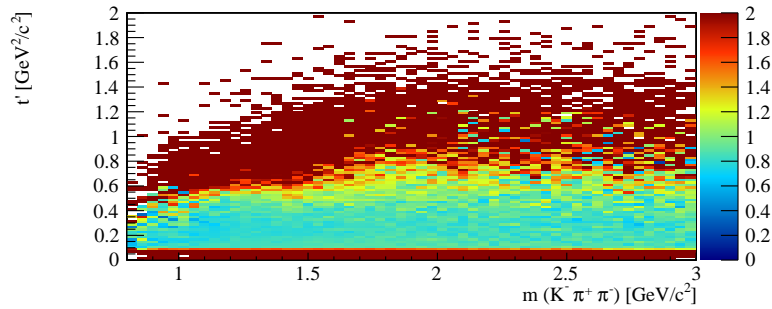


Figure 6.3: Ratio of the real data t' distribution 5.5 over the MC distribution after reconstruction. In the range of interest ($0.07 < t' [\text{GeV}^2/c^2] < 0.7$) a good agreement was found apart from the low mass region where some deviation for higher t' was observed.

frame. The COMGEANT simulation program was directly fed with those events for propagation through the spectrometer.

COMGEANT COMGEANT is based on GEANT3 and contains already the COMPASS spectrometer material description as well as the definition of active detector volumes [76]. This software allowed to propagate particles through materials and to simulate interaction with traversed matter. Processes taken into account were [77]:

- positron annihilation
- bremsstrahlung
- Compton scattering
- decay in flight
- delta-ray production
- hadron interactions
- energy loss
- multiple scattering
- muon-nucleus interactions
- pair production
- photoelectric effect

The deposited energy and position of the hits in active media of detectors were written into ZEBRA storage files and were used to simulate the detector response by the reconstruction package CORAL.

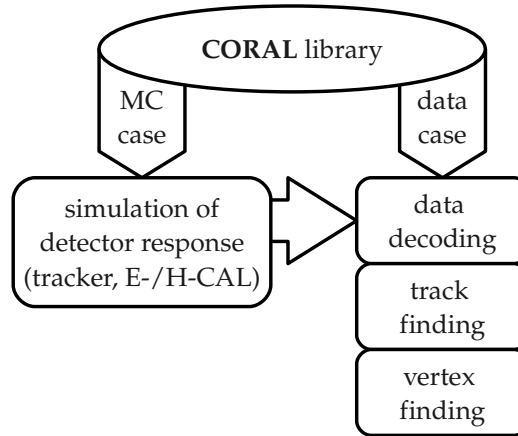


Figure 6.4: Illustration of the main processes implemented in the [CORAL](#) library. See text for discussion.

CORAL The [CORAL](#) software package played a central role in data analysis at [COMPASS](#) [76]. Some key points are illustrated in figure 6.4. As raw data from detectors were processed by this library, too, was it just a logical consequence to implement the simulation of the detector response in the same library. [COMGEANT MC](#) hits were transformed into detector response taking the resolution and efficiency into account. Detector hits were calculated to physically meaningful values in the following processes:

- Transformation of hits in tracking planes into tracks.
- Propagation of tracks through the spectrometer magnets.
- Calculation of momenta of charged tracks.
- Vertex reconstruction based on charged tracks.
- Energy and hit reconstruction of showers in Calorimeters.
- Likelihood calculations for [RICH](#) data.

Most of the detectors were simulated in this package. Some detectors needed special treatment and were exceptionally simulated during data analysis by the [PHAST](#) program.

PHAST The PPhysics Analysis Software Tools ([PHAST](#)) program had mostly two occurrences. On the one hand the [CORAL](#) library was included to produce [mDSTs](#) for end user analysis. On the other hand were those [mDSTs](#) also analysed with the help of [PHAST](#) [78]. [PHAST](#) provided to the user simplified access to important values and allowed for final event reconstruction and selection. In addition some detector response

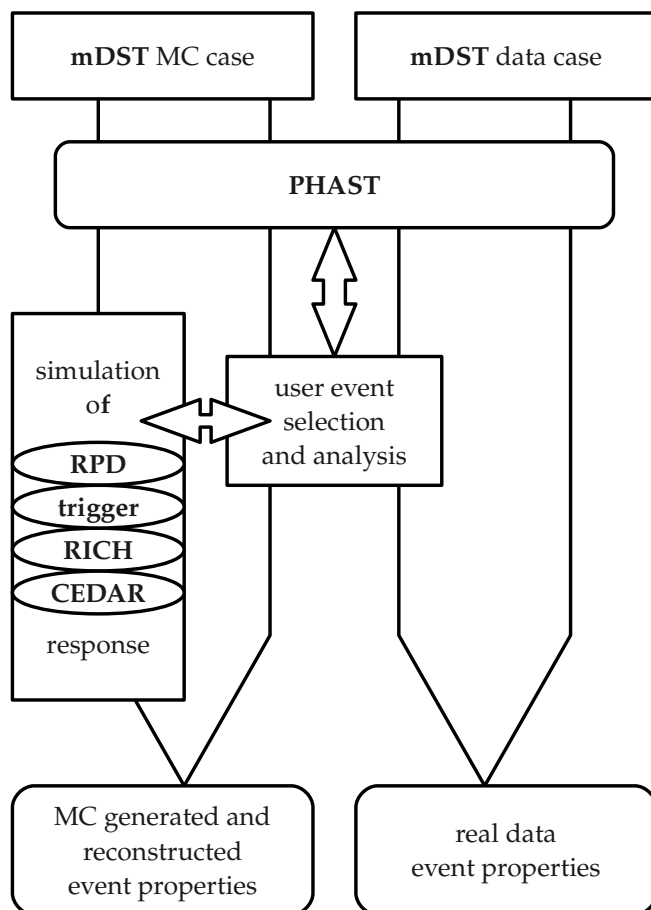


Figure 6.5: Illustration of **MC** detector response simulations implemented at the end-user level in **PHAST**.

simulations were implemented on the **PHAST** level which is illustrated in figure 6.5.

Real data was processed by a user event selection and analysis the same way as reconstructed **MC** data. To make use of **RPD** reconstructed track properties as well as **CEDAR** and **RICH PID**, separate classes were included and reconstruction functions from it were called. Those functions distinguished real data from **MC** data, simulating in the **MC** case the detector response based on the original **MC** track information.

The **CEDAR** acceptance simulation needed beam tracks as an input that was not provided at **CORAL** level. The **RPD** real data decoding needed reconstructed vertices as an input. Therefore the simulation was placed in **PHAST**, too. Moreover the official simulation of **RICH** likelihoods on **COMGEANT** level did not give satisfactory results and had to be replaced by measured probability distributions.

In the following, details on the simulation of those detector components are given. But first the parametrization of primary vertex properties is discussed as a pre-step to the **CEDAR** acceptance simulation.

6.2 PRIMARY VERTEX PROPERTIES

In order to take the properties of the incoming beam into account the *genpw* event generator was extended by a beam property simulation. The aim was to re-enact the characteristics of positive and negative hadron beams in 2008 and 2009 on the liquid hydrogen target.

INPUT BASED ON REAL DATA The primary vertex properties were simulated based on real data. Therefore diffractive dissociation into three pions was analysed. The spacial distribution of primary vertices was already discussed in chapter 5.1 and is concluded in figure 5.1. Those distributions were directly used as an input to the simulation of the primary vertex position. The region was restricted to the inside of the target cell.

In addition the direction of the beam particle and its momentum was determined. The x-y plane was divided into small squares, big enough to provide a statistically significant number of events in each. For each of those squares, horizontal and vertical track angle distributions were fitted by a Gaussian shape. The mean value of the track direction and the standard deviation are shown in the histograms of figure 6.6.

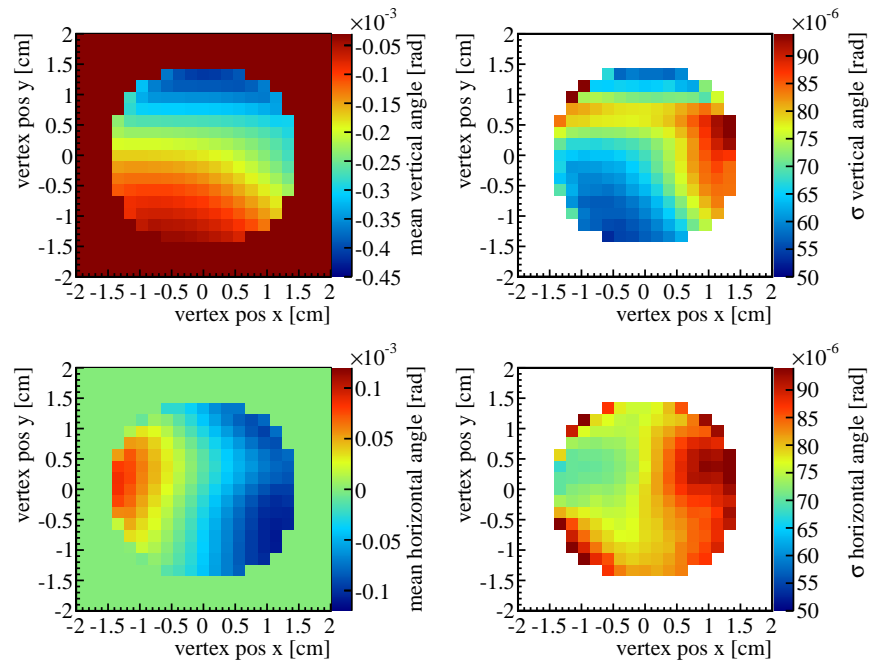


Figure 6.6: The beam track spread and direction in dependence of the primary vertex position. The horizontal distribution replays the beam pointing to the ground (compare also figure 2.6).

The vertical distribution of mean values shows an overall negative value. It was intended during beam commissioning to shoot the beam non-parallel to the ground but a little bit downwards. The horizontal mean track angle distribution evinces the focused nature of the beam as mean values negative in x have positive angles and positive in x negative

ones. Further details on the beam line and its properties are given in section 2.2.

The beam momentum was assumed to be independent from the vertex properties¹ and was taken from the measured energy distribution 5.3 of $K^-\pi^+\pi^-$ events. The standard deviation was lowered by the simulated energy resolution.

COMPARISON OF MC RESULTS TO REAL DATA Figure 6.7 demonstrates the properly simulated beam characteristics as the relative difference between the measurement (see figure 5.1) and the reconstructed MC distributions is uniform in the target region. Larger differences were observed specially in the regions with a low number of events. In addition falsely reconstructed primary vertices were distributed around the target.

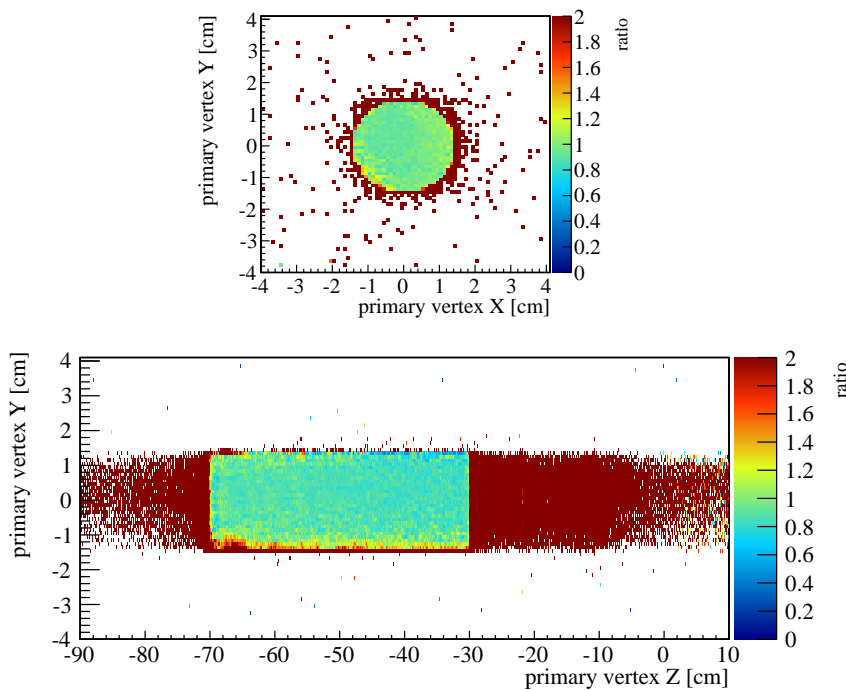


Figure 6.7: Ratio of primary vertex distributions in the x-y-plane (upper) and the vertical-plane (lower) over real data results shown in figure 5.1. The simulated and the measured distributions were normalized to the sum of weights. Apart from some wrongly reconstructed vertices outside the target a very good agreement was found.

The reconstructed MC energy distribution 6.8 is shown together with the ratio of the measured distribution 5.3 over the MC reconstructed one. The simulated distribution is wider than the real distribution. A further iteration of the simulation could be used to correct this discrepancy but

¹ It should be mentioned that in reality beam momentum depended on the vertex position as well as the beam direction. In addition the correlation between those two values was found to be low which complicated the situation. A further attempt to take at least the position of the vertex into account was made by Florian Haas and was work in progress.

no impact on the acceptance was expected. The cut on the energy balance covered anyhow the widened region.

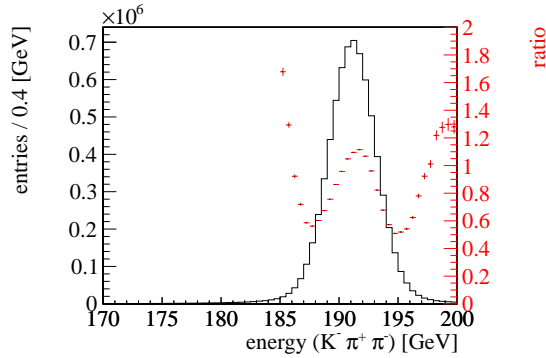


Figure 6.8: Ratio of the reconstructed energy of the 3 outgoing $K^- \pi^+ \pi^-$ tracks compared to the measurement shown in figure 5.3. For a relative comparison both distributions were normalized to the same sum of weights. The reconstructed distribution of the simulation is wider than the real one.

6.3 THE CEDAR ACCEPTANCE

The main purpose of a correct implementation of beam properties was the successive simulation of the CEDAR acceptance. The fitted acceptance distributions 3.10 were used as a direct input to the simulation. That probability distribution gave the efficiency of the CEDAR response as a function of the track angle. As no pion background was simulated purity was not taken into account.

The resulting detector acceptance from MC data is shown in figure 6.9 together with a relative comparison to real data from figure 3.10. 48% of events were rejected in the horizontal plane and 24% in the vertical. Overall 39% of events were accepted which is in good agreement with observations in real data.

As no correlation was found with angular acceptance distributions in rest decay frames, it was decided to abandon the CEDAR acceptance simulation in the final analysis to increase the number of events describing the accepted phase space.

6.4 THE RESPONSE OF THE RPD

Real RPD TDC data as well as ADC data from the PMs was passed to the RPD helper class at PHAST level. The code was developed and implemented mainly by Johannes Bernhard and was based on a first code piece written by Etienne Brutin.

Owing to Pawel Sznajder RPD material volumes were placed in the COMGEANT simulation giving already hits in active materials of the slabs. Those hits were stored to mDSTs awaiting further treatment in terms of

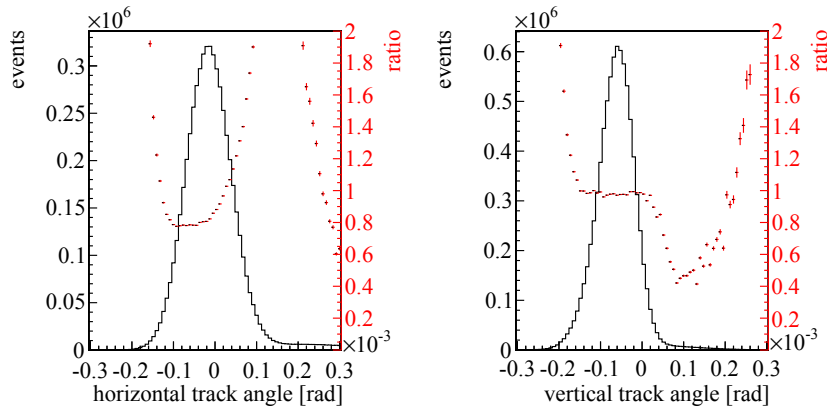


Figure 6.9: Track angles accepted by CEDAR 2 at the CEDAR region compared to the real data distributions 3.10. Apart from the tails good agreement between the simulated track acceptance and the measured one was found.

PROPERTY	RING A	RING B	REFERENCE
target center	−48 cm	−48 cm	figure 5.1
slab offset	2 cm	12 cm	[79] (slide 6)
TDC t_0 offset	−15 cm	−20 cm	adjusted
scintillator lg	50 cm	106 cm	[80] (slide 5)
light collector lg	21.5 cm	24.5 cm	[81]
light guide lg	(6.8 + 3.5) cm	3.5 cm	[81]
attenuation lg	64 cm	68 cm	[79] (slide 9)
time resolution (σ)	0.209 ns	0.400 ns	[79] (slide 7/8)

Table 6.1: Key properties as used in the simulation of the RPD response

detector response. The implementation of the missing link between those hits and simulated TDC ADC data was part of the work presented here.

IMPLEMENTATION OF BASIC PROPERTIES Table 6.1 contains key values used for the simulation of the detector response. It is pointed out that MC hits were given in world coordinates. The positions of the active volumes were determined as cited. Therefore a change of the RPD position in COMGEANT would not be taken automatically into account in the simulation of the detector response.

The implemented code discriminated automatically real data events from MC data events. In case of MC events, hits with the keyname "RP" were searched providing the hit position and energy loss in COMPASS coordinates. The hit position was mapped to a slab of an inner or outer ring. The hit time was then transformed to a time relative to the slab center. Finally a TDC hit was generated in each PM upstream and downstream according to the effective light speed in the slab convoluted

by a measured time resolution. The ADC integral was calculated taking the attenuation length into account. The SADC signal shape was formed by a Landau distribution where the area corresponded to the calculated integral.

DISCUSSION OF SIMULATION RESULTS The most characteristic feature is the cut in the acceptance below $t'=0.07 \text{ GeV}^2/c^2$ as visible in the reconstructed t' distribution 6.10. The momentum transferred to the proton below this value was too low to pass ring A. Giving no signal in ring B no recoil proton was identified. This feature was well described by the COMGEANT simulation and should be compared to the real data distribution 5.4.

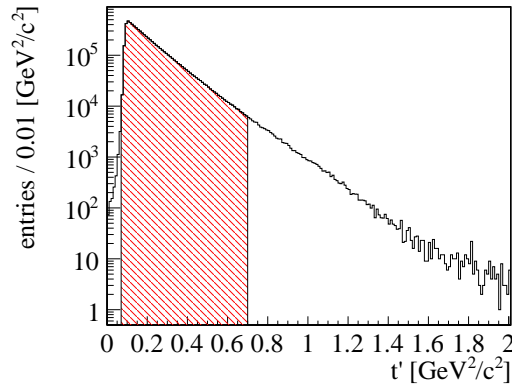


Figure 6.10: The reconstructed t' distribution in MC data. The characteristic cut at $t'= 0.07 \text{ GeV}^2/c^2$ due to the acceptance of the RPD was well reproduced (compare to fig. 5.4).

The measured Φ angle in the x-y-plane was used to test the co-planarity with the recoil proton and the resonance. As the resolution of the angle depended mainly on the granularity of the RPD scintillator slabs a good agreement between simulation and reality was found also here. The ratio between the real data co-planarity distribution 5.2 and the MC reconstructed distribution 6.11 shows only larger deviations at the tails where real data was contaminated by non exclusive background events.

6.5 THE RICH PERFORMANCE

For a detailed discussion of the RICH simulation the reader is referred to chapter 4 section 4.5. The RICH probability matrices were created based on the cuts applied to the likelihood ratios (see section 5.1).

The comparison between data (see figure 5.9) and the simulation is displayed in figure 6.12. Low track momenta were described quite well in their acceptance. Even the RICH pipe acceptance was taken into account but was less in agreement. Real data was worse described at high momenta where the simulated efficiency lower then the measured one was. The simulation suffered for example from imprecisely determined

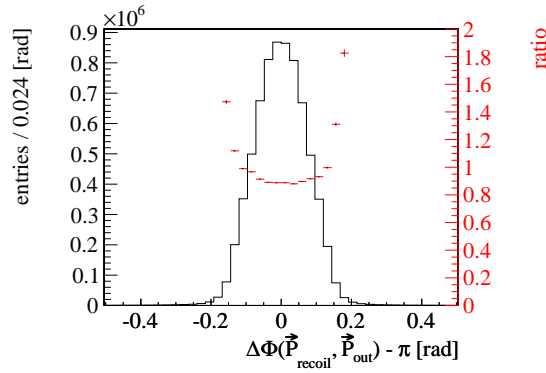


Figure 6.11: MC simulated coplanarity distribution and the ratio to the measured one (see figure 5.2). The larger discrepancy between real data and MC simulation at the tails is due to non exclusive background events in real data.

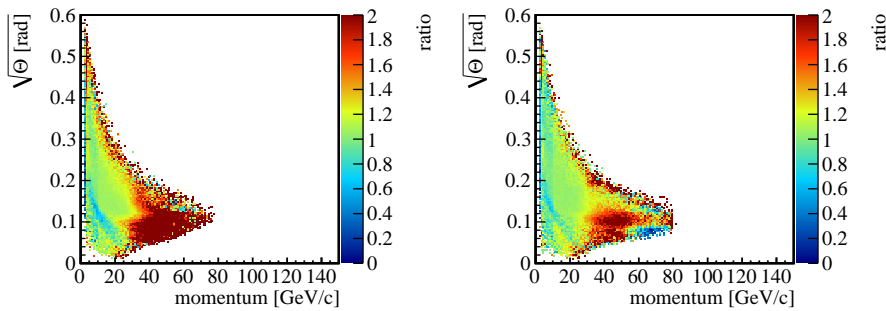


Figure 6.12: The simulated RICH track acceptance for positively charged tracks (left) and for negatively charged tracks (right) compared to real data as presented in figure 5.9. The agreement was good in regions of high efficiency. The regions with lower efficiency seem to be systematically underestimated in MC simulations.

probability matrices for kaon tracks which is clearly visible at momenta larger than 40 GeV/c. Above this region it was not possible to evaluate suitable RICH probabilities. The real efficiency seems to be systematically underestimated.

But some more aspects should be taken into account before drawing final conclusions. On the one hand background processes, such as diffractive three pion production in the pion beam or events with hidden strangeness, might distort the picture. On the other hand no resonant behaviour was taken into account in the kinematic distributions. The distributions are expected to change when simulating a weighted phase space driven by PWA fit results. This would be needed in order to validate the simulation chain as well as the data fits themselves.

6.6 SIMULATION OF $K^-\pi^+\pi^-$ FLAT PHASE SPACE EVENTS

400 000 $K^-\pi^+\pi^-$ events were generated and analysed in each mass bin of 110 in the invariant mass range of $0.8 \text{ GeV}/c^2$ to $3 \text{ GeV}/c^2$. Many distributions of those 4.4 million events were already discussed in the preceding sections. The simulated data was subjected to the following spectrometer performance, efficiency and acceptance studies. For this MC exact values as given by the generator were compared to MC reconstructed values after the COMGEANT-CORAL-PHAST analysis chain.

6.6.1 Spectrometer resolutions

Figure 6.13 shows the energy resolution for reconstructed $K^-\pi^+\pi^-$ events as a function of the invariant mass bin. The energy resolution was slightly decreasing with increasing mass. The resolution was about $0.30 - 0.36\%$ (rms) for a $191 \text{ GeV}/c^2$ hadron beam.

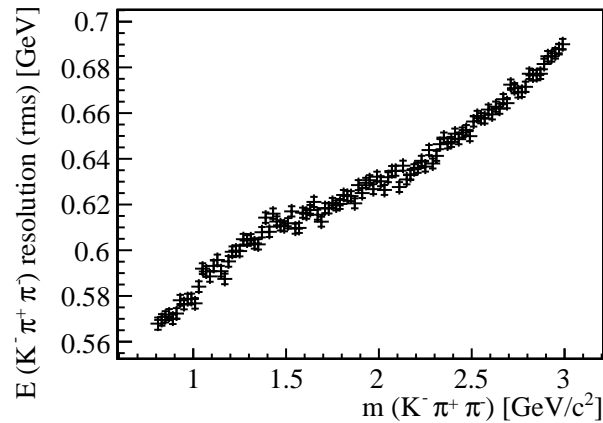


Figure 6.13: The energy resolution of the final $K^-\pi^+\pi^-$ state as evaluated by the MC simulation as a function of the invariant mass.

The non linear behaviour near the threshold region was observed since a t' dependence on the invariant mass had to be introduced (see figure 5.6). The momentum transfer is directly related to the energy of the recoil proton. When the fraction of the energy that was carried away by the recoil proton decreases the reconstructed energy of the remaining system will increase. A steeper t' slope at low invariant masses was corresponding to a shift to lower mean momentum transfers.

The relative invariant mass resolution 6.14 had a Gaussian shape. The width converged for high masses to $\sim 0.4\%$ (σ). Best resolution was found in the simulation of very low invariant masses. A resonance at for example $2.5 \text{ GeV}/c^2$ would have therefore an uncertainty of $\sim 10 \text{ MeV}/c^2$. This is quite a lot compared to the chosen bin width of $20 \text{ MeV}/c^2$ and plays a major role in the definition of acceptance as reflected in the following section.

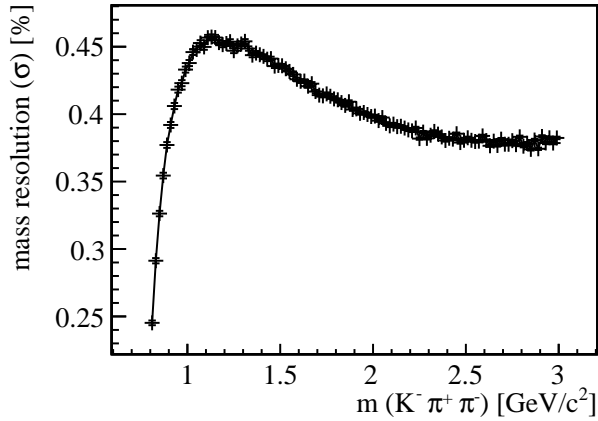


Figure 6.14: The Invariant mass resolution of the final $K^-\pi^+\pi^-$ state as evaluated by the MC simulation as a function of the invariant mass.

The resolution of the momentum transfer t' was evaluated and is shown in figure 6.15. Also here a strong dependence on the invariant mass was observed. The resolution was rising as a function of the invariant mass giving the worst resolution of ~ 0.11 GeV²/c² for high masses.

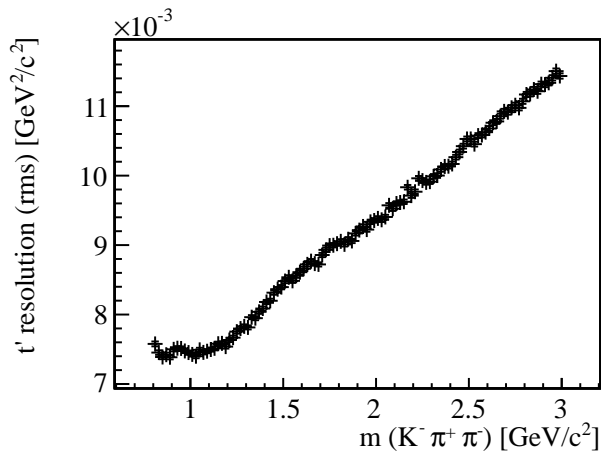


Figure 6.15: The MC simulated t' resolution as a function of the invariant $K^-\pi^+\pi^-$ mass.

To summarize, resolutions became slightly worse with increasing invariant $K^-\pi^+\pi^-$ masses which is consistent with spectrometer performances from analyses performed in parallel in other charged channels. Compared to the 2004 analysis of a $\pi^-\pi^+\pi^-$ final state, that was produced on a lead disc [21], resolutions were even slightly improved. One reason was probably multiple scattering in a solid state target reducing the spectrometer performances in 2004.

6.6.2 Spectrometer acceptances

An event was marked and counted as accepted when a correctly reconstructed event was found after all cuts presented in chapter 5. In this case the information of the MC truth was stored and not as one might anticipate the MC reconstructed value. The PWA formalism adapted later to this data was not foreseen to treat smeared values.

A WORD ON MC RECONSTRUCTED VALUES The question would simply be how to assign those reconstructed events to corresponding invariant mass bins. As in reality the true invariant mass was blurred by the spectrometer resolution. This resulted in so-called bin movement where generated events of one invariant mass bin count in neighbour bins.

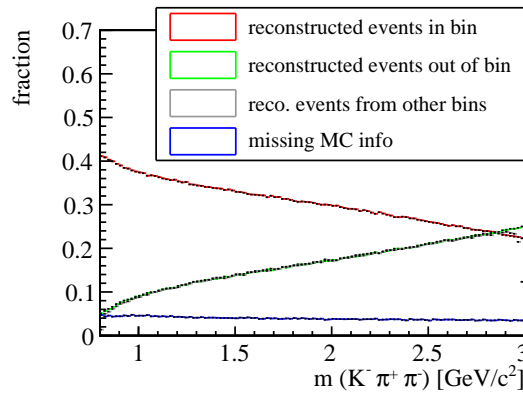


Figure 6.16: The reconstructed $K^-\pi^+\pi^-$ invariant mass differed due to the limited spectrometer resolution from the MC exact mass. The fraction of correctly reconstructed events in and out of MC exact $K^-\pi^+\pi^-$ invariant mass bins is shown here. The flux out of bins corresponds to the flux in the bins apart from the high mass region. The fraction of 50% combinatorial background is not displayed.

This effect is visualized in the graphs 6.16. While low masses were reconstructed into the correct bins, higher mass events moved more and more into neighbored bins. In fact this effect was compensated by neighbour bins themselves as events moved from there to the leaking bin. Only bins at the edges of the overall invariant mass range, meaning next to $3\text{ GeV}/c^2$, would suffer from a lowered efficiency as no bins with higher masses can contribute to the flux back. And indeed in practice, exemplary PWA studies with those reconstructed events were performed showing no significant differences compared to MC truth events.

But also no advantage was found. So all acceptance corrections applied to data in this thesis were calculated with MC truth events.

INVARIANT MASS ACCEPTANCES The spectrometer acceptance 6.17 as a function of the invariant mass of $K^-\pi^+\pi^-$ was reduced for lower masses as low break up momenta between tracks lead to nearby traces. The simulated reconstruction efficiency by tracking devices was dropping

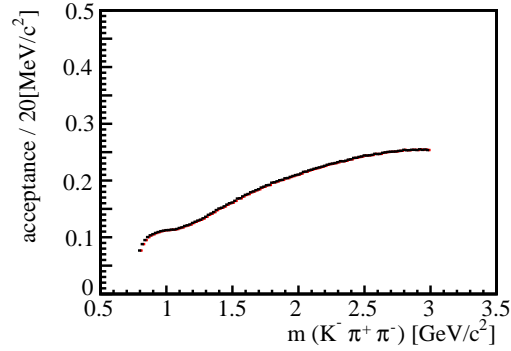


Figure 6.17: The acceptance as a function of the invariant $K^-\pi^+\pi^-$ mass exhibits a lowered spectrometer performance for nearby tracks. The opening of the available phase space as a function of the $K^-\pi^+\pi^-$ mass gave a larger probability for negative tracks with a reduced momentum where [RICH](#) acceptance was larger.

in those cases. The $K^-\pi^+\pi^-$ acceptance curve was following a strange shape in the low mass region caused by the t' dependence on the invariant mass. Events below t' acceptance had a bigger fraction for steeper t' slopes (compare also figure 5.6).

For high masses the available phase space was larger. As a result the probability for slow tracks was rising. Only tracks with a reduced momentum could be identified positively by the [RICH](#) necessary to choose one out of two ambiguities.

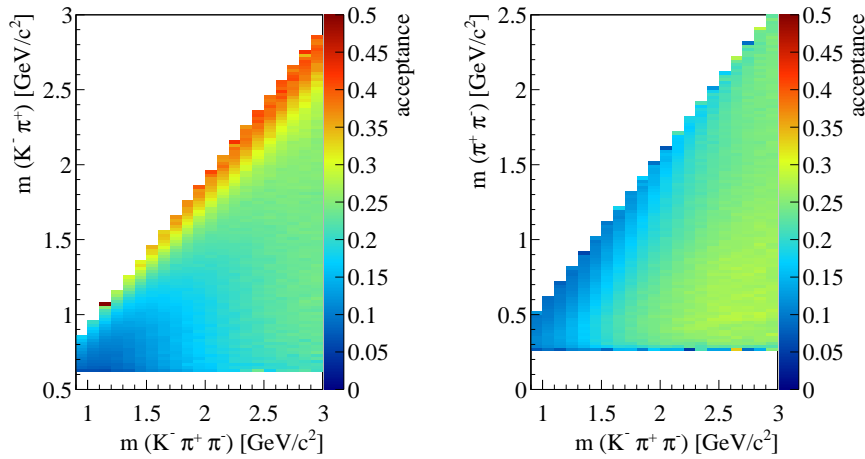


Figure 6.18: The acceptance as a function of the invariant $K^-\pi^+$ mass (left) and invariant $\pi^+\pi^-$ mass (right) over the invariant $K^-\pi^+\pi^-$ mass. While acceptance in the $\pi^+\pi^-$ branch is nearly flat in individual bins of the invariant $K^-\pi^+\pi^-$ mass $K^-\pi^+$ acceptance shows always an enhancement at large $K^-\pi^+$ masses. This is due to the small energy of the remaining π^- entering the momentum acceptance of the [RICH](#) detector.

The acceptance in the $K^-\pi^+$ and $\pi^+\pi^-$ isobar branch is shown in the two dimensional histograms 6.18 as a dependence also on the $K^-\pi^+\pi^-$

mass. The acceptance along the invariant $\pi^+\pi^-$ mass was nearly flat for each $K^-\pi^+\pi^-$ mass bin. This was not the case for the $K^-\pi^+$ branch. High invariant $K^-\pi^+$ masses had a larger acceptance as a slow π^- was remaining entering the momentum acceptance of the **RICH** detector.

It should be pointed out that the absolute reconstruction efficiency was somehow arbitrary as it depended strongly on the lower t' cut in the generator. The more events were generated below the **RPD** acceptance the less was the overall efficiency.

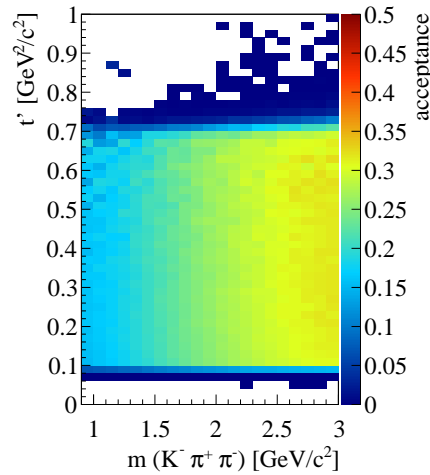


Figure 6.19: The **MC** truth t' acceptance is shown to be flat in an invariant $K^-\pi^+\pi^-$ mass bin. The edges at $t'=0.07\text{ GeV}^2/c^2$ and $t'=0.7\text{ GeV}^2/c^2$ originate from the t' cut. The edges are not sharp as the reconstructed t' value, where a cut was applied to, is smeared.

T' ACCEPTANCE The simulated acceptance in t' was flat in each invariant $K^-\pi^+\pi^-$ mass bin (see figure 6.19). The t' cut is not appearing sharp. The edges are smeared as the t' **MC** truth acceptance is shown here. The reconstructed t' value with the cut applied was smeared in respect to the **MC** truth value (compare also figure 6.15). The flat distribution proves also that a measured t' slope could directly be used as an **MC** generator input value.

ACCEPTANCE IN THE RAPIDITY For the inspection of rapidities in a later chapter the acceptance of those was important, too. The acceptance region in the rapidity axis was growing with the invariant $K^-\pi^+\pi^-$ mass as shown in the acceptance distributions 6.20 due to the available phase space. A band of small acceptance is visible introducing an artificial rapidity gap. A fast kaon left a slow $\pi^+\pi^-$ track combination where the π^- entered the **RICH** momentum acceptance. A slow kaon on the other hand was identified itself by the **RICH** detector. Same held for the $\pi^+\pi^-$ track combination.

ACCEPTANCES IN THE GOTTFRIED-JACKSON FRAME The acceptance in the **GJ** decay rest frame of a $K^-\pi^+\pi^-$ resonance decaying into $K^-\pi^+$ and

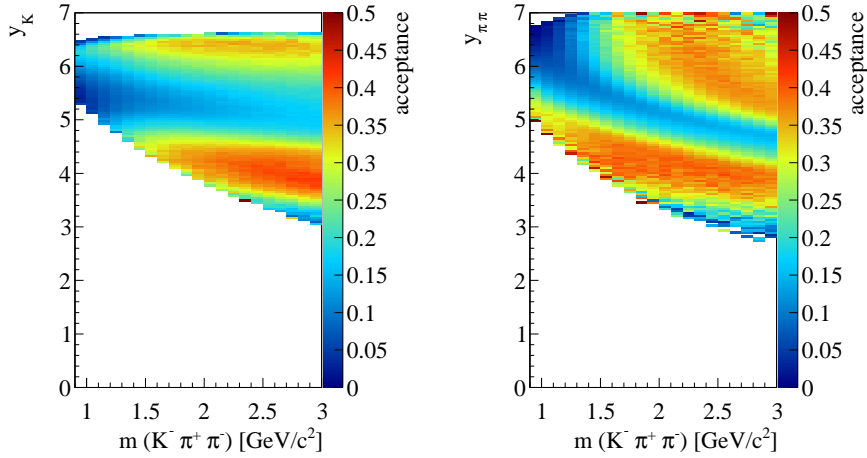


Figure 6.20: The acceptance over the K^- rapidity (left) and $\pi^+ \pi^-$ (right) rapidity in dependence on the $K^- \pi^+ \pi^-$ dropped for middle values of rapidities. A very fast particle or particle combination left a slow partner in the momentum acceptance of the RICH detector. Very slow particles or particle combinations entered the acceptance themselves.

the bachelor π^- and $\pi^+ \pi^-$ with a bachelor K^- is shown in figure 6.21 for the polar angle and in figure 6.22 for the azimuthal angle in dependence on the $K^- \pi^+ \pi^-$ mass. The z-axis points to the direction of the beam in this frame. The reader will find a detailed description of this frame in section A.1.4.

A particle combination pointing in direction of the beam equals a $\cos \theta_{GJ} \rightarrow 1$. The acceptance was generally growing in this case as the decay partner was pointing backwards. This resulted in a reduced velocity of the decay partner in the laboratory frame entering the RICH momentum acceptance. This is even more pronounced for the $K^- \pi^+$ branch as the higher kaon mass carried anyhow a larger fraction of the available beam energy. The $\pi^+ \pi^-$ branch on the other hand needed a larger phase space only available for high $K^- \pi^+ \pi^-$ masses to produce this effect.

The opposite direction of particle combination had also an improved acceptance. In that case the K^- of the $K^- \pi^+$ branch and the π^- of the $\pi^+ \pi^-$ branch were directly affected by the RICH cut. Again the reduced phase space is explaining the low acceptance, now for the $K^- \pi^+$ branch.

The azimuthal angle of the decay plane in respect to the production plane is the ϕ_{TY} angle. The decay of a $K^- \pi^+$ combination and the pion showed an enhanced acceptance for smaller $K^- \pi^+ \pi^-$ masses when the decay was happening in the production plane. The opposite was found for the $\pi^+ \pi^-$ combination with a remaining kaon. The bump in the $(K^- \pi^+) \phi_{TY}$ angle was an important signature of the RICH acceptance in the $K^- \pi^+ \pi^-$ data to be reproduced for the acceptance corrected PWA.

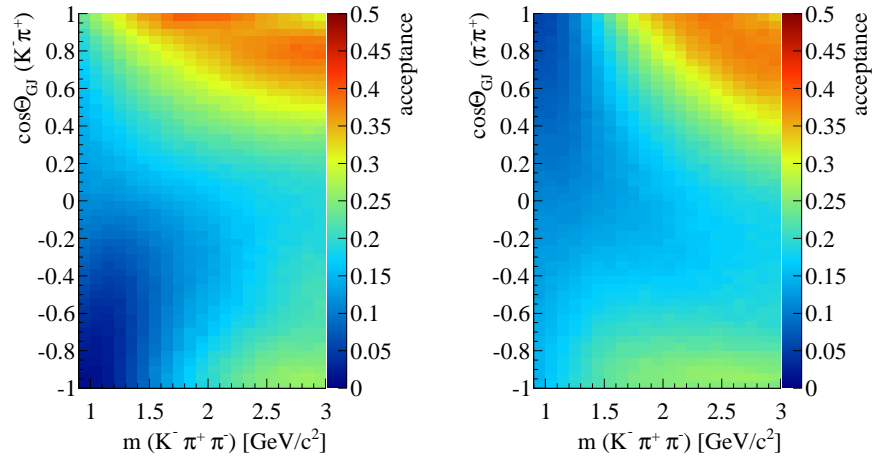


Figure 6.21: The acceptance as a function of the polar angle in the GJ frame and the invariant $K^- \pi^+ \pi^-$ mass. The decays into $K^- \pi^+$ with a bachelor π^- and $\pi^+ \pi^-$ with the bachelor K^- shows strong acceptance effects discussed in the text.

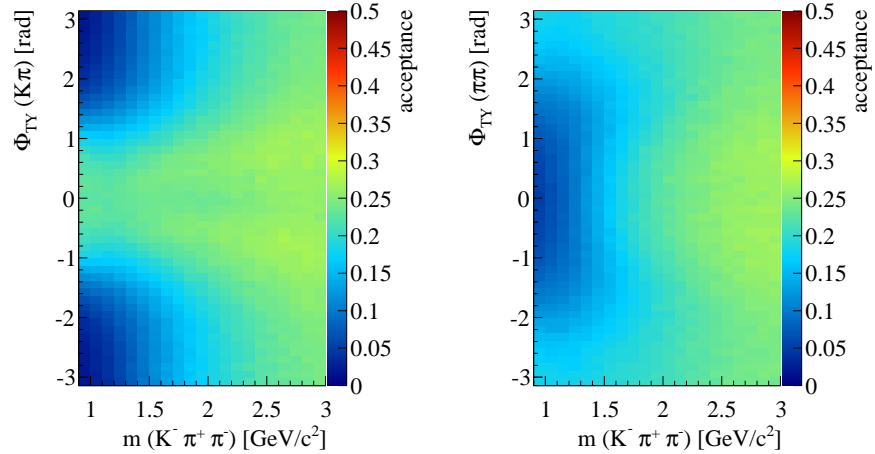


Figure 6.22: The acceptance as a function of the azimuthal angle in the GJ frame and the invariant $K^- \pi^+ \pi^-$ mass. The acceptance distribution of the decays into $K^- \pi^+$ with a bachelor π^- and $\pi^+ \pi^-$ with the bachelor K^- is discussed in the text.

6.7 SUMMARY

After many modifications of the existing [COMPASS MC](#) simulation software, in total 44 million events were generated. Those were flat in the invariant $K^-\pi^+\pi^-$ mass without any resonant structure between final tracks. That so-called flat phase space simulation was used to determine the spectrometer acceptance in important variables helping to understand the distorted distributions in the real data. All strong acceptance effects were found to originate from the small momentum acceptance of the [RICH](#) detector as without a [RICH](#) cut mostly flat distributions were observed.

As far as possible, were simulated distributions compared to those from real data showing all-in-all a good agreement between the simulation and the reality. Only the efficiency of the [RICH PID](#) seems underestimated in regions of higher track momenta and lower [RICH](#) efficiency. In fact, that was the region where most of the $K^-\pi^+\pi^-$ tracks were observed in real data. So even small discrepancies between the simulation and the real data were raised to higher powers. This impairment was populated to the acceptance corrected [PWA](#) in the next chapter and is found in final quality checks.

It was shown that the invariant mass distribution 5.10 of $K^-\pi^+\pi^-$ tracks had resonant structure and some of the resonances were already assigned to possible meson states by the resonance peak position itself. Moreover resonant structure was found in the $K^-\pi^+$ invariant mass distribution 5.10 as well as the $\pi^+\pi^-$ distribution 5.12. But there is certainly more information hidden in the four-momenta of the final state tracks.

It turned out in the past that observed track distributions could be parametrized by so called partial waves allowing to distinguish overlapping resonances. Those waves are containing amplitudes determined by a decay model of coupled spin states, or call it particles. This chapter is dedicated to Partial Wave Analysis (PWA) applied to the $K^-\pi^+\pi^-$ track distributions. The terminology, needed to understand the results, is briefly introduced here before it's application. The notation is the one commonly used by COMPASS, motivated by S.U. Chung [82].

A mass independent fit of a decay model was performed and the conclusions for a mass dependent fit are discussed.

7.1 THE PARAMETRISATION OF THE REACTION PROCESS

To summarize from section 5: Only three-momenta of the final states were measured together with properties of the initial state such as the track direction and particle identity. A mass hypothesis was applied to the final state tracks and wrong combinations were dismissed by the application of the RICH PID detector. Moreover structure in the invariant mass spectrum of all exclusive $K^-\pi^+\pi^-$ events as well as in the sub-states was observed. Finally a proton coming from the target was identified, transferring momentum t' to the sum of the final states and fulfilling general requirements of an exclusive diffractive processes together with the final state. No color nor charge was exchanged.

All observations together make the sketch 7.1 of the observed process plausible. It is showing an initial kaon in the beam being excited by reggeon exchange with the proton in the hydrogen target to a resonance X with an invariant mass m_X . The excited state emits a bachelor meson, a negative pion (kaon), and a mesonic resonance that decays into a final meson pair of opposite charge namely a negative kaon (pion) and a positive pion. This process is described in the so-called isobar model.

The cross section for this specific process was parametrized [82] by

$$\sigma(\tau, m) = \sum_{\epsilon=\pm 1} \sum_{r=1}^{N_r} \left| \sum_i^{N_{waves}} T_{ir}^\epsilon(m_X) A_i^\epsilon(\tau) \right|^2 \quad (7.1)$$

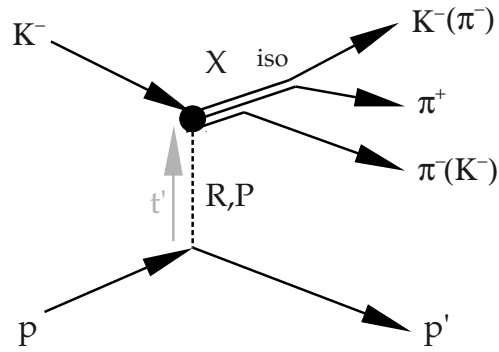


Figure 7.1: Feynmanlike graph for the picture behind diffractive dissociation of kaons on a nuclear target. The kaon excited to a resonance X by reggeon exchange with the target proton emits a bachelor particle to become a neutral isobar that decays further into two particles.

containing a coherent sum of production amplitudes $T_{ir}^\epsilon(m_X)$ and decay amplitudes A_i^ϵ for a set of quantum numbers $J^P M^\epsilon [\text{isobar}] \ell$ represented by i . J^P is the spin and parity of a possible particle with its spin projection M and a reflectivity quantum number ϵ ¹. That particle can decay into an isobar in the $\pi^+ \pi^- (K^- \pi^+)$ -branch and a bachelor particle with an orbital angular momentum ℓ between those.

These quantum numbers characterize the decay amplitude. It describes the consecutive decay process for the i^{th} partial wave in dependence on the available phase space τ . This process is nearly fully calculable based on some assumptions about the contributing intermediate states and the final states. It defines the angular distributions of the final state tracks. Details on the calculation of the decay amplitudes are given in appendix A.1 as well as explicit examples are given for the construction of partial waves.

The production amplitude on the other hand expresses the probability to produce a resonance X with an invariant mass m_X decaying into a specific decay chain parametrized by the decay amplitude. It is the parameter to be determined by a fit to the data as it will be shown in a later section.

The incoherent sum over the rank r stands mostly for the missing information about the polarisation of the target proton. It is assumed to have mostly two possibilities: One where the spin of the target stays intact and one where the spin of the recoil proton flips. Both possibilities were taken into account by increasing the rank to two. This means that two different production amplitudes T_{ir}^ϵ were combined incoherently with the same decay amplitude A_i^ϵ . Also other sources of incoherent background such as double diffraction, an excitation of the proton to an N^* resonance, might be covered by the rank, too.

¹ In the reflectivity basis the spin projection M is only the magnitude of M in the canonical basis. The sign is represented by the reflectivity ϵ . For details see section A.1.3.

The incoherent sum over the reflectivity $\epsilon = \pm 1$ takes the incoherence of partial waves with opposite magnetic sub-states M into account. The concept of the reflectivity and its connection to parity exchange and the spin projection M is explained in section [A.1.3](#).

Inspecting the explicit form for [7.1](#) given by [A.15](#) with [A.11](#) and [A.13](#) it is noticed that all parameters are calculable apart from $a_{\ell_S}^J(m, p)$, the decay strength into the isobar and its bachelor particle. That parameter was separated off

$$A_i^\epsilon(\tau) = \quad \quad \quad i a_{\ell_S}^J(m_X, p) \Psi_i^\epsilon(\tau)$$

$$\quad \quad \quad \quad \quad \quad \quad \quad \quad \downarrow$$

$$\sigma(\tau, m) = \sum_{\epsilon=\pm 1} \sum_{r=1}^{N_r} \left| \sum_i^{N_{\text{waves}}} T_{ir}^\epsilon(m_X) i a_{\ell_S}^J(m_X, p) \Psi_i^\epsilon(\tau) \right|^2 \quad (7.2)$$

De facto one may fit directly this cross section to the data and indeed it was one ansatz followed by groups at Lawrence Berkeley National Laboratory (LBL)-SLAC [\[83\]](#) as well as the ACCMOR [\[1\]](#) Collaboration for the WA03 $K^- \pi^+ \pi^-$ PWA.

But COMPASS was applying the concept of spin density matrices as developed by Ascoli and the Illinois Group [\[84\]](#). A spin density matrix is defined by

$$\rho_{ij}^\epsilon(m_X) \equiv \sum_{r=1}^{N_r} T_{ir}^\epsilon(m_X) T_{jr}^{\epsilon*}(m_X) \quad (7.3)$$

and equation [7.2](#) becomes then

$$\sigma(\tau, m) = \sum_{\epsilon=\pm 1} \sum_{i,j}^{N_{\text{waves}}} \rho_{ij}^\epsilon(m_X) i a_{\ell_S}^J(m_X, p) j a_{\ell_S}^{J*}(m_X, p) \Psi_i^\epsilon \Psi_j^{\epsilon*} \quad (7.4)$$

Instead of inspection of individual spin density matrix elements, three important quantities of partial waves were derived [\[21\]](#):

1. The intensity of the i^{th} partial wave are the diagonal elements

$$\text{intensity}_i^\epsilon(m_X) = \rho_{ii}^\epsilon(m_X). \quad (7.5)$$

It is the magnitude of the production amplitude and therefore a real number.

2. The phase $\phi_{ij}^\epsilon(m_X)$ between two waves i and j was contained in

$$\rho_{ij}^\epsilon(m_X) = |\rho_{ij}^\epsilon(m_X)| \cdot \exp \{i\phi_{ij}^\epsilon(m_X)\}; i \neq j. \quad (7.6)$$

A summation over off-diagonal complex numbers was expressing the interference between two waves.

3. For ranks $r > 1$ the coherence was introduced with

$$\frac{|\rho_{i \neq j}^\epsilon(m_X)|}{\sqrt{\rho_{ii}^\epsilon(m_X) \cdot \rho_{jj}^\epsilon(m_X)}} \quad (7.7)$$

A resonance is then probably present if significant intensity is observed varying as a function of the invariant mass m_χ . The corresponding phase between two waves would ideally then vary over π for one particle decaying into one channel. The phase motion is only a strong argument if coherence between two waves is close to 1.

All this does unfortunately not fully apply to the real measurement. The intensity of a signal may be not clear when statistical errors are large. The phase motion might be reduced or even compensated when one or more resonances overlap and/or resonances are decaying into several channels. Moreover coherence between two decay branches as it is the case for $K^-\pi^+\pi^-$ events is rather poor as only one solution per event is physical.

7.2 THE FIT PROCEDURE

Elements of the spin density matrix as well as the decay strengths can be determined by a χ^2 fit to the data. But to do this one has to model a functional form for $a_{\ell S}^J(m_\chi, p)$. In a first order a simple relativistic Breit-Wigner might hold but is for kaon resonances by far not sufficient as it will be demonstrated by a mass independent fit.

In order to get a feeling for contributing partial waves and a good description of the $a_{\ell S}^J(m_\chi, p)$ the data was divided into small bins of 20 MeV in m_χ . As small as possible to distinguish narrow resonances, as wide as necessary to contain a sufficient number of events per bin to fit the partial wave model properly. In such narrow bins $a_{\ell S}^J(m_\chi, p)$ was assumed to be constant in every bin and was absorbed by the spin density matrix elements as a value to be determined by a fit. The cross section 7.4 becomes then

$$\sigma(\tau, m_\chi) = \sum_{\epsilon=\pm 1} \sum_{i,j}^{N_{\text{waves}}} \rho_{ij}^\epsilon \Psi_i^\epsilon \Psi_j^{\epsilon*} \quad (7.8)$$

It is recalled from A.11 that Ψ_i^ϵ still depend on the available phase space as well as the invariant mass. By normalization of the decay amplitude by the integral over the available phase space inside an invariant mass bin, the fit procedure was stabilized as the dependence on m_χ cancelled out.

$$\Psi_i^\epsilon(\tau, m_\chi) \mapsto \frac{\Psi_i^\epsilon(\tau, m_\chi)}{\sqrt{\int |\Psi_i^\epsilon(\tau', m_\chi)|^2 d\tau'}} = \bar{\Psi}_i^\epsilon(\tau) \quad (7.9)$$

Finally an extended logarithmic likelihood function was derived [85] to the final form

$$\ln L = \sum_{n=1}^{N_{\text{events}}} \ln \sum_{\epsilon} \sum_{i,j} \rho_{ij}^\epsilon \bar{\Psi}_i^\epsilon(\tau_n) \bar{\Psi}_j^{\epsilon*}(\tau_n) - \sum_{\epsilon} \sum_{i,j} \rho_{ij}^\epsilon I A_{ij}^\epsilon \quad (7.10)$$

with the phase space integral containing the detector $\text{Acc}(\tau_n)$ acceptance in the available phase space

$$IA_{ij}^{\epsilon} = \int \Psi_i^{\epsilon}(\tau) \bar{\Psi}_j^{\epsilon*}(\tau) \eta(\tau) d\tau = \frac{1}{N_{\text{flat}}} \sum_n^{N_{\text{acc}}} \Psi_i^{\epsilon}(\tau_n) \bar{\Psi}_j^{\epsilon*}(\tau_n) \quad (7.11)$$

that was calculated numerically by an integration of amplitudes. The accepted integral consists of N_{acc} accepted flat phase space events divided by the number of all events in this bin N_{flat} . The number of accepted events was evaluated by the MC simulation of the detector measuring flat phase space events as treated off in chapter 6.

The fit procedure performed a minimization of the logarithmic likelihood function 7.10 by varying the complex spin density matrix elements. For every set of proposed matrix elements the total amplitude from data was calculated and compared to a weighted phase space. Notice the major importance of a well described acceptance of the available phase here.

When a fit converged to a minimum of the log likelihood the spin density matrix elements ρ_{ij}^{ϵ} were inspected. A possibly observed resonance would give not only significant intensity but also phase motion between two partial waves as a function of the invariant mass bin should be observed.

This procedure was called *mass independent fit* and was used here to determine the wave set describing the angular distributions the best. The results of these studies are a basis for a *mass dependent fit* where finally also the resonance parameters of $\alpha_{\ell S}^{J*}(m_X, p)$ would be determined.

7.3 THE PWA SET

A fastidious choice of the partial wave set was crucial for the result. Not only the input in terms of available quantum numbers could change the outcome of a fit dramatically. As already mentioned a good knowledge of the composition of the isobars was mandatory.

PARAMETRIZATION OF THE ISOBARS The decay of the $K^- \pi^+ \pi^-$ resonance in the decay chain model was described by an emission of a negative pion or kaon becoming a neutral isobar (figure 7.1) decaying further into a $K^- \pi^+$ or $\pi^+ \pi^-$ preserving charge, spin, isospin and energy. The $K^- \pi^+$ and $\pi^+ \pi^-$ spectrum was measured by previous experiments mostly in elastic scattering or central production and is summarized as particle states in the PDG review [11]. The resonances found there were used to parametrize the resonant behaviour of the partial wave decay amplitude (see A.13).

Table 7.1 summarizes the set of isobars considered to contribute to the observed $K^- \pi^+$ and $\pi^+ \pi^-$ isobar mass spectrum. Apart from the $(\pi^+ \pi^-)$ -S wave $f_0(600)$ all other waves were parametrized with relativistic Breit-Wigner functions including barrier factors for a converging behaviour at production thresholds (see section A.1.2 for details).

J^P	$\pi^+\pi^-$	model	$K^-\pi^+$	model
0^+	$f_0(600)$	K-matrix [86]	$K(800)$	BW
0^+	$f_0(980)$	BW	$K_0^*(1430)$	BW
0^+	$f_0(1370)$	BW		
0^+	$f_0(1500)$	BW		
1^-	$\rho(770)$	BW	$K^*(892)$	BW
1^-	$\rho(1450)$	BW	$K^*(1680)$	BW
2^+	$f_2(1270)$	BW	$K_2^*(1430)$	BW
3^-	$\rho_3(1690)$	BW	$K_3^*(1780)$	BW

Table 7.1: The initial set of isobars considered to contribute to the invariant mass distributions of the $K^-\pi^+$ and $\pi^+\pi^-$ subsystems. Values for mass and width in relativistic Breit Wigner (BW) functions were taken from the PDG's review [11]. The $f_0(600)$ (σ) was parametrized with a multi pole K-matrix approach [86]. The corresponding $K(800)$ (κ) was a simple BW function. See also section A.1.2 for a discussion on the parametrization of resonances.

The whole isobar set was kept somewhat symmetric as far as possible. The ($K^-\pi^+$)-S wave $K(800)$, although still controversial, was also considered as a simple Breit-Wigner function to describe the low mass background region in the $K^-\pi^+$ spectrum.

CONSTRUCTION OF DECAY AMPLITUDES The partial wave set for the $K^-\pi^+\pi^-$ resonance was constructed by a combination of table 7.1 with the respective bachelor particle. The reader not experienced in spin couplings is asked to read section A.2 first before proceeding.

The decay amplitude $a_{\ell S}^J(m_X, p)\Psi_i^\epsilon(\tau)$ in equation 7.2 is recalled. It was already mentioned that $\Psi_i^\epsilon(\tau)$ was fully calculable with the knowledge about quantum numbers of isobars and a coupling with a bachelor particle for every set of quantum numbers $J^P M^\epsilon$ [isobar] ℓ . Once calculated for every event it could be reused in every fit constellation. A large pool, consisting of 446 amplitudes in total, was created by the following restrictions:

- The highest total spin J reported in a three particle strange meson resonance was summarized as a $K_4^*(2045)$ [11] resonance with a spin of 4. The wave set here was bound to spins $J \leq 5$.
- Orbital angular momenta ℓ greater than 3 would give very small angular variations not distinguishable by fits to the current data sample. The orbital angular momentum was restricted to $\ell \leq 4$.
- Also spin projections M showed in previous studies negligible contributions beyond $|M| \leq 1$.

This rich pool of pre-calculated partial waves allowed for systematic studies with a very large variety of contributing partial waves.

THE SYSTEMATIC EXPLORATION Surely it was not possible to fit all available partial waves simultaneously. The large number of degrees of freedom described the observables well but clear structure in the individual partial waves was not found.

So it was started from a wave set based on well known quantum numbers as the $J^P = 1^+, 2^+$ and 2^- waves and the main decay channels into $K^*(892)$, $\rho(770)$, $K_2(1430)$ and $f_2(1270)$ isobars that were already identified by eye in the corresponding invariant mass distributions. It was found then that several $(\pi^+\pi^-)$ -S waves and $J^P = 0^-$ waves must be included in order to describe the data in the low mass region.

Then waves were systematically removed to observe the intensity dependence between waves. Other waves of higher spins were included. Less good described regions specially at high masses were tried by extension with weaker isobars higher in the invariant mass. But as very high spins did not give significant signals also isobars with higher spins were not needed.

Other studies concerned the naturality of the exchange process of a pomeron that was known to produce predominantly resonances with positive reflectivity [1, 21]. This behaviour could be confirmed as no significance was found for waves with negative reflectivity when positive reflectivity was simultaneously proposed in the wave set.

The finalized wave set was tuned with an eye on the logarithmic likelihood, structure in the individual waves, the flat wave and the difference between the fitted angular distributions as well as the description of the real data which is summarized in section 7.5.

To overcome the problem of local minima in the fits, every invariant mass bin was fitted several times with different starting values. In the following only the most likely solution in every invariant mass bin is shown among all fit results with one partial wave constellation.

THE PARTIAL WAVE NOTATION A common notation for the individual partial waves formed by the quantum numbers $J^P M^\epsilon [\text{isobar}] \ell$ and their final states is used, namely

$$J^{P(C)} M^\epsilon \text{ meson 1 } \left[\begin{matrix} \ell \\ S \end{matrix} \right] \text{ meson 2} \quad (7.12)$$

meaning a total spin and parity J^P with a magnetic sub-state M and it's parity ϵ formed by two mesons with a coupled spin projection of both S and an angular momentum ℓ between them.

7.4 MASS INDEPENDENT FIT RESULTS

The partial waves were grouped to the same spin and parity J^P since those were strongly mixing. So it was supposed that one or even more resonances X in a fixed J^P may decay into different channels described by

J^P	M^e	meson 1	$\begin{bmatrix} \ell \\ S \end{bmatrix}$	meson 2
0^-	0^+	$K^*(892)$	$\begin{bmatrix} 1 \\ 1 \end{bmatrix}$	π^-
0^-	0^+	$\rho(770)$	$\begin{bmatrix} 1 \\ 1 \end{bmatrix}$	K^-
0^-	0^+	$f_0(600)$	$\begin{bmatrix} 0 \\ 0 \end{bmatrix}$	K^-
1^+	0^+	$K^*(892)$	$\begin{bmatrix} 0 \\ 1 \end{bmatrix}$	π^-
1^+	0^+	$\rho(770)$	$\begin{bmatrix} 0 \\ 1 \end{bmatrix}$	K^-
1^+	0^+	$K^*(800)$	$\begin{bmatrix} 1 \\ 0 \end{bmatrix}$	π^-
1^+	1^+	$K^*(892)$	$\begin{bmatrix} 0 \\ 1 \end{bmatrix}$	π^-
1^+	1^+	$\rho(770)$	$\begin{bmatrix} 0 \\ 1 \end{bmatrix}$	K^-
1^+	1^+	$K^*(800)$	$\begin{bmatrix} 1 \\ 0 \end{bmatrix}$	π^-
1^+	1^+	$f_0(600)$	$\begin{bmatrix} 1 \\ 0 \end{bmatrix}$	K^-
1^+	0^+	$\rho(770)$	$\begin{bmatrix} 2 \\ 1 \end{bmatrix}$	K^-
1^+	0^+	$K^*(892)$	$\begin{bmatrix} 2 \\ 1 \end{bmatrix}$	π^-
1^-	1^+	$K^*(892)$	$\begin{bmatrix} 1 \\ 1 \end{bmatrix}$	π^-
1^-	1^+	$\rho(770)$	$\begin{bmatrix} 1 \\ 1 \end{bmatrix}$	K^-
2^+	1^+	$K^*(892)$	$\begin{bmatrix} 2 \\ 1 \end{bmatrix}$	π^-
2^+	1^+	$\rho(770)$	$\begin{bmatrix} 2 \\ 1 \end{bmatrix}$	K^-
2^-	0^+	$K^*(892)$	$\begin{bmatrix} 1 \\ 1 \end{bmatrix}$	π^-
2^-	0^+	$\rho(770)$	$\begin{bmatrix} 1 \\ 1 \end{bmatrix}$	K^-
2^-	0^+	$K_2^*(1430)$	$\begin{bmatrix} 0 \\ 2 \end{bmatrix}$	π^-
2^-	0^+	$f_2(1270)$	$\begin{bmatrix} 0 \\ 2 \end{bmatrix}$	K^-

Table 7.2: The final most evident partial wave set as found after many iterations of systematic studies.

the partial waves. Therefore not only single partial waves are discussed but also the coherent sum of those in the group representing the total resonances in this particular channel. The groups are already sorted according to their total intensity. $J^P = 1^+$ and 2^- total spins were always the strongest in all fits. The integrals of total intensities of $J^P = 0^-$, 2^+ and 1^- waves were on the other hand very similar to each other. The order of the intensities depended on the model adapted to the fit.

7.4.1 The final partial wave set

The final wave set 7.2 was found to describe the observed angular distributions and invariant mass spectra the best with a minimal number of partial waves. It turned out that a wave set consisting mainly of the largest visible resonances in the invariant mass distributions of the isobars gave the most evident results. Other isobars did not contribute

significantly. The statistical uncertainty was simply too large to find resonances low in intensity.

Although developed from scratch many similarities were found when comparing this final wave set to a published one by the ACCMOR collaboration [1]. The differences were:

- No thresholds were adapted as a properly parametrized resonance should converge at the limits.
- The $f_0(600)$ was parametrized with an up to date model.
- The $K^*(800)$ resonance was a broad resonance around $1.2 \text{ GeV}/c^2$ in the old publication.
- Masses and widths of other isobars slightly changed.
- In the Ascoli fit approach as used by the ACCMOR collaboration explicit proton spin flip waves were included. In contrast allowed the spin density matrix with a rank of 2 spin flips in all waves.
- $J^P = 1^-$ waves were included.

The overlap between both wave sets in main waves allowed a direct comparison of individual partial waves. It led to the confirmation of many observations in the ACCMOR analysis but also remarkable differences were found.

7.4.2 The total intensity

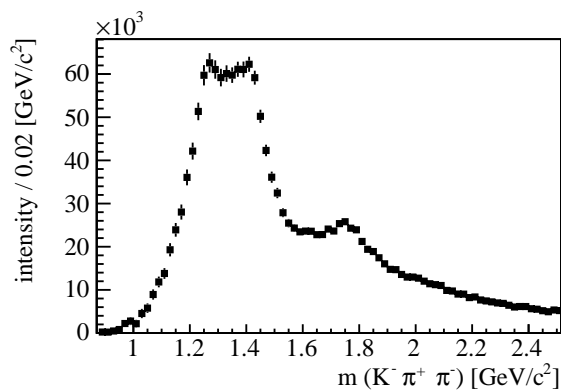


Figure 7.2: The coherent sum over all partial waves gives the total intensity. It can be understood as an acceptance corrected $K^-\pi^+\pi^-$ invariant mass distribution.

The coherent sum over all amplitudes gave the total intensity 7.2. Acceptance corrected PWA took the angular correlation in a $K^-\pi^+\pi^-$ decay into account and replayed the spectrometer acceptance in all variables of the available phase space in a proper way. The total intensity can then be understood as an acceptance corrected $K^-\pi^+\pi^-$ invariant mass

distribution. Comparing this total intensity with the invariant mass distribution 5.10 a reduced intensity for higher masses is observed. The total intensity is well in agreement with the invariant mass distribution 1.7 presented by the ACCMOR collaboration [1] where acceptance was known to be flat. The distribution of the total intensity was very stable against changes in the PWA wave set. Only the inclusion of a $(K^-\pi^+)$ -S wave forming a $J^P = 1^+$ resonance showed destructive interference in the low mass region separating the two strong resonances even more.

7.4.3 $J^P = 1^+$ waves

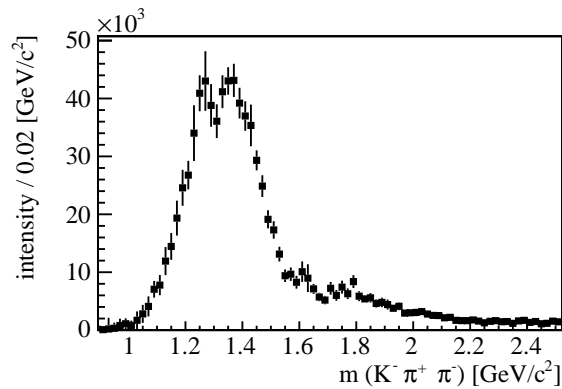


Figure 7.3: Spin total of all $J^P = 1^+$ waves showing a clear double structure identified to be K_1 resonances from the spin triplet and singlet states in a simple $q\bar{q}$ model.

THE SPIN TOTAL The strongest intensities were always found in $J^P = 1^+$ waves and this was not surprising from the point of a $q\bar{q}$ model as discussed in chapter 1. As the spin $S = 0$ singlet state and spin $S = 1$ triplet state were mixing both states should be found in the same wave. Indeed a double structure was clearly visible in the spin total distribution 7.3. The spin total was dominating the low mass region below $1.6 \text{ GeV}/c^2$ but structure was also found in the high mass region.

THE LOW MASS REGION The double peak structure is most pronounced in the $1^+ 0^+ K^*(892) [1^0] \pi^-$ wave intensity in figure 7.4. Other partial waves contained also a smaller or bigger admixture of both waves but the intensities were not separated very well anymore. The strongest indication was found in the phase motion between two waves where two inflection points of the second derivative were always present around $1.3 \text{ GeV}/c^2$ and $1.4 \text{ GeV}/c^2$. Those resonances, namely $K_1(1270)$ and $K_1(1400)$ (see also table 1.2 for a complete list), are well known in literature and were very stable against changes in the wave set. The strong intensity and stability of the $1^+ 0^+ K^*(892) [1^0] \pi^-$ and $1^+ 0^+ \rho(770) [1^0] K^-$

waves makes them favourite waves to measure the relative phase motion of other partial waves.

COMPARISON TO WAO3 RESULTS A direct comparison of the mass independent fit results to results in figure 7.6 as published by the ACCMOR collaboration [1] resulted in an interesting finding: The second resonance in the 1^- waves was much more pronounced in the $1^+ 0^+ K^*(892) \begin{bmatrix} 0 \\ 1 \end{bmatrix} \pi^-$ wave in COMPASS data. The coupling to the $1^+ 0^+ \rho(770) \begin{bmatrix} 0 \\ 1 \end{bmatrix} K^-$ wave on the other hand was lowered. An enhanced coupling to K^* branches wound through all $\rho(770)$ and $K^*(892)$ wave pairs specially in the 1^+ waves. Even more interesting was to see that it was possible to reproduce intensity distributions and phase motions in nearly perfect agreement with the published distributions by application of additional events with wrong $K^- \pi^+ \pi^-$ mass combinations. In that case the fit always favoured the $\rho(770)$ branch. It turned out that wrong mass combinations had a larger impact on the angular distributions of the $K^- \pi^+$ track combinations than on $\pi^+ \pi^-$ track combinations (for details see appendix B). And indeed, the issue of wrong track combinations was visibly a larger one in the ACCMOR analysis than in COMPASS data. Strong reflections were observed in the invariant mass distributions of the $K^- \pi^+$ and $\pi^+ \pi^-$ track combinations published by ACCMOR.

A PROPOSAL FOR A PARAMETRIZATION In order to measure the intensity, width and branching ratios into the different channels a mass dependent fit with a K-matrix approach would be favoured as interference between two waves cannot be expressed correctly with a simple Breit-Wigner shape assumption only (see section A.1.2).

THE HIGH MASS REGION Apart from the lower K_1 resonances the literature reports several states in the higher mass region listed in the PDG review as the $K_1(1650)$ waiting for further confirmation. Indeed one mentioned resonance was observed also in the D-wave intensities 7.5. The resonant behaviour around $1800 \text{ MeV}/c^2$ is visible in the intensity but less pronounced in the phase motion. Those resonances were observed in partial waves containing an excited orbital angular momentum $\ell = 2$ between the isobar and bachelor particle. Lower angular momenta provided no evidence for those resonances what confirms the observations by the ACCMOR collaboration. The resonance seems to be observable in diffractive production only. The interpretation might be therefore difficult in terms of a simple meson resonance.

A PROPOSAL FOR A PARAMETRIZATION For a mass dependent fit in the high mass region a simple coupled Breit-Wigner might be used. A fit over the whole mass range would of course introduce a third pole to the K-matrix approach.

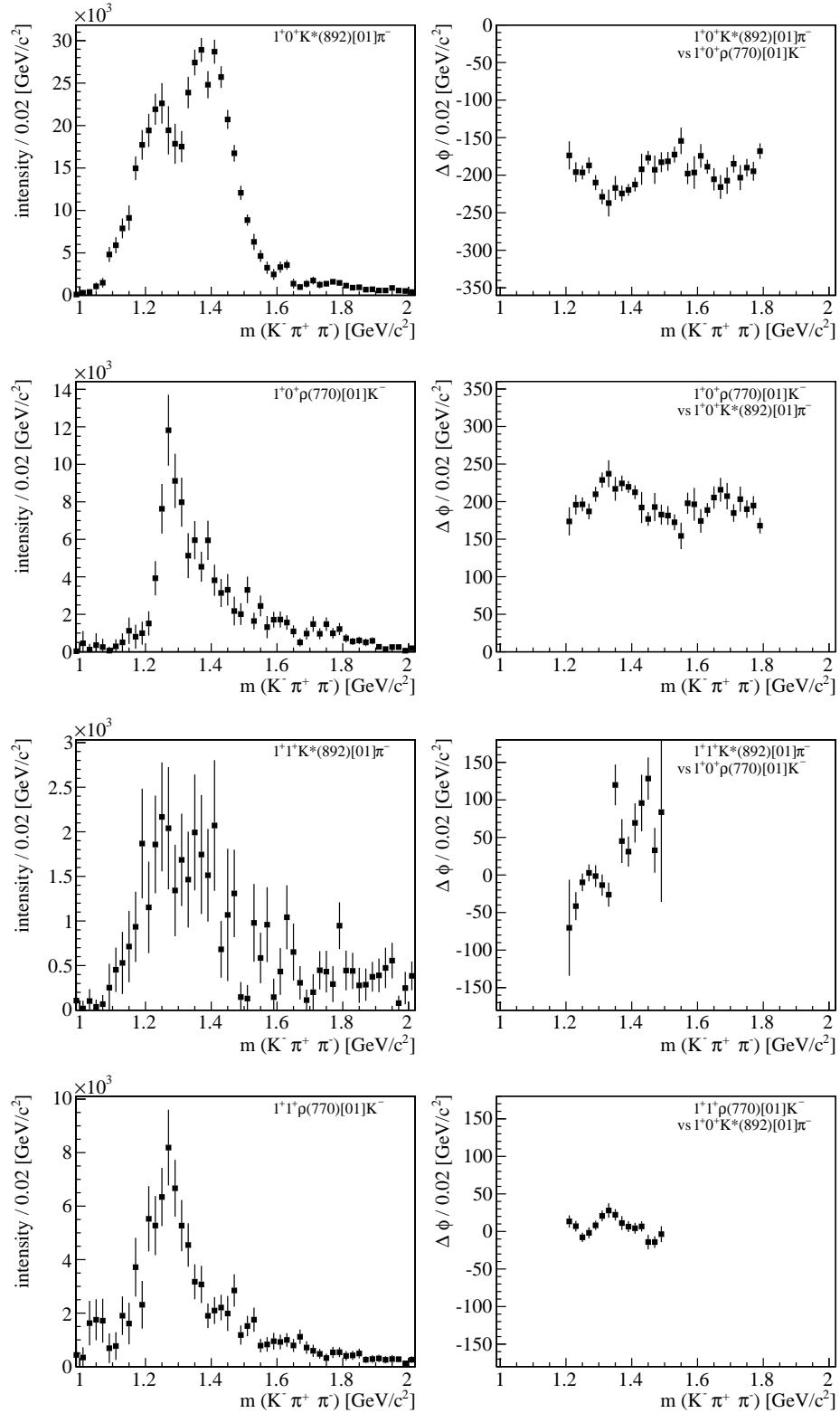


Figure 7.4: $J^P = 1^+ M = 0/1$ wave intensities and the relative phase motion in respect to the strongest intensity of the counter branch. Only the $1^+ 0^+ K^*(892)[0] \pi^-$ wave intensity shows a clear double structure. Other waves have only the same characteristic phase motion. The $K_1(1400)$ resonance couples much stronger to the $(K^- \pi^+)$ -isobar branch than in published results by the ACCMOR collaboration.

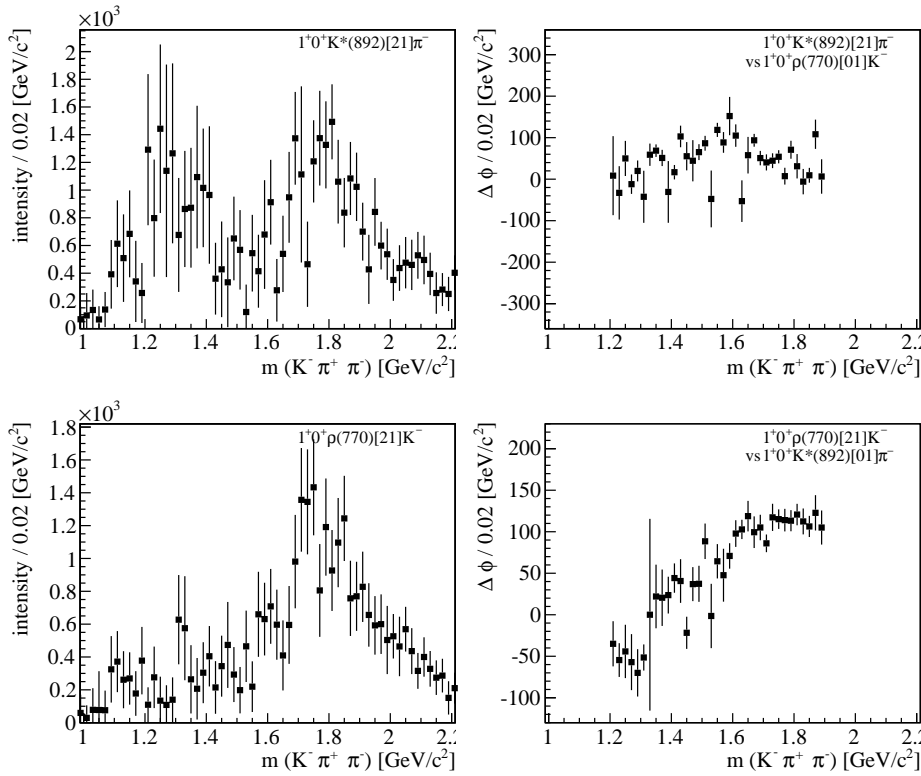


Figure 7.5: $J^P = 1^+ M = 0$ D-waves showing a resonant behaviour around $1.8 \text{ GeV}/c^2$. The intensity distributions were well in agreement with observations by the ACCMOR collaboration.

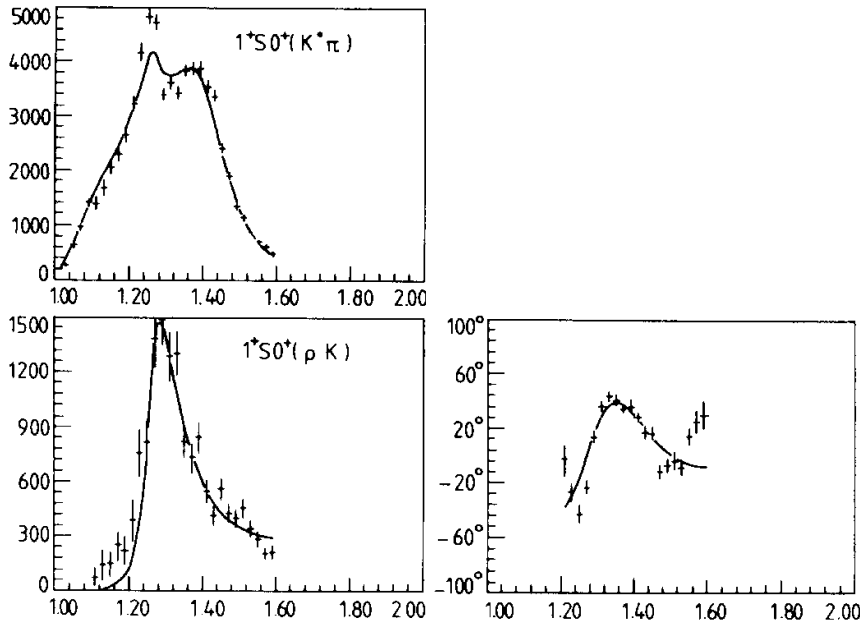


Figure 7.6: Left: the intensity over the $K^-\pi^+\pi^-$ mass of the two main $J^P = 1^+$ waves as published by the ACCMOR collaboration [1] in 1981. Right: The relative phase motion between them. Axis titles are same like in figure 7.4 and the upper figures can be directly compared. The range of momentum transferred is $0.05 \leq t' \leq 0.7 \text{ GeV}^2/c^2$. The continuous line is a mass dependent fit to the data.

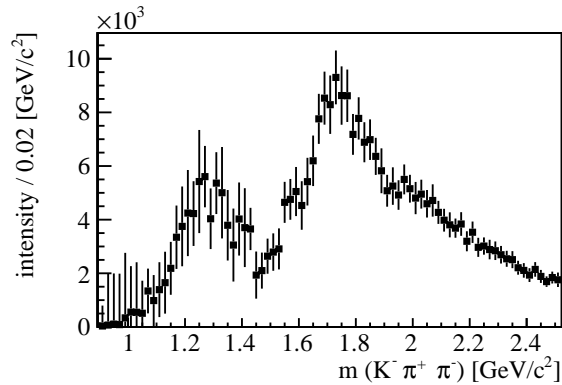
7.4.4 $J^P = 2^-$ waves

Figure 7.7: The spin total of the $J^P = 2^-$ waves. The lower resonance is most probably an uncompensated effect as the origin is only found in the $K^*(892)$ wave. The upper resonant structure is expected to contain at least two resonances by mixing spin singlet and spin triplet states.

THE SPIN TOTAL The same spin singlet and triplet mixing as observed in the $J^P = 1^+$ waves applies also to the $J^P = 2^-$ domain. The spin total intensity 7.7 has most of the intensity above $1.5 \text{ GeV}/c^2$. The low mass peak, probably an artefact, is discussed below at the level of individual waves. The total intensity was stable for high masses but changed at the low mass region when manipulating the adapted wave set. A strong interplay between the $(\pi^+\pi^-)$ - $S J^P = 0^-$ wave was observed. The inclusion of the $0^- 0^+ f_0(600) \begin{bmatrix} 0 \\ 1 \end{bmatrix} K^-$ wave reduced the intensity of the 2^- total spin by nearly a factor of two at the low mass region below $1.6 \text{ GeV}/c^2$. Moreover intensity was lost at the high mass region when including higher spins as $J = 3, 4, 5$.

THE PARTIAL WAVES The 2^- partial wave intensities 7.8 show resonances coupling mostly to $K_2^*(1430)\pi^-$ and $f_2(1270)K^-$ waves for invariant masses above $1.6 \text{ GeV}/c^2$. The picture for $K^*(892)\pi^-$ and $\rho(770)K^-$ waves is less clear: The low mass region shows peaks also reported by the ACCMOR collaboration as a "curiosity". As this intensity was not stable against changes in the wave set it is most probably a wave compensating a small effect by a large intensity as the available phase space is small in this region. This is also indicated by the large statistical uncertainty. The high mass region had significant intensity but vanished mostly in the $K^*(892)\pi^-$ wave with the inclusion of a 3^+ wave. Those waves were sensitive to background from central production as discussed later in this chapter. Nevertheless the fit required this waves for a likely result.

No clear evidence for a $K_2(1580)$ was found. It was anyhow reported by one early experiment [87] and was seen only the K^* partial wave branches

although observed in the same channel and production mechanism as COMPASS was exploring.

The higher mass region of $K_2^*(1430)\pi^-$ and $f_2(1270)K^-$ waves was found to be dominated by at least two strong resonances known today as the $K_2(1770)$ and $K_2(1820)$ spin singlet and triplet $q\bar{q}$ -state. A two pole interpretation is also indicated by the phase motion although two resonances are barely seen. The $K_2^*(1430)\pi^-$ wave appeared to have a wider shoulder compared to the $f_2(1270)K^-$ wave but this shoulder degenerated with the inclusion of a 3^+ wave. Also here background from central production was compensated. There was no clear evidence found for a $K_2(2250)$, reported by various hyperon formation analyses [11]. A mass dependent analysis might change this picture when two resonances only are not sufficient to describe these fit results.

A PROPOSAL FOR A PARAMETRIZATION The possible existence of two resonances in the 2^- waves leads again to a recommended K-matrix approach in a mass dependent fit to the data. In addition one should consider removing those waves below $1.6\text{ GeV}/c^2$ to improve the fit stability in the 0^- and high spin waves. Only the $K_2^*(1430)\pi^-$ and $f_2(1270)K^-$ waves should be considered for a fit.

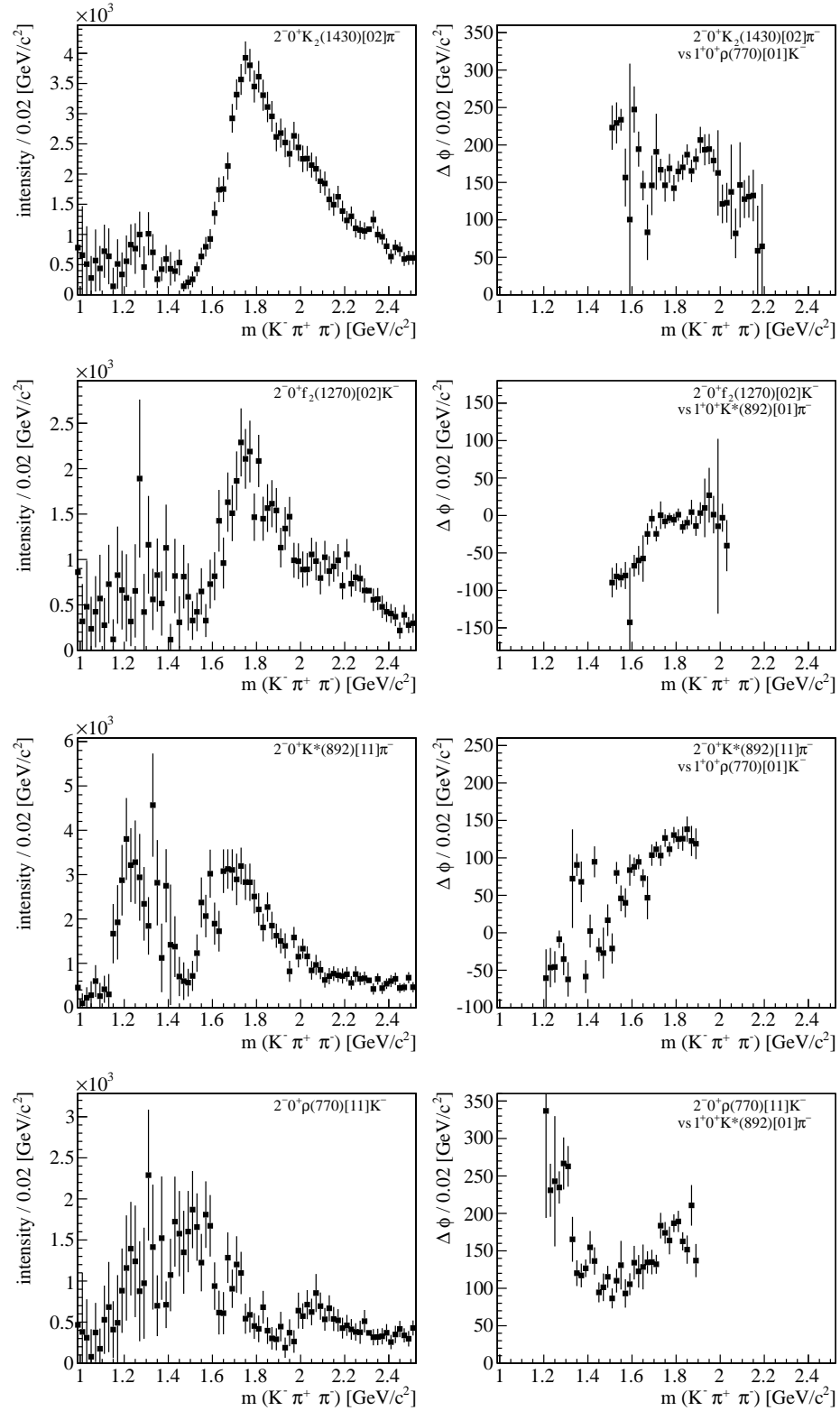


Figure 7.8: $J^P = 2^-$ waves. Resonances above $1.6 \text{ GeV}/c^2$ are coupling mainly to $K_2^*(1430)$ and $f_2(1270)$ partial waves. The intensity in the $K^*(892)$ wave vanished with the inclusion of 3^+ waves.

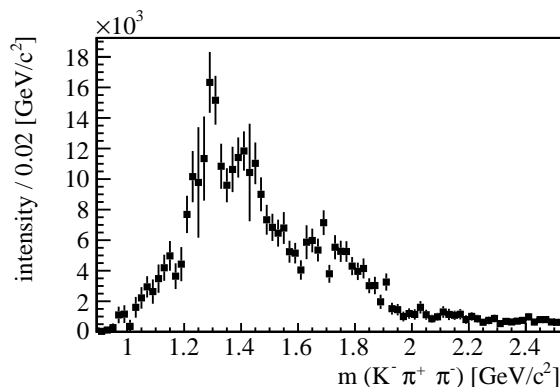
7.4.5 $J^P = 0^-$ waves

Figure 7.9: The spin total of the $J^P = 0^-$ waves showing a large intensity in the region where a $K(1460)$ resonance was reported. The structure in the wave was not stable when changing parts of the wave set.

THE SPIN TOTAL The fit results with $J^P = 0^-$ waves provided a massive intensity in the low mass region around $1.4 \text{ GeV}/c^2$. The figure 7.9, showing the spin total $J^P = 0^-$ wave, would suggest at least one clear resonance.

THE PARTIAL WAVES This peak was mostly dominated by the $f_0(600)K^-$ wave. Other waves showed a more pronounced two peak structure in case of the absence of the $f_0(600)K^-$ wave which itself gathered most of the intensity from the 2^- wave as well as the flat wave. The phase moves very little what was also observed in previous analyses [1]. The fits by the ACCMOR collaboration emerged a large Deck-like background contributing to this resonance. No wonder as a resonance decaying into an isobar with the vacuum quantum numbers $J^{PC} = 0^{++}$ and a spin $J = 0$ kaon had a flat spherical angular distribution, not only in the reference system of the resonance X but also in the $f_0(600)$ isobar reference system of the $\pi^+\pi^-$ -decay branch. A $K^*(800)$ wave could principally be included but a fit would not be able to distinguish between the $(\pi^+\pi^-)$ -S wave and the $(K^-\pi^+)$ -S wave.

A PROPOSAL FOR A PARAMETRIZATION A mass dependent fit would contain a non resonant Deck like background with a coupled Breit-Wigner resonance as proposed by the ACCMOR collaboration [1]. A clear confirmation of a $K(1460)$ might be difficult. Not only the large non resonant background complicates the interpretation of the fit result. In addition a $K(1460)$ was only seen in the diffractive charged three-particle decays so far. An other radial occurrence of the kaon, as one would interpret this resonance, might be still questionable.

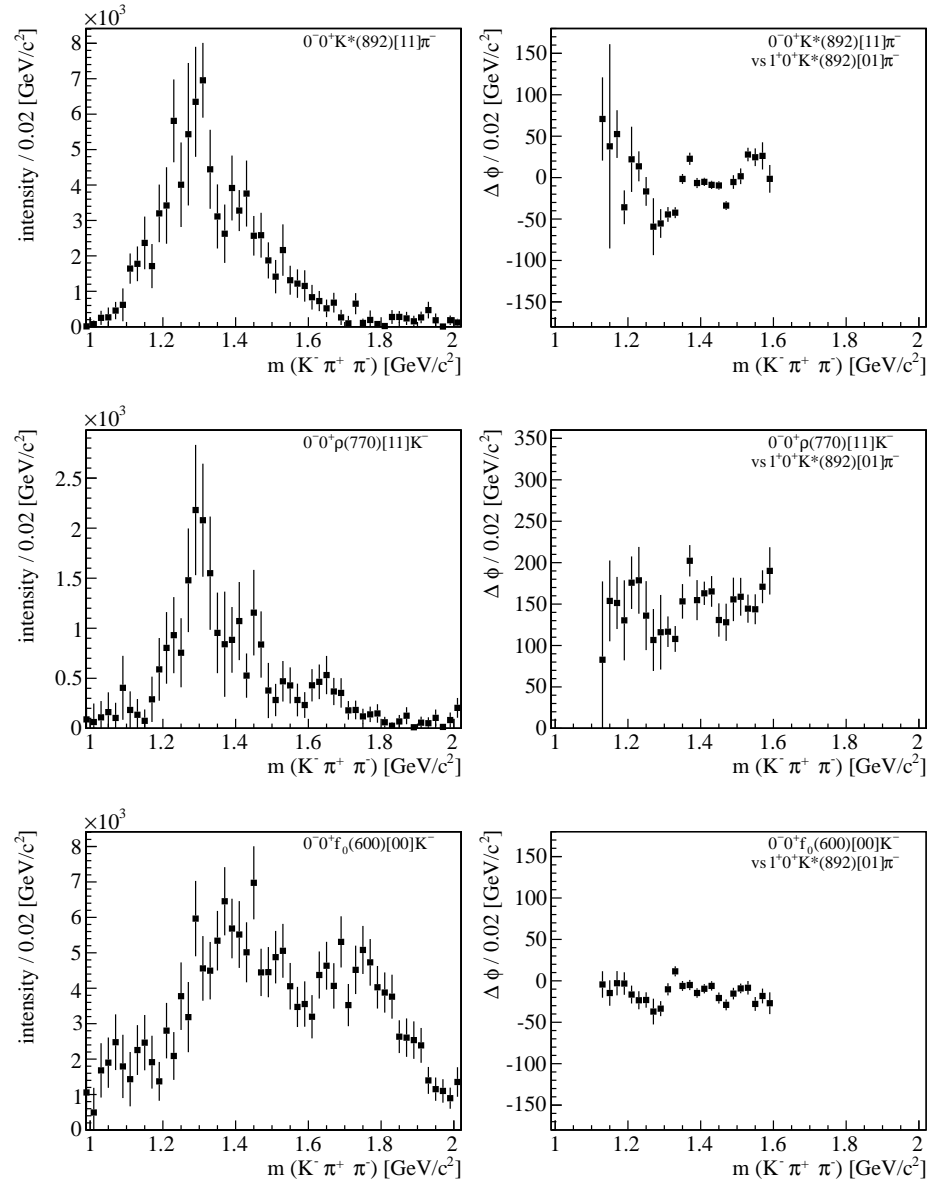


Figure 7.10: $J^P = 0^-$ waves are showing a large intensity in the low mass region. Same phase motion is observed in all channels.

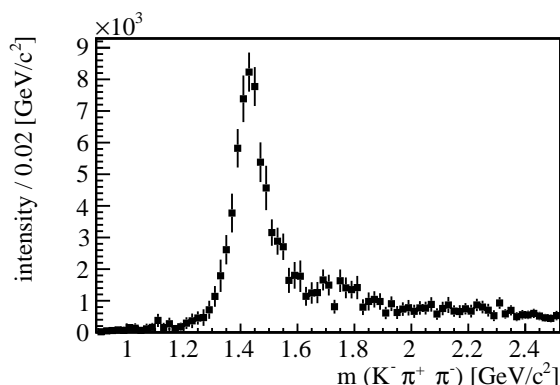
7.4.6 $J^P = 2^+$ waves

Figure 7.11: The Spin total of $J^P = 2^+$ waves has a very strong peak at the region of the $K_2(1430)$.

THE SPIN TOTAL The spin total distribution 7.11 of all $J^P = 2^+$ states shows a clear peak in the region of the $K_2^*(1430)$ resonance. The intensity is mostly flat in higher mass region but is non zero. Little motion was observed between $1.6 \text{ GeV}/c^2$ and $1.8 \text{ GeV}/c^2$.

THE PARTIAL WAVES The $J^P = 2^+$ waves were expected to contain not only the well established $K_2^*(1430)$. Mostly the LASS-collaboration observed a resonance in a formation process $K^- p \rightarrow \bar{K}^0 \pi^+ \pi^- n$ little below $2 \text{ GeV}/c^2$ [88], summarized as the $K_2^*(1980)$ in the PDG review. The $K_2^*(1430)$ resonance is dominant in the individual partial wave intensities in figure 7.12. The phase motion is strong in the region of the $K_2^*(1430)$ and the influence of the chosen wave set was only small. The intensity changed (by exclusion of the $(\pi^+ \pi^-)$ -S wave for example) but the shape and phase motion remained stable.

An indication for a $K_2^*(1980)$ resonance was not observed. If there might be an other resonance it would be most probably situated around $1.7 \text{ GeV}/c^2$. But also there intensity is barely observable.

A PROPOSAL FOR A PARAMETRIZATION For a mass dependent fit procedure a single coupled Breit-Wigner would be sufficient. Even when a small resonance around $1.7 \text{ GeV}/c^2$ would exist, it would not disturb the fit procedure significantly as no strong evidence in this channel was found.

DETERMINATION OF RESONANCE PARAMETERS As only one $J^P = 2^+$ resonance was dominating, a simple fit was performed of a coupled Breit-Wigner distribution to the data, to judge on the quality of the mass independent fit results. Function A.16 was fit to the intensity distribu-

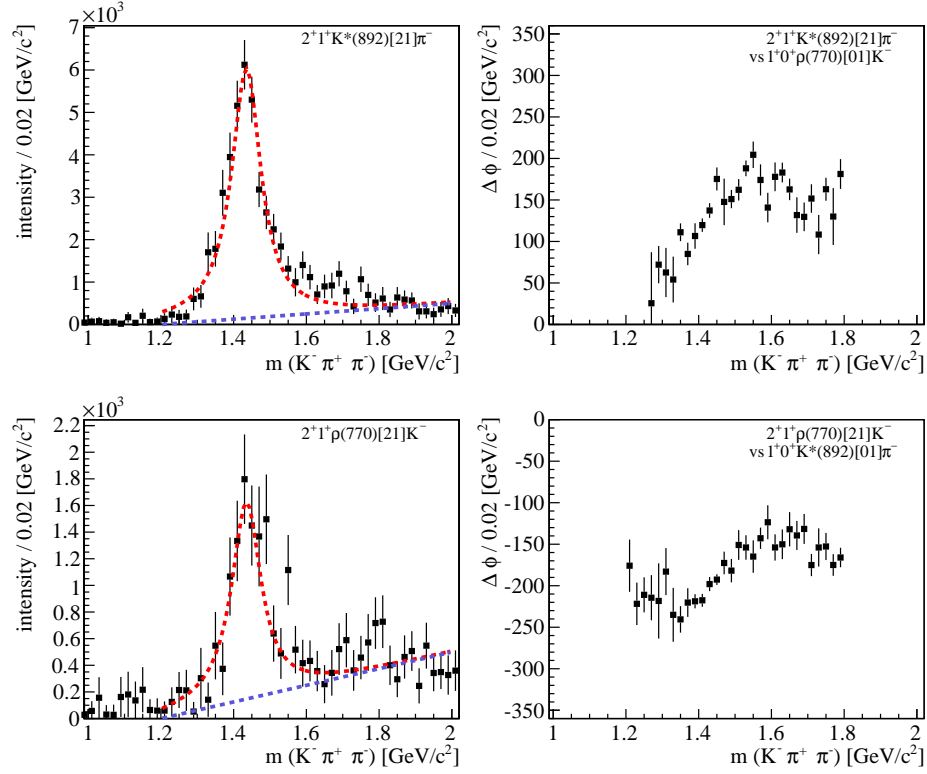


Figure 7.12: The $J^P = 2^+ M = 1$ waves show clearly the $K_2^*(1430)$ resonance. Clear evidence for further resonances was not found. The dashed line is a fit of a coupled Breit-Wigner intensity distribution to the data and is summarized in table 7.3. See text for details.

tions, neglecting phase motion in respect to the remaining production amplitudes. Both channels were simultaneously fit with the mean and the width as common parameters. In addition three simple parametrisations of the background function were tried. A fit of a linear background starting from $1.2 \text{ GeV}/c^2$ is visualised in figure 7.12. Furthermore a constant background was tried as well as a polynomial background function of 2nd order. Those fit results were taken as systematic errors since those were larger than remaining systematic uncertainties discussed in section 7.6. A physically meaningful description of the non resonant background was not implemented yet since a proper treatment needs the framework of a mass dependent analysis.

The fit results are summarized in table 7.3. The slope of the linear background function was fit to $(623 \pm 46)/(20 \text{ MeV})$ and a reduced χ^2 of 1.35 was achieved. A parabolic background enhanced the fit result with a reduced χ^2 of 1.033 in contrast to a value of 2.26 in case of a constant background. The latter fit results were taken as the upper systematic uncertainty, the former as the lower. The branching ratio was calculated from the intensities at the peak of the Breit-Wigner distribution. The notation is following the one used by the LASS collaboration in [88].

The mean value by the $K_2^*(1430)$ resonance distribution of $(1.433 \pm 0.0028) \text{ GeV}/c^2$ was found to be slightly greater than the summarized

parameter	value	PDG's average [11]
χ^2/ndf	$96.88/72^{+0.91}_{-0.31}$	
$\frac{d\sigma}{dM_{K\pi\pi}}(K^*\pi^-)$	$5869 \pm 385^{+209}_{-46}$	
$\frac{d\sigma}{dM_{K\pi\pi}}(\rho K^-)$	$1475 \pm 163^{+219}_{-215}$	
mass [GeV/c ²]	$1.433 \pm 0.0028^{+0.004}_{-0.002}$	1.426 ± 0.0015
width [MeV/c ²]	$98.6 \pm 6.67^{+1.12}_{-6.59}$	98.5 ± 2.9
BR($\rho K^-/K^*\pi^-$)	$0.335 \pm 0.0322^{+0.0640}_{-0.0511}$	0.354 ± 0.033

Table 7.3: The fit parameters of a coupled Breit-Wigner over a linear background fit to the distributions in figure 7.12. Values are compared to the PDG's averaged value [11]. The branching ratio of the amplitudes was corrected for isospin by a factor of 1/0.75 (see section A.3). The systematic errors origin in fits with other parametrisations of the background intensity. See the text for details.

value in the PDG review [11] of $(1.426 \pm 0.0015) \text{ GeV}/c^2$. But on the other hand it was well in agreement with fit results by the ACCMOR collaboration alone [1]. The width of $98.6 \pm 6.67 \text{ MeV}/c^2$ nearly equals to $(98.5 \pm 2.7) \text{ MeV}/c^2$ by the PDG.

The isospin corrected² $\rho(770)K^-/K^*(892)\pi^- = (33.5 \pm 3.22)\%$ branching ratio compares to the averaged value of $(35 \pm 3)\%$ in the PDG review. The systematic uncertainty of the branching ratio was dominating in contrast to other fit values which had comparable systematic and statistical errors.

The fit to the intensity distributions demonstrates the good quality of the mass independent fit results. Not only resonance parameters were replayed like the mass and width but also the branching ratio into the two isobar states was well in agreement with previous findings.

7.4.7 $J^P = 1^-$ waves

The $J^P = 1^-$ spin total distribution is shown in figure 7.13. Some enhanced intensity was observed at low masses near the thresholds. Only one partial wave carried this intensity as shown in figure 7.14. This was observed in all wave sets with 1^- waves of positive reflectivity. Either contained the $K^*(892)\pi^-$ wave that structure or if absent then the $\rho(770)K^-$ wave. An artificial introduction of a higher threshold should be considered here to remove this fake resonance. The higher peak could be related to the $K^*(1680)$ but the phase motion gives no real evidence for an existence of this resonance. A simple Breit-Wigner resonance might be fitted to this waves in a mass dependent analysis, clarifying the necessity of this partial wave.

Moreover, it should be noted that those waves took the intensity mostly from the flat wave leaving a dip around this value. The exclusion pro-

² See section A.3 for the discussion on the isospin correction factor of 0.75.

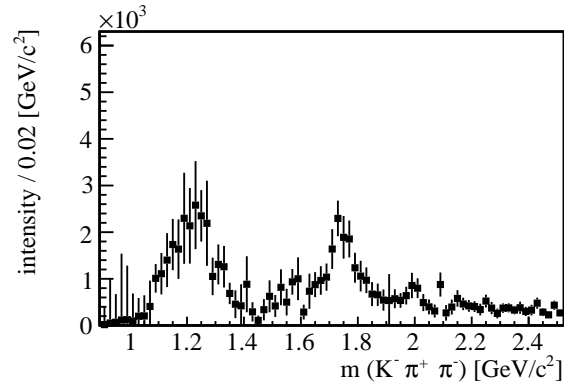


Figure 7.13: The spin total of the $J^P = 1^-$ waves contains one resonant structure in the region of a $K^*(1680)$. The lower intensity peak was not stable and appeared in only one partial wave.

vided a smooth flat wave but the fit was less well describing the data. This intensity demonstrates nicely the difficulty in PWA finding a proper unbiased model.

7.4.8 Higher spins

It was tried to include several waves of higher spins. All tested $J^P = 3^-$ waves gave no intensity. The intensity 7.15 of $J^P = 3^+$ waves was significant at high masses but only $K^*\pi^-$ branches contributed. Included $J^P = 3^+$ partial waves reduced in addition the intensities at the high mass region of the 2^- waves of the $K^*\pi^-$ branches. This is demonstrated exemplary by the $J^P = 2^-$ intensities in figure 7.16. Again a compensation of background from central production is suspected to affect the $K^*\pi^-$ branch more than the ρK^- branch. The flat wave was not affected by that change in the partial wave set.

7.4.9 The flat wave

The flat wave was only a constant term normalized to the available flat phase space. It was compensating angular distributions that were not described by the adapted partial wave set. It was indicating missing partial waves in the PWA set when significant structure was found in it.

The intensity 7.17 of the flat wave shows structure. Some intensity was transferred to the $J^P = 1^-$ waves leaving a dip in that flat wave. All-in-all was the intensity very small, demonstrating the ability of the adapted PWA wave set to describe the $K^-\pi^+\pi^-$ distributions. The intensity got stronger with a lowered rank in the fit what is depicted in section 7.6.3.

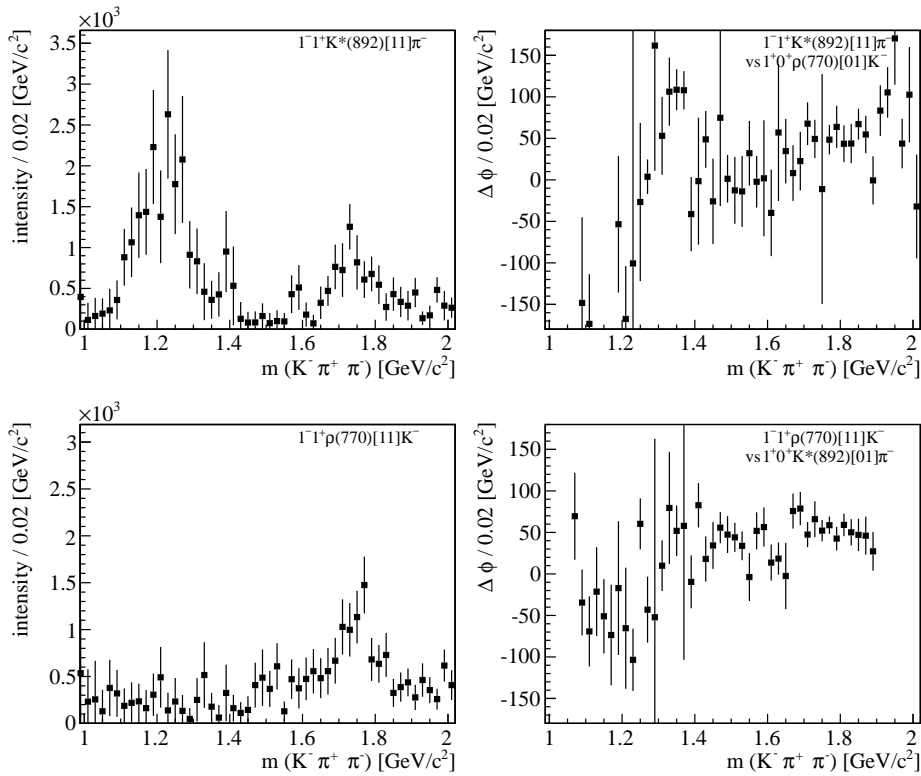


Figure 7.14: $J^P = 1^-$ $M = 1$ waves are both showing a resonant structure around $1.75 \text{ GeV}/c^2$ although phase motion is not clear. Only one partial wave contains a further intensity peak in the low mass region what is a clear hint for a fake resonance.

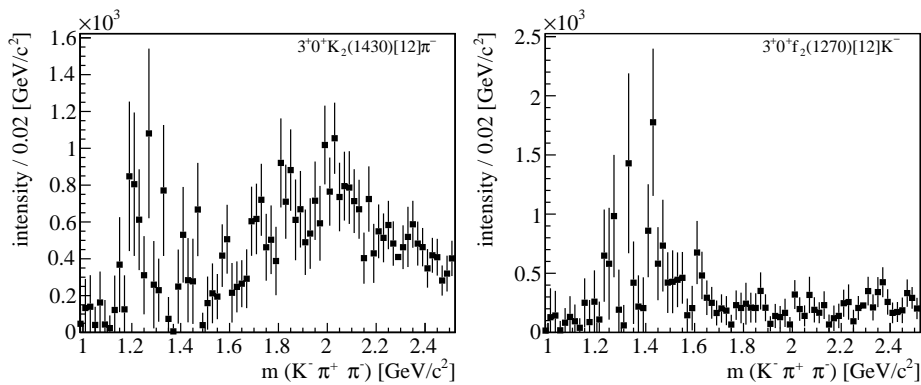


Figure 7.15: Two $J^P = 3^+$ waves shown exemplary for the systematic studies with higher spins. Only K isobars carried significant intensity in the high mass region.

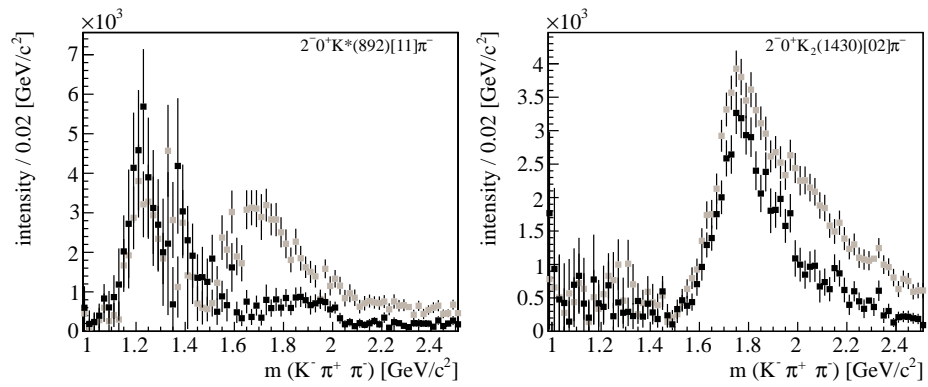


Figure 7.16: The impact of the inclusion of the $J^P = 3^+$ waves on the $J^P = 2^-$ waves with K isobars. The waves (grey) in the $K^*\pi^-$ branch lost about 30% of their original intensity when including the $J^P = 3^+$ waves (black). The $K^*(892)\pi^-$ wave became barely significant in the higher mass range.

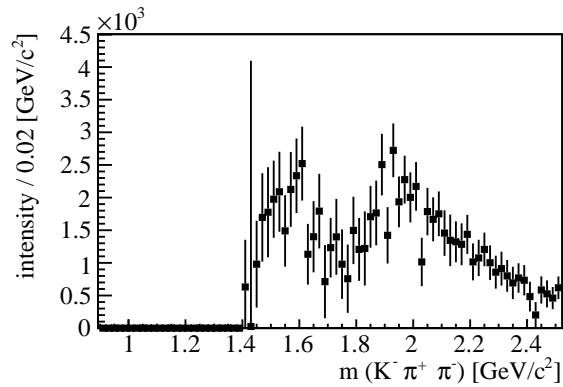


Figure 7.17: The flat wave in the proposed wave set has a dip at the same region where the $J^P = 1^-$ intensity peak was observed.

7.5 KINEMATIC VALIDATION

A very important check of the PWA fit result is the predictability of the fitted model in terms of angular distributions. The flat phase space simulation, same as used for integral calculations, was weighted according to the determined intensity distributions. Naturally the accepted MC events were considered as real data were compared.

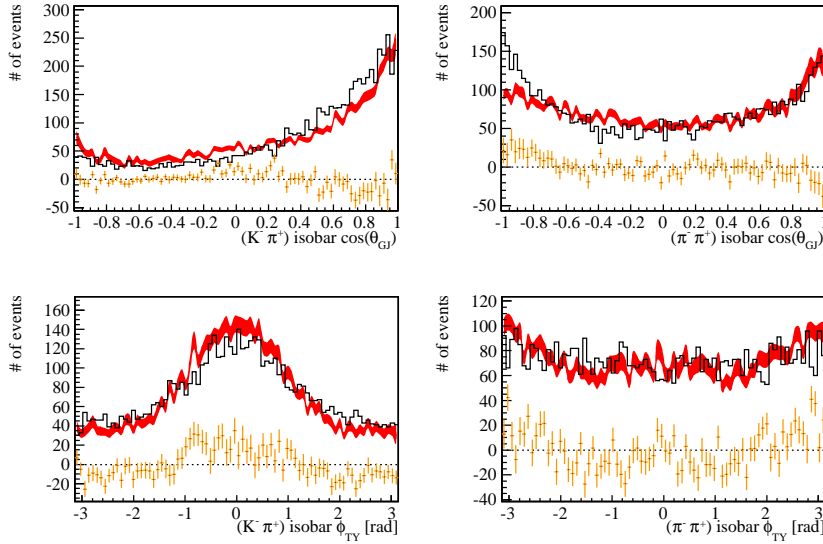


Figure 7.18: Comparison of real angular distributions (black) with predicted from weighted MC data (red) in the GJ-frame. The difference between both is plotted orange. One invariant mass bin $1.26 \leq m(K^- \pi^+ \pi^-) [\text{GeV}/c^2] < 1.28$ is exemplary shown for the low mass region where the $J^P = 1^+$ wave is dominant. Left the $(K^- \pi^+)$ -isobar track combination right the $(\pi^+ \pi^-)$ -isobar track combination. For a discussion see the text.

Most valuable information was found in the angular track distributions in the GJ-frame. Those low mass distributions 7.18 show a well agreement between the weighted MC and real data for both isobar branches. The $\cos(\Theta_{GJ})$ angular distribution of the $(\pi^+ \pi^-)$ -isobar is a bit more dominant in the backward direction in real data in contrast to the forward trend of the $(K^- \pi^+)$ -isobar. Φ_{TY} illustrates very good the importance of acceptance corrections in the $K^- \pi^+ \pi^-$ event selection. The observed bump in the $(K^- \pi^+)$ -branch is well reproduced by accepted MC data. This feature was already seen in the corresponding angular acceptance distribution 6.21. It would not be possible to model this distribution by a partial wave. As a comparable structure was missing in the $(\pi^+ \pi^-)$ -branch a fit would automatically prefer the $(\pi^+ \pi^-)$ -isobar decay without the acceptance correction. In fact a wrongly modelled acceptance correction could at least partially explain the differences between the observations in COMPASS data and results published by the ACCMOR collaboration.

The agreement between weighted MC distributions and real data was worse for the high mass region. Again an exemplary invariant mass bin

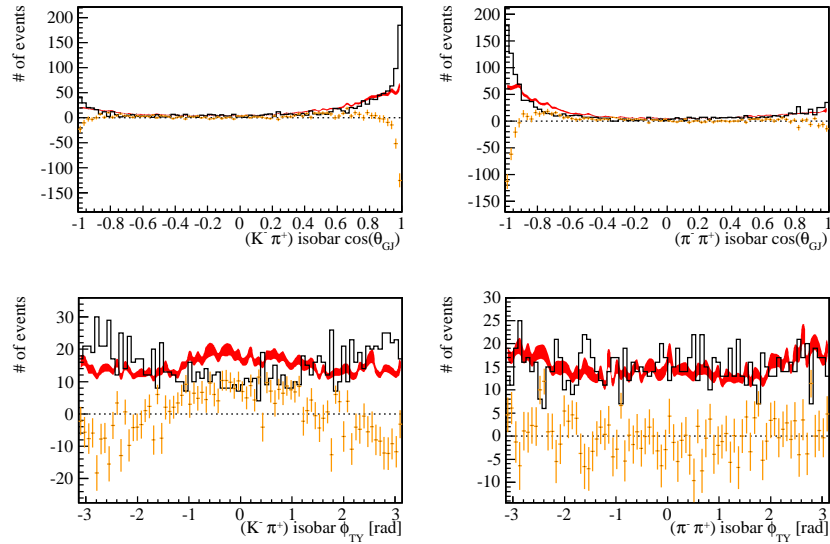


Figure 7.19: Comparison of real angular distributions (black) with predicted from weighted MC data (red) in the GJ -frame. The difference between both is plotted orange. One invariant mass bin $2.50 \leq m(K^- \pi^+ \pi^-) [\text{GeV}/c^2] < 2.52$ is exemplary shown for the high mass region where the $J^P = 2^-$ wave is dominant. Left the $(K^- \pi^+)$ -isobar track combination right the $(\pi^+ \pi^-)$ -isobar track combination. For a discussion see the text.

$2.50 \leq m(K^- \pi^+ \pi^-) [\text{GeV}/c^2] < 2.52$ was chosen for the distributions 7.19. The nature of the $(\pi^+ \pi^-)$ -isobar decay changed and is mainly pointing backwards to small $\cos(\Theta_{GJ})$. This is not replayed by PWA fit results. It was only partially possible to compensate this difference by inclusion of higher spins. This backward asymmetry can explain the sensibility of $J^P = 2^-$ waves and $J^P = 3^+$ waves to changes in the partial wave set (recall figure 7.16). Also the $(\pi^+ \pi^-)$ -branch was affected to the other direction.

One possible explanation is motivated by the difference between the Φ_{TY} angle of the $(K^- \pi^+)$ -isobar and the real data in the same mass bin. While real data shows a dip MC data still predicts a bump originating from the RICH acceptance. It was already pointed out in section 6.5 that RICH efficiencies seemed to be underestimated. Figure 6.12 was an indication for this finding.

But this can only be a partial explanation. MC simulations of the flat phase space predicted for both isobar branches an increased forward acceptance in $\cos(\Theta_{GJ})$ (see figure 6.21). In the real data distributions $(\pi^+ \pi^-)$ track combinations were pointing preferably backward. The other source for this angular asymmetry could be centrally produced events as discussed in the following.

7.6 SYSTEMATIC INFLUENCES

Systematic influences on PWA results had various sources. The most important were pinned down to be the possibility for centrally produced events where the scattered beam kaon is still carrying significant amount of the beam energy and misidentified pions in the beam producing resonances with three charged pions in the final states. For an estimation of influences by incoherent sources as spin flipping recoil protons fits of rank one were additionally performed.

7.6.1 Central production

Centrally produced events are classified by a rapidity gap between the centrally produced system and the beam particle (see section 1.3.3). The analysis of $K^- \pi^+ \pi^-$ final states had therefore the advantage to know which particle is the beam candidate for a spectator only emitting a pomeron and no final state interaction. In case of $\pi^- \pi^+ \pi^-$ analysis one has to guess and is usually taking the *fastest* particle in terms of X_F .

The disadvantage on the other hand was the big influence of the RICH momentum acceptance. The acceptance of rapidity distributions 6.20 was always dropping in the mean region introducing an artificial rapidity gap. This acceptance distributions were directly used for acceptance correction of the rapidity distributions 7.20.

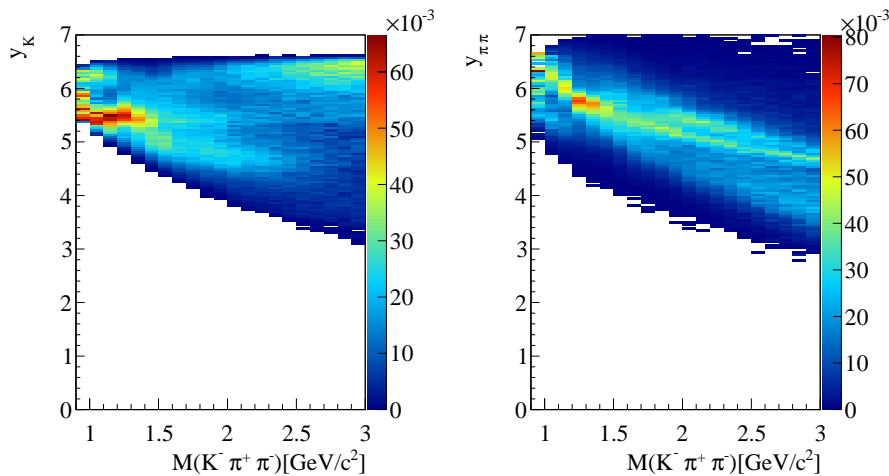


Figure 7.20: Acceptance corrected rapidity distributions of K^- tracks (left) and $(\pi^+ \pi^-)$ -track combinations (right) as a function of the $K^- \pi^+ \pi^-$ mass. Each bin in $m(K^- \pi^+ \pi^-)$ was normalized in addition to the $K^- \pi^+ \pi^-$ bin with the largest sum of weights. A comparison between the kaon and the $\pi^+ \pi^-$ system shows a rapidity gap appearing for high masses above $2.2 \text{ GeV}/c^2$, an indication for central production.

It was observed that the $\pi^+ \pi^-$ system was constantly getting slower with increasing an invariant $K^- \pi^+ \pi^-$ mass. Same is visible for the rapidity distribution of the kaon for masses up to $2 \text{ GeV}/c^2$. Above kaons

seem to cluster at high rapidities. The difference between the $\pi^+\pi^-$ cluster and the $(\pi^+\pi^-)$ -rapidity band reveals a rapidity gap dominating at masses above $2.5 \text{ GeV}/c^2$. It becomes clear that a fast kaon was therefore shifting a $(K^-\pi^+)$ -track combination into forward directions while the slow $\pi^+\pi^-$ system was pointing backwards in the GJ -frame.

Knowing this systematic uncertainty does not solve automatically the problem how to deal with it. A simple cut on the difference between the $(\pi^+\pi^-)$ and K^- rapidities had a dramatic impact on the angular distributions. Even acceptance correction would not be able to reconstitute the missing information. The best solution would most probably be to *model* this angular behaviour as a separate partial wave what needs unfortunately major interventions in the overall analysis framework. As a first estimation partial waves with high spins could be included. They gather those background intensities and rectify the distributions of waves with lower spins.

7.6.2 Background by pions in beam

In section 5.5 it was demonstrated that $K^-\pi^+\pi^-$ invariant mass spectra showed weak resonant behaviour for π^- in the initial state. A beam pion misidentified as a kaon produced mostly $\pi^-\pi^+\pi^-$ background leading to a smeared $\pi^-\pi^+\pi^-$ distribution. That distribution was smeared out to higher masses when assuming to have one kaon track in the final state. It is known from chapter 5 to have below 10% pion background that cannot be removed completely. In order to estimate the influence of those pions on the PWA results a dedicated PWA was performed with an event selection containing 10% additional pion background.

It was found that no wave was specially affected by the additional contribution and shapes remained stable. Moreover it was found that all total intensities gained around 8% in intensity apart from the $J^P = 2^-$ spin total with only 4.6% and the 2^+ spin total with 12.3%. Most intensity was gathered by the flat wave with an increase by 20.7% in intensity.

An other observation was that $(\pi^+\pi^-)$ -isobar branches gained significantly more intensity in the partial waves than $(K^-\pi^+)$ -isobar branches. Exemplary the two strongest $J^P = 2^-$ partial waves are shown in figure 7.21. This is understood as the invariant $\pi^+\pi^-$ mass distributions were not affected by wrong mass combinations in contrast to the invariant $K^-\pi^+$ mass distributions that were diluted by $\pi^+\pi^-$ background (compare figure 5.17 and 5.18). The assumption to see a $\rho(770)$ and $f_2(1270)$ resonance became more likely than to see a $K^*(892)$ and $K_2^*(1430)$ resonance. Background from pions is then expected to shift the branching ratios of resonances to $(\pi^+\pi^-)$ resonances. In this case coupling to the $f_2(1270)K^-$ wave was 2% stronger than without the additional three pion background. This value varied for the different partial waves and is expected to change also with a mass dependent fit result as phase motion was not taken into account yet.

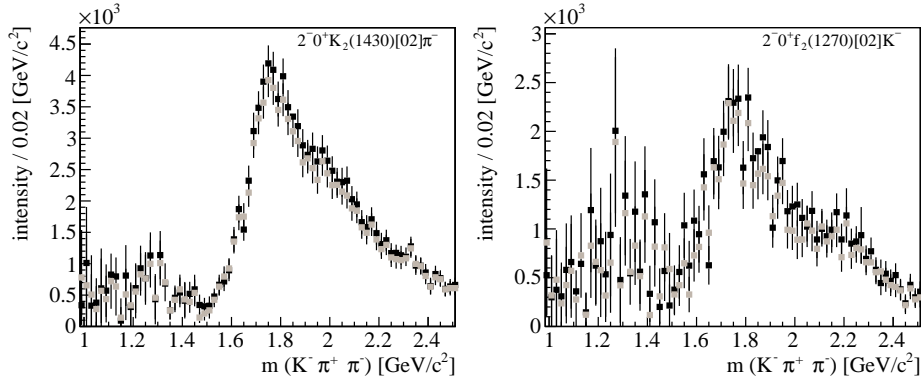


Figure 7.21: The intensity distribution of the main $J^P = 2^-$ waves (gray) compared to a PWA result with additional 10% pion background in the beam (black). The overall shape was not distorted. The K branch gained 4.9% in intensity. The $\rho(770)$ branch has increased by 6.7%. Similar behaviour was observed in other partial waves.

7.6.3 Incoherent sources

Consider the parametrization 7.1 of the cross section once again to recall the role of the rank in the fit. A fit of a rank 1 forces all partial waves to interfere. The coherence between the waves becomes per definition 1. This assumption would hold if no other incoherent process would be observed then only diffractive scattering into $K^- \pi^+ \pi^-$ with a recoil proton.

That this assumption did not hold in our data is visible when comparing a fit of rank 1 with a fit of rank 2 like presented here. In addition to the wave set 7.2 the $1^+ 0^+ f_0(600) [1_0]$ K^- wave was included to demonstrate an additional interesting feature.

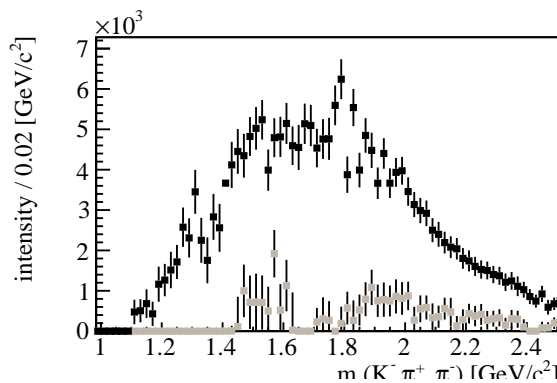


Figure 7.22: The flat wave for a rank 2 fit (grey) compared to a rank 1 fit (black). The removal of incoherent fit parameters reduced the statistical uncertainty but increased the intensity of the flat wave significantly.

The intensity 7.22 of a flat wave in both ranks exhibits two general features. For a rank 1 fit a quite large intensity of the flat wave was observed.

The partial wave model was not able to describe the angular distributions fully so intensity was caught by the flat wave. This picture changed with the increase of the rank to 2. The spin density matrix 7.3 grows quadratic with the rank and allows two different complex production amplitudes adding incoherently to each other. Obviously a model with a larger number of free parameters is better describing angular distributions by partial waves.

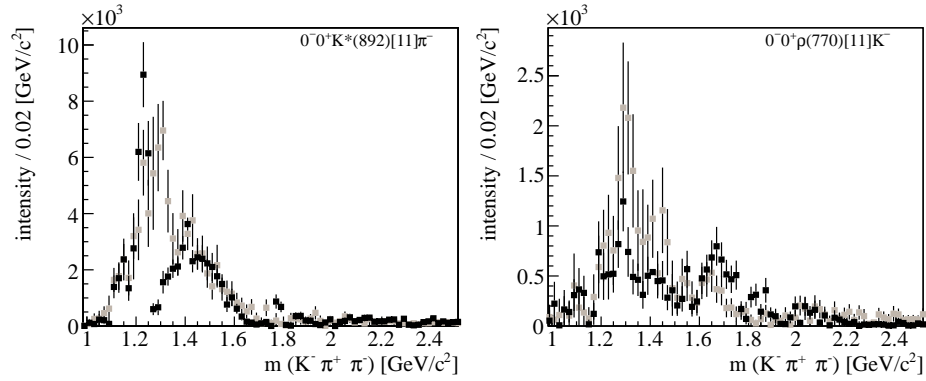


Figure 7.23: $J^P = 0^-$ partial wave intensities for a fit of rank 1 (black) compared to a fit of rank 2 (grey). The $(K^-\pi^+)$ -isobar branch suffers from strong destructive interference indicating an incoherent production mechanism. The $(\pi^+\pi^-)$ -isobar branch is less affected. The inclusion of a $(\pi^+\pi^-)$ -S wave seems to stabilize the intensity.

The intensity distributions 7.23 show exemplary two $J^P = 0^-$ waves, one for each branch. While intensity in the $(K^-\pi^+)$ -branch is breaking down the $(\pi^+\pi^-)$ -branch seems to be less affected. A look to the wave set 7.2 explains this behaviour. The $(\pi^+\pi^-)$ -branch contained the $(\pi^+\pi^-)$ -S wave forming also a $J^P = 0^-$ wave and allowed constructive interference. The $(K^-\pi^+)$ -branch was missing the S-wave as the fit was stabilized offering only one S-wave.

More or less similar observations were made in other partial wave intensities. Most waves kept their shape but were reduced in the total intensity, some waves nearly disappeared like the previously included $1^+ 0^+ f_0(600) \begin{bmatrix} 1 \\ 0 \end{bmatrix} K^-$ wave. All in all the fit became very unstable. Solutions were not clear. Many local minima produced ambiguous fit results. A fit with rank 2 was stable and the applied wave set could explain the angular distributions nearly without any intensity in the flat wave. Higher ranks were therefore not necessary.

7.7 SUMMARY

To understand and distinguish the structure in the invariant mass distributions of the diffractive $K^-\pi^+\pi^-$ channel at COMPASS, methods of mass independent partial wave analysis in the spin density matrix approach were adapted. With the help of the *rootpwa* package, which had to be extended and modified for the analysis of strange mesons, a large number

J^P	mass [GeV/c ²]	possible state
0^-	1.30	K(1460)
1^+	1.25	$K_1(1270)$
1^+	1.35	$K_1(1400)$
1^+	1.80	$K_1(1650)$
1^-	1.75	$K^*(1680)$
2^+	1.44	$K_2^*(1430)$
2^-	1.70	$K_2(1770)$
2^-	1.85	$K_2(1820)$
2^-	1.9 – 2.2	several

Table 7.4: Summary of observed resonant structures in the partial waves. The invariant $K^-\pi^+\pi^-$ mass was estimated by a combination of the peak intensity and the inflection points of the second derivative in the relative phase motion. Possible states as summarized in the review of particle physics [11] are given in addition.

of fits was performed. The systematic studies concluded a final partial wave set able to describe main features of observed variables. Only the very high mass region deviated in the behaviour from the model of a simple diffractive decay chain as signature by central production was present there.

The intensity distributions and their relative phase motions showed resonant structure summarized in table 7.4. Apart from the $J^P = 1^-$ state all other waves gave a consistent picture of strange meson spectroscopy in the diffractive production mechanism as it is summarized in the PDG review [11]. The absence of a further symmetry, able to distinguish between isospin $I = 1/2$ singlet and triplet states emerged in mixed states in the 1^+ and 2^- waves.

The quality of the fit was only tested for the $J^P = 2^+$ $K_2^*(1430)$ resonance as it had a well separated intensity. A fit of a coupled Breit-Wigner function to the intensity distributions in both decay channels showed good agreement with previous measurements for the mass, width and the isospin corrected branching ratio.

Apart from the clean $J^P = 2^+$ resonance, all other channels need a treatment in the mass dependent framework to decompose overlapping resonances and background contribution. The necessary infrastructure was under construction by Sebastian Neubert but not yet ready for an application to the $K^-\pi^+\pi^-$ data. Nevertheless a strategy for such a fit was presented based on observations in the mass independent fit results.

CONCLUSION

The hadron program of the [COMPASS](#) collaboration was dedicated in large parts to hadron spectroscopy. A huge variety of single diffractive and central processes were addressed with a minimum bias trigger. Special emphasis was put there on the detection of a recoil proton with a scattered excited particle. [COMPASS](#) took data in the years 2008 and 2009 with negatively and positively charged hadron beams on a 40 cm liquid hydrogen target. The beam with 190 GeV/c particle momentum was consisting of pions (anti)protons and a small admixture of kaons of about 2.4%.

To distinguish between those beam particles two [CEDAR](#) detectors were set-up 30 m upstream of the target and equipped with a full read out chain for the analogue signal of the photo multipliers. Since it turned out that an operation in a high energetic beam with large beam divergence was difficult, strategies had been developed to distinguish kaons from pions with a high purity of better than 80%. The cost for the high purity was a lowered angular acceptance, so only 30% of all kaons were identified. Promising likelihood methods that are taking beam divergence into account, are expected to increase the efficiency to more than 80%. Those had been under development.

The identification of an initial state kaon allowed, in parallel to the dominating $\pi^- + p \rightarrow \pi^- \pi^+ \pi^- p_{recoil}$ process, the measurement of excited kaons in $K^- + p \rightarrow K^- \pi^+ \pi^- p_{recoil}$ events. It was demonstrated in this thesis how to filter 270 000 final state events with a high quality, showing typical structures in the invariant mass spectra. As only data from 2008 were processed it is presumed to double the number of events with the inclusion of data from 2009.

The cost for a high purity like a negligible contamination of wrongly assigned $K^- \pi^-$ masses, was a distorted acceptance in nearly all variables. Intensive studies on the [RICH PID](#) of the final states emerged in pure solutions but only in a narrow track momentum acceptance region. Those [RICH](#) efficiency and purity results were moreover used as a direct input to the [MC](#) simulations of a diffractive $K^- \pi^+ \pi^-$ process in a flat phase space decay. 44 million events of those were generated and passed through a simulation chain that was modified and extended by several detector responses such as the [CEDAR](#), [RPD](#) and the [RICH](#) detector. The results confirmed the large influence of the [RICH](#) cuts on the acceptance of the analysed $K^- \pi^+ \pi^-$ channel.

The proper simulation of the flat phase space was one of the key points for an acceptance corrected partial wave analysis of resonances decaying into the $K^- \pi^+ \pi^-$ final state. The *rootpwa* package was co-implemented and applied for a mass independent fit of partial wave amplitudes to the data. Extensive systematic studies with many iterations of addition

and removal of different partial waves led to a final partial wave set describing the features of the $K^-\pi^+\pi^-$ decay in all important variables. The comparison of the fit results with real data showed good agreement up to an invariant mass of $m(K^-\pi^+\pi^-) = 2 \text{ GeV}/c^2$. The discrepancy above was traced down to centrally produced background processes not describable by the simple decay chain in the [PWA](#).

The mass independent fit results were viewed and compared with results by the [ACCMOR](#) collaboration quoted to be the best analysis so far. Many features observed by the [ACCMOR](#) collaboration were also seen in [COMPASS](#) data. Apart from the well known resonances as $K_1(1270)$, $K_1(1400)$ and $K_2^*(1430)$ evidence for resonant structure in the $J^P = 0^-$ wave was found. A candidate for a $K_1(1650)$ in the 1^+ D-wave was observed as well as a resonance in $J^P = 1^-$ waves. The latter spin parity wave was not included in previous analyses. The high mass region was found to be dominated by $J^P = 2^-$ waves, sensitive to background from central production. But even with twice the number of events in the high mass region compared to the [ACCMOR](#) analysis, it was not possible to distinguish contributing resonances by eye as those are too broad. Final conclusion on the contributing states and their properties can be only drawn with a mass dependent fit to the presented results. The necessary infrastructure for this task was under development by Sebastian Neubert at the TU-munich.

Once more the potential of the [COMPASS](#) experiment was demonstrated to contribute significantly to results in the field of meson spectroscopy. It can be expected to change or at least to improve the picture in the isospin $I = 1/2$ sector that is still poorly explored. Furthermore the number of $K^-\pi^+\pi^-$ events will probably be doubled by the analysis of the run in the year 2009 and a mass dependent fit analysis will finally give the information about particle masses and widths contributing to the invariant $K^-\pi^+\pi^-$ mass spectrum observed in [COMPASS](#) data.

BEHIND THE CURTAINS

This appendix contains deeper knowledge of some topics discussed in this thesis. Although important to reproduce some results those formulae are destructing the text flow when just reading by. The reader is referred to this appendix by time if interested on details. These sections are not very important to understand results presented in this thesis.

A.1 MORE DETAILS ON PARTIAL WAVE ANALYSIS

The methods of partial wave analysis were developed since more than 35 years. It is natural that many details, nomenclature and methods changed and improved over the years. The basic idea was kept so far the same. Namely expressing a process measured with continuous variables such as particle momenta and angles by interfering orbital functions with discrete quantum numbers as variables.

The formalism for the 3-particle analysis was derived in detail in [84] providing many useful comments to the user that cannot be covered fully in this thesis. For a more general disquisition on this topic the user is referred to papers by S. U. Chung like [82] used here. Finally technical details on the specific formalisms used are given in [89] that were implemented in the software package described in [90]. For an up to date overview one might also consider [91].

The following sections were written with the intent to provide a feeling for the concepts used for the analysis and to summarize important formulas derived and discussed already in a condensed form in the sources mentioned before. It is recommended to read chapter 7 first once before going into details presented here.

A.1.1 *The fully differential cross section of the diffractive process*

It is mandatory to introduce first the helicity basis before describing the diffractive process shown in figure A.1 as a product of amplitudes. Parts of the amplitudes can be calculated using knowledge about some sub processes. Others have to be fitted to the data.

A PROPER BASIS FOR PARTICLE STATES Consider a free particle in motion of a mass m and the spin \vec{J} . The state of this particle can be completely described in the helicity basis by

$$|\vec{p}mJ\lambda\rangle \tag{A.1}$$

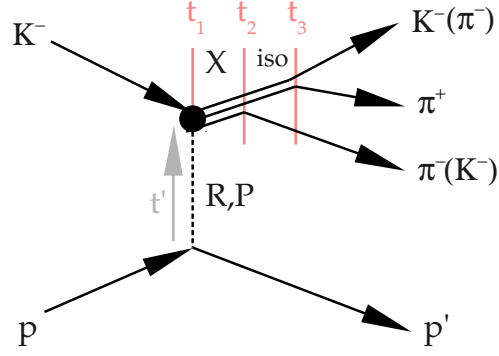


Figure A.1: Feynmanlike graph for diffractive dissociation of kaons on a nuclear target in the t -channel. The time scale is from left to right showing three important time points discussed in the text.

where \vec{p} the three-momentum of the particle is, $J = |\vec{J}|$ and λ the corresponding spin projection on the z -axis in the rest frame of this particle are. The difference to the usually better known canonical (orbital) basis

$$|\vec{p}mJM\rangle, \quad (\text{A.2})$$

is only the quantization axis of the spin projection M , in both cases the z -axis. The transformation into the rest frame in the helicity basis rotates the z -axis into the direction of the particles momentum and the y -axis orthogonal to the $\hat{z} \times \hat{p}_z$ plane while the orientation of axes in the canonical basis does not change.

TOWARDS THE AMPLITUDE TO THE CROSS SECTION The amplitude f_{fi} for the diffractive dissociation into $K^- \pi^+ \pi^-$ (see figure A.1)

$$K_{\text{beam}}^- + p \rightarrow K^- + \pi^- + \pi^+ + p_{\text{recoil}} \quad (\text{A.3})$$

is described by a transition amplitude \mathcal{M}_{fi} from the initial state $|i\rangle$ to the final state $|f\rangle$:

$$\begin{aligned} f_{fi} &\equiv \langle f | \mathcal{M}_{fi} | i \rangle \\ &= \langle \vec{p}_{K^-} \vec{p}_{\pi^+} \vec{p}_{\pi^-}, \vec{p}_{p_{\text{recoil}}} \lambda_{p_{\text{recoil}}} | \mathcal{M}_{fi} | \vec{p}_{K_{\text{beam}}^-}, \vec{p}_p \lambda_p \rangle \end{aligned} \quad (\text{A.4})$$

The helicity basis (see eq. A.1) was already chosen not writing the mass state and the spin down. In addition it is included that initial and final state mesons are spinless and therefore $\lambda = 0$. The comma separates the meson part of the baryon as it is assumed to have no final state interaction between the recoil proton and the resonance. This assumption is mostly based on the observation that the final state rapidity (energy) of the recoil proton is many orders lower than the one of the resonance and thus the upper vertex in figure A.1 can be considered to factorize.

The cross section can be written as

$$\sigma \propto \sum_i \sum_f |f_{fi}|^2 \quad (\text{A.5})$$

is given by

$$\sigma(\tau, m) \propto \sum_{\epsilon=\pm 1} \sum_{r=1}^{N_r} \left| \sum_i^{N_{\text{waves}}} T_{ir}^\epsilon(m_X) A_i^\epsilon(\tau) \right|^2 \quad (\text{A.6})$$

as a sum over all amplitudes consisting of a production amplitude $T_{ir}^\epsilon(m_X)$ for the time point t_1 shown in figure A.1 and a decay amplitude $A_i^\epsilon(\tau)$ for the time points t_2 and t_3 . The reader is here referred again to the literature mentioned above as no further assumptions are made there. The phenomenological discussion is found in chapter 7 and is not repeated here. The calculation of the decay amplitude based on spin couplings up to a certain extend is discussed in the following.

TWO PARTICLE STATES The big advantage of the helicity basis is the simplified construction of the coupling of two spin-states. Consider first two particles with the helicities λ_1 and λ_2 coupling to a total spin J and a spin projection M . Helicities are invariant under Lorentz boosts as the quantization axis is along this boost (see section A.1.4 for details to the rest frames). The coupled helicity is then given by

$$\lambda = \lambda_1 - \lambda_2 \quad (\text{A.7})$$

taking already the back to back orientation in a latter decay process into account in such a way that helicity quantum numbers remain positive. Note also that an orbital angular momentum $\vec{\ell}$ between those particles with a spin $\vec{S} = \vec{s}_1 + \vec{s}_2$ in the canonical basis $|JM\ell S\rangle$ is fully described by the total spin \vec{J} in the helicity formalism. This is due to the fact that $\vec{\ell} \cdot \vec{p} = 0$.

The coupled spin state can be shown [82] to be

$$|JM\lambda_1\lambda_2\rangle = \sqrt{\frac{2J+1}{4\pi}} \int \int d\phi d\cos\theta D_{M\lambda}^{J*}(\phi, \theta, 0) |\phi\theta\lambda_1\lambda_2\rangle \quad (\text{A.8})$$

with ϕ and θ the spherical angles of the momentum of the particle. The state is therefore specified by intensity distributions following D-Wigner functions of the rotation matrices $D_{M'M}^J(\phi, \theta, \gamma)$ [92] depending on euler angles. Masses are now left out for a better readability.

CONNECTING THE CANONICAL AND HELICITY BASIS The simple projection of the canonical (orbital) state into a helicity state is determined by evaluation of D-function products [82] and gives the recoupling constant

$$\langle JM\lambda_1\lambda_2 | J'M'\ell S \rangle = \left(\frac{2\ell+1}{2J+1} \right)^{\frac{1}{2}} (10s\lambda | J\lambda) (s_1\lambda_1 s_2\lambda_2 | S\lambda) \delta_{JJ'} \delta_{MM'} \quad (\text{A.9})$$

where Clebsch-Gordan coefficients $(s_1 m_1 s_2 m_2 | SM)$ in the Condon and Shortley [92] convention are used. Now it is easily possible to expand a canonical basis into the helicity one and vice versa.

AMPLITUDES FOR TWO BODY DECAYS The decay amplitude for a particle with spin J decaying into two particles with momenta \vec{p} for particle 1 and $-\vec{p}$ for particle 2 (back to back decay) and their corresponding helicities λ_1 and λ_2 is

$$A = \langle \vec{p}\lambda_1 - \vec{p}\lambda_2 | \mathcal{M} | JM \rangle \quad (\text{A.10})$$

with \mathcal{M} the invariant transition amplitude between those two states. This relation is expanded to the helicity basis in order to benefit of the derived coupling properties.

$$\begin{aligned} A &= 4\pi \left(\frac{m}{p} \right)^{\frac{1}{2}} \langle \phi \theta \lambda_1 \lambda_2 | JM \lambda_1 \lambda_2 \rangle \langle JM \lambda_1 \lambda_2 | \mathcal{M} | JM \rangle \\ &= \sqrt{\frac{2J+1}{4\pi}} F_{\lambda_1 \lambda_2}^J D_{M\lambda}^{J*}(\phi, \theta, 0) \end{aligned} \quad (\text{A.11})$$

The "helicity decay amplitude"

$$F_{\lambda_1 \lambda_2}^J = 4\pi \left(\frac{m}{p} \right)^{\frac{1}{2}} \langle JM \lambda_1 \lambda_2 | \mathcal{M} | JM \rangle \quad (\text{A.12})$$

is here introduced taking the available phase space into account for a particle of mass m decaying to two particles with momenta p .

This amplitude can be once again expanded now into the canonical (orbital) basis in the spin formalism using the recoupling constant [A.9](#) and becomes [\[82\]](#)

$$F_{\lambda_1 \lambda_2}^J = \sum_{\ell, s} \left(\frac{2\ell+1}{2J+1} \right)^{\frac{1}{2}} a_{\ell S}^J(m, p) (10S\lambda | J\lambda) (s_1 \lambda_1 s_2 - \lambda_2 | S\lambda) \quad (\text{A.13})$$

finally expressing the decay in terms of so called partial-wave amplitudes

$$a_{\ell S}^J(m, p) = 4\pi \left(\frac{m}{p} \right)^{\frac{1}{2}} \langle JM \ell S | \mathcal{M} | JM \rangle. \quad (\text{A.14})$$

This amplitude describes the probability of a one particle state $|JM\rangle$ to decay to a state $|JM\ell S\rangle$ consisting of two particles coupling to the same J and M but in addition having a spin \vec{S} and an orbital angular momentum $\vec{\ell}$ between those. Notice that this complex amplitude is described in the canonical (orbital) basis allowing a usage of familiar spin coupling formalisms.

PARAMETRIZATION OF THE DECAY PROCESS Let's consider figure [A.1](#) again to express the full decay amplitude in [7.1](#) for the time points t_2 and t_3 as a product of decay amplitudes.

$$A_i^\epsilon = A_{i, t_3}^\epsilon A_{i, t_2}^\epsilon \quad (\text{A.15})$$

with the specific forms given by equation [A.11](#) with [A.13](#). The amplitude chain is now evolved recursively:

A_{i,t_3}^ϵ describes the probability of an isobar to decay into a negative final state kaon (pion) and a positive pion. We have to assume to know the isobars that are forming the invariant $K^-\pi^+(\pi^+\pi^-)$ mass spectra and we refer to results obtained in other experiments and summarized in the [PDGs review \[11\]](#). The input used are masses, widths and spins of those particles. In most cases we can assume $a_{\ell s}^J(m, p)$ to have a dominating resonant behaviour. Different decay channels and couplings can be taken into account as discussed in section [A.1.2](#).

A_{i,t_2}^ϵ is treated very similarly to A_{i,t_3}^ϵ apart from one important difference: We do not know the mass, width, coupling constant nor the spin of this state and the aim is to derive those properties from data. The possible spins for this state are constructed from available isobar bachelor particle spin couplings by introducing an orbital angular momentum between those particles. The mass, width and intensity can be derived by a mass dependent χ^2 fit to the data from the mass independent fit where no resonant shape is needed to describe the data (see chapter [7](#)).

A.1.2 Parametrizations of resonances

The parametrization of the resonant behaviour of amplitudes depends on the physical aspects in a particular channel. The decay process into two particles is in most cases parametrized with simple relativistic Breit-Wigner functions. This works for single resonances or multiple separated resonances but more advanced techniques have to be applied for cases where particles decay into different partially not measured but dominant channels or several overlapping resonances appearing in one channel. An overview of the most commonly used parametrizations is given here.

RELATIVISTIC BREIT-WIGNER FUNCTION A simple relativistic Breit-Wigner distribution is used of the form

$$a_{\ell s}^J(m, p) \equiv \frac{m_0 \Gamma_0}{m_0^2 - m^2 - i m_0 \Gamma(m)} \quad (\text{A.16})$$

with

$$\Gamma(m) = \Gamma_0 \left(\frac{F_\ell(p)}{F_\ell(p_0)} \right)^2 \left(\frac{m_0}{m} \frac{q}{q_0} \right). \quad (\text{A.17})$$

The amplitude depends thus not only on the invariant mass m_0 and the width Γ_0 of the particle but moreover a phase space factor is included. It depends mostly on the break up momenta q and $q_0 = q(m_0)$ in the rest frame. It can be easily calculated from the energy balance

$$E_0 = E_1 + E_2 ; E^2 = p^2 + m^2$$

with a particle 0 decaying back to back into particle 1 and 2

$$\vec{p}_1 = -\vec{p}_2$$

leading to

$$\Rightarrow p = \sqrt{\left| \frac{m_0^4 + m_1^4 + m_2^4 - 2(m_0^2 m_1^2 + m_1^2 m_2^2 + m_2^2 m_0^2)}{4m^2} \right|} \equiv q \quad (\text{A.18})$$

Notice also the so called Blatt-Weisskopf barrier factors [93] $F_\ell(p)$ describing the asymptotic behaviour when reaching thresholds. The factors are connected with spherical Hankel functions depending on the orbital angular momentum ℓ between the two decay particles.

The simple Breit-Wigner ansatz violates the physical unitarity in a scattering/decay process as coupling between different final states is neglected. To overcome this problem the \mathcal{S} -matrix approach has been developed.

K-MATRIX APPROACH A detailed discussion of the \mathcal{K} -matrix formalism is given in [86]. Starting from a \mathcal{S} -matrix

$$\mathcal{S}_{fi} = \langle f | \mathcal{S} | i \rangle \quad (\text{A.19})$$

connecting final states and initial states for a scatter process in a unitarity conserving way a transition operator \mathcal{T} is defined though

$$\mathcal{S} = \mathcal{J} + 2i\mathcal{T} \quad (\text{A.20})$$

with the identity operator \mathcal{J} . It is shown that a \mathcal{K} -matrix defined by

$$\mathcal{K}^{-1} = \mathcal{T}^{-1} + i\mathcal{J} \quad (\text{A.21})$$

must be real and symmetric.

Several forms of the \mathcal{K} -matrix were proposed, specialized for different applications. The origin in the \mathcal{S} -matrix connects always all output channels preserving unitarity. In addition one is able to place several overlapping resonances as poles describing the phase motion between them. In case of a simple decay of a s-channel resonance the \mathcal{K} -matrix degenerates to a so called \mathcal{P} -vector as only one input channel is considered. A further important application is the Flatté-formula, describing an opening of channels with thresholds in the resonance region. In all cases non resonant polynomial background can be included allowing to split the resonance in a fit off.

The \mathcal{K} -matrix plays an important role in the mass dependent fitting of resonances decaying into $K^-\pi^+\pi^-$ final states. On the one hand channels with strongly overlapping resonances of spin singlet and spin triplet $q\bar{q}$ states have to be described. On the other hand the $K^-K^+K^-$ -channel is not measured simultaneously. This channel reduces the phase motion of the determined partial waves and has to be taken into account in a mass dependent fit in order to retrieve correct branching ratios [1].

THE $(\pi^+\pi^-)$ -S WAVE The review of particle physics by the PDG summarized the very controversially discussed status of the $(\pi^+\pi^-)$ -S wave. The quantum numbers of the vacuum ($J^{PC} = 0^{++}$) make it very difficult

to measure clean resonances well separated from background effects. Many resonances are found in the f_0 regime and specially the low mass region is occupied by a broad resonance more often referred as the σ than the $f_0(600)$. The latter nomenclature was used in this thesis to place this resonance in line with other isospin $I = 0$ $q\bar{q}$ resonances although the possibility of multi quark constellations should be considered [11].

For the PWA the origin of those resonances is more or less negligible and only intensity and phase motion should be correctly parametrized. In most cases $f_0(600)$ is described as a broad wave following physical measurements in $\pi\pi$ scattering experiments.

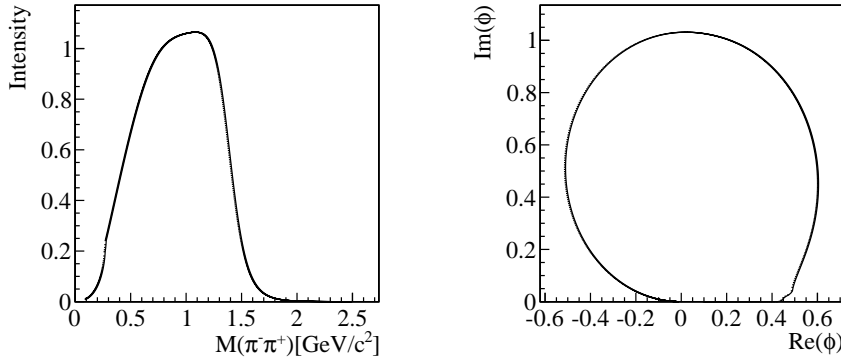


Figure A.2: The Argand diagram of the $(\pi^+\pi^-)$ -S wave as parametrized in [86] by poles in the K-matrix approach.

The Argand-diagram and intensity distribution A.2 of the $(\pi^+\pi^-)$ -S wave used for the PWA in this thesis shows a smooth intensity phase variation and is modelled according to [86]. It is a superposition of several poles (resonances) in the K-matrix approach. A mass range starting from threshold up to $1.5 \text{ GeV}/c^2$ is described without the interference with the $f_0(980)$ resonance that is in fact a very narrow one and was therefore quite well determined.

When it comes to the physical interpretation of mass dependent fit results contribution to the $(\pi^+\pi^-)$ -S wave from single resonances is not negligible any more. Branching ratios to the $(f_0(600) \text{ K})$ waves should be ideally separated into several parts containing the various resonances. In practise this becomes unfortunately difficult.

THE $(K^-\pi^+)$ -S WAVE The picture in the $(K^-\pi^+)$ -S wave is even less clear. For a long time it was disputed if a $K_0^*(800)$ or κ wave is existing or not [86]. Even though strange particles cannot be produced out of the vacuum, measurement of the $K^-\pi^+$ scattering amplitude is a challenging task. First results delivered by the Large Angle Superconducting Solenoid (LASS) collaboration in formation experiments gave first hints for the shape of this wave [16]. PWA was performed and decoupled an intensity with the corresponding phase motion of the $(\pi^+\pi^-)$ -S wave from other partial waves. A composition of individual resonances was not discussed.

Today it is still not clear if such a resonance exists or not. A resonance of several hundred MeV/c^2 width in the region between $650 \text{ MeV}/c^2$ and $900 \text{ MeV}/c^2$ was quoted to be seen. The mean values of those results in a Breit-Wigner shaped resonance were used as a first attempt to provide a counterpart to the $(\pi^+\pi^-)$ -S wave.

A.1.3 The reflectivity basis

The reflectivity basis [94] was introduced to manifestly implement parity conservation. It is expressed by the behaviour of a spin basis under reflections with an own quantum number called the reflectivity ϵ . The basis is defined via

$$|\epsilon JM\rangle = [|\epsilon JM\rangle - \epsilon P(-1)^{J-M}|\epsilon J - M\rangle] \theta(M). \quad (\text{A.22})$$

with J the total spin, M a spin projection in the rest frame of this state (may be canonical or helicity basis) and P the parity of a state. The normalization factor $\theta(M)$ is given by

$$\begin{aligned} \theta(m) &= \frac{1}{\sqrt{2}}, & M > 0 \\ &= \frac{1}{2}, & M = 0 \\ &= 0, & M < 0 \end{aligned} \quad (\text{A.23})$$

In reference [84] are the advantages of this basis described:

- The spin density matrix 7.3 becomes diagonal in respect to ϵ .
- For $M = 0$ reflectivity $\epsilon = +1$ corresponds to state formed by natural parity while $\epsilon = -1$ to the unnatural exchange.

The relation between naturality and reflectivity holds for $M \neq 0$ only approximately in the leading order.

A.1.4 The reference frames

PWA deals intensively with different reference frames what makes it very difficult to introduce the terminology to the inexperienced reader. Unfortunately it is unavoidable. Lorentz-invariant decay formalisms are easily computable in the helicity frame, rotating and boosting the frame from decay to decay. On the other hand the t-channel reggeon exchange process is expressed the best in the Gottfried-Jackson frame. Both frames need a transformation of the Lorentz vectors measured in the laboratory frame what is described here.

PRODUCTION PLANE The first important transformation is the transformation into the production plane where the beam particle (here a kaon), the resonance X , the exchanged reggeon and the recoil proton lie in one plane. This is illustrated in figure A.3. The laboratory frame with the \vec{z} -direction pointing to the nominal beam direction, \vec{x} in the horizontal

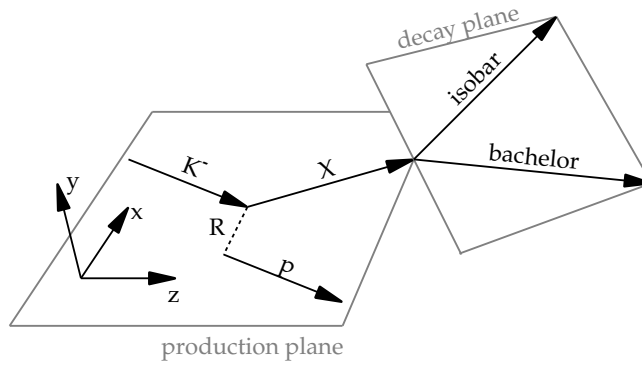


Figure A.3: Illustration of the reference frame defined by the production plane (see text for details).

plane and \vec{y} pointing upwards is rotated such that $\vec{y} = \vec{r}_{K^-} \times \vec{r}_X$ points out of the production plane. The resonance decays as assumed for PWA into a bachelor particle and an isobar with decay plane rotated to the production plane. The decay is further analysed in the rest frame of the resonance X . For a transformation into the rest frame, one rotates the \vec{z} direction of the frame into the direction of the resonance X with a rotation matrix R around \vec{y} . Afterwards one applies a Lorentz boost $L(X)$ to all measured vectors into the rest frame of X . The orientation of the rest frame makes now the difference between the important frames.

CANONICAL REST FRAME The canonical rest frame is restored by a rotation back into the original direction by R^T . The complete procedure $R^T L(X) R$ is also known as a simple Lorentz-transformation. Notice that the orientation of \vec{y} stays untouched during all transformations. The direction of the beam particle changed due to the boost in combination with the rotations.

GOTTFRIED-JACKSON FRAME The Gottfried-Jackson frame is given by the direction of the beam particle in the canonical rest frame (see figure A.4). The azimuthal angle θ_{GJ} is then usually specified between the decay particle larger in mass and the direction of the beam particle. With ϕ_{TY} one denotes the angle between the production plane and the decay plane and is called the Treiman-Yang angle.

HELICITY FRAME To calculate a decay chain, the helicity formalism is used. The helicity rest frame of the resonance X is already given by the first transformation $L(X)R$. To transform into the helicity frame of the isobar a new rotation is performed such that the $\vec{y} \mapsto \vec{y} = \vec{r}_{\text{isobar}} \times \vec{r}_X$ before executing a further Lorentz-transformation into the rest frame of the isobar.

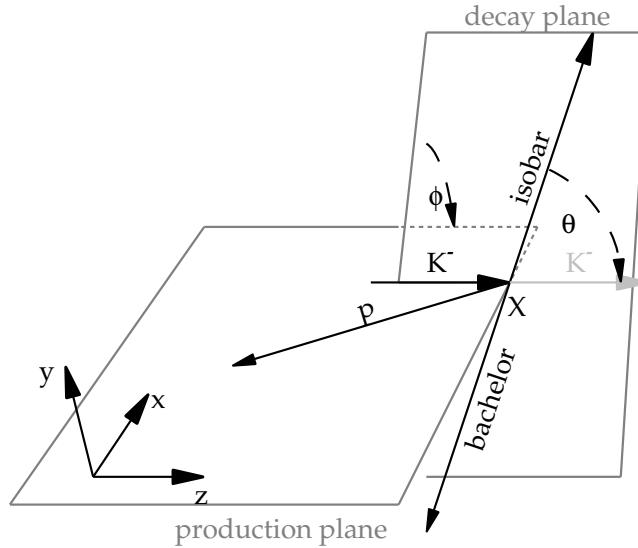


Figure A.4: Illustration of the rest decay frame as defined by Gottfried-Jackson [95] (see text for details).

A.2 EXAMPLES FOR A PARTIAL WAVE CONSTRUCTION

To most of the readers concepts of spin coupling are familiar. Nevertheless some examples are given here to recall those principles. We concentrate here on quantum numbers available in the $K^- \pi^+ \pi^-$ PWA decay chain only. In case of isospin symmetries as they are appearing in non strange spectra one has to extend the formulas also to this quantum number.

The quantum number cooking recipe is simple (but details are not):

1. Lookup the total spin and parity of the decay pair for example in the PDG's review [11]. The lower indexes label particle 1 and 2.

$$J_1^P ; J_2^P \quad (\text{A.24})$$

2. Rename the total spins J to s to couple both to S . Keep in mind that spins are represented by vectors.

$$J_1 \mapsto s_1 \quad ; \quad J_2 \mapsto s_2 \quad (\text{A.25})$$

$$\vec{s}_1 + \vec{s}_2 = \vec{S} \quad (\text{A.26})$$

$$\Rightarrow |s_1 - s_2| \leq S \leq |s_1 + s_2| \quad (\text{A.27})$$

3. Add the additional degree of freedom between two particles called orbital angular momentum $\vec{\ell}$ and couple it finally to the total spin J .

$$\vec{\ell} = 0, 1, 2, \dots \quad (\text{A.28})$$

$$\vec{S} + \vec{\ell} = \vec{J} \quad (\text{A.29})$$

$$\Rightarrow |S - \ell| \leq J \leq |S + \ell| \quad (\text{A.30})$$

J^P	$\pi^+\pi^-$	$K^-\pi^+$
1-	$\rho(770)$	$K^*(892)$
2+	$f_2(1270)$	$K_2^*(1430)$

Table A.1: A smaller isobar set in the $K^-\pi^+$ or $\pi^+\pi^-$ decay chain. See text for an construction example.

4. Finally calculate the parity P of the wave function.

$$P = P_1 \cdot P_2 \cdot (-1)^\ell \quad (\text{A.31})$$

The spin and parity of a pion and kaon is

$$J_K^P = J_\pi^P = 0^- \quad (\text{A.32})$$

meaning in a $q\bar{q}$ model the lowest possible energy state where spins of the quarks are anti parallel.

For the sake of simplicity let's consider a smaller isobar set in the decay chain shown in table A.1 and verify the quantum numbers appearing there as a coupling of the decay channels $K^-\pi^+$ and $\pi^+\pi^-$.

The wave function for a $\rho(770) \rightarrow \pi^+\pi^-$ decay is then constructed following the receipt.

1.

$$J_{\pi^+}^P = 0^- ; J_{\pi^-}^P = 0^-$$

2.

$$\begin{aligned} \Rightarrow |0-0| \leq S \leq |0+0| \\ \Rightarrow S = 0 \end{aligned}$$

3.

$$\begin{aligned} \vec{\ell} = 1 \\ \Rightarrow |0-1| \leq J \leq |0+1| \\ \Rightarrow J = 1 \end{aligned}$$

4.

$$\begin{aligned} P = (-1) \cdot (-1) \cdot (-1)^1 = -1 \\ \Rightarrow J^P = 1^- \end{aligned}$$

This was easy as only orbital angular momentum enters as an additional degree of freedom. Same happens in the case for a $K^*(892)$ decay into $K^-\pi^+$. In order to construct an $f_2(1270)$ or $K_2^*(1430)$ wave function we would need to enhance the orbital angular momentum to $\ell = 2$ and get then positive parity.

To construct now possible quantum numbers for partial wave amplitudes of the $K^-\pi^+\pi^-$ resonance we have to combine the bachelor particles wave function with the isobars from table A.1. As an example $K_2^*(1430)$ is coupled with π^- and an orbital angular momentum of $\ell = 1$ between those:

1.

$$J_{K_2^*(1430)}^P = 2^+ ; J_{\pi^-}^P = 0^-$$

2.

$$\begin{aligned} \Rightarrow |2 - 0| &\leq S \leq |2 + 0| \\ \Rightarrow S &= 2 \end{aligned}$$

3.

$$\begin{aligned} \vec{\ell} &= 1 \\ \Rightarrow |2 - 1| &\leq J \leq |2 + 1| \\ \Rightarrow J &= 1, 2, 3 \end{aligned}$$

4.

$$\begin{aligned} P &= (-1) \cdot (+1) \cdot (-1)^1 = +1 \\ \Rightarrow J^P &= (1, 2, 3)^+ \end{aligned}$$

The degrees of freedom are now much larger. In addition one has the spin projections M , needed to describe the wave function, given by

$$M = -J, -J + 1, \dots, +J \quad (\text{A.33})$$

so all-in-all already 21 partial waves for only this combination. This small example makes clear how big the efforts are one has to spend for systematic studies on partial wave sets. Fitting all possible quantum numbers (even when restricting the orbital angular momentum to small values) would give too many degrees of freedom to get any physically relevant results out of a fit to the data. Instead one starts usually with main isobars and low spins and momenta before increasing the number of partial waves step by step.

A.3 CLEBSCH-GORDAN COEFFICIENTS AND THE ISOSPIN

Literature sometimes does not remind the reader to respect isospin couplings in decays when comparing branching ratios in intensity distributions [1]. Therefore it is reviewed shortly here in the context of isospin $I_3 = -1/2$ particle decays into $K^- \pi^+ \pi^-$ final states. Same conclusions apply also for the charged decay channel $K^- p \rightarrow \bar{K}^0 \pi^+ \pi^- n$ as published in [88].

The $K^- \pi^+ \pi^-$ final state, as considered in this thesis, can be constructed as an consecutive decay of particles. In the constituent quark model it can follow two paths illustrated in figure A.5. The corresponding particles and their properties can be looked up in figure 1.3.

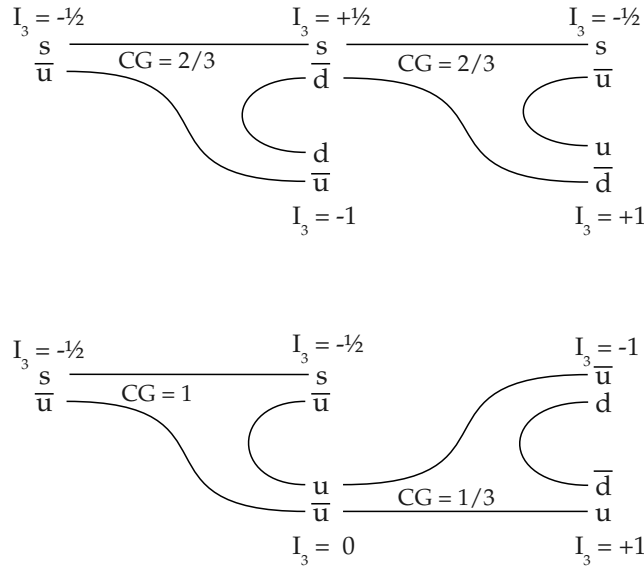


Figure A.5: A sequential decay into the $K^- \pi^+ \pi^-$ final state in the constituent quark model. The two possibilities of intermediate states give also two different amplitudes in terms of coupled isospins. The Clebsch-Gordan coefficients of the decay amplitudes give a ratio of 0.75 for the isospin $I = 0$ over isospin $I = 1/2$ isobar decay mode.

A K resonance of isospin $I_3 = -1/2$ can either emit an isospin $I_3 = -1$ pion and become an isospin $I_3 = 1/2$ K resonance such as an $K^*(892)$ or emit an isospin $I_3 = -1/2$ kaon and become an isospin $I_3 = 0$ resonance such as a $\rho(770)$. The first decay amplitude is suppressed by a factor of $2/3$ according to the Clebsch-Gordan coefficients in the Condon and Shortley conventions [11]. The isospin $I_3 = 0$ particle decays further into two pions coupling with an coefficient of $\sqrt{1/3}$. The $I_3 = 1/2$ particle is a coupling of a kaon and a pion. The corresponding Clebsch-Gordan coefficient is $\sqrt{2/3}$.

A measured branching ratio of a ρK^- resonance to a $K^* \pi^-$ must be hence corrected by a factor of 0.75.

PWA OF EVENTS WITH A RICH VETO

The event selection as presented in chapter 5 has the disadvantage of strong acceptance effects by the RICH detector momentum restrictions. It was shown that RICH efficiencies and purities are difficult to describe with a high precision for kaon tracks. One possibility to bypass this complication is discussed in the following with the drawback of a worse applicability to the PWA model as used in this thesis.

B.1 EVENT SELECTION

In order to eliminate the strong momentum acceptance effects of the RICH detector (see chapter 4 and chapter 6) a modified event selection was tried out. The requirement for an identified negatively charged final state track in section 5.1 was dropped. Still a cut on a possible RICH veto on the mass assumption was kept to benefit from a reduced combinatorial background.

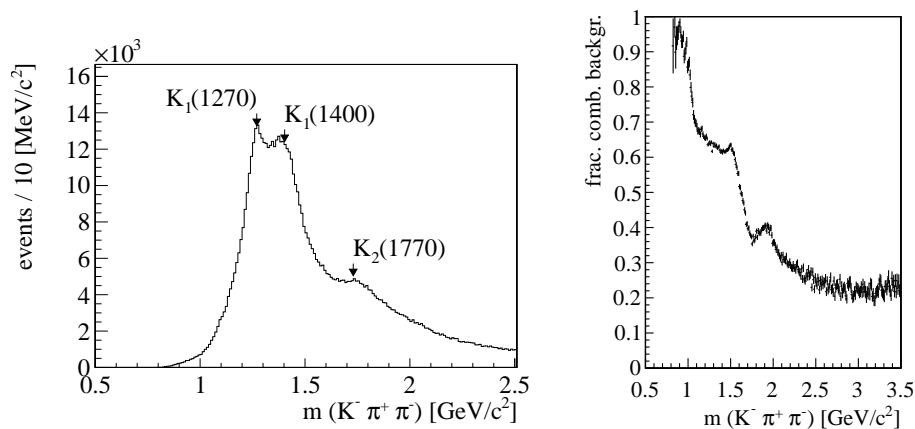


Figure B.1: Left: The invariant mass distribution of $K^- \pi^+ \pi^-$ tracks after all cuts. Established and visible resonances are indicated by labels. The distribution is not directly affected by the RICH acceptance (compare also figure 5.10) as only combinatorial background counts in. Right: The fraction of events where combinatorial background could not be rejected by a RICH veto.

The right distribution in figure B.1 is the fraction of events with combinatorial background as a function of the invariant $K^- \pi^+ \pi^-$ mass. For those events no RICH veto could be applied. All events gave the left $K^- \pi^+ \pi^-$ invariant mass distribution from about 600 000 events. Half of the events contained combinatorial background leading to a contami-

nation of 30%. A direct comparison of this distribution with published results by the ACCMOR collaboration [1] showed already very good agreement. As expected the low mass region had more entries as contribution by combinatorial background was larger.

B.2 SPECTROMETER ACCEPTANCES

Again 44 000 000 MC simulated events were subjected to acceptance studies. An event was considered as *accepted* only when the correct combination was reconstructed to correct only the right combination for the phase space acceptance. Ideally wrong combinations would be gathered by the *flat wave*.

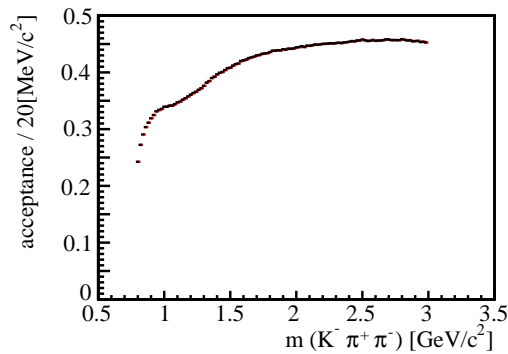


Figure B.2: The acceptance as a function of the invariant $K^-\pi^+\pi^-$ mass exhibits a lowered spectrometer performance for nearby tracks. The t' cut effect around $1.2\text{ GeV}/c^2$ is more pronounced than in figure 6.17. The overall acceptance is more than doubled.

The acceptance distribution B.2 in the invariant $K^-\pi^+\pi^-$ mass is only affected by tracking efficiencies dropping at low invariant masses. The overall acceptance increased nearly by a factor of 2 in comparison to the selection in section 5.1. Only the strong shape between $1.0\text{ GeV}/c^2$ and $1.5\text{ GeV}/c^2$ became even more pronounced. The connection to the cut on t' was pointed out in section 6.6.2.

Without the RICH cut on the positive identification of one negative track angular acceptances in the GJ frame could be shown to be very flat. The acceptance in the GJ angles as well as in the Treiman-Yang (TY) angles depend mostly on the $K^-\pi^+\pi^-$ invariant mass only.

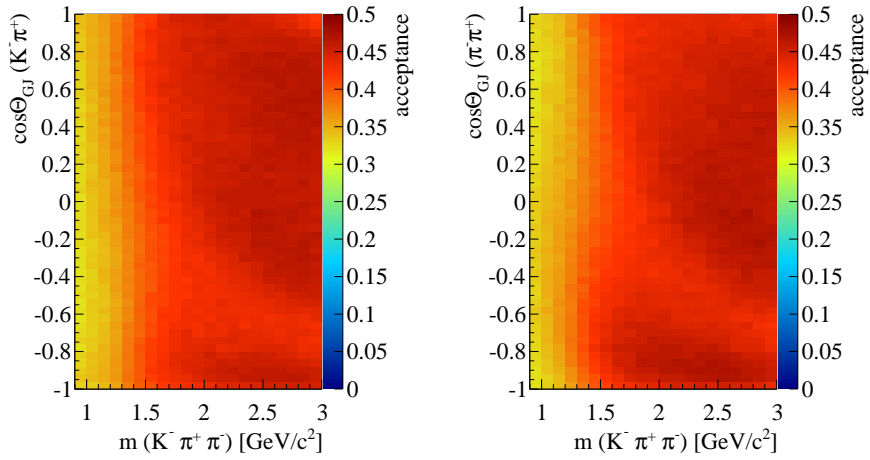


Figure B.3: The acceptance as a function of the polar angle in the GJ frame and the invariant $\text{K}^-\pi^+\pi^-$ mass. In contrast to the acceptance distributions 6.21 no strong angular dependence is observed.

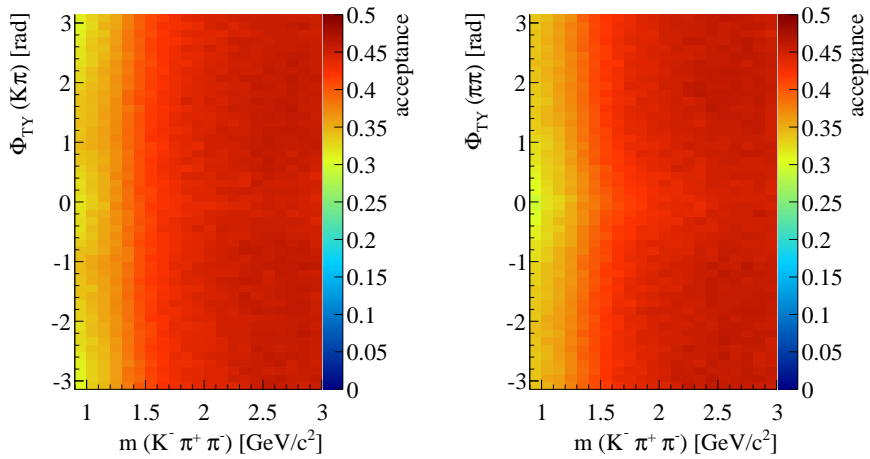


Figure B.4: The acceptance as a function of the azimuthal angle in the GJ frame and the invariant $\text{K}^-\pi^+\pi^-$ mass. In contrast to the acceptance distributions 6.22 no strong angular dependence is observed.

B.3 PARTIAL WAVE ANALYSIS

Exemplary for all PWA studies with this event set a mass independent fit with the constellation from section 7.4.1 is discussed. This set was not considered by the fitting routine to be the most likely but allows to compare the results directly with those from chapter 7.

Generally all fits were quite unstable specially below $1.2 \text{ GeV}/c^2$ what was replayed in large errors of several partial waves with low intensities. Nevertheless it was remarkable how well results from the ACCMOR collaboration [1] were reproduced. The main waves were observed with nearly the same intensity structure and phase motions were in good agreement.

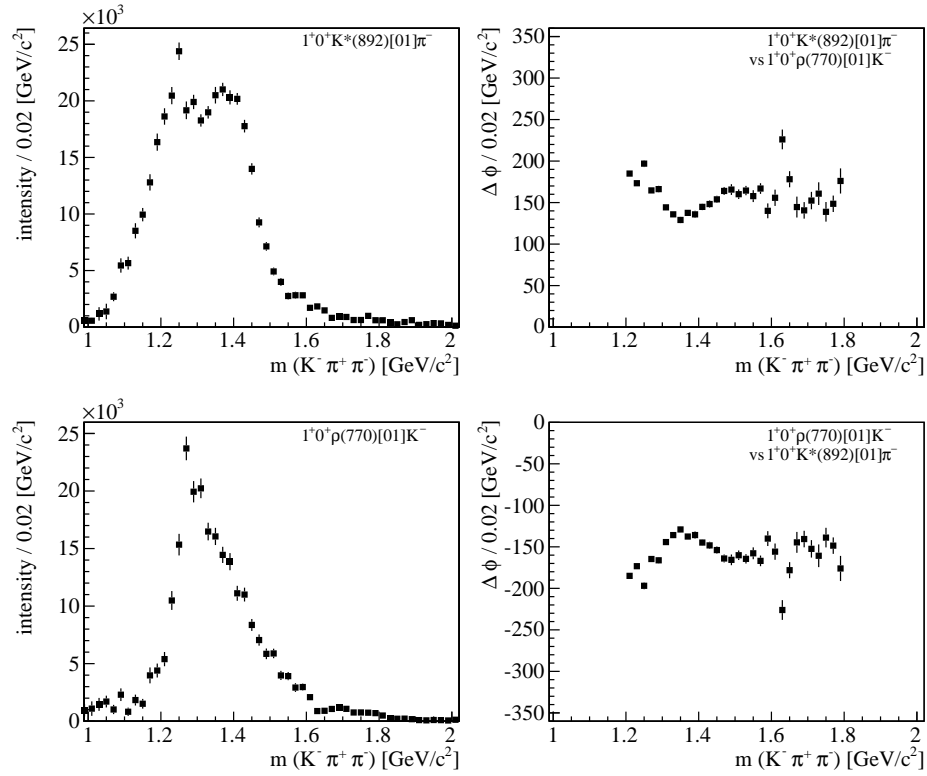


Figure B.5: $J^P = 1^+ M = 0$ wave intensities and the relative phase motion in respect to the strongest intensity of the counter branch. Only the $1^+0^+ K^*(892) \begin{bmatrix} 0 \\ 1 \end{bmatrix} \pi^-$ wave intensity shows a clear double structure. Compared to the intensities 7.4 a reduced coupling to the $(K^- \pi^+)$ branch is observed. The structure shows good agreement with figure 7.6 by ACCMOR.

Among all partial wave intensity distributions here only the $J^P = 1^+$ waves are shown in figure B.5 and are comparable with figure 7.6 by ACCMOR. One peculiarity is clearly visible when comparing to fit results without combinatorial background from figure 7.4: The Intensity for the K^* branch is lowered and the intensity for the ρ branch enhanced. Moreover the second resonance is less pronounced in the sample with combinatorial background.

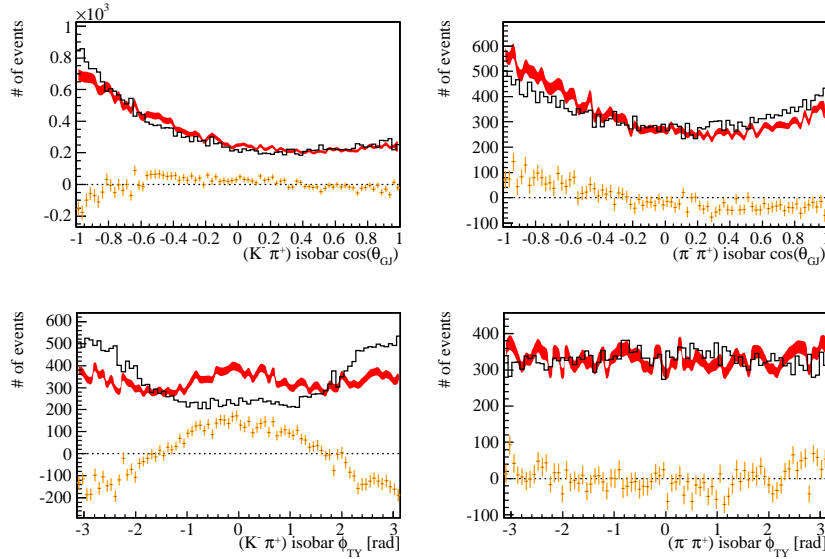


Figure B.6: Comparison of real angular distributions (black) with predicted from weighted MC data (red) in the GJ-frame. The difference between both is plotted orange. One invariant mass bin $1.26 \leq m(K^- \pi^+ \pi^-) [\text{GeV}/c^2] < 1.28$ is exemplary shown for the low mass region where the $J^P = 1^+$ wave is dominant. Left the $(K^- \pi^+)$ -isobar track combination right the $(\pi^+ \pi^-)$ -isobar track combination. Compared to the distributions 7.18 combinatorial background is distorting the Φ_{TY} distribution of the $(K^- \pi^+)$ -branch.

The reason for this was found in the angular distributions B.6 where the weighted MC sample is directly compared to the real data in one invariant mass bin. A large deviation between the MC sample, weighted by the fitted partial wave composition, and the real data sample was observed. Mostly the Φ_{TY} angle of the $(K^- \pi^+)$ -isobar branch was affected while the distribution in the $(\pi^+ \pi^-)$ -branch was in agreement. Wrongly assigned masses to $(\pi^+ \pi^-)$ tracks in combination with the acceptance of the RICH detector are the reason for this structure.

Only a part of this structure was applied to the flat wave by the fit. The total intensity of the flat wave was about 10%. The remaining 20% of intensity by combinatorial background was described by partial waves amplitudes. As the impact of the combinatorial background on the $(\pi^+ \pi^-)$ -branch was less pronounced than on the $(K^- \pi^+)$ -branch an isobar model could be fit much better to the latter. The intensities for the $(\pi^+ \pi^-)$ -branches were artificially enhanced giving unbalanced branching ratios.

In fact also the publication by ACCMOR reveals difficulties to describe the results of a mass independent fit with a mass dependent fit specially in for the low mass region. Unfortunately further information about acceptance studies on ACCMOR data was completely missing so a clear statement could not be made.

B.4 SUMMARY

It was possible to get rid of acceptance effects for correctly reconstructed events originating in the RICH selection criterion. A simple veto on the mass assumption could at least reduce the combinatorial background down to 30% with the largest fraction at low invariant masses. But specially there background produced angular distributions not applicable to the PWA isobar model particularly in the $(K^-\pi^+)$ -branch giving additional intensity in the $(\pi^+\pi^-)$ -branch. On the one hand the difficulty to describe the RICH detector response in MC simulations was avoided and the number of physically correctly reconstructed events was increased by a factor of two. On the other hand background was introduced which could not be handled correctly by the fitting procedure.

MORE DETAILS ON CEDARS

C.1 CEDAR PHOTON PROPAGATION MATRICES

To propagate a photon from the point of cherenkov emission to the diaphragm, the following matrix operations were used [64]:

A photon is parametrized with an angle Θ and a distance to the principal axis Y . The transportation is a multiplication with a matrix \hat{M} .

$$\begin{pmatrix} Y' \\ \Theta' \end{pmatrix} = \hat{M} \cdot \begin{pmatrix} Y \\ \Theta \end{pmatrix} \quad (\text{C.1})$$

The full transportation matrix for a photon impact at the first lens is given by

$$\hat{M} = \begin{pmatrix} 1 & l_4 \\ 0 & 1 \end{pmatrix} \begin{pmatrix} 1 & 0 \\ 0 & \frac{n_s}{n_H} \end{pmatrix} \begin{pmatrix} 1 & l_3 \\ 0 & 1 \end{pmatrix} \begin{pmatrix} 1 & 0 \\ \frac{n_H - n_s}{n_s(-R_3)} & \frac{n_H}{n_s} \end{pmatrix} \begin{pmatrix} 1 & l_2 \\ 0 & 1 \end{pmatrix} \cdot \\ \begin{pmatrix} 1 & 0 \\ \frac{n_s - n_H}{n_H(-R_1)} & \frac{n_s}{n_H} \end{pmatrix} \begin{pmatrix} 1 & l_1 \\ 0 & 1 \end{pmatrix} \begin{pmatrix} 1 & 0 \\ \frac{2}{R_2} & 1 \end{pmatrix} \begin{pmatrix} 1 & l_1 \\ 0 & 1 \end{pmatrix} \begin{pmatrix} 1 & 0 \\ \frac{n_s - n_H}{n_H R_1} & \frac{n_s}{n_H} \end{pmatrix} \quad (\text{C.2})$$

with constants taken from various sources [61] [62] and summarized in table C.1.

The dispersion formulae for Suprasil I (n_s) and Helium (n_H) are given by

$$n_s = \left(C_1 + \frac{C_2}{(\lambda^2 - A_2)} + \frac{C_3}{(\lambda^2 - A_3)} + C_4 \cdot \lambda^2 + C_5 \cdot \lambda^4 \right)^{\frac{1}{2}} \quad (\text{C.3})$$

$$n_H = 1 + \frac{p}{760} \cdot \frac{273}{T} \cdot \frac{E_1}{(D_1 - 1/\lambda^2)} \quad (\text{C.4})$$

with

$$\begin{aligned} C_1 &= 1.33251 \\ C_2 &= 8523.7 \\ A_2 &= 11382.0 \\ C_3 &= 7.8946 \cdot 10^7 \\ A_3 &= -1.0268 \cdot 10^8 \\ C_4 &= 31.0026 \cdot 10^{-9} \\ C_5 &= -78212.4 \cdot 10^{-18} \\ E_1 &= 0.014757 \cdot 10^{-6} \\ D_1 &= 425.91 \cdot 10^{-6} \end{aligned} \quad (\text{C.5})$$

radiator length	5880 mm	l_{rad}
lens with vaporized mirror		
glass	Suprasil I	$\mapsto n_s$
outer diameter	300 mm	Y_{max}
inner diameter	100 mm	Y_{min}
radius of reflective surface	8913 mm	R_2
radius of deflective surface	8074 mm	R_1
thickness	40 mm	l_1
achromat		
glass	Suprasil I	$\mapsto n_s$
outer diameter	270 mm	
inner diameter	150 mm	
radius of entrance surface	2885 mm	R_3
radius of exit surface	> 5000 mm	$R_4 \rightarrow \infty$
thickness	20 mm	l_3
diaphragm		
radius	100 mm	
slit	0 mm-20 mm	
distances		
mirror-achromat	3440 mm	l_2
achromat-diaphragm	992 mm	l_4
Cherenkov angle	$\arccos(\frac{1}{n_H\beta})$	Θ

Table C.1: A list of dimensions of the CEDAR-N detector as gathered from various sources [61] [62].

C.2 THE FRONTEND-ELECTRONICS

The photograph C.1 shows the the frontend electronics placed next to the CEDAR detectors next to the beam line. The request for a kaon trigger in the hadron run 2008 made it necessary to optimize the trigger signal in respect to the Primakov test run 2004. The demands for a fast trigger decision and a signal treatment with COMPASS electronics separated from the M2-beam line readout chain led to the signal treatment solution sketched in the flow chart C.2.

The analogue signal from 8 PMs per each CEDAR were split by active NIM FAN-out modules. One was placed separated from the rack next to CEDAR 1 the other in the rack itself. The longer analogue signal cables from CEDAR 1 to the rest of the readout chain suppressed noise coming from reflections at the PM bases. CEDAR 2 was suffering therefore from double hits resulting in a reduced efficiency at high beam intensities.

Small differences in time between each analogue signal were corrected by additional cables before passing the analogue signal to **LE** discriminators allowing for thresholds down to zero in contrast to Constant Fraction (**CF**) discriminators that would on the other hand correct for time walk. Signals by **PMs** had a mean amplitude of below 30 V what motivated the choice of **LE** discriminators. Those modules featured a multiplicity unit with a majority threshold set to a majority of 6 of 8 **PMs**. Each **CEDAR** was discriminated by a separate **LE** discriminator unit with the majority and multiplicity signal sent to the trigger barrack at the very end of the **COMPASS** experiment. In order to guarantee an efficient trigger signal discriminators were run in non-updating mode. This means that a pileup signal within the length of a discriminated output signal was extending the output signal.

The discriminated signals with **ECL** specification were transformed to **LVDS** levels needed by **F1-TDC**-cards run in single precision mode. A side effect of the non-updating mode in the discriminators was the low **TDC** efficiency for **CEDAR 2** at high beam intensities. An extended signal was still recorded as only one hit in the **TDC**.

For the Primakov run in 2009 **F1** cards were run in double precision mode in order to double the buffer length. A shift in the trigger time caused even with the larger record length buffer overflows every few spills. Regular hadron runs were not affected.

In the last two weeks of the of the run 2008 the analogue split signal was recorded by **SADC** cards in combination with an active shaper extending the signals of a length of some nano seconds to signals with lengths of several micro seconds. This hardware, developed originally for **ECAL** readout, was used to monitor the **PM** stability. As it was also recorded further studies might be done on signal properties.

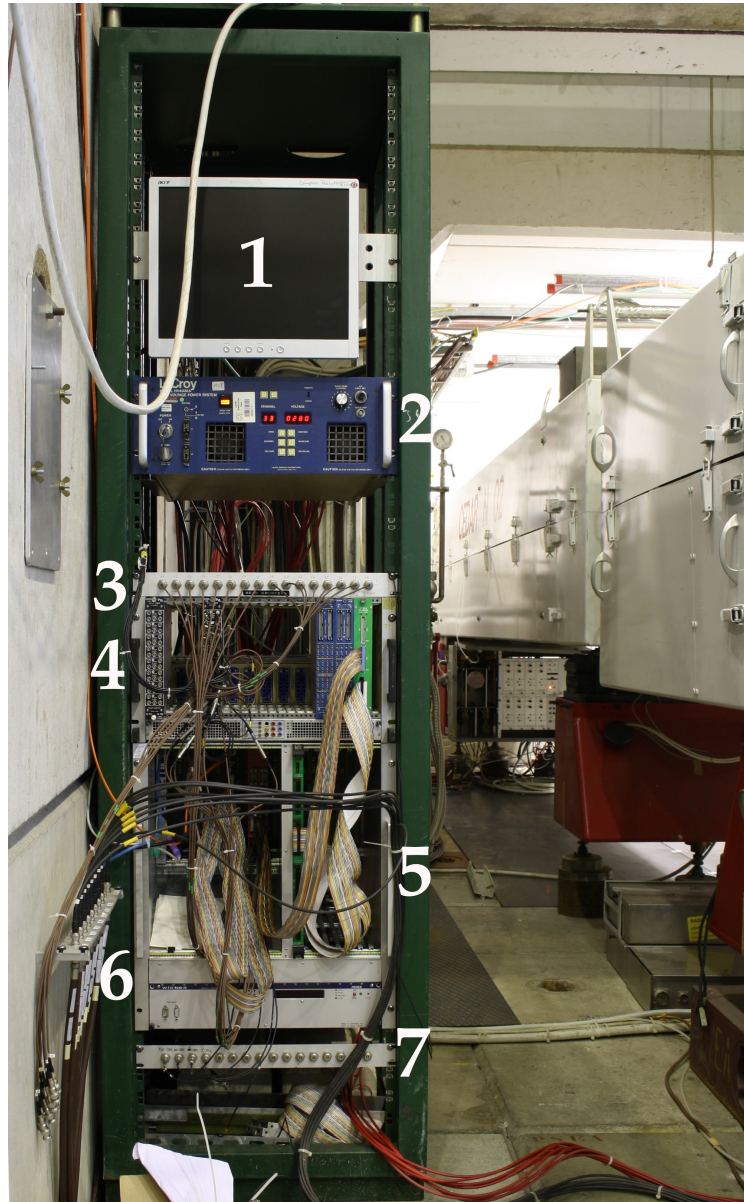


Figure C.1: A photograph of the frontend electronics placed left of CEDAR 2. (1) A monitor was connected to the VME CPU what is actually a PC plugged on the VME board (5). Below (2) an additional HV power supply was placed for the last stages of the PMs. A plug panel (3) provided the analogue PM signals, not split for CEDAR 2. CEDAR 1 signal was split next to this detector (not visible), the splitter for CEDAR 2 was placed in the NIM-Crate (4). The VME-Crate (6) housed the CPU, LE-discriminators with multiplicity units as well as a TDC unit. For a short period a sampling ADC was used together with a shaper. As the LE-discriminator featured ECL signal outputs but the TDC needed LVDS signals a corresponding converter was plugged into the NIM-Crate. The fast multiplicity signal was also the output of the LE-discriminators (7). Also visible are the CEDAR 2 M2 beam line analogue connectors (6) fed with the split signal.

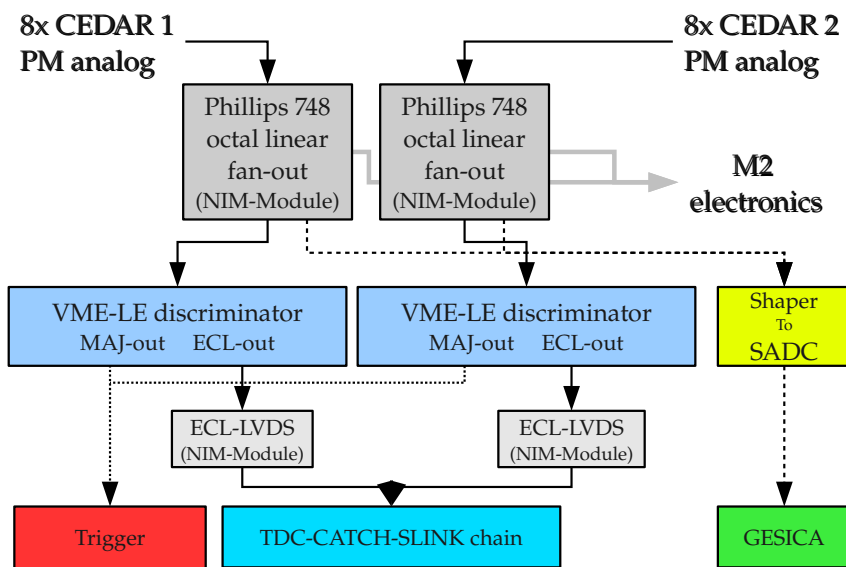


Figure C.2: A sketch of the signal flow at the CEDAR frontend side. A discussion is found in the text.

A large fraction of the work for this thesis was coding mainly in C++. In total over 20 000 lines of code were written and 2 000 lines of documentation are to be found in the files. Almost all files were placed in a svn repository¹ dedicated to hadron data analysis, accessible by most COMPASS members. This appendix gives an overview on the software created for and used in this thesis. Detailed documentation is to be found in the header files of C++ code.

D.1 BASICS FOR PHAST

The main analysis code is accumulated in `UserEvent_basics.cc/.h` with the corresponding visualization tool `UserEvent_basics_rootscripts.cc`. The idea to reuse parts of analysis code for different channels motivated the implementation of a class pluggable to a *UserEvent* in PHAST. Complete event selections and analyses as

- $K^- p \rightarrow K^- \pi^+ \pi^- p_{\text{recoil}}$
- $\pi^- p \rightarrow \pi^- \pi^+ \pi^- p_{\text{recoil}}$
- $K^- p \rightarrow K^- \pi^+ \pi^- \pi^0 p_{\text{recoil}}$
- $\pi^- p \rightarrow \pi^- K_s K_s p_{\text{recoil}}$
- Analysis of RICH purities and efficiencies
- Analysis of beam properties
- Analysis of CEDAR efficiencies
- Analysis of CEDAR offline pressure scans
- Analysis of the spectrometer uniformity

use in parts methods for

- ECAL cluster search
- V_0 search ($K_s, \Lambda, \bar{\Lambda}$)
- in target analysis
- neutral channel reconstruction of γ s and π^0 s
- cut flow analysis

¹ `svn+ssh://<username>@lxplus.cern.ch/afs/cern.ch/compass/HadronGroup/svn/hadrontools/trunk`

- [RICH PID](#) for [MC](#) and real data analysis
- [RICH](#) track property analysis
- diffractive exclusive analysis of any particle combination
- calculations of t' , pseudo rapidities, coplanarity, reference frame transformations
- Armenteros plot studies
- [MC](#) performance studies
- code performance studies

providing a huge amount of output information in form of histograms, graphs and trees. To generate final results in form of printable files the visualization tool is provided. It features preparation of histograms, labeling, data fit procedures a reanalysis of [RICH](#) efficiencies with changed [PID](#) likelihood cuts and much more.

D.2 THE CEDAR HELPER

The [CEDAR](#) analysis code is substantial to most analyses in hadron beams and therefore provided in a separate file `CEDAR_Helper.cc/.h`. It consists mainly of an implemented particle identification taking the [CEDAR](#) settings for the runs of the years 2008 and 2009 into account. Additionally methods of ranking and likelihood calculations by Jan Friedrich modified by Tobias Weisrock were added. Naturally it uses databases included to the same folder containing purity values [CEDAR PID](#) settings and likelihood parametrizations. Also basic tools for beam parallelism analysis were implemented. Last to mention is the implementation of the [CEDAR](#) acceptance in [MC](#) data case simulating a [CEDAR](#) set on kaon identification with 6-fold selection criteria. For a correct functionality it is mandatory to simulate the beam properties based on real data.

D.3 THE RPD HELPER

The [RPD](#) analysis code is stored in `RPD_Helper.cc/.h`. Johannes Bernhard implemented the real data decoding tools based on Etienne Burtin's first sketches. The code was extended by t_0 calibration tools, the corresponding data base and a basic [MC](#) detector response simulation. The user need not be concerned if (s)he is analysing real data or [MC](#) data as the calls are identical in both cases.

D.4 CEDAR PID ANALYSIS

The program `calculate_CEDAR_purities` is in fact a collection of several features. It started with a simple purity and efficiency analysis of pressure

scans based on mirroring and was extended by the creation of a purity data base for the CEDAR helper code. As an input recorded temperature and pressure values from DCS are mandatory. The DCS values are also used to define the PID setting of a CEDAR taking also the diaphragm opening into account. A further output is a file with p/T settings for each recorded time point. This output is used for the offline pressure scan analysis.

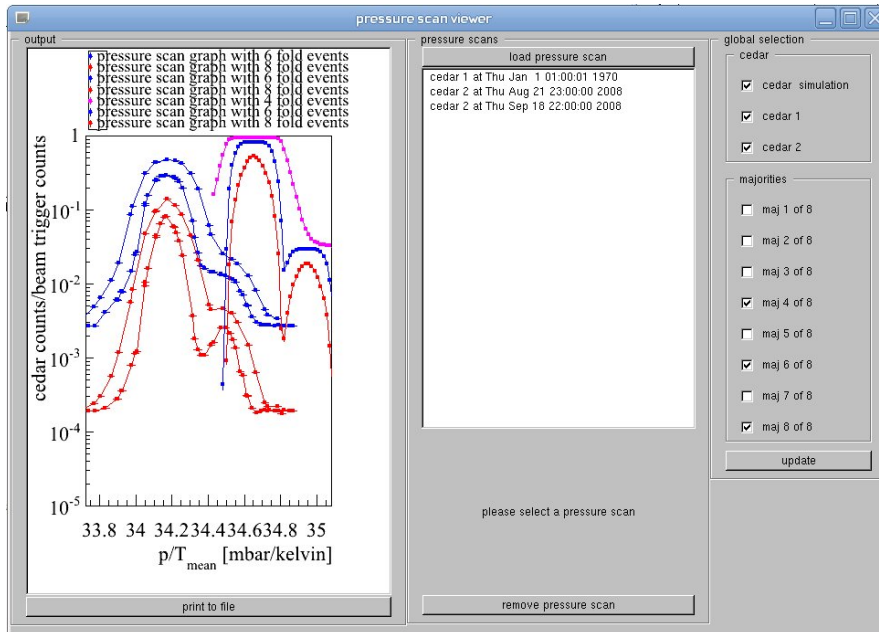


Figure D.1: A simple GUI for basic comparison of pressure scans from several sources.

Also a simple GUI (see screenshot D.1) was implemented in order to compare several pressure scans from various sources. Pressure scans from M2 online analyses are accepted as well as pressure scans from offline analyses and MC simulations. Notice that online pressure scans need to be completed with the recorded time and the temperature inside the vessel for a proper function. In case temperature values are given by a DCS data base, those values are used.

D.5 CEDAR OFFLINE PRESSURE SCAN ANALYSIS

Offline pressure scans are filtered and recorded with the help of the corresponding method in the `UserEvent_basics.cc/.h` file. A final analysis using p/T values from DCS is implemented in the program `analyze_pressurescans`. It is used to analyse the separation quality of beam particles for different cuts. Not only majorities between PMs can be considered but also time, track divergence, ranking and other cuts may be applied. A direct comparison with online pressure scans is also foreseen.

D.6 THE CEDAR MC SIMULATION

The MC simulation of the CEDAR based on propagation matrices is discussed in chapter 3. The program behind is cedar_MC.

D.7 PARTIAL WAVE ANALYSIS PACKAGES AT COMPASS

There are currently two software packages in use by the COMPASS collaboration. Each package is developed, maintained and used by different members testing more or less similar ways to determine partial wave contributions to invariant mass spectra.

SOFTWARE BY DMITRI RYABCHIKOV Dmitri Ryabchikov is today the main contributor to a software package that started more than 40 years ago. It is based on the "Ascoli" fitter and the "Illinois" approach [84]. It features a completed package providing all tools needed for a complete PWA. But it needs special manual intervention at several points for each channel. The language Fortran makes it in addition difficult to maintain and develop it as Fortran is a discarded language presently replaced by object oriented approaches.

ROOTPWA For the analysis described in this thesis the software package *rootpwa* was chosen and co-developed. *Rootpwa* is evolved from the *pwa2000* software package [90] and is written with the programming language C++. It makes hard use of other packages as the *ROOT* software package and *BOOST* libraries. This package allows the user to create his own partial waves to adapt it to his/her data quite easily. The amplitude generator, the integrator of the *pwa2000* package as well as some architecture are still being used. Already at an early stage the fitter was replaced by an implementation of Sebastian Neubert allowing for faster and more diverse operation than the original one. An implementation of a flat phase space generator, *genpw*, that is also capable of weighting events with partial wave intensities, was added to the features.

Another main contribution comes by Boris Grube and his team which is implementing a more generalized access to partial waves also fitting the demands of baryon spectroscopy. It should be also mentioned that the implementation of an optional fitter using *CUDA* libraries is increasing the speed by many orders. This is since *CUDA* makes use of *NVIDIA* Graphics Processor Unit (*GPU*)s allowing for parallel calculation of loops within the fitter. This branch of the software was not used in the current analysis.

The software package is being extended mostly by the user themselves based on the specific demands. Therefore, to meet the claims for a full-blown analysis of $K^- \pi^+ \pi^-$ diffractive events with many iterations and branches, a GUI was developed having a coordinating background software as a basis. The GUI is managing projects, setting up the workspaces, binning data, handling the sub programs, sending jobs to batch farms

of different kinds, checking data for consistency, allowing the user for a simplified partial wave selection, inspecting and storing the fit results and so on.

Rootpwa is being developed independently from the software of Dmitri Ryabchikov. This helps to overcome the problem that errors in the implementation of both software packages might lead to incorrect results. Final [PWA](#) results can be cross checked using the respective software package.

Up to date details are given in the software repository itself <http://sourceforge.net/projects/rootpwa/>.

BIBLIOGRAPHY

- [1] C. Daum et al. Diffractive production of strange mesons at 63-GeV. *Nucl. Phys. B*, 187:1, 1981.
- [2] C. Burgess and G. Moore. *The Standard Model, A Primer*. Cambridge University Press, 2007.
- [3] W. Marciano and H. Pagels. Quantum chromodynamics. *Phys. Rep.*, 36(3):137–276, 1978.
- [4] S. Scherer. Introduction to chiral perturbation theory. *Adv. Nucl. Phys.*, 27:277, 2003.
- [5] A. Pich. Quantum chromodynamics. *arXiv:hep-ph/9505231v1*, 1995.
- [6] B.B. Brandt et al. Form factors in lattice QCD. *arXiv:hep-lat/1106.1554v1*, 2011.
- [7] G. Zweig. An SU(3) model for strong interaction symmetry and its breaking. *CERN Report*, (8182), 1964.
- [8] M. Gell-Mann. A schematic model of baryons and mesons. *Phys. Lett.*, 8(3):214 – 215, 1964.
- [9] H. F. Jones. *Groups, Representations and Physics*. Hilger, 1990.
- [10] A. P. Balachandran and C. G. Trahern. *Lectures on Group Theory for Physicists*. Bibliopolis, 1984.
- [11] K. Nakamura and PDG. Review of particle physics. *J. of Phys. G*, 37(7A):075021, 2010.
- [12] W. Dunwoodie. The status of strange meson spectroscopy. *Nucl. Phys. B*, 21:16 – 24, 1991.
- [13] S. Godfrey and N. Isgur. Mesons in a relativized quark model with chromodynamics. *Phys. Rev. D*, 32:189–231, 1985.
- [14] M. Gell-Mann and Y. Ne’eman. *The Eightfold Way*. Benjamin, 1964.
- [15] K. Nishijima. Charge independence theory of V particles. *Prog. of Theor. Phys.*, 13(3):285–304, 1955.
- [16] D. Aston et al. A study of $K^- \pi^+$ scattering in the reaction $K^- p \rightarrow K^- \pi^+ n$ at 11 GeV/c. *Nucl. Phys. B*, 296(3):493 – 526, 1988.
- [17] E. Klempt and A. Zaitsev. Glueballs, hybrids, multiquarks: Experimental facts versus QCD inspired concepts. *Phys. Rep.*, 454(1-4):1 – 202, 2007.

- [18] K. Goulianos. Diffractive interactions of hadrons at high energies. *Phys. Rep.*, 101(3):169 – 219, 1983.
- [19] K. Goulianos. Diffraction in hadron-hadron interactions. *Nucl. Phys. Proc. Suppl. A*, A:9, 2001.
- [20] S. Mandelstam. Determination of the pion-nucleon scattering amplitude from dispersion relations and unitarity. general theory. *Phys. Rev.*, 112(4):1344–1360, 1958.
- [21] Q. Weitzel. *Precision Meson Spectroscopy: Diffractive Production at COMPASS and Development of a GEM-based TPC for PANDA*. PhD thesis, TU Munich, 2008.
- [22] M. L. Good and W. D. Walker. Diffraction dissociation of beam particles. *Phys. Rev.*, 120(5):1857–1860, 1960.
- [23] T. Regge. Introduction to complex orbital momenta. *Nuovo Cimento*, 14:951–976, 1959.
- [24] A. P. Contogouris et al. Regge poles and inelastic scattering at high energies. *Phys. Rev.*, 129(2):974–981, 1963.
- [25] E. A. Kuraev et al. The Pomernanchuk Singularity in Nonabelian Gauge Theories. *Sov. Phys. JETP*, 45:199–204, 1977.
- [26] E. Levin. An Introduction to pomerons. *arXiv:hep-ph/9808486*, 1998.
- [27] G. W. Brandenburg et al. Observation of two strangeness-one axial-vector mesons. *Phys. Rev. Lett.*, 36(13):703–706, 1976.
- [28] Y. M. Antipov et al. Analysis of the reaction $K^-p \rightarrow K^- \pi^- \pi^+ p$ at 40 GeV/c. *Nucl. Phys. B*, 86(3):381 – 402, 1975.
- [29] C. Daum et al. Inclusive ϕ -meson production in 93 and 63 GeV hadron interactions. *Nucl. Phys. B*, 186(2):205 – 218, 1981.
- [30] H. Guler et al. Study of the $K^+ \pi^+ \pi^-$ Final State in $B^+ \rightarrow J/\psi K^+ \pi^+ \pi^-$ and $B^+ \rightarrow \psi' K^+ \pi^+ \pi^-$. *Phys. Rev. D*, 83:032005, 2011.
- [31] G. Baum et al. COMPASS: A proposal for a common muon and proton apparatus for structure and spectroscopy. *CERN/SPSLC*, 1996.
- [32] E. Nappi et al. Semi-inclusive muon scattering from a polarised target. *CERN/SPSLC*, 1995.
- [33] J. Ashman et al. An investigation of the spin structure of the proton in deep inelastic scattering of polarised muons on polarised protons. *Nucl. Phys. B*, 328(1):1 – 35, 1989.
- [34] B. Adeva et al. Spin asymmetries A_1 and structure functions g_1 of the proton and the deuteron from polarized high energy muon scattering. *Phys. Rev. D*, 58(11):112001, 1998.

- [35] A. Yuri et al. Charm experiment with omni-purpose setup. *CERN/SP-SLC*, 1995.
- [36] O. Kouznetsov. Prospects for dvcs measurements using the COMPASS spectrometer at CERN. <http://www.cs.infn.it/diff2010/talks/Kouznetsov.pdf>, 2010.
- [37] R. Hermann. *Die Messung der Gluonpolarisation durch die Produktion von Hadronpaaren mit grossen Transversalimpulsen in tiefinelastischen Myonstreuung am Nukleon*. PhD thesis, Johannes-Gutenberg Universität Mainz, 2009.
- [38] M. Alekseev et al. Gluon polarisation in the nucleon and longitudinal double spin asymmetries from open charm muoproduction. *Phys. Lett. B*, 676(1-3):31 – 38, 2009.
- [39] E.S. Ageev et al. Gluon polarization in the nucleon from quasi-real photoproduction of high-pt hadron pairs. *Phys. Lett. B*, 633(1):25 – 32, 2006.
- [40] M. Alekseev et al. The polarised valence quark distribution from semi-inclusive DIS. *Phys. Lett. B*, 660(5):458 – 465, 2008.
- [41] M.G. Alekseev et al. Measurement of the Collins and Sivers asymmetries on transversely polarised protons. *Phys. Lett. B*, 692(4):240 – 246, 2010.
- [42] S. Takekawa. *Study of T-odd parton distribution functions in polarised Drell-Yan processes at COMPASS*. PhD thesis, university degli studi di trieste, 2009.
- [43] M. Alekseev et al. Double spin asymmetry in exclusive rho muoproduction at COMPASS. *Eur. Phys. J. C*, 52:255–265, 2007.
- [44] M. Bettinelli. *Exclusive omega pi pi production with muons at COMPASS*. PhD thesis, LMU Munich, 2010.
- [45] M. Alekseev et al. Measurement of the longitudinal spin transfer to lambda and hyperons in polarised muon DIS. *Eur. Phys. J. C*, 64:171–179, 2009.
- [46] A. Guskov. *Analysis of the charged pion polarizability measurement method at COMPASS experiment*. PhD thesis, university di torino, 2010.
- [47] A. Austregesilo. Baryon Spectroscopy at COMPASS. *JPCS*, to be published, 2011.
- [48] J. Bernhard. Study of central production of charged pionic modes at COMPASS. *AIP Conf. Proc.*, 1257:482–486, 2010.
- [49] M. G. Alekseev et al. Observation of a $J^{PC} = 1^{-+}$ exotic resonance in diffractive dissociation of 190 GeV/c π^{-} into $\pi^{-}\pi^{-}\pi^{+}$. *Phys. Rev. Lett.*, 104(24):241803, 2010.

- [50] F. Nerling. Diffractive pion production at COMPASS-first results on 3π final states-neutral mode. *AIP Conf. Proc.*, 1257:286–292, 2010.
- [51] S. Neubert. Diffractive Pion Dissociation into $\pi^-\pi^+\pi^-\pi^+\pi^-$ at COMPASS. *AIP Conf. Proc.*, 1257:298–302, 2010.
- [52] A. Austregesilo et al. Status of physics with hadron beams in COMPASS. *COMPASS-Note*, 2010-07.
- [53] R. Ley. Cern accelerators. <http://ps-div.web.cern.ch/ps-div/PSComplex/accelerators.pdf>, 1996. last call: 29.03.2011.
- [54] M2 beam for compass. <http://sl.web.cern.ch/SL/eagroup/NewM2/M2beam.ps>, 2000. last call: 29.03.2011.
- [55] A. Ambrosini et al. Measurement of charged particle production from 450 GeV/c protons on beryllium. *Eur. Phys. J. C*, 10:605–627, 1999.
- [56] L. Gatignon. M2 beam propagation matrix. private communication, 2009.
- [57] P. Abbon et al. The COMPASS experiment at CERN. *Nucl. Instr. Methods A*, 577(3):455 – 518, 2007.
- [58] J. Bernhard. Aufbau des inneren rings eines recoildetektors am COMPASS-experiment. Master’s thesis, Johannes-Gutenberg Universität Mainz, 2007.
- [59] T. Schlüter et al. Large-area sandwich veto detector with WLS fibre readout for hadron spectroscopy at COMPASS. *COMPASS-Note*, 2011-03.
- [60] V. Kolosov et al. Present performances of COMPASS electromagnetic calorimetry from data analysis. *COMPASS-Note*, 2008-05.
- [61] C. Bovet et al. The CEDAR project. Technical report, CERN, 1975.
- [62] C. Bovet et al. The CEDAR counters for particle identification in the SPS secondary beams. Technical report, CERN, 1982. Yellow Report 82-13.
- [63] P. A. Cerenkov. k.a. *Dokl. Akad. Nauk SSSR*, 2:451, 1934.
- [64] P. Jasinski. Aufbau und Betrieb eines Teststandes für Strahlscherenkowdetektoren am COMPASS-Experiment. Master’s thesis, Johannes-Gutenberg Universität Mainz, 2007.
- [65] D. Meschede. *Optik, Licht und Laser*, volume 2. IB.G. Teubner, 2005.
- [66] Fotovervielfacher, Elektronenvervielfacher, Einzelkanäle, Vielkanalplatten. Technical report, Valvo, 1987.
- [67] J. Friedrich. CEDAR performance 2009. *COMPASS-Note*, 2010-15.

- [68] The COMPASS RICH-group. compass picture collection of RICH. http://wwwcompass.cern.ch/compass/detector/rich/RICH1_4.ps.gz, 2011.
- [69] P. Abbon et al. The COMPASS RICH-1 detector upgrade. *Eur. Phys. J.*, 162:251–257, 2008.
- [70] P. Schiavon. Particle identification in COMPASS RICH-1, progress report. *COMPASS-Note*, 2001-12.
- [71] P. Schiavon. Hints for PID in RICH-1. *COMPASS-Note*, 2003-02.
- [72] P. Schiavon et al. A method to extract RICH purity from data. *COMPASS-Note*, 2006-14.
- [73] J. Podolanski and R. Armenteros. *Phil. Mag.*, 45, 1954.
- [74] M. Schott. First look at the pion and kaon identification performance of the RICH detector in 2008 hadron data. *COMPASS-Note*, 2009-10.
- [75] V. Aleksakhin et al. Geometrical event reconstruction in the COMPASS experiment. *Phys. of Part. and Nucl. Lett.*, 4:350–362, 2007.
- [76] The COMPASS collaboration. <http://wwwcompass.cern.ch/compass/software/offline/welcome.html>, 2011.
- [77] K. Schoening. Option cards for MC simulations of hadron data. http://afs.cern.ch/compass/HadronGroup/HadronAnalysis/20101115/schoenning_MC_101115.pdf, 2010.
- [78] Sergei Gerassimov et al. <http://ges.home.cern.ch/ges/phast/>, 2011.
- [79] N. d’Hose. Status of the RPD project. http://wwwcompass.cern.ch/compass/gpd/meetings/2008RPD/NdH_forRPD2008.ppt, 2008.
- [80] E. Brutin. Recoil proton detector calibration and reconstruction. http://wwwcompass.cern.ch/compass/collaboration/2008/co_0811/pdf/burtin_2008-11-20.pdf, 2008.
- [81] P. Sznajder. RPD volume properties. private communication, 2009.
- [82] S. U. Chung. Spin formalisms. page 81 p. CERN, 1971.
- [83] D. Aston et al. SLAC three-body partial wave analysis system. Technical report, 1985.
- [84] J. D. Hansen et al. Formalism and assumptions involved in partial-wave analysis of three-meson systems. *Nucl. Phys. B*, 81(3):403 – 430, 1974.
- [85] S. Neubert et al. Release note on $\pi^- \pi^+ \pi^- \pi^+$ from diffractive dissociation at COMPASS version II: partial wave analysis. *COMPASS-Release-Note*, 2011-04.

- [86] K. L. Au et al. Meson dynamics beyond the quark model: Study of final-state interactions. *Phys. Rev. D*, 35(5):1633–1664, 1987.
- [87] G. Otter et al. Partial wave analysis of the $(K\pi\pi)$ system in the L region in $K^-p \rightarrow (K^-\pi^+\pi^-)p$ at 10-GeV/c, 14.3-GeV/c and 16-GeV/c. *Nucl. Phys. B*, B147:1, 1979.
- [88] D. Aston et al. The strange meson resonances observed in the reaction $K^-p \rightarrow \bar{K}^0\pi^+\pi^-n$ at 11-GeV/c. *Nucl. Phys. B*, 292:693–713, 1987.
- [89] D. J. Herndon et al. Generalized isobar model formalism. *Phys. Rev. D*, 11(11):3165–3182, 1975.
- [90] J. P. Cummings and D. P. Weygand. An object-oriented approach to partial wave analysis. Technical Report physics/0309052, 2003.
- [91] K. Peters. A primer on partial wave analysis. *Int. J. Mod. Phys.*, A21:5618–5624, 2006.
- [92] E. P. Wigner. *Gruppentheorie und ihre Anwendung auf die Quantenmechanik der Atomspektren*, volume 2. F. Vieweg und Sohn, 1931.
- [93] F. v. Hippel and C. Quigg. Centrifugal-barrier effects in resonance partial decay widths, shapes, and production amplitudes. *Phys. Rev. D*, 5(3):624–638, 1972.
- [94] S. U. Chung. Formulas for partial-wave analysis version II. GNL-QGS-93-05, 1993.
- [95] K. Gottfried and J. Jackson. On the connection between production mechanism and decay of resonances at high energies. *Nuovo Cimento*, 33:309–330, 1964.

CURRICULUM VITAE

Personal Information

Prometeusz Kryspin Jasinski
Kaiserstrasse 19A
55116 Mainz
Germany
tel: +49 177 55 26367
Promme@web.de



I was born on the 14th of February, 1980 in Duszniki Zdr. (Poland). One year later I moved with my parents to Germany where I was raised and educated for the past years. Despite the long time I have spend in Germany I still do have the Polish citizenship and I do speak polish, too.

Education

- 1986–1990 : Attending the primary school at the *Carl-Zuckmayer-Schulzentrum* in Mainz
- 1990–2000 : Attending the *Rabanus-Maurus-Gymnasium* (secondary school) in Mainz
- 2000–2007 : Graduating in Physics at the *Johannes-Gutenberg Universität* in Mainz
- 2007–2011 : Ph.D. student at the *Institut für Kernphysik* in Mainz

I was studying physics at the University of Mainz with the emphasis on computing in all varieties. For my diploma thesis I was performing quality studies on the photomultiplier tubes of the CEDAR detectors of the COMPASS experiment at CERN.

As a Ph.D. student I continued the work with those detectors, giving me the great opportunity to perform a full physics measurement: I was involved in the operation of the CEDAR detectors, responsible for the data acquisition chain and the data decoding in the years 2008 and 2009. The subsequent analysis of excited kaons in the beam required, moreover, to run a full MC-simulation chain of the COMPASS detector with several modifications and upgrades of the available software.

Despite the full-time employment for the COMPASS collaboration as well as education services at the University, I was lucky to start my own small family with my lovely wife, my daughter and my son by my side.